Probing the function of $\alpha_2\delta$ voltage-gated calcium channel subunits in the genetic model system *Drosophila melanogaster*

Laurin Heinrich

Dissertation, 2019

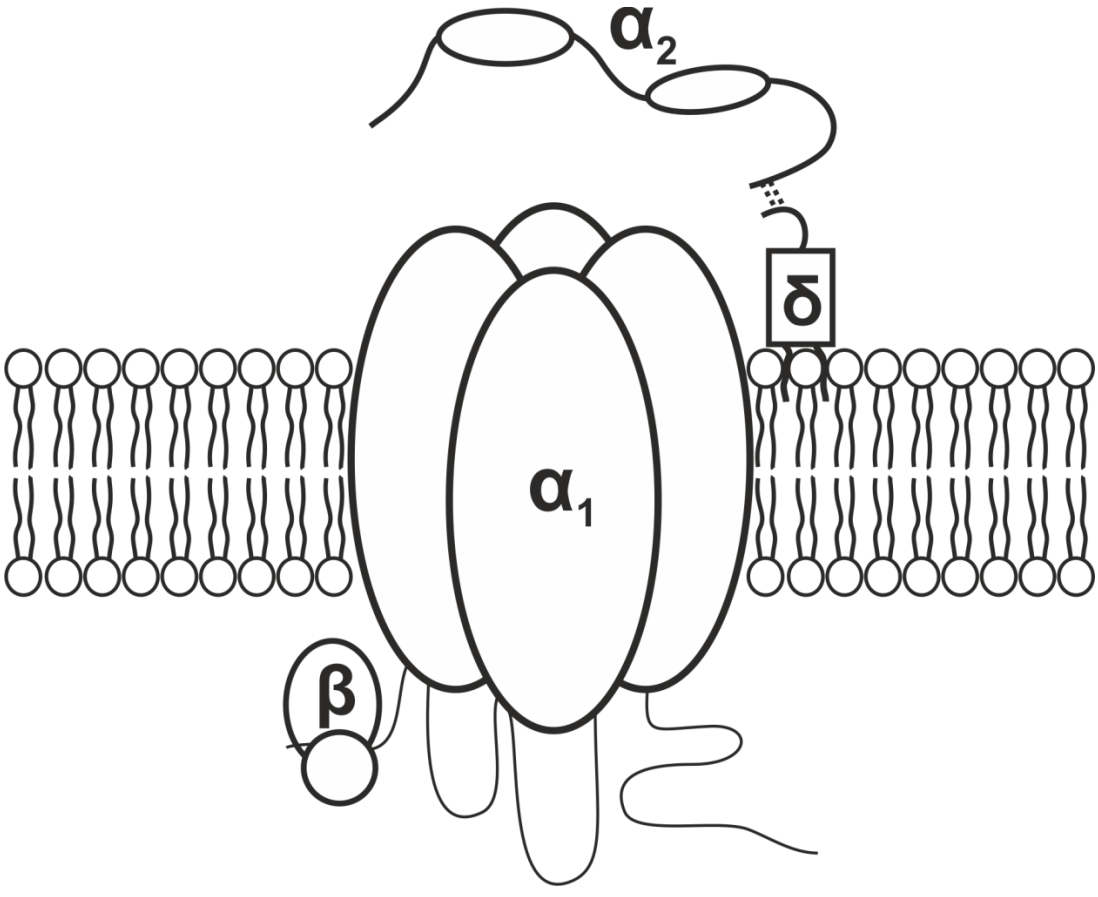

Probing the function of $\alpha_2\delta$ voltage-gated calcium channel subunits in the genetic model system *Drosophila melanogaster*

Dissertation zur Erlangung des Grades

Doktor der Naturwissenschaften

Am Fachbereich Biologie der

Johannes Gutenberg-Universität Mainz

Laurin Heinrich

geb. am 11.05.1991 in Potsdam

Mainz, 2019

Tag der mündlichen Prüfung: 23.10.2019

Table of Contents

Acknowledgments

I thank Dr. S. R. and Prof. Dr. C. D. for supervision, support and many helpful discussions in the course of my doctoral thesis.

I further thank Dr. S. R. for collaboration in my project: Stefanie was responsible for recording calcium currents from larval, pupal and adult motoneurons. She further conducted calcium imaging experiments with activation of MN5 via current injections.

I thank N. K. for conducting two-electrode voltage clamp (TEVC) recordings at the larval neuromuscular junction, to study the effect of gabapentin.

Last but not least, I thank my colleagues for all the fun, the vital coffee breaks and helpful conversations. I especially thank C. and L. for critical reading of the manuscript.

Abstract

Voltage-gated calcium channels (VGCCs) are crucial for the normal function of excitable cells, and thus, of the nervous system. Correct function of VGCCs depends on their biophysical properties, localization, and density. In vertebrates, there are 10 genes for the pore-forming α_1 subunit, but still, the number of Ca^{2+} dependent mechanisms seems to largely outcompete the number of VGCC genes. The interaction of high voltage-activated (HVA) α_1 subunits with additional accessory subunits, like $\alpha_2\delta$, increases the number of functionally different HVA VGCC complexes, but the underlying functional code for α_1-$\alpha_2\delta$ interaction remains incompletely understood. This study aims to unravel the combinatorial code of functional α_1-$\alpha_2\delta$ interactions by testing whether (i) different α_1-$\alpha_2\delta$ combination serve different or redundant functions, (ii) whether different $\alpha_2\delta$ subunits modulate distinctly different properties of VGCCs, and (iii) whether different $\alpha_2\delta$ subunits are specifically required at different subcellular compartments. We use the relatively simpler situation of *Drosophila melanogaster*, where only 8 instead of the 112 possible vertebrate α_1-$\alpha_2\delta$-β combinations exist. We further focus our analysis on individually identified motoneurons (MNs) with well-described functions for the *Drosophila* Ca_V1 and Ca_V2 homologs in different subcellular compartments.

Our findings show that both Stj ($d\alpha_2\delta_3$) and $d\alpha_2\delta_1$ are expressed in many types of neurons, including MNs, but predominantly localize to different subcellular compartments, thus, indicating functional differences. Electrophysiological analysis demonstrates that Stj is required for correct calcium current amplitudes of both Ca_V1 and Ca_V2, while $d\alpha_2\delta_1$ is not. Stj is required for normal Ca_V2 current amplitudes at all developmental stages (larva, pupa, and adult) and in all subcellular compartments (somatodendritic, axon & axon terminal) of *Drosophila* MNs. By contrast, $d\alpha_2\delta_1$ is required for allocation of Ca_V2 channels specifically to dendrites. Loss of $d\alpha_2\delta_1$, therefore, results in shifts of dendritic Ca_V2 channel to the axon. In conclusion, we find that at least Stj and $d\alpha_2\delta_1$ serve distinctly different functions in the same MNs and are not able to functionally compensate for each other. This contrasts data from heterologous expression systems where redundant functions have been reported, but is in accord with specific $\alpha_2\delta$ mutations causing different human brain diseases. One possible explanation could be that full functional diversity of $\alpha_2\delta$-α_1 interactions may unfold only in the brain, because our data hint on functional redundancy of Stj and $d\alpha_2\delta_1$ in larval muscles. Our findings start unraveling how different α_1-$\alpha_2\delta$ combinations regulate functional calcium channel diversity in different sub-neuronal compartments, and may provide an entry point toward understanding how mutations of different $\alpha_2\delta$ genes underlie brain diseases.

1. Introduction

Correct function of neuronal circuits depends on the properties of its component neurons and the synaptic connections between them. The properties of neurons are mainly defined by the complement of ion channel proteins localized to the membranes (Hille, 2001). Thus, ion channel function is crucial for normal brain function. Vice versa, ion channel malfunction is implicated in numerous brain disorders such as epilepsy, episodic ataxia or dystonia (Adelman *et al*., 1995; reviewed by Dworakowska & Dolowy, 2000; Jun *et al*., 1999; Ophoff *et al*., 1996; Sprunger *et al*., 1999; Steinlein *et al*., 1995). Voltage-dependent ion channels are transmembrane proteins that open and close depending on the membrane potential of the cell. In their open state, they are selectively permeable to certain ions (reviewed by Hille, 2001). Charge transfer through voltage-gated ion channels shapes neural excitability by causing action potential initiation and propagation, mediating synaptic input computations and translating membrane excitability to intracellular signaling (Abbott & Regehr, 2004; Dolmetsch *et al*., 1997; Fletcher *et al*., 2011; Takahashi & Momiyama, 1993; Wheeler *et al*., 2012). Especially with respect to the last point, voltage-dependent calcium channels (VGCCs) occupy a special position.

1.1 Voltage-gated calcium channels (VGCC)

The activity-dependent influx of Ca^{2+} ions through VGCCs serves not only as a charge carrier but also as a ubiquitous intracellular messenger. Thus, the activation of VGCCs influences not only the electrical activity of a nerve cell but also a large number of intracellular processes (reviewed by Berridge *et al*., 1998). These include, for example, activity-dependent exocytosis of synaptic vesicles (Neher & Sakaba, 2008; Schneggenburger *et al*., 2012), calcium-mediated transcription (West *et al*., 2001; West & Greenberg, 2011), calcium-mediated activity-dependent translation in dendrites (E. P. Huang, 1999), as well as a large number of calcium-dependent neuronal differentiation processes during development (Spitzer, 2002, 2006). Ca^{2+} as charge carrier plays a role in neuronal excitability including, among others, the amplification of postsynaptic potentials in spinal motoneurons (Heckman *et al*., 2003), rhythmic oscillations in thalamocortical neurons (Contreras,

2006), coincidence detection via dendritic calcium channels in pyramidal cells (Larkum *et al*., 1999) and much more. Thereby, the specific functions of VGCCs in a particular nerve cell depend on both, the biophysical properties of the channel and its sub-neuronal localization:

The biophysical properties of VGCCs are defined by the activation and inactivation voltages and kinetics as well as the single-channel conductivities for calcium. Different biophysical channel properties underlie vastly different functions in neurons. For example, postsynaptic potentials in spinal motoneurons as well as in *Drosophila* larval crawling motoneurons (Kadas *et al*., 2017) are amplified by L-type calcium channels (Heckman *et al*., 2003). These open at approximately -40 mV, inactivate relatively slowly and have relatively high single-channel conductivity. The low inactivation kinetics of L-Type currents contribute to persistent inward current (PIC, Heckmann *et al*., 2003) and are well suited to ensure sufficiently long-lasting depolarization upon synaptic input that is splayed out in time during waves of excitatory input to spinal motoneurons. By contrast, T-type calcium channels contribute to rhythmic oscillations in thalamocortical neurons during mammalian sleep (Contreras, 2006). T-type channels open already at -60 mV, inactivate fast and have low single-channel conductivity. The negative activation voltage is essential to bring H-current mediated depolarizations over a firing threshold so that each hyperpolarization is followed by the sequential depolarization via HCN and T-type channel activation (McCormick & Huguenard, 1992). Therefore, the different activation voltages and kinetics of L-type versus T-type channels are well suited to accommodate these different functions in motoneurons versus thalamocortical neurons. Assuming a similar number of channels being expressed this would result in a fundamentally different amount of Ca^{2+} ions entering the cell, which may in turn differentially affect downstream mechanisms.

Second, the function of VGCCs depends on their subcellular localization and expression levels. Exocytosis of synaptic vesicles requires VGCCs at the active zone in the axon terminal (Borst & Sakmann, 1996; Catterall, 2000; Dunlap *et al*., 1995; Neher & Sakaba, 2008; Takahashi & Momiyama, 1993). In order to mediate activity-dependent transcription, VGCCs must be localized in the membrane of somata. For the amplification of postsynaptic potentials, VGCCs need to be localized in dendrites (Heckman *et al*., 2003). Thus, the central functions of nerve cells are decisively determined by the biophysical properties, localization, and number of VGCCs.

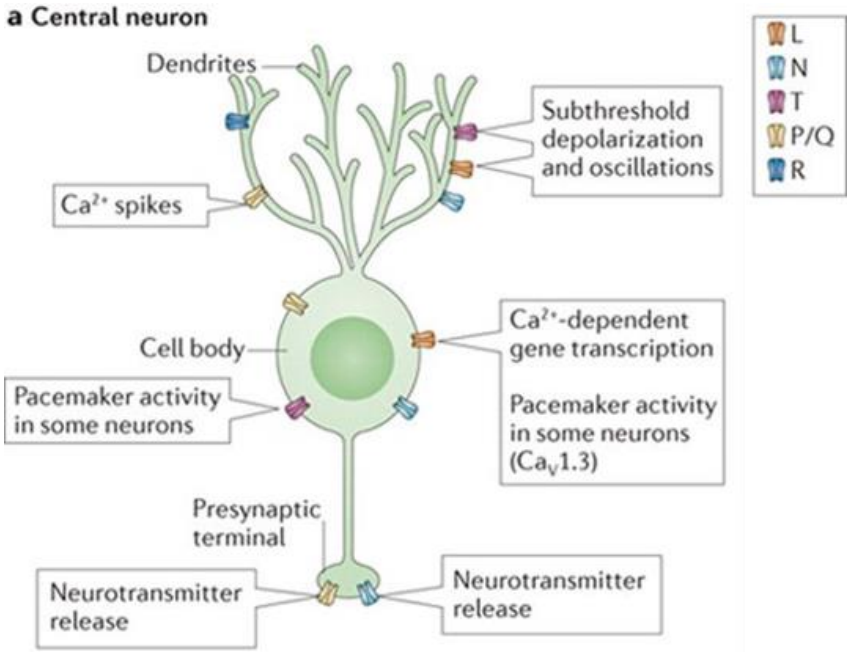

Fig.1: Functions and distribution of different calcium channels in central neurons
Schematic representation of the main Ca_V channel localization and functions in dendrites, cell body and axon terminals of central neurons. Specific functions seem to require a specific localization of the channel and a specific channel type (L-, N-, T-, P/Q- & R-Type). Please note that localization and function of different channel types can vary greatly between different classes of neurons. (Modified from Dolphin, 2012)

1.2 The α_1 subunit of VGCCs

The number of Ca^{2+} dependent mechanisms seems to largely outcompete the number of VGCC genes. In vertebrates, ten different genes are known to encode for the pore-forming α_1 subunit. The α_1 subunit genes are divided into three families (Ca_V1-Ca_V3) according to their amino acid sequences. By contrast in *Drosophila melanogaster,* only one homologous gene exists for each of the three vertebrate VGCC families (see Fig.). As the pore-forming subunit, α_1 consists of four homologous domains each containing 6 transmembrane α-helices, which are linked by intracellular loops (Tanabe *et al.*, 1987). By carrying the voltage sensor, α_1 fundamentally defines the biophysical properties of the channel. Based on their biophysical properties α_1 VGCC subunits are further subdivided (Catterall, 2011). The four vertebrate Ca_V1 channels ($Ca_V1.1$-$Ca_V1.4$) as well as the *Drosophila* Ca_V1 channel homolog (Dmca1D) mediate so-called L-type currents (see above) and have relatively high activation voltages (HVA) (Catterall, 2011; Worrell & Levine, 2008). Ca_V1 channels are known to play an important role in excitation-contraction coupling in the skeletal muscle (Catterall, 1991, 2011). In neurons, among other functions, Ca_V1 channels regulate neuronal excitability by amplification of synaptic input in dendrites (Heckman *et al*., 2003; Kadas *et al*., 2017). Depending on the neuron type, Ca_V1 channels can be found in all subcellular compartments (soma, axon, dendrites; Kadas *et*

al., 2017 and axon terminals; e.g. Brandt *et al*., 2005). Ca_V2 channels are also known to mediate HVA currents. According to their pharmacological profile and their properties, the three vertebrate Ca_V2 channels ($Ca_V2.1$ - $Ca_V2.3$) are further distinguished into N-, PQ-, and R-type (Nowycky *et al*. 1985; Llinas *et al*., 1989 ; Randall & Tsien, 1995). Ca_V2 channels including the *Drosophila* Ca_V2 homolog (Dmca1A, also called cacophony) constitute the prominent channel in axon terminals of most neurons and mediate vesicle exocytosis (Wheeler et al., 1994). Still, Ca_V2 channels can also be localized somatically or dendritically (Ryglewski *et al*., 2012). In specific neurons, Ca_V2 channels may even exhibit relatively negative activation (LVA) thresholds (Ryglewski *et al*., 2012). The three vertebrate Ca_V3 α_1 subunits (CaV3.1-CaV3.3) and the *Drosophila* homolog (DmαG) activate transiently (T-Type) and at more negative membrane voltages (LVA) (Nowycky *et al*., 1985; Perez-Reyes *et al*., 1998). Among other functions, Ca_V3 channels play a role in the repetitive firing of action potentials and oscillatory activity in neurons (Cain & Snutch, 2010; Chevalier *et al*., 2006; Destexhe & Sejnowski, 2003; Huguenard & Prince, 1992). Like Ca_V1 and Ca_V2, Ca_V3 channels can also be functional in axon terminals (Pan *et al*., 2001).

This indicates that all VGCC families can adopt several different functions, and vice versa, that a certain function is not necessarily mediated by only one specific calcium channel family. Since Ca_V2 channels can also mediate LVA currents in some neurons the classical view of Cav1 and Cav2 as HVA VGCCs and Cav3 as LVA VGCCs has to be viewed with caution. This might be the reason for contradictive data on the pharmacology of e.g. T-type channels, which is a problem for many clinical applications, for instance in the treatment of certain forms of epilepsy (reviewed by Heady *et al*., 2001).

In addition, this finding might suggest an additional modification of HVA calcium channels regarding their channel properties. Indeed, the α_1 subunit is known to interact with so-called accessory subunits (Fig.2), which may add to the wealth of VGCC functional diversity. However, it is unclear to what extent the properties, localization, and abundance of α_1 subunits are regulated by different accessory subunits.

1.3 Accessory subunits of VGCCs

The regulatory subunits of HVA calcium channels are divided into $\alpha_2\delta$, β and γ subunits. In vertebrates, four different $\alpha_2\delta$ ($\alpha_2\delta_1$ - $\alpha_2\delta_4$) and β genes (β_1 - β_4), as well as eight different genes of the γ subunit (γ_1 - γ_8) are known (reviewed by Dolphin, 2013). By contrast, *Drosophila melanogaster* also contains four different genes for $\alpha_2\delta$ ($d\alpha_2\delta_1$ - $d\alpha_2\delta_4$), but only one gene each for the β and the γ subunit. In heterologous expression systems, a minimal co-expression of all three subunits, α_1, $\alpha_2\delta$, and β, is required for surfacing, normal biophysical properties and current amplitudes of HVA calcium channels (reviewed by Campiglio *et al*., 2015; Buraei & Yang 2013). Therefore, accessory subunits seem indispensable for the normal function of these channels. The β and γ subunits will not be discussed here, as this project examines the functions of the $\alpha_2\delta$ subunit.

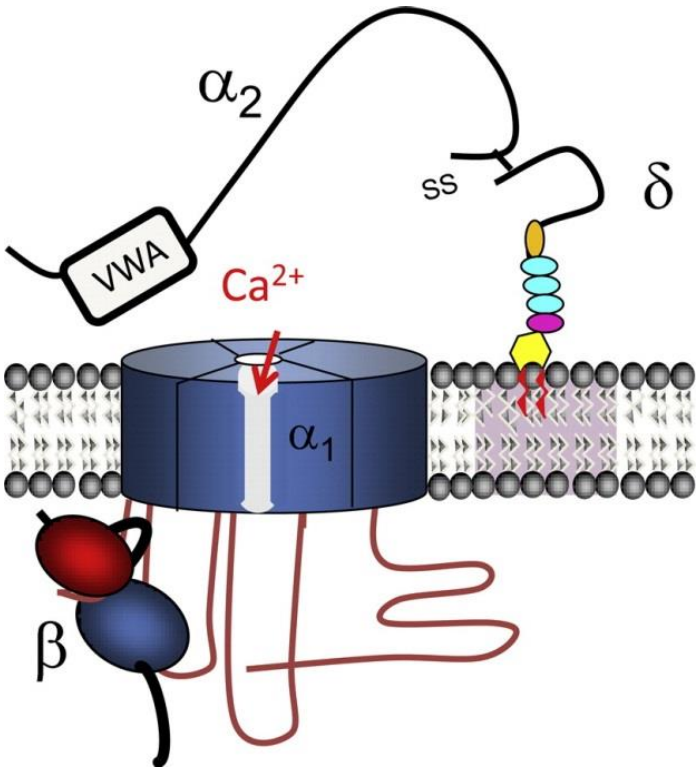

Fig.2: Schematic representation of a HVA Ca_V channel
High voltage activated (HVA) calcium channels consist of a pore-forming α_1, which is a transmembrane protein. α_1 associates with accessory subunits called $\alpha_2\delta$ and β. β is cytosolic and binds to an intracellular loop of α_1. $\alpha_2\delta$ localizes extracellularly and is coupled to membranes via a GIP anchor. $\alpha_2\delta$ interacts with α_1 via the Von Willebrand Factor A (VWA) domain. (Dolphin, 2013)

1.4 The $\alpha_2\delta$ subunits

$\alpha_2\delta$ subunits consist of an α_2 and δ protein, which are both encoded by the same gene. After post-translational cleavage of α_2 and δ, both proteins are transported into the endoplasmic reticulum via a signal sequence. In the ER, they are coupled to each other via

disulfide bonds and glycosylated (reviewed by Dolphin, 2012). The complete construct yields an extracellular protein, which is attached to the membrane via a glycophosphatidylinositol (GIP) anchor (Davies *et al*., 2010, Kadurin *et al*., 2012). The α_2 component of the protein carries a Von Willebrand Factor A domain (VWA domain) with a metal ion-dependent adhesion site (MIDAS) and two chemosensor-like cache domains necessary for protein-protein interactions (reviewed by Dolphin, 2012).

As an accessory subunit, $\alpha_2\delta$ is believed to influence VGCC function by modulating the biophysical properties, cell-surface expression, and transport of the channel. $\alpha_2\delta$ subunits seems to play a role in amplifying the calcium currents and modulating the voltage dependency and the steady-state inactivation of α_1 (Davies *et al*., 2010; Felix *et al*., 1997; Fuller-Bicer *et al*., 2009; Herlitze *et al*., 2003; Klugbauer *et al*., 1999; Singer *et al*., 1991; Wakamori *et al*., 1999). However, $\alpha_2\delta$ subunits do not alter the single-channel conductivity but increase the surface expression of HVA calcium channels (Barclay *et al*., 2001; Brodbeck *et al*., 2002; Shistik *et al*., 1995). Together with the β subunit, $\alpha_2\delta$ is important for correct transportation, stabilization and/or targeting of HVA calcium channels (Campiglio & Flucher, 2015). Thus, mutations in $\alpha_2\delta$ can lead to a reduction in Ca_V channel density and transportation (e.g. Cantí *et al*., 2005). For example, $\alpha_2\delta_3$ is needed for the functionally adequate localization of Ca_V2 channels at the larval neuromuscular junction of *Drosophila* (Kurshan *et al*., 2009; Ly *et al*., 2009).

In the last few years, new functions and interaction partners of $\alpha_2\delta$ subunits were found (reviewed by Dolphin, 2018). Some are related to, but some are also apart from interaction of $\alpha_2\delta$s with VGCCs. α-neurexins and BK channels are believed to interact with $\alpha_2\delta$ subunits, leading to changes in calcium current amplitudes (Brockhaus *et al*., 2018; Tong *et al*., 2017; Zhang *et al*, 2018). For example, retrograde inhibition is mediated by the interaction of postsynaptic neurexin (NRX-1) with presynaptic $\alpha_2\delta_3$ at the neuromuscular junction of *C. elegans* (Tong *et al*., 2018). $\alpha_2\delta$ subunits are further known as therapeutic targets for the anti-epileptic drugs gabapentin and pregabalin (Marais *et al*., 2001; Taylor *et al*., 2007).

Apart from their interaction with HVA calcium channels, $\alpha_2\delta$ subunits play a role in synaptogenesis. $\alpha_2\delta_3$ is crucially needed for normal bouton formation of the embryonic NMJ of *Drosophila* even before calcium channels locate there (Kurshan *et al*., 2009). In addition,

in the CNS of mice, $\alpha_2\delta_1$ was identified as a receptor for thrombospondin, a protein involved in synaptogenesis (Eroglu *et al.*, 2009). Furthermore, $\alpha_2\delta$ subunits can increase pre- and postsynaptic activity by modulation of NMDA receptors, as recently shown in the hypothalamus of rats and in medium spiny neurons of mice (Chen *et al*., 2018; Zhou *et al*., 2018).

Mutations in $\alpha_2\delta$ genes can result in severe neuronal defects and neurological diseases. The $\alpha_2\delta_2$ mouse mutant '*ducky*' displays symptoms of epilepsy and cerebellar ataxia (Barclay *et al*., 2001) and $\alpha_2\delta_3$ mutant flies die due to severe motor deficits in the late embryonic stage (Kurshan *et al*., 2009). This proves that $\alpha_2\delta$ subunits must have essential functions. However, the system of modification and modulation of α_1 channels by $\alpha_2\delta$ subunits is incompletely understood. It is unclear whether specific $\alpha_2\delta$ proteins always interact with only some α_1 subunits, i.e. whether there is a clear combinatory code between α_1 and $\alpha_2\delta$ and whether different α_1-$\alpha_2\delta$ combinations serve different or partly redundant functions. It is also largely unknown whether different $\alpha_2\delta$ subunits are responsible for the correct localization of α_1 subunits in different neuronal compartments (soma, dendrites, axon & axon terminals).

To solve these questions, we will use the relatively simpler situation of *Drosophila melanogaster*. Until now, most studies on the function of $\alpha_2\delta$ on the Ca_V channel kinetics were done in heterologous expression systems, where some might endogenously express concentrations of $\alpha_2\delta$ (Kaldurin *et al*., 2012; Singer-Lahat *et al*., 1992) and β (Canti *et al.*, 2001; Leroy *et al*., 2005) of their own. Furthermore, different $\alpha_2\delta/\alpha_1/\beta$ combinations could reveal different functions for $\alpha_2\delta$ proteins and not all of them might be physiologically relevant. Thus, conflicting data arises. For example, several studies suggest that $\alpha_2\delta$ hyperpolarizes the voltage dependence of HVA calcium channels (Felix *et al*., 1997; Platano *et al*., 2000). By contrast, other studies report that $\alpha_2\delta$ seems to have no effect on the voltage-dependent activation of Ca_V channels (Brodbeck *et al*., 2002; Wakamori *et al*., 1999). Additionally, some studies, show a hyperpolarized steady-state inactivation of different α_1 subunits through various $\alpha_2\delta$s (Davies *et al*., 2010; Felix *et al*., 1997; Fuller-Bicer *et al*., 2009; Wakamori, *et al*., 1999), but in other studies no effects of $\alpha_2\delta$ on the steady-state inactivation was found (Qin *et al*., 1998). We, therefore, think that *in situ* or even *in vivo* studies are required to assess the functions of different α_1-$\alpha_2\delta$ combinations.

1.5 Drosophila melanogaster

We believe that *Drosophila* presents a suitable model system. As mentioned, vertebrates possess 8 different genes for HVA α_1 subunits and 4 genes each for the $\alpha_2\delta$ and β subunit. Thus, even without considering isoform diversity there are 112 possible HVA calcium channel combinations, making it nearly impossible to probe the functions of all possible α_1-$\alpha_2\delta$ interactions. With only 2 different genes for HVA α_1 subunits, 4 genes for the $\alpha_2\delta$ and only one gene for the β subunit, possible HVA calcium channel combinations are reduced to 8 in *Drosophila* (see Fig.3). Hopefully, this will allow us to investigate the functions of the individual $\alpha_2\delta$ proteins *in situ* or even *in vivo*. Furthermore, *Drosophila* has two well-identified motoneurons (one larval crawling neuron and one adult flight neuron) with well-described functions for the *Drosophila* Ca_V1 and Ca_V2 homolog in all subcellular compartments, which can be used for investigation. Additionally, *Drosophila* has a high variety of genetic manipulations and tools, making it possible to assess the function of single α_1-$\alpha_2\delta$ combinations and thus unraveling a possible functional combinatory code of α_1 and $\alpha_2\delta$ subunits. It must be noted, however, that d$\alpha_2\delta$ subunits of *Drosophila* are not equal to $\alpha_2\delta$s of vertebrates in a one to one fashion, like the nomenclature might indicate (Ly *et al.*, 2008).

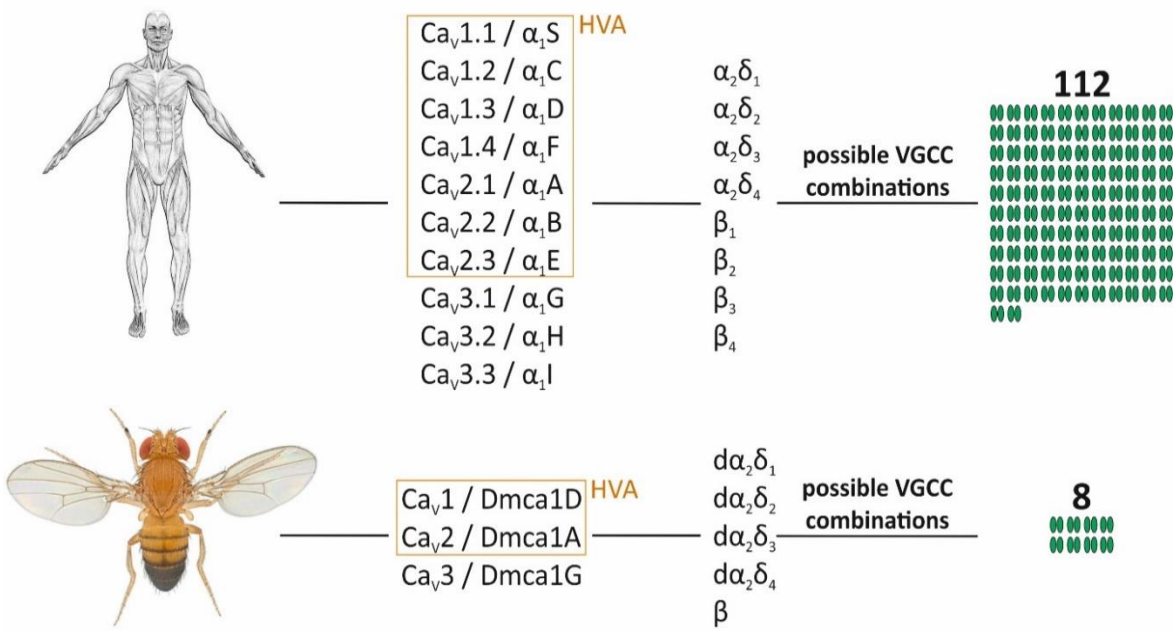

Fig.3: Amount of possible VGCC combinations in vertebrate vs *Drosophila*
The 10 vertebrate α_1 calcium channel genes are listed by their IUP/SU name (human figure). *Drosophila* has 3 α_1 genes, one homolog per vertebrate Ca_V1, Ca_V2 & Ca_V3 family. Drosophila α_1 genes are listed by their vertebrate homolog/*Drosophila* gene name. High voltage-activated (HVA) Ca_V genes are framed (orange square). They interact with $\alpha_2\delta$ & β subunits (gene names are listed). The number of HVA α_1 genes multiplied by the number of $\alpha_2\delta$ & β genes will give the amount of possible voltage-gated calcium channel (VGCC) combinations for each vertebrates and *Drosophila*.

1.5.1 The larval crawling motoneurons RP2 & aCC are used for investigation

The larval and embryonic neuromuscular system of *Drosophila m*. is a popular and well-characterized model system due to its stereotypical morphology and its relative simplicity. Each abdominal hemi-segment consists of 30 body wall muscles which are innervated by 34 motoneurons (Bossing & Technau, 1994; Landgraf *et al*., 1997; Sink & Whitington, 1991). The motoneurons approach their specific target muscles via one of 6 different nerve branches (ISN, ISNb, ISNd, SNa, SNc, and TN) (Landgraf *et al*., 1997; Schmid *et al*., 1999), where they form the neuromuscular junction (Fig. 4). Neuromuscular synapses also called synaptic boutons, are classified into four different bouton types according to their size (Hoang & Chiba, 2001): Type *Ib* (3-6 µm), Type *Is* (2-4 µm), Type *II* (1-2 µm) & Type *III* (2-3 µm).

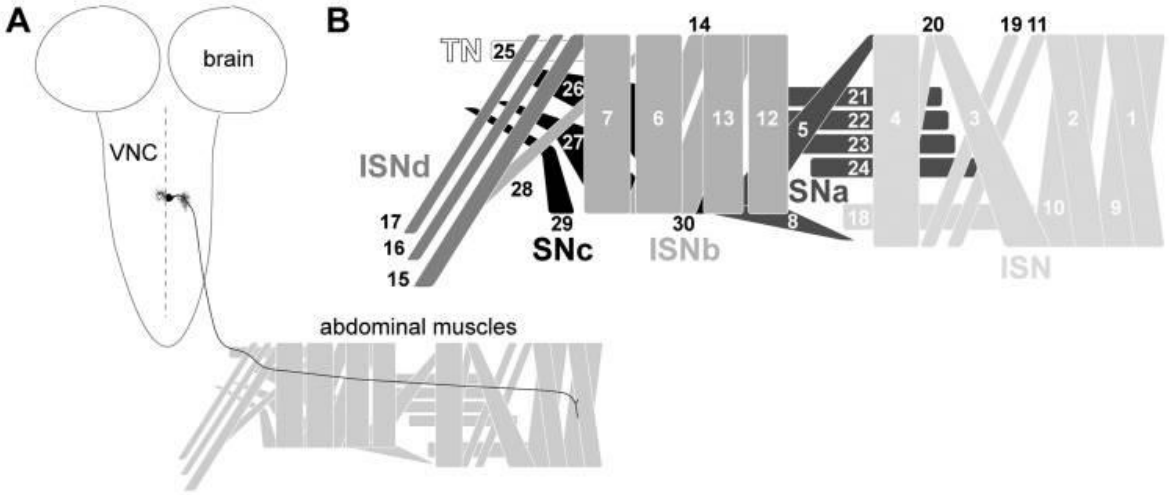

Fig.4: Larval body wall muscles of one hemi-segment
[**A**] Somata of larval crawling motoneurons are localized in the ventral nerve cord (VNC) of *Drosophila* larvae. Their axons project onto body wall muscles via six different nerve branches (ISNd, TN, SNc, ISNb, SNa & ISN) where they form the neuromuscular junction. [**B**] Each hemi-segment consists of 30 body wall muscles, which are numbered (Kim *et al.*, 2009).

For this study, the two well-characterized crawling motoneurons RP2 and aCC were used: The RP2 neuron, which is also called MNISN-Is forms *Is* type boutons on the muscles 1, 2, 3, 4, 9, 10, 18, 19 & 20. By contrast, the aCC neuron also called MN1-Ib forms *Ib* type boutons on muscle 1 (Hoang & Chiba, 2001). Due to their characteristic morphology and dorsal localization in the VNC, both neurons are easily identifiable and approachable for electrophysiological recordings. In contrast to aCC, RP2 neurons show a unique firing pattern which is characterized by a delayed spiking onset. This delay is believed to be controlled by a voltage-dependent potassium channel (*Shal*) (Landgraf *et al*., 1997), but also the Ca_V1 homolog Dmca1D seems to be involved (Schützler *et al*., 2019).

Dmca1D and Dmca1A are differentially localized in larval RP2 and aCC motoneurons (Worrell & Levine, 2008). Immunohistochemical staining indicates that the Ca_V1 channel localizes to every compartment (soma, axon, dendrites & axon terminals) of these neurons (Kadas *et al*., 2017; Klein, 2016). Voltage-dependent calcium currents measured from the soma are mainly generated by Dmca1D (Fig.5) (Worrel & Levine, 2008; Kadas *et al*., 2017). In dendrites, Ca_V1 channels are believed to amplify excitatory synaptic input (Kadas *et al*., 2017). Axonal Ca_V1 channels were found to increase the delay to the first spike and decrease the firing response of RP2 neurons to somatic current injections at low firing frequencies. At high firing frequencies, Dmca1D increases the firing response of RP2 neurons (Kadas *et al*., 2017). At the neuromuscular junction, Dmca1D localizes to the periactive zone of synaptic boutons and could possibly be involved in vesicle endocytosis (Klein, 2016; Kuromi *et al*., 2010). Thus, the Ca_V1 channel also might play a role in synaptic depression (Klein, 2016). In contrast, Dmca1A was found to co-localize with active zones at axon terminals. Vesicle exocytosis is mainly generated by calcium influx through the Ca_V2 homolog Dmca1A (Bódi *et al*., 1995; Hou *et al*., 2008; Kawasaki *et al*., 2000, 2002 & 2004).

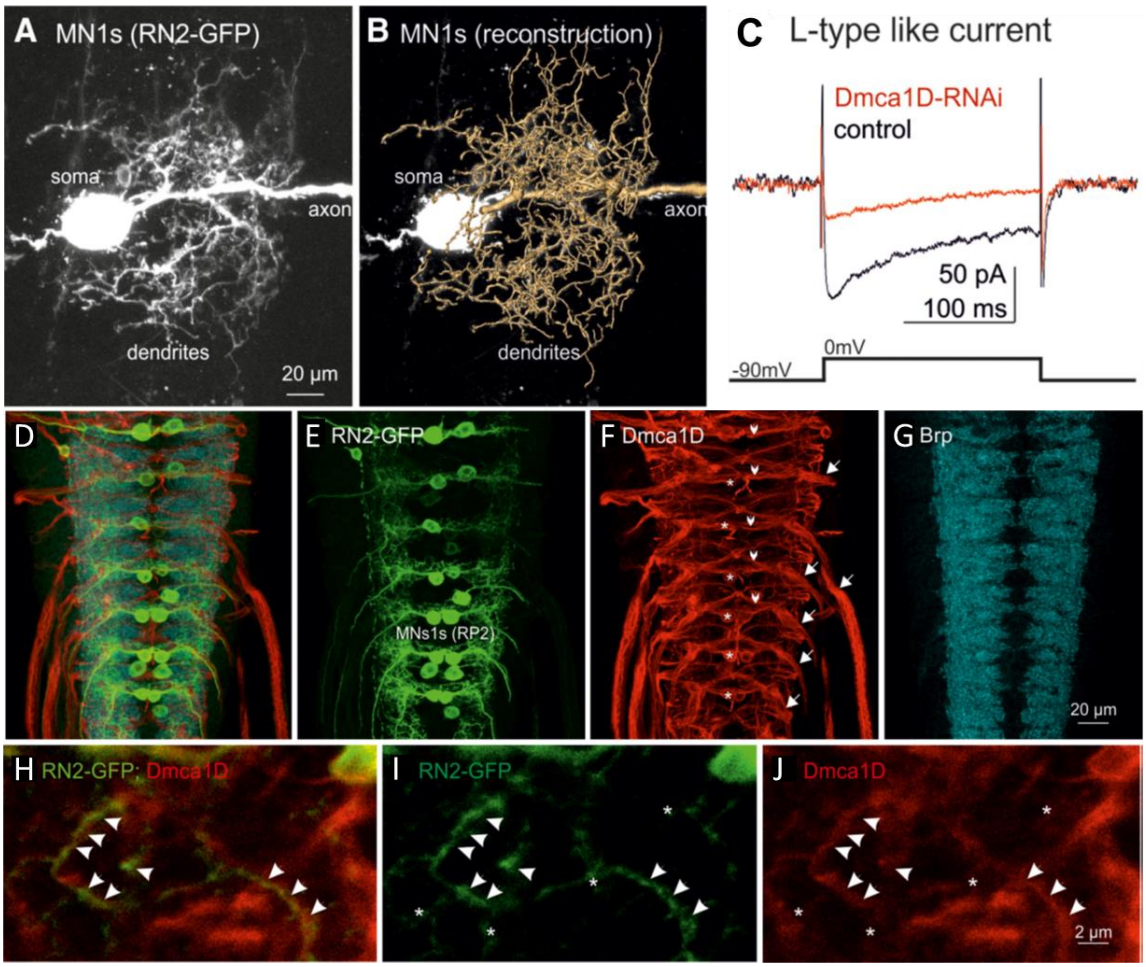

Fig.5: Ca_V1 localizes to every compartment of larval crawling motoneurons RP2 & aCC
[**A**] A representative image of an RP2 larval crawling motoneuron with [**B**] reconstruction of the dendritic tree. [**C**] Somatodendritic voltage-activated calcium currents measured from the soma, are mediated by the *Drosophila* Ca_V1 homolog Dmca1D. [**D-G**] Labeling of Dmca1D in RP2 and aCC reveals localization to [**F**] soma (asterisks), segmental nerve roots (arrows) & axons (arrowheads). [**H-J**] Dmca1D also localizes to dendrites (arrows). (Modified from Kadas *et al*., 2017)

1.5.2 The adult flight motoneuron MN5 is used for investigation

In the adult ventral nerve cord of *Drosophila,* there are five flight motoneurons per side, called MN1-5, which innervate the six dorsal longitudinal wing depressor muscles (DLMa-f). Thereby, MN1-4 each project onto only one muscle fiber on their ipsilateral side, while MN5 projects contralateral on DLMa and DLMb (Coggshall, 1978). Due to its dorsal localization and characteristic morphology, MN5 is easy to identify and approach for electrophysiological recordings (Ikeda & Koenig, 1988; Ryglewski & Duch, 2009). MN5 is a monopolar neuron and possesses a large dendritic tree with a total dendritic length of about 6500 µm (Vonhoff & Duch, 2010). The electrophysiological properties of MN5; e.g. its firing behavior and voltage-dependent potassium and calcium currents are well identified

(Duch *et al*., 2008; Ikeda & Koenig, 1988; Levine & Wyman, 1973; Ryglewski & Duch, 2009; Ryglewski *et al.*, 2012).

The Ca_V2 homolog of *Drosophila* the Dmca1A channel also called cacophony seems to be the main VGCC in these neurons, which makes it a useful model system for probing the functions of different $\alpha_2\delta$-Dmca1A combinations. Thus, Dmca1A mediates somatodendritic calcium currents of MN5. Interestingly, the Ca_V2 homolog has the ability to expresses HVA currents as well as LVA currents in these neurons (Fig.6; Ryglewski *et al*., 2012). Furthermore, cacophony is known to contribute to neuronal development and dendritic growth (Ryglewski *et al*., 2014). Indeed, VGCC are the first functionally expressed ion channels during MN5 pupal development and pupal (P7-P10) sodium carried action potentials are additionally shaped by Dmca1A calcium currents.

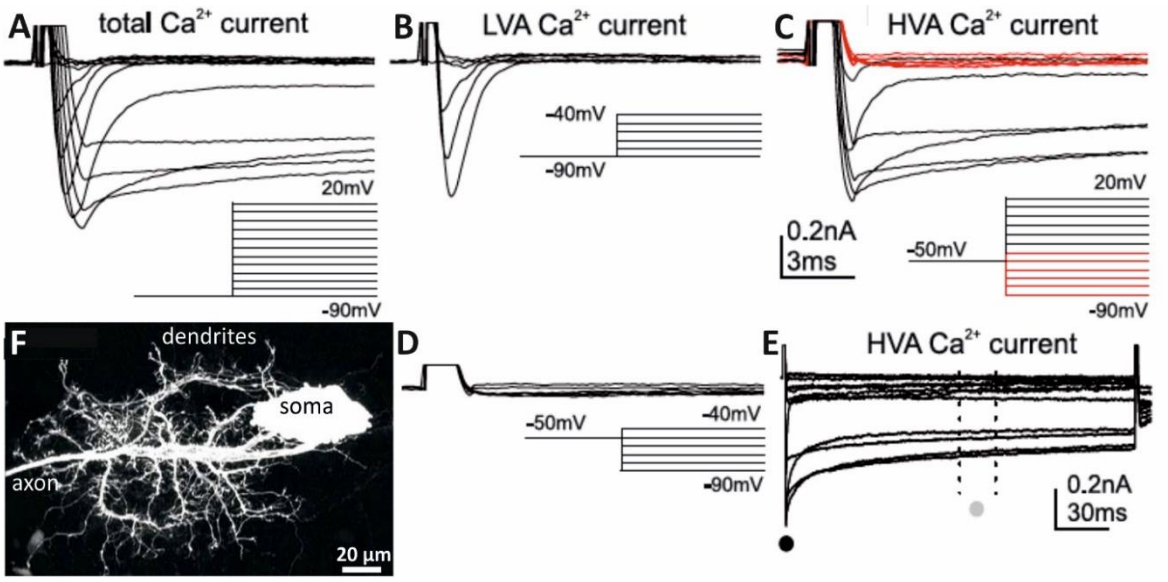

Fig.6: Ca_V2 channels mediate HVA and LVA currents in adult DLM neuron MN5
[**A-E**] Somatodendritic calcium currents measured from the soma of [**F**] MN5 DLM neurons. The Ca_V2 channel mediates [**C,E**] HVA as well as [**B**] LVA currents in those motoneurons. [E] Electrically isolated HVA currents reach their maximal current amplitude fast (black dot) and have a long-lasting sustained current (gray dot). (Modified from Ryglewski et al., 2012)

1.6 Aim of this study

In order to fulfill a manifold of different functions throughout the nervous system, a high diversity of VGCCs is needed. This diversity is further increased by the interaction of HVA calcium channels with additional accessory subunits, but the system of modulation of the α_1 through different $\alpha_2\delta$ proteins is largely unknown. The aim of this study is to provide

fundamentally new insights into the regulation of VGCCs by $\alpha_2\delta$ subunits. Thus, we want to address the following questions:

- Is there a combinatory code between different α_1- $\alpha_2\delta$ proteins, with different α_1-$\alpha_2\delta$ combinations serving distinctly different functions, or can different $\alpha_2\delta$ protein compensate for each other?

- Do different α_1-$\alpha_2\delta$ combinations serve distinctly different functions in different sub-neuronal compartments?

- Is there a division of labor among different $\alpha_2\delta$ subunits in different types of neurons or even within single neurons?

Previous findings from heterologous expression systems suggest that in principle any $\alpha_2\delta$ protein can interact with any α_1 HVA subunit (Campiglio & Flucher, 2015). However, different $\alpha_2\delta$ subunits seem to have different effects on different α_1 subunits, suggesting specific functional combinatorics (reviewed by Dolphin, 2013). For example, in HEK293T cells, transfected with $Ca_V1.4$ channels show a more depolarized activation voltage with $\alpha_2\delta_1$ than with $\alpha_2\delta_4$ (Lee *et al*., 2015). Additionally, co-expression of $Ca_V1.2$ and $\alpha_2\delta_1$ in oocytes increased calcium current amplitude more than co-expression of $Ca_V1.2$ and $\alpha_2\delta_2$ (Felix *et al*., 1997; Gao *et al*., 2000). Furthermore, especially in vertebrates, $\alpha_2\delta$ subunits were found to have cell- and tissue-specific expression patterns (Cole *et al*., 2005; Dolphin, 2012). This suggests that specific neuron types only express very specific α_1-$\alpha_2\delta$ combinations. For example, excitatory neurons seem to preferably express $\alpha_2\delta_1$, while inhibitory neurons seem to preferably express $\alpha_2\delta_2$ (Cole *et al*., 2005). This hypothesis is also supported by the fact that e.g. $\alpha_2\delta_2$ and $\alpha_2\delta_3$ mouse mutants only have functional and structural defects in some specific cell types. While the morphology and Ca_V2 current density of Purkinje cells were altered in $\alpha_2\delta_2$ mouse mutants (Brobeck *et al*., 2002), normal function and synaptogenesis of auditory nerve terminals were disrupted in $\alpha_2\delta_3$ mutants (Pirone *et al*., 2014). Whether different $\alpha_2\delta$ subunits also have differential functions in different subcellular compartments is not well investigated yet. The subcellular localization of different $\alpha_2\delta$ subunits is difficult to examine in vertebrates due to lack of appro-

priate antibodies. In the rat CNS, $\alpha_2\delta_1$ mainly localizes to neuropil regions and presynaptic terminals but was also found in the soma of neurons (Bauer *et al*., 2009; C P Taylor & Garrido, 2008). By contrast, both $\alpha_2\delta_1$ and $\alpha_2\delta_3$ were mainly found in the soma of multiple cell types in the retina (Huang *et al*., 2013; Müller *et al*., 2015)). In *Drosophila*, $\alpha_2\delta_3$ localizes to axon terminals in larval crawling motoneurons, where it is required for correct Dmca1A channel density and synaptogenesis (Ly *et al*., 2008; Dickman *et al*., 2008; Kurshan *et al*., 2009).

$\alpha_2\delta_3$ mutant flies are embryonic lethal, which further suggests that at least this $\alpha_2\delta$ subunit has specific functions that cannot be compensated for by other $\alpha_2\delta$ proteins (Ly *et al*., 2008; Ly *et al*., 2008; Kurshan *et al*., 2009). Although $\alpha_2\delta$ proteins might have at least partly redundant functions, based on the available data we do not believe this to be the case. Thus, we hypothesize a division of labor between different $\alpha_2\delta$ subunits regarding the modification of channel properties and channel localization.

To test this hypothesis, we will assess whether $\alpha_2\delta$ subunits are also differentially expressed in *Drosophila melanogaster*. We'll further try to assess whether they localize to different subcellular compartments, which is rather difficult to investigate in the CNS of mammals. In the larval crawling motoneurons RP2 and aCC, we can probe for distinct functions of different Dmca1D-$\alpha_2\delta$ combinations. We will test, whether different $\alpha_2\delta$ proteins are needed for correct localization of the 1D channel to different cellular compartments (dendrites, axon & axon terminals) of these neurons and/or whether the biophysical properties of this channel are altered through interaction with different $\alpha_2\delta$s. $d\alpha_2\delta_3$-Dmca1A interaction is already known at axon terminals. Still, we want to assess whether the Ca_V2 channel also interacts with $d\alpha_2\delta_1$ at the *Drosophila* NMJ. Additionally, we will use the adult wing depressor motoneuron MN5 to investigate functional differences of different Dmca1A-$\alpha_2\delta$ combinations. We will test whether different $\alpha_2\delta$ proteins are needed to enable the channel to mediate two distinctly different calcium currents (HVA & LVA currents) and whether Ca_V2 channel localization to different sub-neuronal compartments is mediated by different $\alpha_2\delta$ subunits. In the long term, this may provide an important basis for the development of new strategies for diseases based on VGCC malfunctions.

2. Material & Methods

2.1 Fly keeping

If not noted otherwise, flies were kept and raised in plastic vials (ø 2 cm) on standard cornmeal-agarose food (see appendix 6.6.1) in a 25 °C incubator with a 12 h light/dark cycle. Flies with temperature-sensitive constructs had to be kept on 18 °C. Staging of larvae or pupae was done as already described (Bainbridge & Bownes, 1981). All used fly lines are listed in the appendix (see 6.1)

2.2 Producing a MiMIC protein trap

Due to lack of appropriate antibodies against $d\alpha_2\delta$ subunits in *Drosophila*, Stj and $d\alpha_2\delta_1$ needed to be tagged endogenously in order to assess their expression and localization pattern. Therefore, the MiMIC protein trap technique was used. The *Minos* mediated integration cassette (MiMIC) is randomly integrated into the genome of *Drosophila melanogaster*. Flanked by two inverted φC31 bacteriophage *attP* sites it contains a gene-trap cassette and the *yellow*$^+$ marker. Thus, through expression of the φC31 integrase driven by a *vasa* promoter the gene-trap cassette can be exchanged by recombinase-mediated cassette exchange (RMCE) through different constructs, which are flanked by inverted *attB* sites (Venken *et al*., 2011). These constructs carry a synthetic exon encoding a variety of protein tags (e.g. GFP, mCherry, Gal4) flanked by an acceptor splicing site (SA) and a splice donor site (SD). If integrated into a coding intron this allows for various genetic manipulations of the affected gene (Venken *et al*., 2011). Therefore, when exchanging the MiMIC core with such a construct, an artificial exon within the ORF of the gene is created that is then integrated into the mature protein. If successful, this leads to expression of a new exon thus e.g. resulting in GFP-tagged proteins.

A functional MiMIC protein trap was available for $d\alpha_2\delta_1$. The GFP tag is located between the first and second exon (between amino acids 38 and 39) and thus, clearly before the DNA sequence coding for the VWA domain. Therefore, the tag must be localized in the α_2 part of the protein (flybase.com). Fly lines with a MiMIC gene trap in a coding intron of Stj

(BDSC_34109) were available. The construct is located between the second and the third exon of Stj (between amino acid 66 and 67), also clearly before the DNA sequence coding for the VWA domain of Stj. Therefore, the tag must also be localized in the α_2 part of the protein (flybase.com). To look for differential expression and localization of Stj and $d\alpha_2\delta_1$, both proteins should have different tags. Since $d\alpha_2\delta_1$ was tagged with GFP, we decided to tag Stj with *mCherry*. Plasmids containing a *mCherry* construct (GDP1299_pBS-KS-attB1-2-PT-SA-SD-0-mCherry) were obtained from the Drosophila Genomics Resource Center (DGRC, https://dgrc.bio.indiana.edu/Home). The constructs had to be compatible with the splicing phase (0) of the affected intron.

2.2.1 Injection procedure

2.2.1.1 Prearrangements for injection

To increase the amount of fertilized eggs laid during the injection procedure, as many female virgins of the *vasa* integrase line (*vasa*;Cyo/Sna^{Sco}) as possible (> 100) were crossed 1:1 with male flies of the MiMIC line (yw;Mi[*yellow*$^{+}$]MIC) three days before injections. Flies were crossed and held in vials with grape juice agar (see appendix 6.6.2) sprinkled with some active yeast at 25 °C. To increase the survival rate of the females, flies were split up on 2-3 vials and put on new food every 1-2 days. Furthermore, the vials were always kept lying on their side.

At the beginning of the first injection day, all male flies were removed from the vials, to further improve egg-laying. If possible, all female flies were put together in one single vial (not more than 100 females per vial). Henceforth, the vial was always plugged with a sponge to reduce the space as much as possible. Stressed by the reduced amount of space female flies tend to lay more eggs. Vials were again always kept laying on the side at 25 °C. For removal of old eggs withheld by the females, the flies were put on new food every 30 min for 2 h and the old vials were discarded.

2.1.1.2 Injection procedure

During injection cycles female flies were then put in a new vial every 40-45 min and embryos were collected from the old vials. To be able to inject as many embryos as possible, the whole injection procedure is therefore not supposed to exceed 45 min in duration. As many injection cycles as possible were done per day (6-10). The yield will be particularly well during the first 2-3 days.

After placing the female flies in a new vial, the vial withholding the freshly laid embryos was used in order to harvest the embryos. Hereafter, every step was done at a room temperature of approx. 18 °C. To dechorionate the embryos before injection, the vial was filled with approx. 3 ml 50 % bleaching solution (see appendix 6.6.2) and gently swayed for 2.5 min. The bleaching solution was then poured onto a clean mesh basket. Embryos that stuck to the agar or the wall of the vial were flushed out with distilled water using a squirt bottle and again captured with the mesh basked. To remove the bleach and yeast residues, the mesh basket containing the embryos was then thoroughly washed with distilled water using a glass beaker and a squirt bottle. Thereby the water spurt was never targeted directly onto the embryos.

To harvest the embryos a moist medium-sized brush was used. The embryos were placed on a blue stained agarose gel and gently aligned, with the posterior pole always pointing in the same direction, by using a preparation needle. After alignment, embryos were transferred to a coverslip coated with double-sided tape by gently pressing the coverslip onto the embryos. The coverslip was then stuck onto a microscope slide using a drop of water. Afterward, embryos were dried in an exsiccator for 8 $\pm$ 1 min and then covered with Voltalef 10s injection oil using a Pasteur pipette.

Injections were done on an inverted microscope (Axiovert 135) and with a FemtoJet injector. Injection needles (Sutter Instruments Co., Model P-97 pulled with Flaming/Brown micropipette puller) were filled with 1.8 µl blue-stained DNA solution containing the reporter plasmid (300-400 µg/µl) and inserted into the capillary holder of the injector. First, the microscope was focused on the first embryo. Then, the capillary tip was brought into focus as well by moving the capillary with a micromanipulator. To inject the right amount of DNA solution into the embryos, the compensation pressure (Pc) and the injection pressure (Pi) had to be adjusted before every injection cycle. Thereby Pc should be higher than Pi (e.g. Pc = 3,8 / Pi = 1,8) and Pi has to be higher than the pressure inside the em-

bryos. If adjusted correctly, a small amount of DNA solution automatically leaves the capillary by entering the embryo. If it is not possible to eject any or only a small amount of DNA solution even with the cleaning function of the injector, the capillary is probably too thin. Consequently, the capillary needs to be opened up by gently poking its tip against the coverslip edge. When the capillary is working properly, insert the capillary tip into the posterior part of the embryo by moving the microscope table. The capillary tip was inserted far enough to not inject into the perivitelline fluid of the embryo and a visible amount of DNA was injected. If the DNA solution did not leave the capillary tip automatically, the DNA was manually injected by pressing the foot control of the injector. As little harm as possible was caused to the embryos during the injection procedure. Only fertilized stage 2 embryos were injected because at that stage, injected DNA is inserted into the germline, thereby enabling inheritance to the next generation. Otherwise, only single cells would carry the inserted construct and inheritance would be precluded. Embryos older than stage 2 were destroyed by piercing them completely with the injection capillary. The injection capillary was cleaned by pressing the 'Clean' button occasionally during injection cycles. The capillary was also cleaned at the end of every injection cycle and the pressure was switched off by setting the injector from 'Injection mode' to 'Change capillary mode' before exiting the oil. The coverslip with the freshly injected embryos was placed into a Petri dish (ø 3.5 cm) and covered with 1 ml Voltalef 3s injection oil. This petri dish was further placed inside a moist chamber (ø 10 cm Petri dish lined with wet tissues) and kept at 25 °C.

24 h after injection hatched larvae were harvested with a preparation needle and put into a vial with very moist instant food. Furthermore, all embryos, which developed and showed movement were harvested. The plates were again checked at approx. 48 h after injection. Afterward, inactive yeast was sprinkled onto the instant food to increase the survival rate of the injected flies. The vials were kept at 25 °C.

2.1.1.3 Collection and crossing of injected flies

The vials were checked occasionally and flies were gently harvested at pupal stage and placed in individual vials. Thereby, males and females were separated. Every male fly (yw,*vasa*/Y;Mi[*yellow*$^{+}$]MIC/Cyo and yw,*vasa*/Y;Mi[*yellow*$^{+}$]MIC/Sna^{Sco}) was crossed indi-

vidually with female virgins of a balancer/marker fly line (yw; Cyo/Sna^{Sco}). To prevent crossing-over, female flies carrying the Sna^{Sco} marker were discarded. Thus, only females carrying the CyO balancer (yw,vasa/yw;Mi[*yellow^{+}*]MIC/Cyo) were individually crossed with male flies of the balancer/marker line (yw/Y;Cyo/Sna^{Sco}).

If RMCE happened during embryonal development of the injected flies, these flies will carry a Mi[*mCherry*]MIC in the germline. Therefore, at least some offspring should inherit the Mi[*mCherry*]MIC transposon. Through the integration of the *mCherry* construct, the *yellow^{+}* dominant body-color marker was replaced. Thus, offspring carrying the Mi[*mCherry*]MIC can be identified through their yellow body color.

Single males displaying the yellow phenotype (yw/Y;Mi[*mCherry*]MIC/Cyo or yw/Y;Mi[*mCherry*]MIC/Sna^{Sco}) were again crossed with female virgins of the balancer/marker fly line (yw;Cyo/Sna^{Sco}). From the offspring of these crosses, female virgins (yw;Mi[*mCherry*]/Cyo) and male flies (yw/Y;Mi[*mCherry*]/Cyo) were collected and intercrossed to establish stocks (see Fig.7). Furthermore, the offspring were used for PCR validation of the integration events.

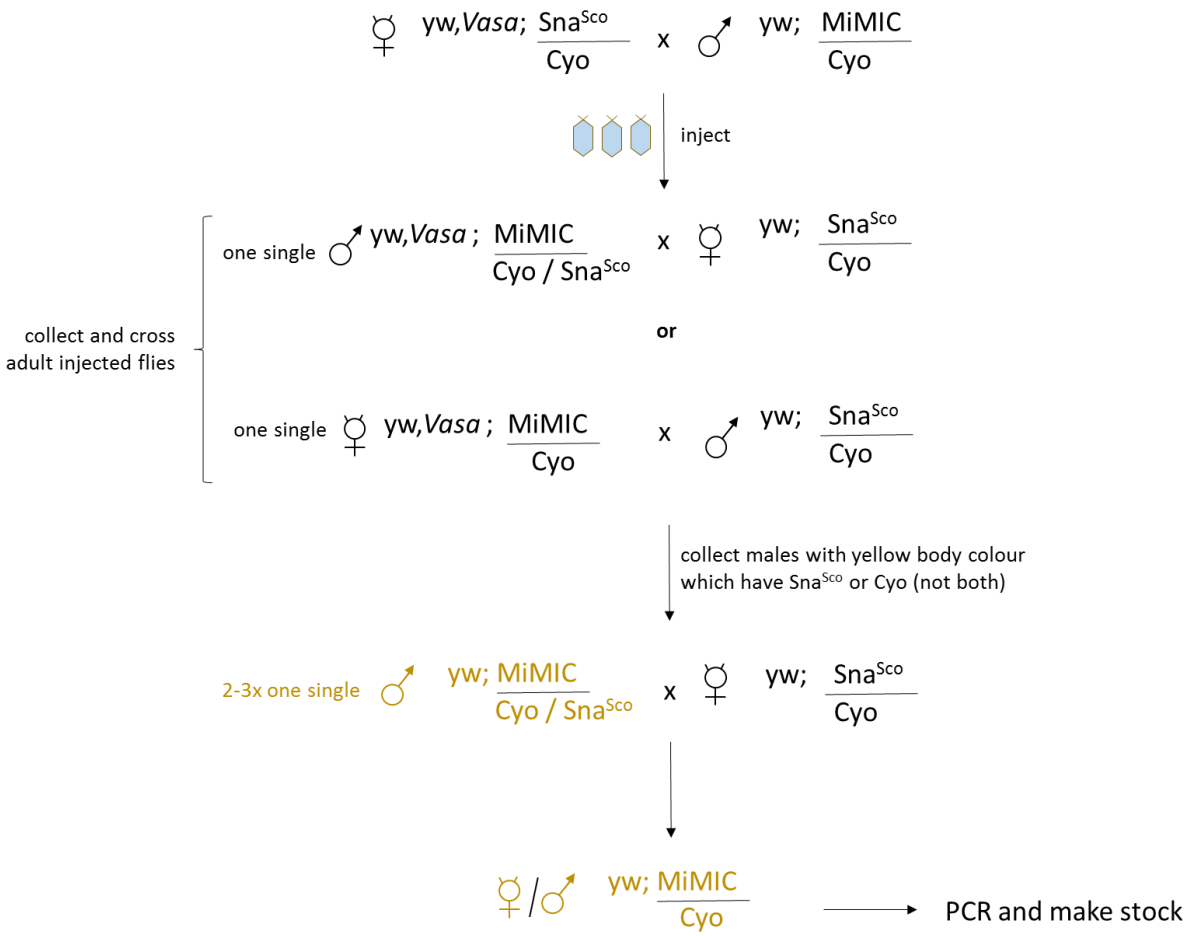

Fig.7: Crossing scheme for generation of MiMIC protein trap flies
Female virgins (♀) of yw,Vasa;Sna^{Sco}/Cyo were crossed to male balancer flies (♂) yw;MiMIC/Cyo. Offspring embryos were injected and raised to adulthood. Single males yw,Vasa;MiMIC balanced over either Cyo or Sna^{Sco} were then crossed to balancer virgins yw;Sna^{Sco}/Cyo. In addition, injected virgin females balanced over Cyo but not Sna^{Sco} (yw,Vasa;MiMIC/Cyo) were crossed to balancer males. From the offspring, males (yw;MiMIC/Cyo or Sna^{Sco}) with yellow body-color (yellow letters) were collected, which were expressing Cyo or Sna^{Sco} phenotype but not both. From the offspring, a stock was made. Offspring flies were also used for PCR validation of MiMIC integration events.

2.2.1 PCR verification of RMCE integration events

To isolate genomic DNA, single flies were put into empty 0.5 ml Eppendorf tubes and cooled on ice. The squishing buffer was freshly prepared by adding Proteinase K stock solution to a final concentration of 200 µg/ml. 50 µl of this prepared squishing buffer was then applied to each fly. The fly was thoroughly homogenized and immediately incubated in a preheated water bath at 37 °C for 20 min. To inactivate the Protease K the samples were incubated at 96 °C for 2 min. The isolated DNA was stored at - 28 °C until needed for further use.

For the correct characterization of the integration event, one of the F3 offspring was used. Since the RMCE event happens in the originally injected fly all the offspring generations (F2, F3…) of this fly will have the same integration. Therefore, even if more stocks were generated per originally injected fly, only one F3 offspring had to be tested.

The PCR was done with MiMIC-specific (Orientation-MiL-F; Orientation-MiL-R) and construct-specific primers (mCherry-Seq-F; mCherry-Seq-R), for which the sequences were obtained from previous studies (Venken *et al*., 2011). For the PCR reaction conditions: 2 µl 10x Thermopol buffer, 0.5 µl 10 mM dNTP's, 0.5 µl forward primer, 0.5 µl reverse primer, 0.1 µl Taq DNA polymerase, 15.4 µl ddH_2O (RNAse free) and 1 µl DNA were used. A touchdown PCR was done (Biometra®, TGradient, Labexchange):

Tab.1: Touchdown PCR for validation of RMCE events

N_{Cycles}	T [°C]	t [s]	$T_{Touchdown}$ [°C]
1x	94 °C	600 s	
8x	94 °C	30 s	
	68 °C	30 s	+ -1 °C
	68 °C	90 s	
32x	94 °C	30 s	
	60 °C	30 s	
	68 °C	90 s	
1x	68 °C	600 s	

For the correct characterization of the RMCE integration, four different PCR reactions were performed for each event. The following primer combinations were used (for primer sequences see appendix 6.5):

1. Orientation-MiL-F / mCherry-Seq-R
2. Orientation-MiL-F / mCherry-Seq-F
3. Orientation-MiL-R / mCherry-Seq-R
4. Orientation-MiL-R / mCherry-Seq-F

The construct can be integrated into the MiMIC cassette in two different orientations. Only one of those will be functional. If the MiMIC cassette was inserted on the same DNA strand as the gene, correct integration of the construct would be shown by positive PCR reactions for the primer combinations 1 and 4. If the MiMIC cassette instead was inserted

on the opposite DNA strand, positive PCR reactions for the primer combinations 2 and 3 would show a correct integration of the construct (Fig.8) (Venken *et al*., 2011). Since the MiMIC cassette is located on the same strand as the Stj gene, we would therefore expect PCR products for the primer combinations 1 and 4 to indicate correct integration of the *mCherry* construct.

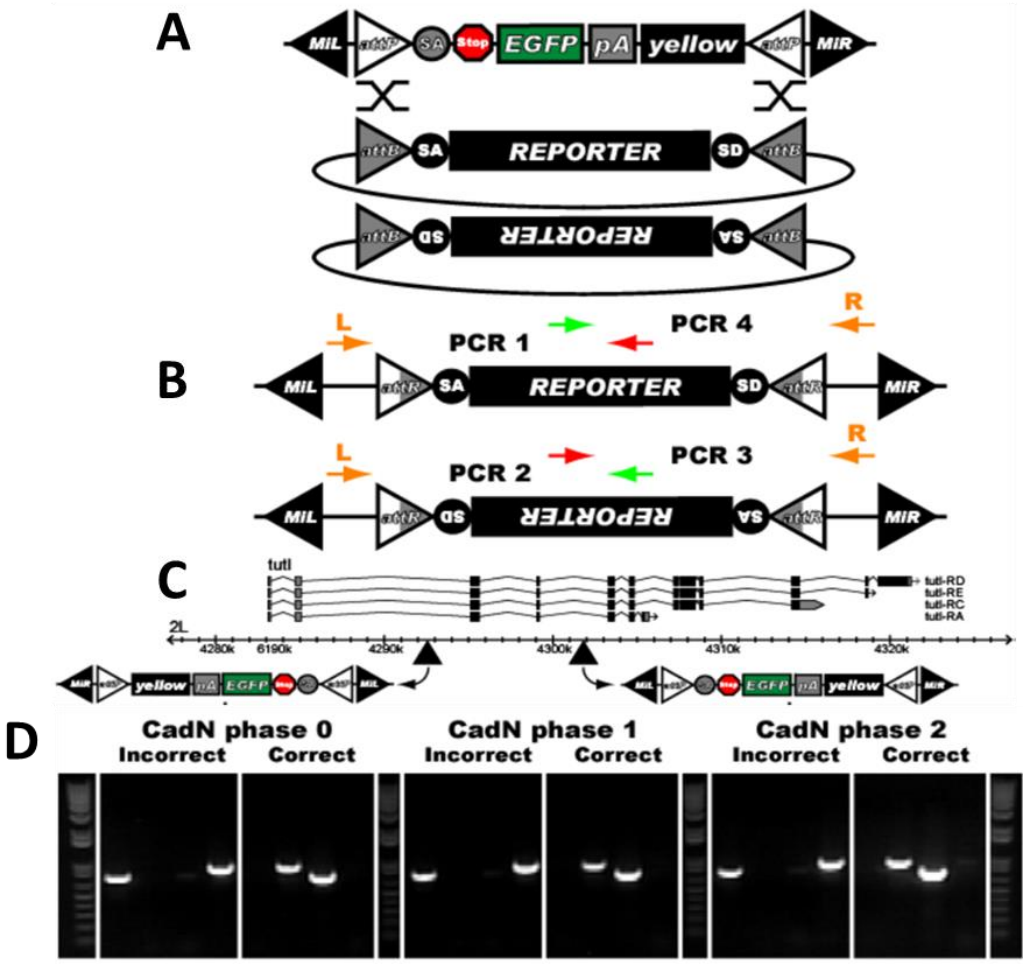

Fig.8: Validation of RMCE events during MiMIC protein trap generation via PCR

[**A**] The MiMIC cassette can be replaced with a plasmid construct via recombinase-mediated cassette exchange (RMCE, black crosses). Thereby, the construct will be integrated with either of two different orientations. Only one of those two orientations will result in the expression of the desired construct. [**B**] To validate for correct integration of the construct, four PCR reactions are done (PCR1-4). [**C**] Correct integration depends on the orientation of the MiMIC cassette relative to the respective gene. If both MiMIC cassette and gene are on the same strand, correct integration will result in PCR products for PCR1 & 4. If the MiMIc and the gene are on opposite strands, one will get PCR products for PCR2 & 3, [**D**] as exemplarily shown for CadN. (Modified from Venken *et al*., 2011)

2.3 Dissection

2.3.1 Dissection of L3 larvae

Drosophila larvae were collected from a vial and placed on ice inside an Eppendorf tube for at least 5 min. Afterward, a larva was put onto a ø 4 cm Sylgardsilicone-filled Petri dish, with the dorsal side facing upwards. Metal pins were stuck through the abdominal end and the head (mouth hooks) of the larva to stretch and fixate it onto the gel. After covering the larva with saline solution (see appendix 6.6.4), it was cut open along the midline from the abdomen to the head. Subsequently, the body wall with the body wall muscles was stretched open by applying two sharp metal pins per side. Afterward, the organs and the trachea were carefully removed. Thereby, the CNS and the body wall muscles were mostly left intact. In the end, the preparations were thoroughly washed with saline.

2.3.2 Dissection of adult flies & pupae

Adult flies were stunned on ice inside an empty plastic vial for at least 10 min. Single flies were then put on a ø 4 cm Sylgardsilicone-filled petri dish and the legs and wings were cut off. With the dorsal side facing up, it was then stretched and fixated to the gel by applying one metal pin through the abdomen and one through the head of the fly. After covering the fly with saline, it was cut open along the dorsal midline from the abdomen to the head. Then, the cuticle is opened by carefully applying one pin at the outer edge of the flight muscles of each side. After removing the inner organs, the preparation was thoroughly rinsed with saline.

Before dissection of pupal stages P5-P15, the pupal case had to be carefully removed. At earlier pupal stages (P1-P4) the pupal case was cut and pinned open as already described for larval dissections.

2.4 Immunocytochemistry

2.4.1 Standard protocol

Stainings were performed in ø 4 cm Sylgard/silicone-filled Petri dishes at RT. If not noted otherwise, dissected flies/larvae were fixated in 4% PFA / PBS solution for 45/30 min and then thoroughly washed three times for 30 min with PBS. To allow better penetration of the antibodies the preparations were permeabilized in 0.5 % Triton-X / PBS solution six times for 30 min. Meanwhile, the primary antibodies were diluted in 0.3 % Triton-X / PBS solution. Incubation with the primary antibodies was performed overnight at 4 °C on a platform rocker. After washing the preparations 8x for 30 min, the secondary antibody diluted in PBS was applied. Henceforth, preparations were always kept under a light-cover, to prevent a decrease of the antibody fluorescence. Incubation with the secondary antibody was done at 4 °C overnight. The preparations were again washed with PBS 6x 30 min and then dehydrated with an ascending ethanol series (50, 70, 90, 100 % each for 10 min). Finally, they were mounted in methylsalicylate.

2.4.2 Immunostaining with blocking

After fixation, the preparations were washed in PBS for 3x 20 min and then permeabilized and blocked in 0.5 TritonX-PBS + blocker (5% BSA or 10 % NDS) solution 5x 1h. Incubation of the first antibody diluted in 0.3 % TritonX / PBS + blocker (5% BSA or 10 % NDS) solution was done at 4 °C overnight. The washing procedure, incubation with the secondary antibody and mounting was performed as described in the standard protocol (see 2.4.1).

All antibodies used are listed in the appendix (see 6.4). In addition, all antibody combinations with the respective blockers, which were used for antibody stainings in the course of this work are provided. (see. 6.4.2)

2.5 Testing & repairing of VDRC KK-RNAi Fly lines

For generation of VDRC KK RNAi lines (VDRC Vienna Drosophila Resource Center), an empty pKC43 landing site was inserted into the second chromosome of the *Drosophila*

genome. The pKC26 vector carrying the RNAi construct is supposed to integrate into this annotated site (40D landing site) but mostly integrates into a second non-annotated site (30D landing site) (Green *et al*., 2014). In approx. 25 % of the generated KK fly strains the construct will integrate into both sites, which can lead to the expression of a toxic protein called Tiptop (Tio). Thus, KK lines used for this study were tested via PCR in order to prevent unspecific effects. For each tested fly line, genomic DNA was isolated from a single fly and four primer reactions were done (Green *et al*., 2014):

1. C_Genomic_F / pKC26_R
2. C_Genomic_F / pKC43_R
3. NC_Genomic_F / pKC26_R
4. NC_Genomic_F / pKC43_R

The following PCR reaction conditions: 2 µl 10x Thermopol buffer, 0.5 µl 10 mM dNTP's, 0.5 µl forward primer, 0.5 µl reverse primer, 0.1 µl Taq polymerase, 1 µl DNA, 15.4 µl ddH_2O (RNAse free) were used and a touchdown PCR was performed (Biometra®, TGradient, Labexchange; for primer sequences see appendix 6.5):

Tab.2: Touchdown PCR to validate correct integration of the RNAi construct during VDRC KK line generation

N_{Cycles}	T [°C]	t [s]	$T_{Touchdown}$ [°C]
1x	95 °C	120 s	
5x	95 °C	15 s	
	68 °C	15 s	+ -1 °C
	72 °C	50 s	
29x	95 °C	15 s	
	62 °C	15 s	
	72 °C	50 s	
1x	72 °C	120 s	

The integration of pKC26 into the annotated site (40D landing site) will result in a PCR product of approx. 450 bp (C_Genomic_F / pKC26_R), while an empty site will result in a product of approx. 1050 bp (C_Genomic_F / pKC43_R). The integration of the construct into the non-annotated site (30D landing site) will result in a PCR product of approx. 600 bp (NC_Genomic_F / pKC26_R). By contrast, an empty 30D landing site results in a product of approx. 1200 bp (C_Genomic_F / pKC43_R).

Flies in which the pKC26 vector was indeed integrated into both landing sites had to be 'repaired'. Via homologous recombination, the unwanted integration site will be removed from the chromosome. To achieve this, female virgins of the RNAi line were crossed to flies with empty landing sites (VDRC_60100). Subsequently, female virgins were collected from the F1 progeny and crossed to a balancer line for the second chromosome. By eye color (red eyes), putatively recombinant offspring could be preselected. One-sided recombination was confirmed via PCR as described above.

2.6 Validation of RNAi knockdowns via Western Blotting

2.6.1 Protein isolation

All materials were autoclaved or disinfected with 70 % ethanol solution before protein isolation. Gloves (Nitrile) were used during the whole procedure. At first, *Drosophila* larvae were dissected in ice-cooled standard saline (see appendix 6.6.4). The whole CNS was then carefully removed and collected in ice-cold sample buffer (see appendix 6.6.3) in 1.5 ml Eppendorf tubes. For StjMi[mCherry] 30 CNS and for $d\alpha_2\delta_1$Mi[GFP] 20 CNS were collected per 80 µl sample buffer. The collected samples were thoroughly homogenized and immediately boiled in preheated water at 96 °C for 3 min. Afterward, samples were centrifuged for 60 s at 6000 rpm and stored at -28 °C.

2.6.2 SDS-PAGE (Sodium Dodecyl Sulfate Polyacrylamide Gel Electrophoresis)

A running gel (see appendix 6.6.3) with a concentration of 8 % bis-acrylamide was prepared and poured into the gel electrophoresis chamber by using a disposable plastic pipette. To avoid gel exposure to oxygen, it was coated with n-butanol. The gel was then polymerized at 37 °C for 60 min. Afterward, the n-butanol was removed and the previously prepared stacking gel (5 % bis-acrylamide) (see appendix 6.6.3) was poured. Sample pockets were formed by the insertion of a comb (1.5 mm teeth). The gel was again polymerized at 36 °C for 30 min. Directly after removing the comb, the pockets were washed with running buffer (see appendix 6.6.3) by using a Pasteur pipette. Before loading, the sample solutions were boiled at 96 °C for 3 min and centrifuged at 10.000 g

for 60 s. Per pocket, 80 µl sample solution was loaded and empty pockets were filled with 80 µl sample buffer. Color Protein Standard Broad Range (New England BioLabs, #P7712S; 25 to 245 kD) diluted in SDS sample buffer 1/7, was used as a molecular marker.
The gel was run in a Hoefer SE 400 Series Sturdier at 4 °C with a constant current of 0.02 A (PowerPac, Bio-Rad) until the dye front had passed through the stacking gel. The current was then increased to 0.03 A.

2.6.3 Protein transfer onto a nitrocellulose membrane

Preliminary, the blotting tank was filled with transfer buffer (see appendix 6.6.2). Then two sheets of blotting paper, two sponges, and a nitrocellulose membrane were incubated in transfer buffer for at least 5 min. When the SDS-Page was finished, the gel was carefully removed from the electrophoresis chamber and the stacking gel was cut off. One sponge, one sheet of blotting paper, the gel, the nitrocellulose blotting membrane, one sheet of blotting paper and again one sponge was assembled in this order into the blotting cassette, which was then tightly closed. The cassette was inserted into the blotting tank so that the membrane was placed on the side of the anode (+). The transfer was run at 4 °C (to avoid overheating) at 40 V overnight, while the buffer was stirred at 90 rpm.

2.6.4 Antibody staining

After protein transfer, the nitrocellulose membrane was removed from the cassette and washed in H_2O_{dd} for 10 min. To check the sample protein bands, the membrane was then stained with Ponceau S for 5 min. Bands were expected at ~200 kDa for $\alpha_2\delta$ (α_2 ~150 kDa; δ ~20 kDa; Tanabe *et al.*, 1987, plus the tag mCherry and GFP ~27 kDa) and at ~43 kDa for the loading control actin. The membrane was cut at about 80 kDa so that loading control and protein band could be stained separately. Both membrane parts were first washed in H_2O_{dd} for 10 min and then in TBST solution (see appendix 6.6.3) 3x 30 min. After blocking the membrane with 10 % milk-TBST solution or BlockAce-TBST solution (see appendix 6.6.3) for 2 h, it was again washed with TBST solution for 3x 20 min. Primary antibodies, diluted in 2,5 % milk-TBST solution or 25 % BlockAce-TBST solution, were applied to the respective membrane part and incubated o/n at 4 °C. Afterward, both membrane pieces

were separately washed 3x 20 min in TBST solution. The secondary antibody was diluted in TBST. Incubation time with the secondary antibody was 2 h at RT. Again, the membrane pieces were washed with TBST for 4x 20 min. Since we found that the Tween-20 in the TBST buffer caused very high background, the membrane was washed with TBS for 20 min before detection. Bands were detected using chemiluminescence via HRP reaction. The HRP reaction was activated via Immunilon Western chemiluminescent HRP substrate (Millipore) for 5 min.

Tab.3: Antibodies and blocking solutions used for staining of sample proteins during Western blot experiments

Sample	Blocking solution	1. Antibody	2. Antibody
$d\alpha_2\delta_1^{GFP}$	10 % milk-TBST solution	rabbit α-GFP, 1:1000 in 2.5 % Milk-TBST sol.	goat α-rabbit IgG, 1:10000 in TBST
$Stj^{mCherry}$	BlockAce-TBST solution	rabbit α-mCherry 1:1000 in 25 % BlockAce-TBST sol.	goat α-rabbit IgG, 1:10000 in TBST
actin	Same as for protein of interest	mouse α-actin 1:10000 in 2.5 % Milk-TBST sol. / 25 % BlockAce-TBST sol.	goat α-mouse HRP, 1:4000 in TBST

2.6.5 Quantification of protein bands

The western blots were detected with a Fusion SL camera (and Fusion software Version 15.16, Vilber Lourmat) and evaluated with Fiji Image J 64 V5. To analyze the western, a profile blot was done of the bands of interest and the integrated areas of those bands were measured (Fig.9). This was repeated for the bands of the actin loading control. To calculate the relative density, the area of the band of interest was divided by the area of the band of its respective loading control.

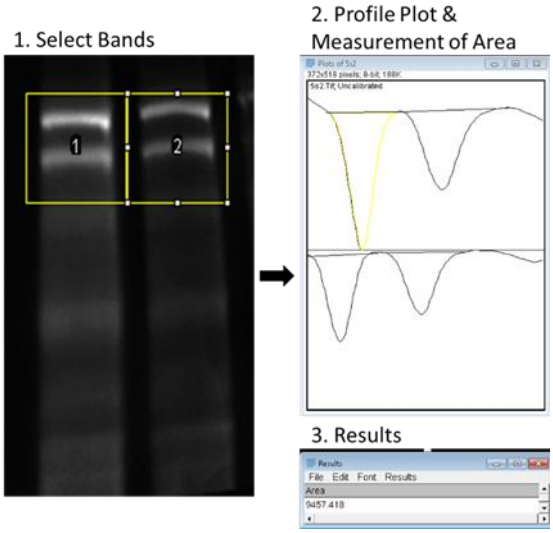

Fig.9: Quantification of protein bands with Fiji ImageJ 64 V5 software
(**1.**) Protein bands were framed with rectangles (yellow). The first lane was selected by Strg+1, while all following lanes were selected by Strg+2. (**2.**) Profile plots of the lanes (yellow rectangles) were performed by selecting Strg+3. Straight lines were drawn to separate the signal from the background. Subsequently, the area of single protein bands (yellow) was measured with the wand tool. (**3.**) Values were taken from the results window.

2.7 Gross effects of $\alpha_2\delta$ RNAi knockdowns on viability and behavior of *Drosophila*

To assess if knockdowns of Stj and d$\alpha_2\delta_1$ result in obvious defects or reduction in viability, the amount of hatched male and female knockdown flies was counted and obvious defects like lethargic behavior or premature death compared to respective controls were noted. To further assess if Stj or d$\alpha_2\delta_1$ are required for normal motor behavior of flies, we performed different assays to test for changes in the climbing speed, flight ability and flight performance of knockdown animals compared to control.

Unless noted otherwise, all flies were raised at 25 °C and tested 3 - 5 days after hatching. All behavioral experiments were done at approx. 25 °C and between 9:00 am – 1:00 pm or 3:00 pm - 5:00 pm.

2.7.1 Recording of the climbing speed

2-3 day old male (♂) or female virgins (♀) were placed individually per vial one day before testing. To measure the climbing speed each vial was placed beside a scale bar and hit on a styrofoam box (Fig.10). This will induce upward climbing behavior, through negative geotaxis. Each fly was tested three times, while the climbing behavior was recorded with a camera. In order to analyze the climbing speed, data were evaluated with “Avidemux V5”. The mean score of three climbing events was calculated per fly. Only climbing events where the fly walked in a straight line (as assessed by video analysis) were used.

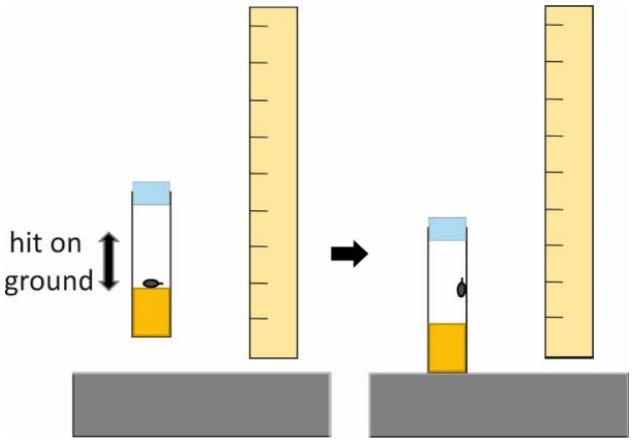

Fig.10: Climbing assay
Single flies were placed individually per vial and the vial was placed beside a scale bar. Hitting the vial on the ground will induce upward climbing of the fly through negative geotaxis. Climbing attempts are recorded and climbing speed is assessed by video analysis.

2.7.2 Cylinder drop test

The cap of a 0.5 ml Eppendorf tube was equipped with a filter paper, which was moistened with 5 µl 10 % sucrose solution (in H_2O_{dd}). 4-5 day old male (♂) or female virgins (♀) were placed individually per tube 1 h before testing. Successively, all tubes were put into the cylinder drop device, which was then placed on top of a 1000 ml measuring cylinder (Fig.11). By pulling and releasing the handle of the device, the fly was pushed through an opening at the bottom of the tube and began to drop. The distance the fly needed to intercept the fall was measured. Thus, the flight ability of the flies could be examined. Flies with a better flight ability should catch the fall faster than flies with a defect in their flight behavior.

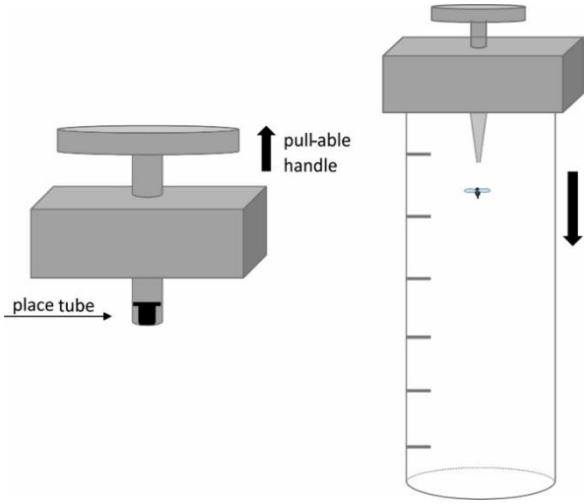

Fig.11: Cylinder Drop test
Flies were placed individually in 0.5 ml Eppendorf tubes, equipped with moistened filter paper (5 µl 10% sucrose solution). After 1h, flies were tested with the Cylinder Drop test. Successively, tubes were placed in the cylinder drop device, which was then put in a 1000 ml cylinder. The handle was released and flies were pushed through an opening at the bottom of the tube. The distance the fly needs to intercept the fall will be measured.

2.7.3 Recording flight behavior

3-5 day old males were stunned in ice for 10 s in an empty plastic vial and put on a cooling plate. With the help of a binocular, a small triangular steel hook was glued between the head and the thorax of the fly. The glue was hardened for 60 s under UV-light application. After a resting period of 30 min on filter paper (moistened with 10 µl 10 % sucrose solution) in an empty vial, the fly was hung up before a horizontally striped (black/white) paper using the metal hook. To prevent the flies from instantly starting to fly, a small Styrofoam ball was given to them.

The removal of the Styrofoam ball will induce flight behavior and thereby start the experiment. If the fly stops flying, flight will be induced again by puffing air onto the fly. If the fly does not start flying after puffing air onto it three times, the experiment will be stopped. The experiment is also stopped after a total flight time of 2 h. For each fly, the flight time before and between the stops was noted. From this data, the total flight time, the number of stops, the initial flight time and the mean flight time between the stops can be calculated.

2.8 Electrophysiological experiments

2.8.1 Intracellular muscle recordings

L3 larvae were dissected (see 2.3.1) in HL3.1 saline (see appendix 6.6.4) with 0.5 mM or 1.0 mM Ca^{2+} concentration. To prevent spontaneous activity, the CNS of the larvae was carefully removed at the end of the dissection procedure, cutting the nerves as close to the ventral nerve cord as possible. Using a fluorescence microscope (Olympus BX5IWI) with a water dipping lens (200 x magnification) and fixed stage, larval muscles M10 from one of the middle segments were selected (Fig.12). To evoke postsynaptic muscle potentials (PSP) the respective nerves were sucked in and stimulated with a saline-filled suction electrode (BF100-50-10 broken individually, Sutter Instrument). Electrodes were pulled with a Flaming/Brown micropipette puller (Model P-97, Sutter instruments). As a reference electrode, a fine silver wire was wrapped around the glass capillary of the electrode. Stimuli were conducted via an Isolated Pulse Stimulator (Model 2100, A-M Systems) and amplified by a Differential AC Amplifier (Model 1700, A-M Systems). Electrical stimuli with

durations of 0.5 ms and the lowest possible current for AP generation (+1 pA) were applied. The evoked PSPs were recorded intracellularly from the muscle with a sharp, potassium chloride (3 M) filled recording electrode (30MΩ; WPI, 1B100F-4 with filament). As a reference electrode, a chlorinated silver wire was placed into the bath solution (HL3.1 saline). An AxoClamp 2B amplifier (Molecular devices) was used in bridge mode to amplify measured signals. Offset alignment of the inherent resistance and the capacity of the electrode were done manually before approaching the muscle. All electric signals were digitized with an Axon Digidata 1550 (Molecular Devices) digitizer at a 10 kHz sampling rate.

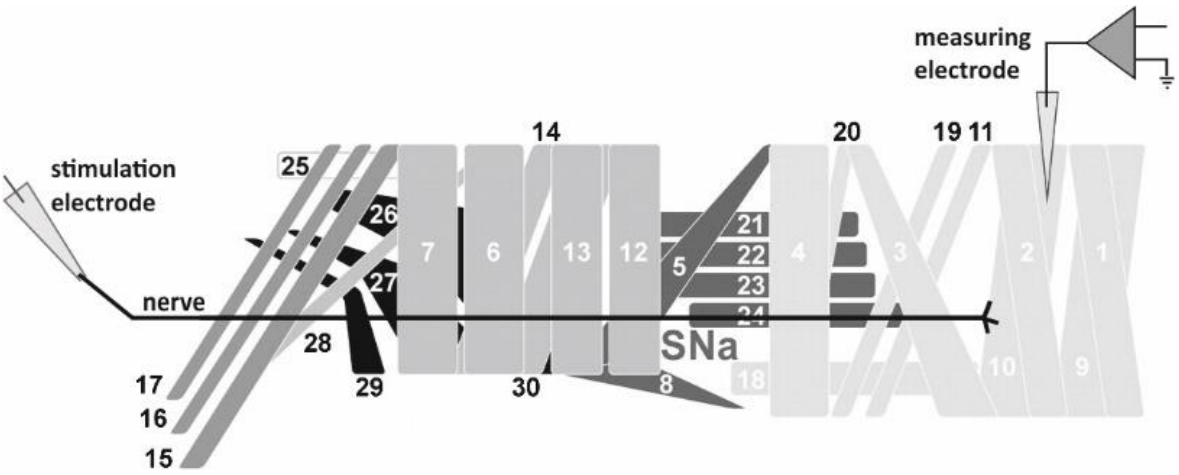

Fig.12: Current clamp recording from larval body wall muscle M10
Each hemi-segment consists of 30 body wall muscles, which are numbered. Axons of larval crawling motoneurons project onto body wall muscles via six different nerve branches. The respective nerve (ISN) to muscle M10 was sucked in with the stimulation electrode. Evoked postsynaptic potentials were recorded intracellularly from muscle M10 with a recording electrode (Modified from Kim *et al*., 2009).

To probe for changes in amplitude or quantal content of evoked PSPs, recordings were done in 0.5 mM Ca^{2+} concentration and stimuli trains of 0.5 Hz (20 s) were applied.
To look at changes in synaptic short-term plasticity at the NMJ, Ca^{2+} concentration within the HL3.1 saline and stimulation protocols had to be adjusted. To assess changes in synaptic depression, a concentration of 1.0 mM Ca^{2+} was used. Furthermore, stimulus trains with frequencies of 5 Hz and 10 Hz were applied for 10 s each. To investigate changes in facilitation, HL3.1 saline with a concentration of 0.5 mM Ca^{2+} was used and paired pulses with an inter-pulse duration of 30, 50, 100 and 130ms were applied.

2.8.2 Patch-Clamp recordings

2.8.2.1 Current Clamp measurements from the soma of larval RP2 neurons

L3 larvae were dissected (see 2.3.1) in standard saline (see appendix 6.6.4) with 1.8 mM Ca^{2+} concentration. To prevent strong movements of the CNS due to muscle contractions, all crawling muscles were cut at the end of the dissection procedure.

Patch-clamp measurements were done with an Axioscope 2 FS plus microscope (Carl Zeiss) and a 40 x objective (LUMPlanFl 40x / 0.80 w, Olympus) with water immersion lens (400 x magnifications). Signals were amplified with an Axopatch 200B amplifier (Molecular Devices) and digitized with a Digidata 1322A (Molecular Devices) with a 20 kHz sampling rate. Patch pipettes (borosilicate glass capillaries without a filament, OD: 1.5 mm, ID: 1.0 mm) were inserted in a capillary holder (1-HL-U, Molecular Devices) of an HS-2A head stage (Molecular Devices), which was moved by an MP-225 micromanipulator (Sutter Instrument). Data acquisition and analysis were done with the pCLAMP10.X software (v 10.2, Molecular Devices).

MNISN-Is (RP2) and MN1-Ib (aCC) neurons expressing the RNAi knockdown could be identified through their GFP signal. For the patch-clamp measurements, only RP2 neurons from thoracic segments were used, which could be distinguished by their morphology and their characteristic firing behavior. In contrast to the bipolar aCC neurons, RP2 are unipolar and their firing pattern is marked by a delayed firing of action potentials (Fig.13). To get access to the somata of RP2 neurons, the ganglionic sheath of the VNS had to be removed first. Thus a suction electrode (WPI, #PG52151-4 pulled with Narishige PC-10 vertical electrode puller and broken individually) was used to apply 1% protease-saline solution onto the dorsal part of the VNS and to remove the dissolving sheath manually. Henceforth, the bath solution was continuously exchanged through a BPS-8 perfusion system (ALA Scientific Instruments). Somata of 1-2 GFP marked RP2 neurons were carefully cleaned using the suction electrode. While washing the preparation with saline for approx. 2 min, a patch electrode (WPI, #PG52151-4 pulled with Narishige PC-10 vertical electrode puller) was filled with internal patch solution (Fig.13) and inserted into the head stage. To keep the tip of the patch electrode clean, positive pressure was continuously applied. As a reference electrode, a chlorinated silver wire was placed into the bath solution. Inside the bath solution, the electrode resistance was supposed to be 6-8 MΩ. Alignment of the pipette offset was done manually, shortly before approaching the soma.

Subsequently, the electrode tip was brought as close to the soma as possible and negative pressure was applied. If a gigaseal was obtained, the electrode pressure rose to ≥1 GΩ. pCLAMP10.X software was set to 'Patch' mode and the offset of the pipette capacitance was aligned using the Cslow dial of the Axopatch 200B patch-clamp amplifier. By application of a short negative pressure, the cell was opened up and a whole-cell patch was achieved. pCLAMP10.X software was set to 'Cell' mode and the 'whole-cell Parameters' were switched on applying a holding potential of -70 mV. Alignment of the series resistance compensation (approx. 90 %), the LAG (2 µs), the whole-cell capacitance (0.85 – 1.15 pF) and the series resistance (8 – 14 MΩ) was done manually. Measurements were performed in current-clamp mode. Thus, changes in membrane potential and action potential firing due to current injections were recorded. Only cells with a membrane potential ≤ - 30 mV were considered healthy enough for usage. Before measurements, the membrane potential of all cells was adjusted to approx. - 60 mV by application of negative current. Current injections were done as square pulses (Fig.13). To analyze the effects of gabapentin on the firing behavior of larval RP2 neurons, saline with 25 µM gabapentin was washed in for 5 min. Afterward, all recording protocols were repeated. The raw data were analyzed in Clampfit 10.7. Per current injection, the number of action potentials (AP) occurring during 400 ms was counted. The frequency (Hz) was calculated in Microsoft Excel and I/F plots were generated and fitted by a modified Boltzmann fit (charge-voltage).

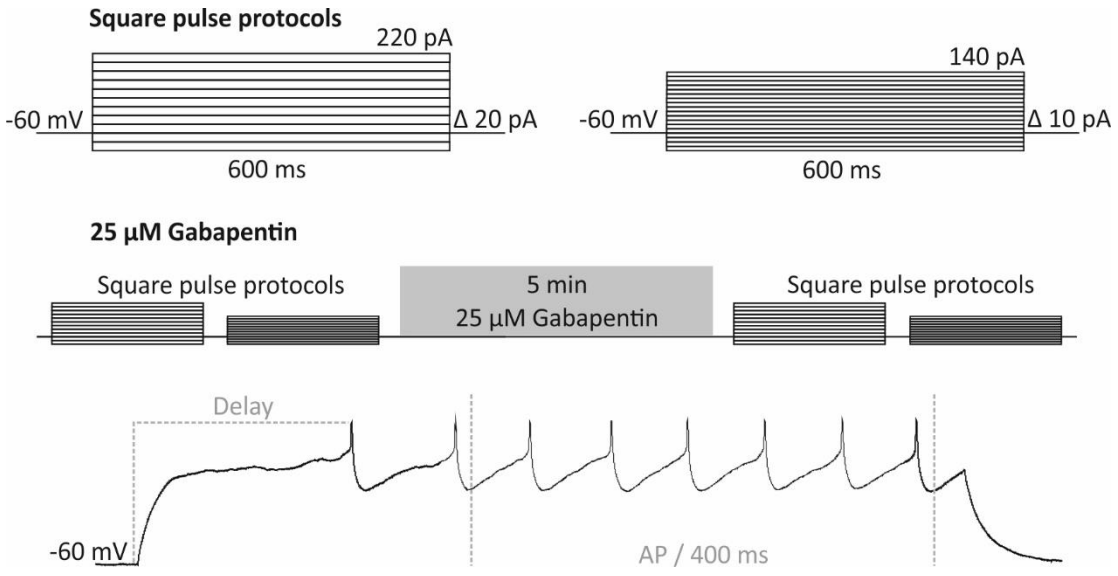

Fig.13: Recording protocols used for current clamp measurements of larval RP2 neurons
Whole-cell current-clamp recordings from the soma of larval RP2 crawling motoneurons were performed. Current injections were done as square pulses from -40 pA to 220 pA in 20 pA intervals and from -40 pA to 140 pA in 10 pA intervals. Both protocols were recorded before and after application of 25 µM gabapentin (5 min). RP2 neurons were identified by their characteristic localization and the delayed onset in action potential (AP) firing. The number of APs per 400 ms (gray bars) was counted to calculate the firing frequency.

2.8.2.2 Ca^{2+} current measurements from L3 larvae

Patch-clamp recording of larval RP2 and aCC neurons were done as described above (see 2.8.2.1), but different intracellular and extracellular recording solutions (see appendix 6.6.4) had to be used to measure Ca^{2+} currents. With Ca^{2+} current recording solutions (see appendix 6.6.4) the resistance of the patch electrode was ~4 MΩ. Measurements were performed in voltage-clamp mode. Command voltage steps of 10 mV with a duration of 200 ms were used from a holding potential of - 90 mV to 0 mV to elicit currents (Fig.14).

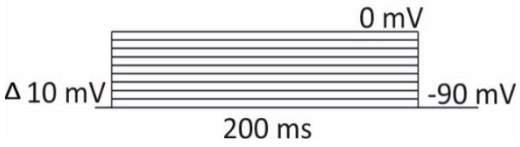

Fig.14: Recording protocol used to record Ca^{2+} currents from larval crawling motoneurons RP2 & aCC

2.8.2.3 Current Clamp measurements from P8 pupa

P8 pupae, which display bright orange eyes (Bainbridge and Bownes 1981) were dissected (see 2.3.2) in standard saline (see appendix 6.6.4) with 1.8 mM Ca^{2+} concentration. Patch-clamp measurements were done under an Axioscope 2 FS plus fluorescence microscope (Zeiss, Germany) and a 40 x objective (LUMPlanFl 40x / 0.80 w, Olympus) with water immersion lens (400 x magnifications). Signals were amplified with an Axopatch 200B amplifier (Molecular Devices) and digitized with a Digidata 1322A (Molecular Devices) with a 20 kHz sampling rate. Patch pipettes (borosilicate glass capillaries without a filament, OD: 1.5 mm, ID: 1.0 mm) were inserted in a capillary holder (1-HL-U, Molecular Devices) of an HS-2A headstage (Molecular Devices), which was moved by an MP-225 micromanipulator (Sutter Instrument). Data acquisition and analysis were done with the pCLAMP10.X software (v 10.2, Molecular Devices).

Motor neurons (MN) expressing the RNAi knockdown could be identified through their GFP signal. For the patch-clamp measurements, only MN5 were used, which could be

distinguished by their characteristic localization and morphology. To get access to the somata of MN5, the ganglionic sheath of the VNS had to be removed first. Thus a suction electrode (WPI, #PG52151-4 pulled with Narishige PC-10 vertical electrode puller and broken individually) was used to apply 1% protease-saline solution onto the dorsal part of the VNS and to remove the dissolving sheath. Note that somata of MN5 additionally have a sheath of their own, which needs to be carefully removed using the suction electrode. From there on the bath solution was continuously exchanged through a BPS-8 perfusion system (ALA Scientific Instruments). While washing the preparation with saline for approx. 2 min, a patch electrode (WPI, #PG52151-4 pulled with Narishige PC-10 vertical electrode puller) was filled with internal patch solution (see appendix 6.6.4) and inserted into the head stage. To keep the tip of the patch electrode clean, positive pressure was continuously applied. As a reference electrode, a chlorinated silver wire was placed into the bath solution. Inside the bath solution, the electrode resistance was supposed to be 6-8 MΩ. The whole-cell patch was obtained and offsets were aligned as described for the larval RP2 neurons (see 5.2.1). The membrane potential of all cells was adjusted to approx. - 60 mV. Current injections were done as square pulses (Fig.15). After washing in 500 µM cadmium for 2 min to block Ca^{2+} currents, the square pulse protocol was repeated.

The raw data were analyzed in Clampfit 10.7. Action potential (AP) amplitude and AP half amplitude width were measured (Fig. 15) at a membrane potential of approx. -10 mV before and after application of Cadmium.

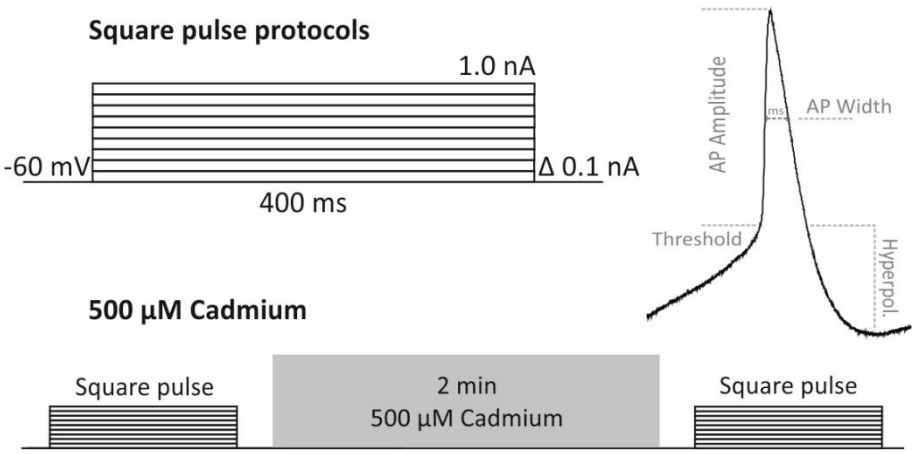

Fig.15: Recording protocols used for current clamp measurements of pupal MN5 neurons

Whole-cell current-clamp recordings from the soma of pupal MN5 motoneurons were performed. Current injections were done as square pulses from 0 to 1.0 pA in 0.1 nA intervals. Recordings were performed before and after application of the calcium channel blocker cadmium (500 µM, 2 min). Action potential (AP) half amplitude width was measured at thresholds of approx. -10 mV.

2.8.2.4 Ca^{2+} current measurements from adult MN5

Patch-clamp recordings of adult MN5 were done as described above (see 2.8.2.3), but different intracellular and extracellular recording solutions (see appendix 6.6.4) had to be used to measure Ca^{2+} currents. With Ca^{2+} current recording solutions the resistance of the patch electrode was ~3.5 MΩ. Measurements were performed in voltage-clamp mode. Command voltage steps of 10 mV with a duration of 200 ms were used from a holding potential of - 90 mV to 0 mV to elicit HVA currents (they activate between -40 and -30 mV). Command voltage steps of 10 mV with a duration of 200 ms were used from a holding potential of - 90 mV to -40 mV to elicit LVA currents (Fig.16).

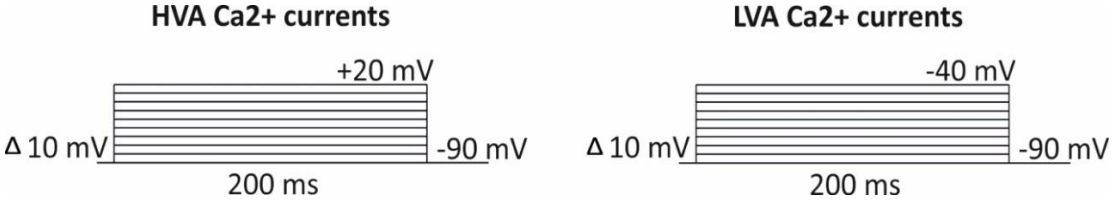

Fig.16: Recording protocols used to record HVA and LVA Ca^{2+} currents from adult wing depressor motoneuron MN5

2.9 Probing for developmental defects of the neuromuscular junction (NMJ)

L3 larvae were dissected (see 2.3.1) and fixated with 4 % PFA solution for 30 min. An immunocytochemistry staining against HRP and Brp was performed as described above (see 2.4.1). For quantification of bouton size and number of Brp puncta per bouton, all preparations were treated and scanned identically. Images (1024x1024pixels) of NMJs on muscle M10 of a thoracic segment were acquired with a TSC SP8 Laser Scanning Microscope (Leica) with excitation wavelengths at 488 nm (Argon laser) and 633 nm (HeNe). A 40x oil immersion objective (1.25 NA; HC PL APO 40x/1.30 Oil CS2, Leica) with Type F immersion oil (Leica Microsystems) was used. A z-step size of 0.3 µm and a zoom factor of 3.5 was used for further magnification. The voxel dimensions were 86 x 86 x 290 nm (x, y, z).
Confocal image stacks were analyzed with Amira 5.4.5 software. The 2D length for x,y & z of 8 boutons per muscle were measured and the volume calculated (Fig.17). Furthermore, the Brp puncta per bouton were counted and normalized by the bouton volume (V_{Bouton}).

The same was done with larvae with endogenously tagged Ca_V2^{GFP} channels. Stainings against GFP and HRP were conducted and Ca_V2^{GFP} points were counted.

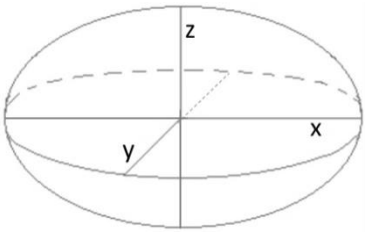

Fig.17: Calculation of synaptic bouton volume
The x,y & z length of synaptic boutons were measured and the volume of the bouton (V_{Bouton}) was calculated, by using the specified formulas.

2.10 Quantification of axonal Ca_V2^{GFP}

Please note that in order to be able to quantify the cac^{GFP} signal, all preparations had to be treated exactly the same way. 2-3 day old flies were stunned on ice for 10 min and dissected as described above (see 2.3.1). The preparations were instantly fixated with 100 % ice-cold ethanol for 10 min and washed with PBS (10 min). Mounted in Vectashield (Vector Laboratories, Lot# X1215) the cac^{GFP} signal was directly scanned with a Leica TSC SP8 Laser Scanning Microscope at a 488 nm excitation wavelength (Argon laser). A 20x glycine immersion objective (HC PL APO 20x/0.75 Imm Corr CS2, Zeiss) with Type-G immersion oil (Leica Microsystems), a zoom factor of 1.8 for further magnification, a z-step size of 0.5 µm and an image resolution of 1024x1024 pixels was used for all samples. Additionally, identical laser and detector settings were applied. The Argon laser was warmed up 1 h before images were taken.

To analyze the cac^{GFP} signal projection views from stacks of 10 sections per fly were made for the axons. In order to be able to properly analyze the pictures, brightness, intensity, and contrast had to be adjusted via CorelDRAW X7 V5. This was done identically for all images. Then, the mean gray value of Ca_V2^{GFP} was measured in the axons bundles with Fiji ImageJ 64 V5 (Fig.18). Per fly, the mean axonal Ca_V2^{GFP} intensity was calculated from the axons of both sides.

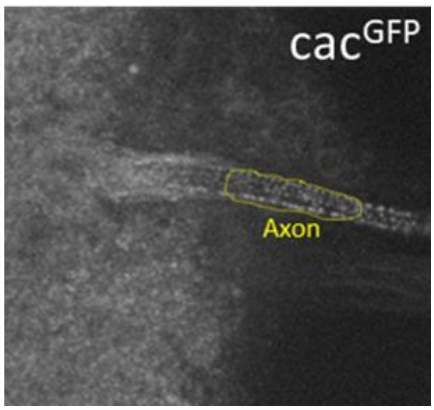

Fig.18: Quantification of axonal Ca_V2^{GFP} signals
Live Ca_V2^{GFP} signal (gray) in axon bundles of MN1-5. MN5 somata were identified by their characteristic localization. For each axon bundle of MN1-5 confocal image stacks from 10 sections were made. Brightness, intensity and contrast were adjusted identically for all analyzed images. The mean gray value of the Ca_V2^{GFP} signal in the marked areas (yellow frame) was measured with Fiji ImageJ 64 V5.

2.11 Calcium imaging of pupal MN5 neurons

To assess differences in calcium channel localization or density, calcium imaging was done. All calcium imaging experiments were performed with GCaMP6s, which is a genetically encoded, protein-based calcium indicator. Compared to other GCaMP6 types, 6s is highly sensitive and has relatively slow Ca^{2+} binding kinetics (high affinity, fast binding, slow-release -> large signal) (Akerboom *et al*., 2012). GCaMPs are circular folded GFP proteins (cpGFP), which have a Ca^{2+} binding protein / Calmodulin-binding peptid (CaM-M13) complex coupled to the cpGFP chromophore. Binding of four Ca^{2+} ions will lead to conformational changes of the CaM-M13 complex and thereby to deprotonation of the cpGFP chromophore. Thus, cpGFP fluorescence will be rapidly increased (Akerboom *et al*., 2009).

2.11.1 Calcium imaging with thermogenetic activation of MN5

P8 pupae expressing a temperature-sensitive TrpA channel ($TrpA^{ts}$) in addition to GCaMP6s in MN1-5 were dissected (see 2.3.2). TrpA channels conduct Na^+ and Ca^{2+} (Pedersen *et al*., 2005). Opening of $TrpA^{ts}$ through temperature shifts > 27 °C will result in depolarization and activation of the neuron through influx of Ca^{2+} and Na^+ ions. Consequently, this will lead to the opening of voltage-dependent Ca_V channels. Since TrpA channels already conduct Ca^{2+}, opening of TrpA alone will lead to changes in GCamp6s fluorescence. Since GCamp6s further binds Ca^{2+} very fast and with a slow-release (see above) changes in Ca_V channel density might be difficult to detect. Still, it might give us

first indications for changes in Ca_V density following knockdown of either Stj or $d\alpha_2\delta_1$, which can then be confirmed in more elaborate experiments e.g. by calcium imaging of MN5 with activation by intracellular current injections.

To keep the volume of the bath solution as constant as possible, the pupae were dissected in a silicone ring (OD: 1.7 mm, ID: 0.9 mm, height: 1 mm). An upright Axioscope 2 FS plus fluorescence microscope (Carl Zeiss) with a 40x objective with water immersion lens (400x magnification, LUMPlanFl 40x / 0.80 w, Olympus) was used for imaging. During the experiment, the bath solution was constantly exchanged by a BPS-8 perfusion system (ALA Scientific Instruments), which was equipped with a heater. The temperature of the bath solution was detected (TC-10, Cornerstone). MN5 neurons were filmed for 10 s (exposure: 0.06) with an ORCA-100 CCD camera (model C4742-95, Hamamatsu) and Simple PCI software (at approx. 23 °C) before the bath solution was heated (approx. 5 min) to 30 °C. This will induce the opening of temperature-sensitive TrpA channels, which will further result in activation of MN5 and thus in changes of GCamp6s fluorescence. At exactly 30 °C, MN5 GCamp6s fluorescence was again filmed for 10 s. Afterward, the temperature was cooled down to approx. 23 °C (approx. 6 min) and GCamp6s fluorescence was again filmed for 10 s. Please note that exposing neurons to the fluorescence light for > 30 s will result in photo-bleaching of GCamp6s fluorescence.

2.11.2 Calcium imaging with activation of MN5 by intracellular current injection

P8 pupae were dissected (see 2.3.2) and current-clamp recordings from the soma of MN5 were performed (see 2.8.2.3). Thereby, only cells with a membrane potential $\leq$ -55 mV were used. Action potentials were induced by depolarizing 400 ms 1nA ramp pulses and changes in GCamp6s fluorescence through activation of MN5 were recorded and analyzed with an Orca Flash 4.0 LT CMOS camera, the HOKAWO 3.10 software and an exposure time of 75 ms.

2.11.3 Analysis of the Imaging data

Analysis of the raw data was done in simple PCI software (v 5.2.1.1609, Hamamatsu). The obtained image series was used to analyze changes in GCaMP6s fluorescence intensity in

specific regions of interest (ROI): soma, primary neurite (PN) dendrites and/or axons (Fig.19). The measured data was imported to excel, where the GCamp6s signal was normalized to the background and $\Delta F/F = (F_{Firing}/F_{Rest})/F_{Rest}$ was calculated.

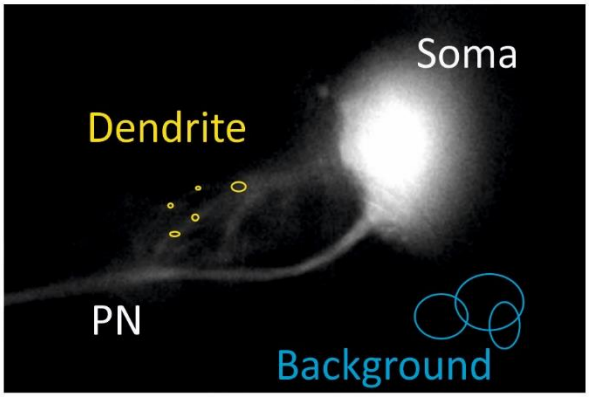

Fig.19: Recording of GCaMP6s signal during calcium imaging of MN5
MN5 neuron expressing GCaMP6s. GCamp6s fluorescence was measured in specific regions of interest in the dendrites (yellow), the axon (not shown) and the background (blue).

2.12 Probing for developmental defects in MN5 dendritic tree

2.12.1 Intracellular fillings of MN5

2-5 day old male flies were collected in empty vials and stunned on ice. Each fly was dissected (see 2.3.1) in fresh saline on a ø 4 cm sylgardsilicone-filled Petri dish. The additional expression of GFP in the targeted neurons enabled the localization of MN5 by using a fluorescence microscope (Olympus, BX51WI). A protease filled cleaning electrode was used to remove the cover layer of the ventral nerve cord and MN5 soma. Afterward, the protease was removed by washing the preparation with saline three times. A sharp electrode (60 MΩ, Sutter BF100-50-10 with filament) pulled with a Sutter P97 Flaming Brown horizontal electrode puller was placed upside down in Neurobiotin/TRITC-Dextran (1:1) 2M KAcetate solution. Through capillary forces, the electrode tip was filled with dye. The shaft of the electrode was then filled with a 3 M KCl solution, leaving an air bubble to avoid dye dilution. MN5 soma was impaled and filled iontophoretically with the dye solution using a positive current of approximately 0.5 - 1 nA for approx. 10 min (Axoclamp 2B in bridge mode). Subsequently, the electrode was carefully removed and the preparation was instantly fixated with 4 % PFA solution for 45 min. After washing with PBS 3x for 20 min, the preparations were permeabilized with 0.5 % TritonX-PBS solution 6x for 20 min. Incubation with a Cy5-Streptavidin polyclonal antibody (1:750; Jackson Immunoresearch,

116-600-084) diluted in 0.3 % TritonX-PBS solution was done overnight at 4 °C. The preparations were again washed with PBS 6 times for 20 min and then dehydrated with an ascending ethanol series (50, 70, 90, 100 % for 10 min each). Finally, they were mounted in methylsalicylate.

The dendritic structure was scanned with a TCS SP8 confocal microscope (Leica) with Leica Application Suite AF software (LAS AF, Leica), a 40x oil immersion lens (HC PL APO 40x/1.30 Oil CS2, Leica, Na = 1.25) with immersion oil (Type F, Leica Microsystems) and a 3.5 zoom factor for further magnification. Images were acquired with a resolution of 1024x1024 and a z-step size of 0.3 µm. Voxel dimensions were 86 × 86 × 290 nm (x,y,z). Cy5 fluorophore was excited with a HeNe laser at 633 nm and detected between 645 - 700 nm. Per neuron, two image stacks had to be taken to enable imaging of the entire neuron.

2.12.2 Reconstruction of the dendritic tree

For the reconstruction of the dendritic tree, confocal image stacks of the filled and stained MN5 were opened with the Amira 5.4.5 software. Per neuron, the two separate image stacks were assembled and transformed into am-data format. To do so, the image stacks were displayed as 'OrthoSlice'. The 'TransformEditor' was applied to one of the two image stacks and they were correctly aligned in all orientations (xy and z) using the "Interact" tool. Subsequently, the translated coordinates ('Translation' values) were copied from the 'Dialog' of the 'TransformEditor' and pasted into the 'CropEditor' (in 'Min coord'). Each value was confirmed ('OK'). Afterward, the 'Dialog' window of the 'TransformEditor' was reset and the images were saved as '.am' files. The transformed images were then opened in Amira 5.3.3 with customized plug-ins for 3D reconstruction (Evers *et al*., 2005; Schmitt *et al*., 2004). A SkeletonTree was generated (Create -> Skeleton -> SkeletonTree) and displayed via 'DisplaySkeletonTree' and reconstruction tools were revealed by selecting the 'GraphEditor'. The SkeletonTree was connected with one of the image stacks displayed as 'OrthoSlice' via the blue square of the 'SkeletonTree' and selection of 'Data'. Finally, the dendritic tree was reconstructed by applying globes and tracing all visible structures of the filled neuron. Globes could be applied by selecting 'Add a new point or branch (A)' and holding 'Strg' while clicking with the mouse on respective structures.

The diameter of each dendrite had to be fitted (‘Select a branch’ & ‘Strg + E’ or ‘Strg + F’). Fitting parameters had to be adjusted in the menu (Skeleton -> Options -> Fitting param). Internal: loc 0.5 / rad 0.5 / step 0.3; External: 0.05 for all values.
Please note that the correct diameter is only displayed, if ‘draw diameter’ is selected in the ‘DisplaySkeletonGroph’ settings and depends on the selected fitting parameters. Furthermore, fitting is only possible if the whole toolbar is visible. An orthographic perspective (eye tool) was always used for reconstruction.

2.12.3 General analysis of the SkeletonTree

For analysis of the dendritic tree, the primary neurite was selected as tree root (‘Set selection as tree root’). Then, the entire dendritic tree was marked and the skeleton statistics were measured (SkeletonTree -> Measure -> Skeleton stats). The ‘Skeleton stats’ data set was saved as txt-file and imported into excel for further analysis. The total dendritic length (TDL), the number of branches (#Branches) and the maximal branch order (max order) could be extracted directly from the raw data. Mean dendritic length (MDL), mean dendritic radius (MDR), mean path length (MPL) were calculated.

2.12.4 Analysis of the dendrite distribution from Cholinergic and GABAergic input domains

The dendritic tree of adult MN5 receives excitatory synaptic input via the cholinergic Dα7 nicotinic acetylcholine receptor and inhibitory input via the Rdl GABAA receptor. Thereby, excitatory input is mostly received from dendrites originating from the proximal primary neurite (meaning closer to the soma), while inhibitory input is received by dendrites originating from the distal primary neurite (meaning further away from the soma towards the axon; Kuehn & Duch, 2013; Ryglewski *et al*., 2017). If the distance between the most proximal and most distal dendrite is measured (approx. 52 µm on average) and the midpoint is taken, the dendritic tree can be divided into a proximal (mainly excitatory input domain) and distal (mainly inhibitory input domain) part (Fig.20; Ryglewski *et al*., 2017). The dendritic length of both parts was measured and the ratio of the proximal/distal length was calculated in Microsoft Excel.

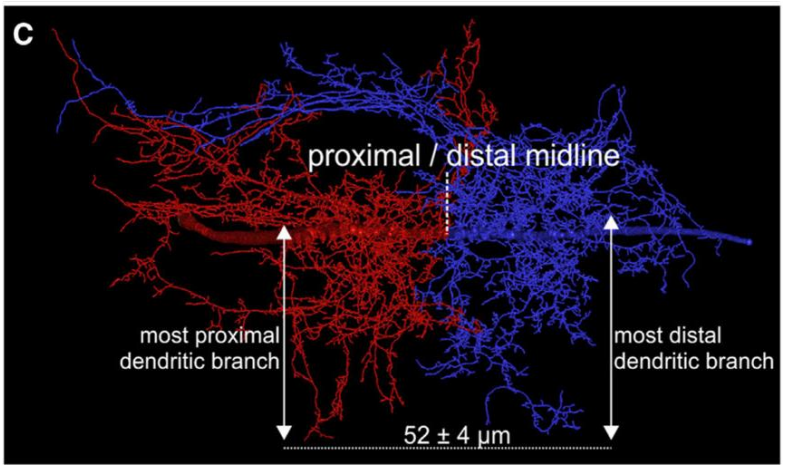

Fig.20: Quantification of proximal vs distal dendritic length for adult MN5 motoneuron
Reconstructions of MN5 dendritic tree. Distance between the most proximal (close to soma) and most distal (close to axon) dendritic sub-branches was measured (approx. 52 ± 4 µm). The midpoint was calculated to divide the MN5 dendritic tree in a proximal (red, mainly excitatory input) and distal (blue, mainly inhibitory input) part. (Modified from Ryglewski *et al*., 2017)

2.13 Statistical analysis of the data

Collection and further analysis of raw data were mostly done in Excel (Microsoft, 2013), while statistical tests were performed in SPSS Statistics 23 V5. Before statistical testing was done, all data sets were tested for normal distribution with a Shapiro-Wilk test. If the p-value of all groups from one data set was ≥ 0.05 the data were normally distributed. If the p-value was < 0.05 for at least one tested group of one data set, the data were further treated as non-normally distributed.

For normally distributed groups > 2 the variance homogeneity was tested with Levene's test. Then a one-way ANOVA was performed. If the p-value of the ANOVA was < 0.05 in groups with variance homogeneity, pairwise testing was done with the LSD posthoc test.

For non-normally distributed data with groups > 2, a Kruskal-Wallis ANOVA was performed. Pairwise testing was done with a Dunn-Bonferroni posthoc test.

Comparison of two related groups with normal distribution was done with paired students T-Test. Two non-related groups with normal distribution were tested with an unpaired T-Test. Two non-normally distributed related groups were compared by Mann-Whitney-U test.

Bar diagrams were generated with Microsoft Excel. They display the mean value plus standard deviation (SD) or standard error (SE) as whiskers. The group size (N) is presented as a single number inside of the bars. Box plots were generated with SPSS Statistics 23 V5. They display the median value plus the upper (25 %) and lower (75 %) quartile. The whiskers display the data in a 1.5 fold interquartile range. The group size (N) is presented

as a single number inside of the boxes. In both diagram types, the level of statistical significance was marked with asterisks: $p < 0.05$ *; $p < 0.01$ **; $p < 0.001$ ***

3. Results

3.1 Stj and dα$_2$δ$_1$ are differentially expressed in the larval and adult VNC, but both localize to motoneurons

In vertebrates, α$_2$δ subunits seem to have cell- and tissue-specific expression patterns (Cole *et al*., 2005). This suggests differential expression patterns of α$_2$δ-α$_1$ combinations in specific neurons, but no data on the expression of different α$_2$δ subunits in the *Drosophila* CNS are available. Since there are no appropriate antibodies against α$_2$δ subunits in *Drosophila*, the MiMIC protein trap technique was used to assess Stj and dα$_2$δ$_1$ localization (see 2.2). A functional MiMIC protein trap endogenously expressing GFP tagged dα$_2$δ$_1$ (dα$_2$δ$_1^{GFP}$) was obtained from the Drosophila Bloomington stock center (BDSC_59289). A MiMIC protein trap endogenously expressing mCherry tagged Stj (Stj^{mCherry}) was produced in the course of this study (see appendix 6.7). To test for differential expression and localization of Stj and dα$_2$δ$_1$, larval and adult flies carrying both protein trap constructs (a) were used.

a) $$; \frac{d\alpha_2\delta_1 Mi[GFP]MIC}{StjMi[mCherry]MIC};$$

Stainings against GFP and mCherry were performed. As a synaptic marker, the active zone protein Bruchpilot (Brp) was co-labeled. Confocal image stacks indicate a broad expression of Stj and dα$_2$δ$_1$ throughout the larval (Fig.21 A,Ai) and adult VNC (Fig.21 C,Ci). Stj^{mCherry} (green) and dα$_2$δ$_1^{GFP}$ (magenta) signal could be detected in somata of many neurons, including larval and adult motoneurons (MNs). While dα$_2$δ$_1$ localizes to the larval and adult neuropil (Fig.21 Bi,Ci), which is co-labeled through the α-Brp signal (cyan), no Stj^{mCherry} signal could be found in the larval or adult neuropil regions (Fig.21 B,C). This does not exclude low expression levels of Stj^{mCherry} in the neuropil, below the detection level of immunocytochemistry and subsequent confocal laser scanning microscopy.

We further tested for expression of Stj and/or dα$_2$δ$_1$ in well-characterized larval and adult motoneurons, which can readily be identified through their characteristic localization in the larval or adult VNC. Interestingly, both Stj and dα$_2$δ$_1$ signal could be detected in the somata of larval RP2 or aCC neurons (Fig.21 Aiii,Aiv; indicated by arrows). Additionally,

Stj^{mCherry} signal was found in the adult MN5 somata (Fig.21 D; indicated by arrows). Since the adult VNC is very dense and dα$_2$δ$_1^{GFP}$ highly localizes to neuropil regions, detection of dα$_2$δ$_1$ in adult MN5 neurons was difficult. However, dα$_2$δ$_1^{GFP}$ signal was found in MN5 somata during late pupal stages (P14) (Fig.1 E,Ei; indicated by arrows). Thus, both Stj and dα$_2$δ$_1$ are expressed in larval RP2/aCC motoneurons, as well as adult MN5 motoneurons.

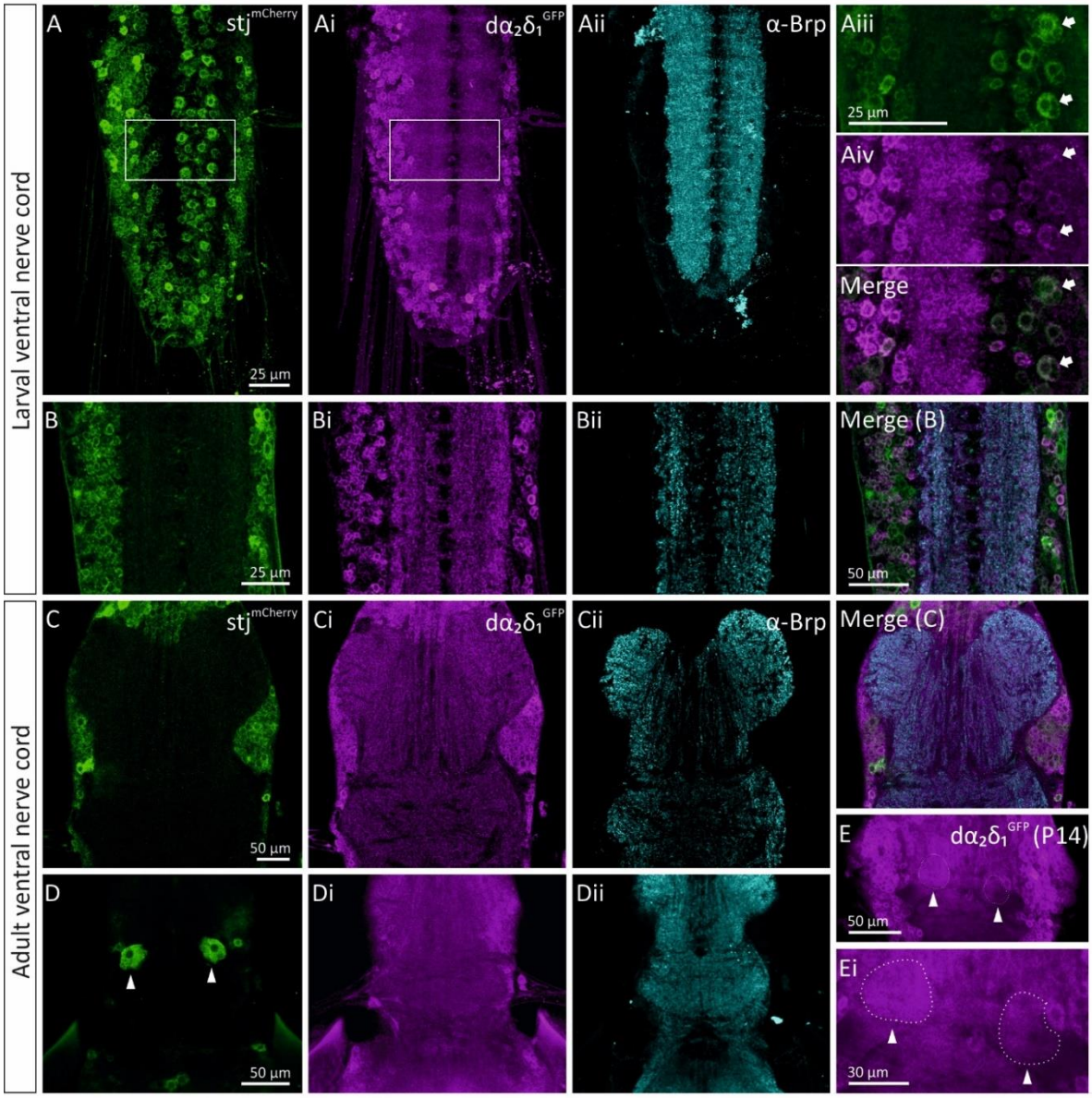

Fig.21: Stj & dα$_2$δ$_1$ are differentially expressed in the larval and adult VNC, but both localize to motoneurons
Triple labeling of Stj^{mCherry} (green), dα$_2$δ$_1^{GFP}$ (magenta) and Brp (cyan) [**A,B**] in larval and [**C,D**] adult VNC. Projection views of 40 sections reveal that both Stj^{mCherry} & dα$_2$δ$_1^{GFP}$ are expressed in a broad number of neurons in the larval VNC [**A-Aii**], including motoneurons (MNs). [**Aiii-Aiv**, **Merge**] Enlargement (from white rectangle) of larval crawling MNs (white arrow) co-expressing Stj^{mCherry} & dα$_2$δ$_1^{GFP}$ (projection view of only five sections). [**B-Bii**, **Merge**] Single sections from the neuropil region reveal differential localization of Stj^{mCherry} and dα$_2$δ$_1^{GFP}$. While [**Bi**] dα$_2$δ$_1^{GFP}$ localizes to the neuropil region, which is co-labeled by the synaptic marker Brp, [**B**] Stj^{mCherry} does not. Both [**C**] Stj^{mCherry} and [**Ci**] dα$_2$δ$_1^{GFP}$ are also broadly expressed in the ganglionic cortex of the [**C-Cii**, single sections] adult VNC. [**D**] Stj^{mCherry} & [**E, Ei** enlargement] dα$_2$δ$_1^{GFP}$ are both expressed in adult flight MNs (white arrows). Due to the abundant signal of dα$_2$δ$_1^{GFP}$ [**Ci-Cii, Merge**] in adult neuropil regions, which are co-labeled by [**Cii,Dii**] Brp, detection of MN5 was easier during late pupal development (P14). (Figure from Heinrich & Ryglewski in submission)

3.1.1 Stj^{mCherry} localization can be confirmed by the overexpression of functional Stj^{HA}

One potential caveat of using tagged proteins in localization studies is that the MiMIC construct could disrupt the function of the $\alpha_2\delta$ subunits, and therefore, impair correct targeting, surfacing, or localization. Stj localization as obtained by Stj^{mCherry} detection was confirmed by the overexpression of a functional HA-tagged Stj construct (UAS-Stj^{HA}; Kurshan *et al.*, 2009) using an Stj-Gal4 promoter. An antibody staining against the HA-tag was performed and confocal images were taken. The localization pattern of Stj^{HA} appears similar to that of Stj^{mCherry} in the larval and adult VNC (Fig.22). This further confirms Stj localization to somata but not the neuropil regions.

Unfortunately, no HA-tagged version of d$\alpha_2\delta_1$ was available to further confirm the localization or expression pattern. But since d$\alpha_2\delta_1^{GFP}$ localizes to the neuropil, the protein seems to be successfully transported out of the soma. One potential way to test if the GFP tag really disrupts the function of the d$\alpha_2\delta_1$ protein would be to test, whether d$\alpha_2\delta_1^{GFP}$ flies display the same behavioral phenotypes as d$\alpha_2\delta_1^{RNAi}$ (as described below).

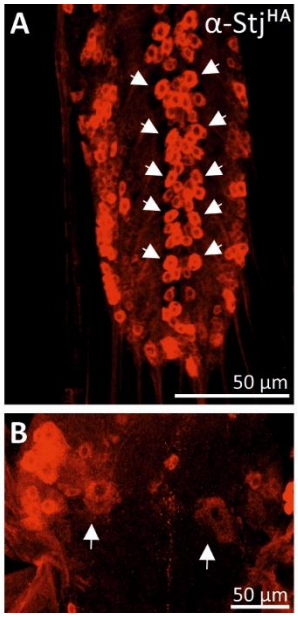

Fig.22: Stj^{HA} localizes to somata in larval and adult VNC.

Labeling of the HA-tag in [**A**] larval and [**B**] adult flies overexpressing UAS-Stj^{HA} under the control of Stj-Gal4. Projection views of confocal image stacks reveal that Stj^{HA} is expressed in a broad number of neurons, including [**A**] larval and [**B**] adult motoneurons (white arrows). (Figure from Heinrich & Ryglewski in submission)

3.1.2 Stj and d$\alpha_2\delta_1$ are also differentially expressed during pupal development

Since d$\alpha_2\delta$ subunits are also known to play a role in development and synaptogenesis (Kurshan *et al.*, 2009; Eroglu *et al.*, 2009; Geisler *et al.*, 2019) we tested for changes of Stj and d$\alpha_2\delta_1$ expression and localization during selected pupal stages. The onset of dendritic

growth and evoked firing of MN1-5 motoneurons starts in P5 (Ryglewski *et al*., 2014; Consoulas *et al*., 2002). In P7-P10 action potentials are shaped by HVA calcium currents, displaying a calcium component. This calcium component is most prominent in P8. HVA calcium currents are further known to be important for normal dendritic growth of MN1-5 (Ryglewski *et al*., 2014; 2017). Thus, $Stj^{mCherry}$ and $d\alpha_2\delta_1^{GFP}$ protein trap flies were dissected at pupal stages: P3, P5, P8, P10 & P14. Antibody staining's against either mCherry and Brp or GFP and Brp were performed as described above and confocal image stacks were taken.

Labeling of $d\alpha_2\delta_1^{GFP}$ reveals $d\alpha_2\delta_1$ localization in the ganglionic sheath in the somata of a broad number of neurons, as well as in the neuropil, which was again counter-labeled by the synaptic marker Brp (Fig.23 $d\alpha_2\delta_1^{GFP}$). This localization pattern was found in all selected pupal stages. Also, $Stj^{mCherry}$ expression was found in a broad number of neurons. Stj seems to be mostly localized in somata in the ganglionic sheath and not in the neuropil regions in all selected pupal stages (Fig.23 $Stj^{mCherry}$). This further confirms the differential localization of Stj and $d\alpha_2\delta_1$ in *Drosophila* VNC. Differential expression of Stj and $d\alpha_2\delta_1$ further suggests functional differences between those two $d\alpha_2\delta$ subunits.

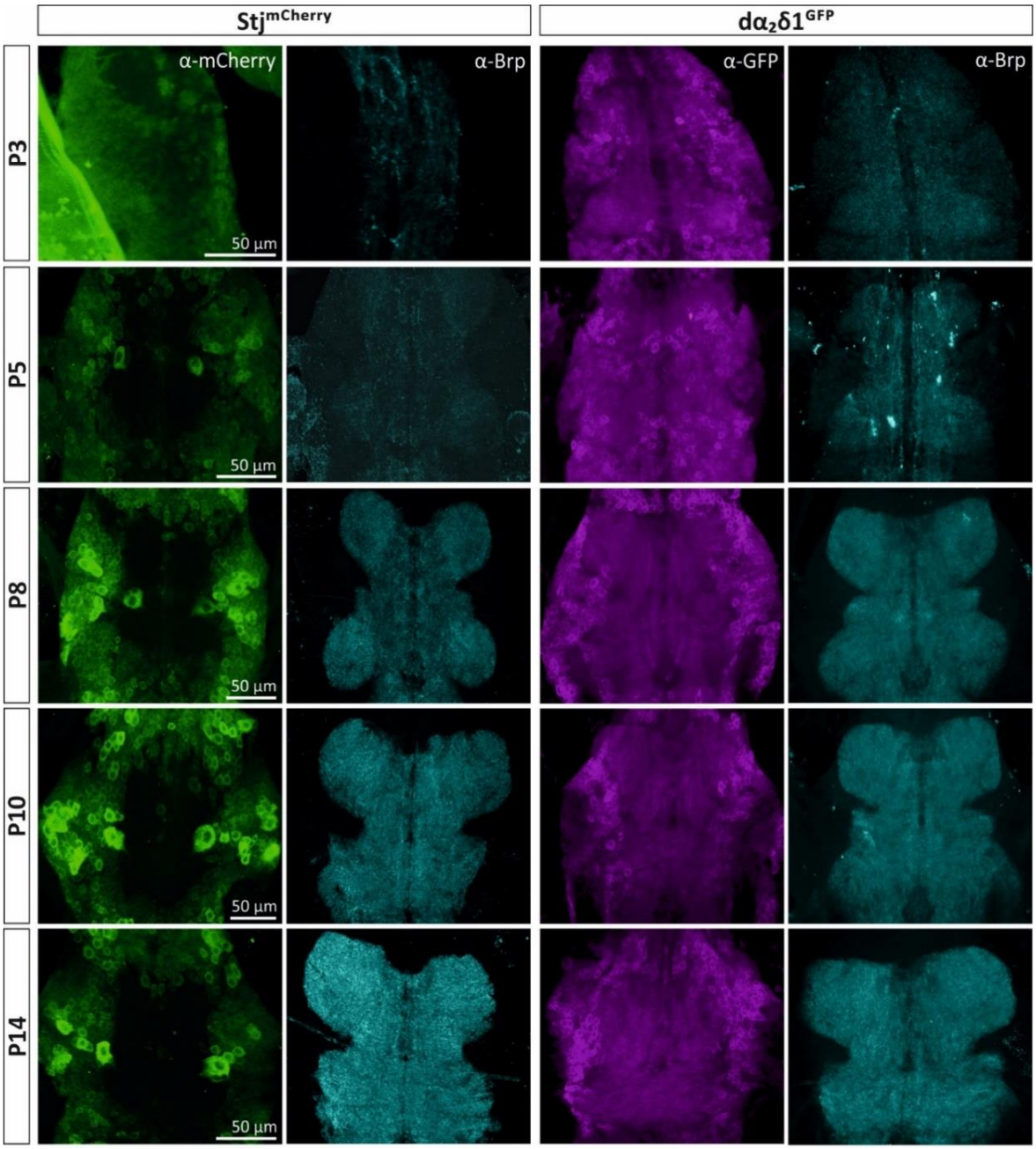

Fig.23: Stj & dα$_2$δ$_1$ are differentially expressed during pupal development
[**Stj^{mCherry}**] Double labeling of Stj^{mCherry} (green) plus the synaptic marker Brp (cyan) and [**dα$_2$δ$_1^{GFP}$**] dα$_2$δ$_1^{GFP}$ (magenta) plus Brp (cyan) in VNC of selected pupal stages [**P3, P5, P8, P10, P14**]. Projection views of approx. 50 sections reveal that both Stj^{mCherry} & dα$_2$δ$_1^{GFP}$ are expressed in the ganglionic cortex in a broad number of neurons in VNC during pupal development. While dα$_2$δ$_1^{GFP}$ localizes to the neuropil region, which is co-labeled by Brp, Stj^{mCherry} does not. (Figure from Heinrich & Ryglewski in submission)

3.2 Stj and dα$_2$δ$_1$ seem to be required for different functions in *Drosophila* nervous system

To test for functional differences of dα$_2$δ subunits in *Drosophila* nervous system (NS), we first tested at gross defects following Stj or dα$_2$δ$_1$ RNAi knockdowns. RNAi knockdowns for

Stj and $d\alpha_2\delta_1$ were obtained from the Vienna Drosophila Resource Center (VDRC). Since both knockdown lines were built with the so-called KK cloning strategy, they needed to be tested for additional insertion of the RNAi-construct into the 40D landing site (see 2.5). Indeed, in the KK $d\alpha_2\delta_1$ RNAi fly line (VDRC_108150) the construct had inserted into both the 30D and 40D landing sites (see appendix 6.8), which can potentially cause off-target effects through expression of the toxic protein tio (Green *et al*., 2014). Therefore, KK $d\alpha_2\delta_1$ RNAi needed to be 'repaired' before usage. Furthermore, knockdown efficacy needed to be quantified for both the Stj (Stj^{RNAi}) and $d\alpha_2\delta_1$ ($d\alpha_2\delta_1^{RNAi}$) RNAi fly lines.

3.2.1 Quantification of Stj and $d\alpha_2\delta_1$ RNAi knockdown efficacy

To quantify the RNAi efficacy on the protein level, Western blots were performed with $Stj^{mCherry}$ and $d\alpha_2\delta_1^{GFP}$ protein trap flies (see 2.6). Following a pan neural RNAi knockdown of either Stj^{RNAi} (b) or $d\alpha_2\delta_1^{RNAi}$ (c) in the respective protein trap fly lines, CNS of L3 larvae were collected from these flies and from the respective controls (a).

a) $\frac{elav^{C155}\text{-Gal4}}{y\,/\,+}\,;\,\frac{+}{StjMi[mCherry]MIC\,/\,d\alpha_2\delta_1Mi[GFP]MIC}\,;\,\frac{UAS\text{-dcr2}}{+}$

b) $\frac{elav^{C155}\text{-Gal4}}{y\,/\,+}\,;\,\frac{UAS\text{-}Stj^{RNAi}}{StjMi[mCherry]MIC}\,;\,\frac{UAS\text{-dcr2}}{+}$

c) $\frac{elav^{C155}\text{-Gal4}}{y\,/\,+}\,;\,\frac{UAS\text{-}d\alpha_2\delta_1{}^{RNAi}}{d\alpha_2\delta_1Mi[GFP]MIC}\,;\,\frac{UAS\text{-dcr2}}{+}$

In controls, the Western Blot revealed two bands at approx. 180 kDa and 200 kDa. The band with the larger molecular weight (200 kDa) perfectly fits with the expected size for $\alpha_2\delta$ (α_2 ~150 kDa; δ ~20 kDa; Takahashi *et al*., 1987) plus the tag (mCherry and GFP ~27 kDa). A fraction of the $\alpha_2\delta$ protein might be cleaved in α_2 and δ during the Western Blot procedure. Thus, the band with the lower molecular weight (180 kDa) will be only the tagged α_2 protein. The detected bands were further analyzed with Image J and normalized to the loading control (actin ~43 kDa) in Excel as described above. Compared to control the amount of $Stj^{mCherry}$ protein was reduced by 64 % in the CNS of Stj^{RNAi} (Fig.24 A). The amount of $d\alpha_2\delta_1^{GFP}$ was reduced by approx. 98 % in $d\alpha_2\delta_1^{RNAi}$ compared to control (Fig.24 B) following pan neural knockdown (elav-Gal4). Although cell-specific Gal4 drivers

may yield different knockdown efficacy due to differences in GAL4 expression levels, this yields a reasonable estimate of knockdown efficacy in further experiments with targeted RNAi expression in motoneurons (see below).

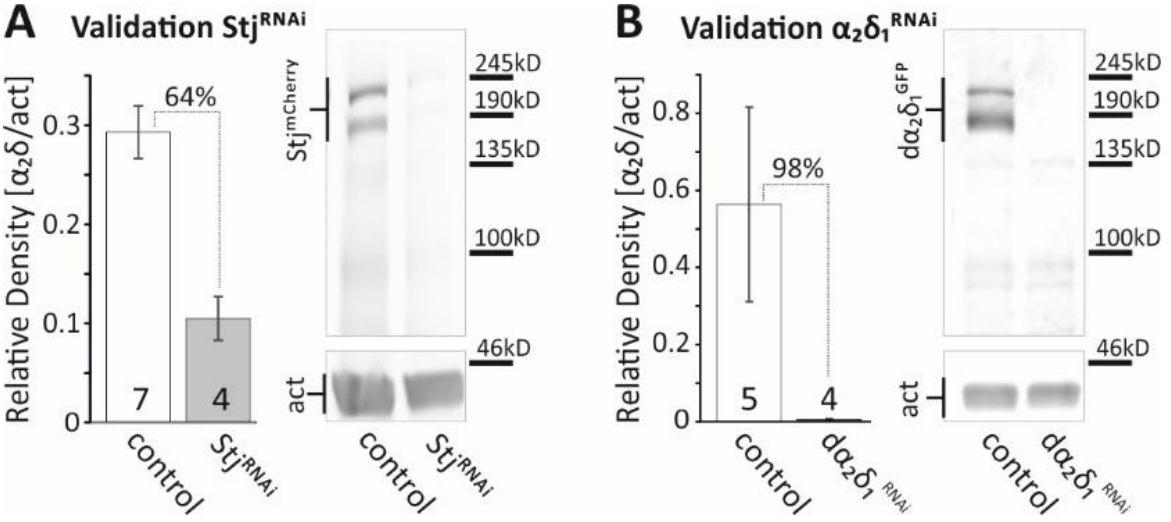

Fig.24: Quantification of Stj^{RNAi} & dα$_2$δ$_1$^{RNAi} knockdown strength
[**A**] Western blot analysis of the protein level of Stj^{mcherry} (30 larval CNS / 80 µl sample buffer) in control (;; UAS-dcr2) and pan-neural knockdown (elav^{C155}-Gal4) of Stj (UAS-Stj^{RNAi}; UAS-dcr2, VDRC_108569). Stj^{mCherry} is reduced by approx. 64 % in Stj^{RNAi} compared to control. [**B**] Protein level of dα$_2$δ$_1$^{GFP} (20 larval CNS / 80 µl sample buffer) was reduced by 98 % in larvae with a pan-neural knockdown of dα$_2$δ$_1$ (UAS- dα$_2$δ$_1$^{RNAi}; UAS-dcr2, VDRC_108150) compared to control (;; UAS-dcr2) [**B**]. The Western reveals two bands for the endogenously tagged dα$_2$δ (approx. 200 & 180 kDa) since the δ part will be cleaved off in a fraction of the sample protein during the western procedure. Actin (43 kDa) was used as a loading control. Mean values are presented as bars with whiskers for the standard error. The number of replicates is given inside the respective bar. (Figure modified from Heinrich & Ryglewski in submission)

3.2.2 Both Stj and dα$_2$δ$_1$ are required for normal motor behavior in *Drosophila*

After quantification of Stj^{RNAi} and dα$_2$δ$_1$^{RNAi} knockdown efficacy, we probed for obvious defects in flies with either Stj or dα$_2$δ$_1$ knockdown in a specific subset of neurons or cells. Flies with a pan-neural knockdown of Stj (Stj^{RNAi}; VDRC_108569) died at pupal stage P15 (Tab.4). By contrast, flies with an even stronger pan-neural knockdown of dα$_2$δ$_1$ were viable and had no obvious defects. To further test, whether Stj is especially important in certain subsets of neurons, we expressed Stj^{RNAi} in all neurons except glutamatergic neurons (elav^{C155}-Gal4; VGlut-Gal80), only in glutamatergic neurons (OK371-Gal4) and only in cholinergic neurons (Cha-Gal4). All Stj knockdown flies were able to hatch but seemed very slow and lethargic and most flies died soon after hatching. Thus, Stj seems to be important in a broad number of neurons. Interestingly, flies with a targeted knockdown of Stj in MN1-5 (23H06-Gal4) are unable to fly, while knockdown of dα$_2$δ$_1$ did not seem to

affect flight ability. Knockdown of either Stj or $d\alpha_2\delta_1$ only in muscles (Mef2-Gal4) resulted in no obvious defects, while flies with a double knockdown of both Stj and $d\alpha_2\delta_1$ in muscles died at pupal stage P15. This indicates, that both Stj and $d\alpha_2\delta_1$ are also functional in muscle cells, where they might mediate at least party redundant functions.

Tab.4: Obvious defects of Stj^{RNAi} and $d\alpha_2\delta_1^{RNAi}$ expressed in different subsets of cells

Promoter	RNAi - Line	hatched flies ♂ ♀	obvious defects in adult flies ♂	obvious defects in adult flies ♀
elav-Gal4	$d\alpha_2\delta_1$ (VDRC_108150);dcr2	✓ ✓	none	none
elav-Gal4	stj (BL_25807);dcr2	✓ ✓	32 % die after hatching	restricted wing motor skills
elav-Gal4	stj (VDRC_108569);dcr2	✗ ✗	don't get older than P15	don't get older than P15
elav-Gal4;dcr2	$d\alpha_2\delta_1$ (VDRC_108150);stj (BL_25807)	✓ ✓	100 % die after hatching	100 % die after hatching
elav-Gal4;VGlut-Gal80	stj (VDRC_108569);dc2	✓ ✓	very slow and lethargic	very slow and lethargic
Cha-Gal4	stj (VDRC_108569);dcr2	✓ ✓	very slow and lethargic	very slow and lethargic
OK371-Gal4;dcr2	stj (VDRC_108569);dcr2	✓ ✓	very slow and lethargic	very slow and lethargic
23H06-Gal4	$d\alpha_2\delta_1$ (VDRC_108150);dcr2	✓ ✓	able to fly	able to fly
23H06-Gal4	stj (VDRC_108569);dcr2	✓ ✓	unable to fly	unable to fly
D42-Gal4,Cha-Gal80	stj (VDRC_108569);dcr2	✓ ✓	36 % of all flies are unable to fly	
Mef2-Gal4	$d\alpha_2\delta_1$ (VDRC_108150);dcr2	✓ ✓	none	none
Mef2-Gal4	stj (VDRC_108569);dcr2	✓ ✓	none	none
Mef2-Gal4;dcr2	$d\alpha_2\delta_1$ (VDRC_108150);stj (BL_25807)	✗ ✗	don't get older than P15	don't get older than P15

Different knockdown lines of straightjacket (Stj) & $d\alpha_2\delta_1$ [**RNAi-Line**] were expressed under the control of different promoters [**Promoter**]. Knockdown strength was increased by additional expression of UAS-dcr2 (dcr2) in most of the cases. Hatching ability [**hatched flies**], as well as obvious defects [obvious defects in adult flies] in male and female adult flies, were noted.

Since flies with a pan-neural knockdown of $d\alpha_2\delta_1$ (b) did not show any obvious defects compared to control (a), normal motor behavior was further tested by applying the climbing assay (see 2.7.1) and the cylinder drop test (see 2.7.2).

a) $\frac{elav^{C155}\text{-Gal4}}{y\,/\,+}\,;\frac{+}{+}\,;\frac{UAS\text{-dcr2}}{+}$

b) $\frac{elav^{C155}\text{-Gal4}}{y\,/\,+}\,;\frac{UAS\text{-}d\alpha_2\delta_1{}^{RNAi}}{+}\,;\frac{UAS\text{-dcr2}}{+}$

The data from the climbing assay was normally distributed and accordingly, an unpaired T-Tests was performed for statistical analysis. Compared to control (2.3 $\pm$ 0.5 cm/s) climbing speed was significantly reduced ($p = 0.000$) in $d\alpha_2\delta_1^{RNAi}$ (1.3 $\pm$ 0.4 cm/s) (Fig.25 A). Also, the flight performance of $d\alpha_2\delta_1^{RNAi}$ (17.5 $\pm$ 8.7 cm; Mann-W, $p = 0.03$) flies was inferior compared to control (10.5 $\pm$ 3,6 cm) (Fig.25 B). Since the data were non-normally distributed a Mann-Whitney-U test was performed.

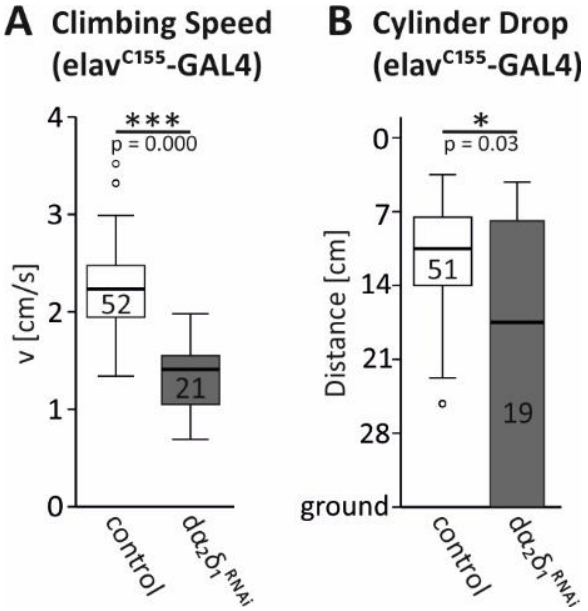

Fig.25: dα₂δ₁ is required for normal motor behavior of adult flies
[**A**] Flies with a pan-neural (elav^{C155}-Gal4) knockdown of dα₂δ₁ (UAS-dα₂δ₁^{RNAi};UAS-dcr2) display a reduced (p = 0.000) climbing speed compared to control (UAS-dcr2). [**B**] In addition the cylinder drop test revealed an impaired flight behavior in dα₂δ₁^{RNAi} (p = 0.03). Boxes display median with 25 and 75% quartiles, whiskers represent 10 and 90% quartiles. The number of replicates is given inside the respective box. An un-paired T-Test [**A**] and a Mann-Whitney-U test [**B**] was done for statistical analysis (p < 0.05*; p < 0.01**; p < 0.001***). (Figure modified from Heinrich & Ryglewski in submission)

These findings indicate, that both Stj and dα₂δ₁ are required for normal motor behavior in *Drosophila*, but both seem to have different functions. Since flies with a strong pan-neural knockdown of Stj die at P15 and Stj null mutants are reported to die at a late embryonic stage (Kurshan *et al*., 2009), it further seems like at least in the *Drosophila* NS Stj has functions which cannot be compensated for by dα₂δ₁ or other dα₂δ proteins.

3.2.3 Stj and dα₂δ₁ are not compensatory upregulated following RNAi knockdown of the other dα₂δ subunit in *Drosophila* CNS

To further test the hypothesis, that at least Stj and dα₂δ₁ are not able to functionally compensate for each other in the *Drosophila* CNS, we tested for compensatory upregulation of either Stj or dα₂δ₁ following a pan-neural knockdown of the other subunit. To do so, we performed Western Blots of Stj^{mCherry} flies expressing a pan neural knockdown of dα₂δ₁ (b) and of dα₂δ₁^{GFP} flies expressing a pan neural knockdown of Stj (c). We again collected CNS of L3 larvae from these flies and from the respective controls (a).

a) $$\frac{\text{elav}^{C155}\text{-Gal4}}{\text{y / +}} ; \frac{+}{\text{StjMi[mCherry]MIC / dα}_2\text{δ}_1\text{Mi[GFP]MIC}} ; \frac{\text{UAS-dcr2}}{+}$$

b) $$\frac{\text{elav}^{C155}\text{-Gal4}}{\text{y / +}} ; \frac{\text{UAS- dα}_2\text{δ}_1{}^{RNAi}}{\text{Stj[mCherry]MIC}} ; \frac{\text{UAS-dcr2}}{+}$$

c) $\frac{elav^{C155}\text{-Gal4}}{y\,/\,+}\,;\,\frac{UAS\text{-}Stj^{RNAi}}{d\alpha_2\delta_1[GFP]MIC}\,;\,\frac{UAS\text{-dcr2}}{+}$

The detected bands were analyzed with Image J and normalized to the loading control (actin) in Excel. All data sets were non-normally distributed and thus statistical comparison was done by performing Mann-Whitney-U tests. The amount of $d\alpha_2\delta_1^{GFP}$ protein was not changed (p = 1.00) compared to control (0.38 ± 0.19) following pan-neural expression of Stj^{RNAi} (0.46 ± 0.13) (Fig.26 A). Additionally, the amount of $Stj^{mCherry}$ was unchanged (p = 0.78) compared to control (0.28 ± 0.03) following pan-neural expression of $d\alpha_2\delta_1^{RNAi}$ (0.30 ± 0.03) (Fig.26 B).

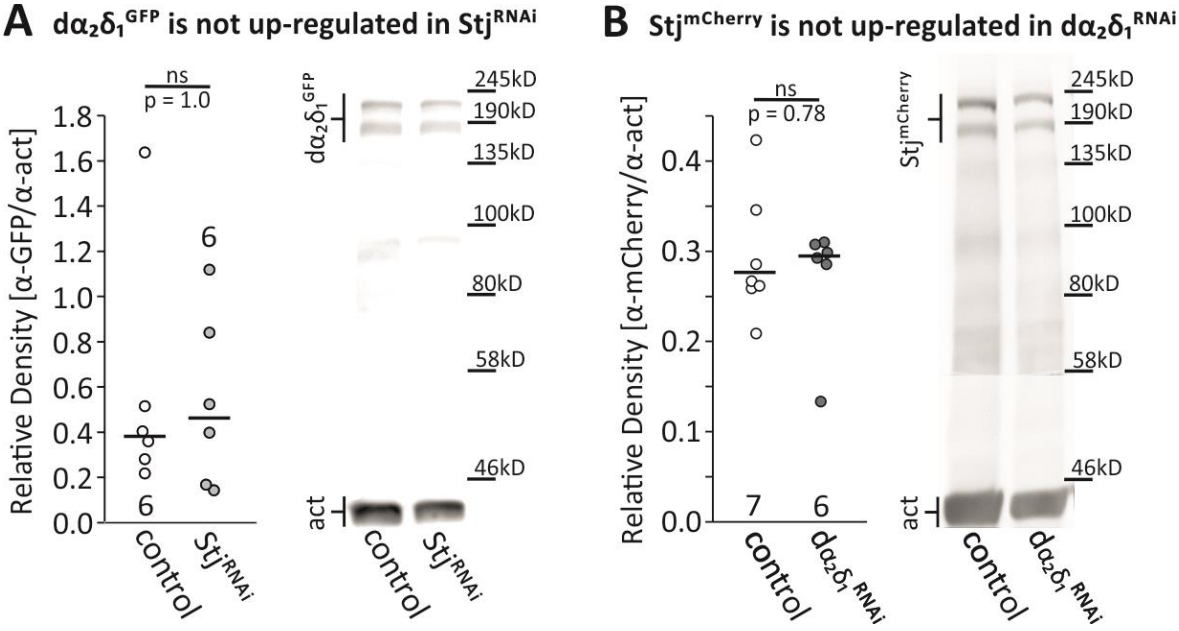

Fig.26: Neither $Stj^{mCherry}$ nor $d\alpha_2\delta_1^{GFP}$ expression is upregulated following knockdown of the other in larval CNS
[**A**] Western blot analysis of the protein level of $d\alpha_2\delta_1^{GFP}$ (20 CNS / 80 µl sample buffer) in control (;; UAS-dcr2) and during pan- neural knockdown ($elav^{C155}$-Gal4) of Stj (UAS-Stj^{RNAi}; UAS-dcr2, VDRC_108569). Compared to control $d\alpha_2\delta_1^{GFP}$ is not compensatory upregulated in Stj^{RNAi} (p = 1.0). [**B**] Western blot analysis of the protein level of $Stj^{mCherry}$ (30 CNS / 80 µl sample buffer) in control (;; UAS-dcr2) and $d\alpha_2\delta_1^{RNAi}$ (UAS- $d\alpha_2\delta_1^{RNAi}$; UAS-dcr2, VDRC_108150). $Stj^{mCherry}$ is not compensatory upregulated in $d\alpha_2\delta_1^{RNAi}$ compared to control (p = 0.78). The western reveals two bands for the endogenously tagged $d\alpha_2\delta$ (approx. 200 & 180 kDa) since the δ part will be cleaved off in a fraction of the sample protein during the western procedure. Actin (43 kDa) was used as a loading control. The data is presented as single data points with the median (bar). The number of replicates is given above or under the respective data points. A Mann-Whitney-U test was done for statistical analysis (p < 0.05*; p < 0.01**; p < 0.001***). (Figure modified from Heinrich & Ryglewski in submission)

3.3 Stj and dα$_2$δ$_1$ seem to be required for different functions in larval crawling motoneurons

In hypomorphic Stj mutants the Ca_V2 channel was found to be missing from the neuromuscular junction (NMJ) of larval crawling neurnons and thereby synaptic transmission was impaired (Ly *et al*., 2008; Dickman *et al*., 2008). Since both Stj and dα$_2$δ$_1$ are expressed in RP2 and aCC (see above), this already indicates that Stj and not dα$_2$δ$_1$ is required for correct localization of Ca_V2 at the NMJ of *Drosophila* larvae. It further indicates differential functions of Stj and dα$_2$δ$_1$ in larval crawling motoneurons of *Drosophila melanogaster*.

3.3.1 Stj and dα2δ1 seem to be required for different functions at the larval NMJ

To test for those different functions, we first wanted to confirm the already existing data (Ly *et al*., 2008; Dickman *et al*., 2008). Until now functional analyses of Stj at the *Drosophila* NMJ were done in mutants. Since our data suggest that both Stj and dα$_2$δ$_1$ are also functional in the muscle (see above), we instead decided to knockdown Stj (b) or dα$_2$δ$_1$ (c) only in glutamatergic neurons (OK371-Gal4) to prevent potential muscular effects. L3 larvae were dissected and intracellular current clamp measurements from muscle M10 were performed in RNAi knockdowns and the respective control (a).

a) $; \frac{+}{\text{OK371-Gal4}} ; \frac{\text{UAS-drc2}}{+}$

b) $; \frac{\text{UAS-Stj}^{\text{RNAi}}}{\text{OK371-Gal4}} ; \frac{\text{UAS-dcr2}}{+}$

c) $; \frac{\text{UAS-d}\alpha_2\delta_1{}^{\text{RNAi}}}{\text{OK371-Gal4}} ; \frac{\text{UAS-drc2}}{+}$

Evoked postsynaptic potentials (EPSP) were induced at 0.5 Hz for 10 s by stimulating the respective nerve with a suction electrode. To test for changes in EPSP amplitude an extracellular calcium concentration of 0.5 mM was used and the mean amplitude of all EPSP was calculated per animal. The data sets of all groups were normally distributed. Thus, for statistical analyses between the different groups, a one-way ANOVA and pairwise comparisons with LSD posthoc tests were performed. We were able to confirm a reduction in

EPSP amplitude by approx. 50 % (ANOVA, p = 0.000; LSD, p = 0.000) in Stj^{RNAi} (9.8 + 4.3 MV) larvae compared to control (17.5 ± 6.5 mV) (Fig.27 A,B). By contrast, EPSP amplitude was unchanged in $d\alpha_2\delta_1^{RNAi}$ larvae (19.5 ± 2.9 mV; LSD, p = 0.282). Interestingly EPSP in $d\alpha_2\delta_1^{RNAi}$ larvae seemed to be narrower and repolarize faster compared to control. To test this, we measured the integrated EPSP area and normalized it to the respective EPSP amplitude. Indeed the EPSP area/amplitude (ANOVA, p = 0.014) was reduced in $d\alpha_2\delta_1^{RNAi}$ (23.5 ± 4.2; LSD, p = 0.01) but not in Stj^{RNAi} (33.03 + 9.4; LSD, p = 0.847) compared to control (32.4 ± 10.8) (Fig.27 A,C).

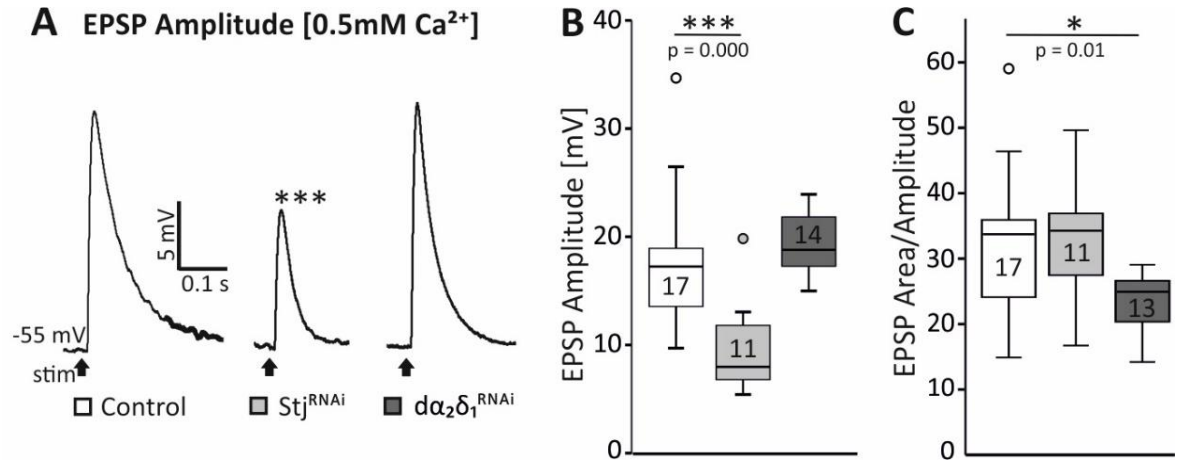

Fig.27: Both Stj and $d\alpha_2\delta_1$ are required for normal EPSPs at the larval neuromuscular junction (NMJ)
Evoked postsynaptic potentials (EPSP) were recorded intracellularly from muscle M10 in current-clamp mode while stimulating the respective nerve. A calcium concentration of 0.5 mM was used for the extracellular bath solution. [**A**] Single EPSP (0.5 Hz) were recorded in controls (UAS-dcr2, white box) and larvae with targeted knockdown of Stj (UAS-Stj^{RNAi}; UAS-dcr2, light gray box) or $d\alpha_2\delta_1$ (UAS- $d\alpha_2\delta_1^{RNAi}$; UAS-dcr2, dark gray box) in glutamatergic neurons (OK371-Gal4). [**B**] The EPSP amplitude was reduced in Stj^{RNAi} (p = 0.000) but not in $d\alpha_2\delta_1^{RNAi}$ (p = 0.282) compared to control (ANOVA, p = 0.000). [**C**] EPSP area/Amplitude was reduced in $d\alpha_2\delta_1^{RNAi}$ (p = 0.01) but not in Stj^{RNAi} (p = 0.847) compared to control (ANOVA, p = 0.014). Boxes display median with 25 and 75% quartiles; whiskers represent 10 and 90% quartiles. The number of replicates is given inside the respective box. A one-way ANOVA and LSD posthoc tests were done for statistical analysis (p < 0.05*; p < 0.01**; p < 0.001***).

To further test for changes in quantal content and release probability we measured the amplitude and frequency of spontaneous postsynaptic potentials (mPSP). The mPSP amplitudes were unchanged (ANOVA, p = 0.51) in both Stj^{RNAi} (0.54 ± 0.03 mV) and $d\alpha_2\delta_1^{RNAi}$ (0.56 ± 0.05 mV) compared to control (0.56 ± 0.05 mV) (Fig.28 A,B)), making postsynaptic changes in glutamate receptor expression or subunit composition following $d\alpha_2\delta^{RNAi}$ expression unlikely. Furthermore, quantal content seems unchanged in both Stj^{RNAi} and $d\alpha_2\delta_1^{RNAi}$, thus indicating a reduced number of vesicles being released during evoked responses in Stj^{RNAi}.

mPSP frequency was increased (ANOVA, p = 0.008) by approx. 30 % in $d\alpha_2\delta_1^{RNAi}$ (2.38 ± 0.6 Hz; LSD, p = 0.014) but unchanged in Stj^{RNAi} (1.65 ± 0.5 Hz; LSD, p = 0.481) compared to control (1.81 ± 0.4 Hz) (Fig.28 A,C). This indicates an increase in spontaneous release of synaptic vesicles in $d\alpha_2\delta_1^{RNAi}$ but not Stj^{RNAi}, and therefore an increased release probability.

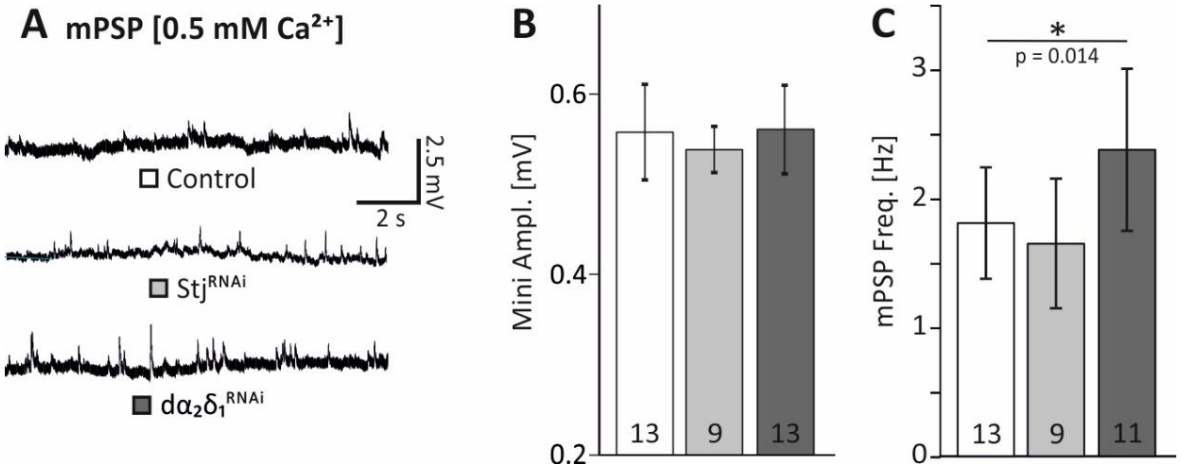

Fig.28: Spontaneous mini PSP (mPSP) frequency is increased in $d\alpha_2\delta_1^{RNAi}$ but not in Stj^{RNAi}
Spontaneous mini PSP (mPSP) were recorded intracellularly from muscle M10 in current-clamp mode with an extracellular calcium concentration of 0.5 mM. [**A**] mPSP amplitude and frequency were measured in controls (UAS-dcr2, white bar) and larvae with targeted knockdown of Stj (UAS-Stj^{RNAi}; UAS-dcr2, light grey bar) or $d\alpha_2\delta_1$ (UAS- $d\alpha_2\delta_1^{RNAi}$; UAS-dcr2, dark grey bar) in glutamatergic neurons (Ok371-Gal4). [**B**] The mPSP amplitude was unchanged in Stj^{RNAi} and $d\alpha_2\delta_1^{RNAi}$ compared to control (ANOVA, p = 0.51). [**C**] mPSP frequency was increased in $d\alpha_2\delta_1^{RNAi}$ (p = 0.01) but not in Stj^{RNAi} (p = 0.48) compared to control (ANOVA, p = 0.008). Mean values are presented as bars with whiskers for the standard deviation. The number of replicates is given inside the respective bar. A one-way ANOVA and LSD posthoc tests were done for statistical analysis (p < 0.05*; p < 0.01**; p < 0.001***).

Since HVA calcium channels are also known to play a role in both synaptic depression and synaptic facilitation (reviewed by Zucker & Regehr, 2002), we tested for changes in short-term plasticity in knockdown animals as compared to control. In synaptic facilitation, residual calcium from the preceding action potential will increase the calcium concentration inside the terminal following a subsequent action potential. Therefore, more vesicles will be released at the subsequent AP and EPSP amplitude increases. Synaptic facilitation will be higher in low extracellular calcium concentrations due to a reduction in the release probability. With fewer vesicles being released at the first EPSP, more vesicles will be available for the subsequent EPSP (reviewed by Jackman & Regehr, 2017). Synaptic facilitation was therefore measured at an extracellular Ca^{2+} concentration of 0.5 mM and was induced through paired pulses (PP) with an inter-pulse interval of 30, 50, 100 and 130 ms.

At 30 and 50 ms, the rising phase of the second EPSP was riding on the falling phase of the first EPSP, and thus, the amplitude of the second EPSP was difficult to determine. At 100 ms inter-pulse interval, the first EPSP was not fully, but mostly repolarized before the second occurred and the amplitude of the second EPSP was facilitated. At 130 ms the muscle was still not fully repolarized from the first EPSP, but PP facilitation was already relatively low (see appendix 6.11). For further analysis, an inter-pulse interval of 100 ms was used. PP facilitation was reduced (ANOVA, p = 0.004) in both Stj^{RNAi} (5.2 ± 7.7 mV; LSD, p = 0.004) and $d\alpha_2\delta_1{}^{RNAi}$ (5.2 ± 4.3 mV; LSD, p = 0.004) compared to control (13 ± 4.7 mV) (Fig.29 A-C), which hints at an increase in release probability in $d\alpha_2\delta_1{}^{RNAi}$, but also in Stj^{RNAi}. However, these findings could also indicate defects in normal synapse development or correct assembly of active zones.

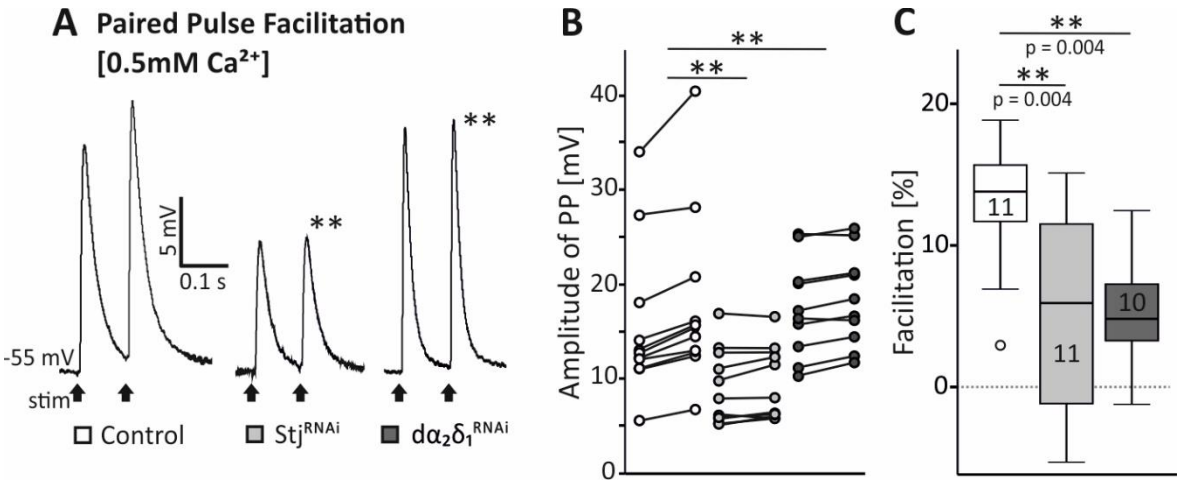

Fig.29: Paired pulse facilitation is reduced in both Stj^{RNAi} and $d\alpha_2\delta_1{}^{RNAi}$

[**A**] Paired pulses (PP) with an interpulse interval of 100 ms (EPSP) were evoked by stimulating the respective nerve while recording intracellularly from muscle M10 in current-clamp mode. A calcium concentration of 0.5 mM was used for the extracellular bath solution. [**B**] The amplitudes of the first and second pulse were measured in controls (UAS-dcr2, white box) and larvae with targeted knockdown of Stj (UAS-Stj^{RNAi}; UAS-dcr2, light gray box) or $d\alpha_2\delta_1$ (UAS-$d\alpha_2\delta_1{}^{RNAi}$; UAS-dcr2, dark gray box) in glutamatergic neurons (OK371-Gal4). The data is represented as data points and the points of the respective first and second spike are connected with a line. [**C**] PP facilitation (second/first EPSP in %) was reduced in Stj^{RNAi} (p = 0.004) and $d\alpha_2\delta_1{}^{RNAi}$ (p = 0.004) compared to control (ANOVA, p = 0.004). Boxes display median with 25 and 75% quartiles, whiskers represent 10 and 90% quartiles. The number of replicates is given inside the respective box. A one-way ANOVA and LSD posthoc tests were done for statistical analysis (p < 0.05*; p < 0.01**; p < 0.001***).

During synaptic depression, the frequent firing of action potentials will deplete the synaptic vesicles in the readily releasable pool. During sustained firing, over time recycling of vesicles will not keep up with release, so that evoked postsynaptic responses will become smaller (reviewed by Zucker & Regehr,2002). If endocytosis and recycling of vesicles are

balanced EPSP amplitude will not be further reduced and thus a steady-state should be reached.

A stimulation frequency of 5 Hz was applied for 10 s at an external Ca^{2+} concentration of 1.0 mM to test for synaptic depression at the *Drosophila* NMJ. The amplitude of all EPSP was measured and normalized to the first EPSP. The normalized EPSP amplitudes were plotted over time and fitted (Boltzmann fit) in Clampfit 10.7. The normalized amplitude of the steady-state and the time constant tau [τ] of depression were calculated.

The steady state was reduced (ANOVA, p = 0.000) in Stj^{RNAi} (59.7 ± 4.4 %; LSD, p = 0.000) but not in $d\alpha_2\delta_1^{RNAi}$ (71.7 ± 3.4 %; LSD, p = 0.705) compared to control (70.7 ± 4.4 %) (Fig.30 B,D). This could hint at a reduction in synaptic vesicle recycling or at defects in synapse development. By contrast the time constant τ was increased (ANOVA, p = 0.002) in both Stj^{RNAi} (-2.7 ± 0.7 s; LSD, p = 0.002) and $d\alpha_2\delta_1^{RNAi}$ (-2.5 ± 1.2 s; LSD, p = 0.001) compared to control (-5 ± 1.3 s) (Fig.30 B,C), which could indicate either an increase in release probability and/or a reduction in RRP size (Henning, 2013).

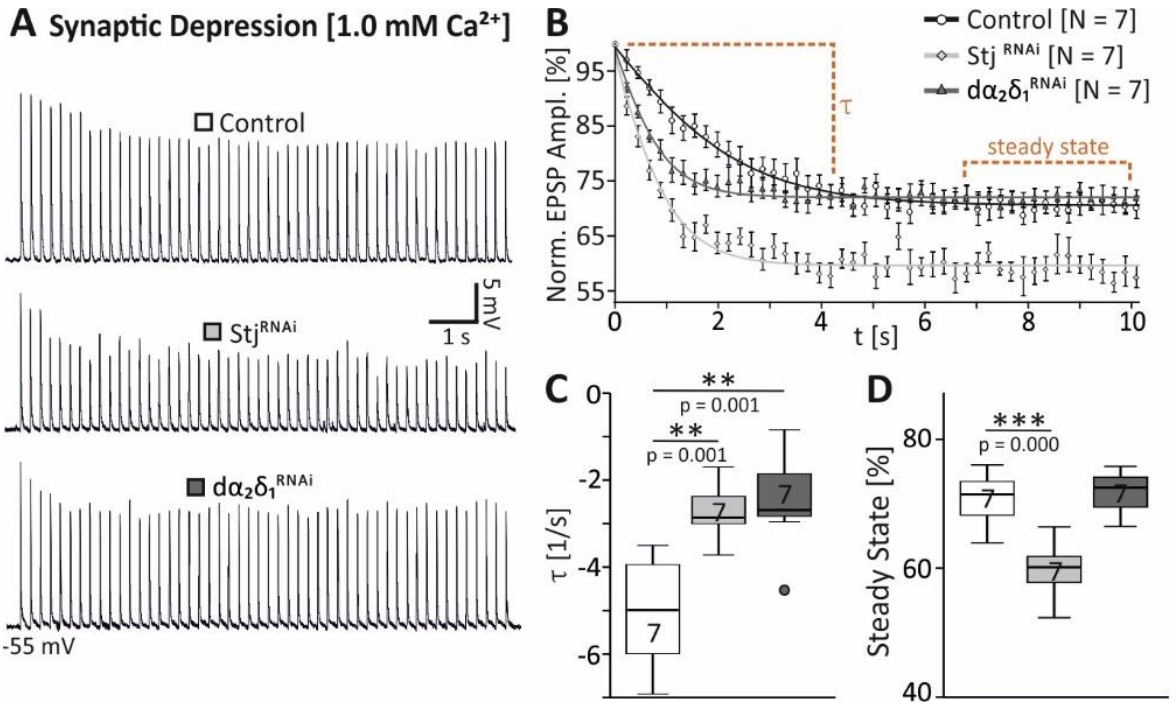

Fig.30: Synaptic depression is impaired in both Stj and $d\alpha_2\delta_1$ at the larval NMJ
Evoked postsynaptic potentials (EPSP) were recorded intracellularly from muscle M10 in current-clamp mode while stimulating the respective nerve. A calcium concentration of 1.0 mM was used for the extracellular bath solution. [**A**] EPSP trains (5 Hz for 10 s) were recorded in controls (UAS-dcr2, white box) and larvae with targeted knockdown of Stj (UAS-Stj^{RNAi}; UAS-dcr2, light gray box) or $d\alpha_2\delta_1$ (UAS- $d\alpha_2\delta_1^{RNAi}$; UAS-dcr2, dark gray box) in glutamatergic neurons (OK371-Gal4). [**B**] EPSP amplitudes were measured and normalized to the first EPSP. The normalized EPSP amplitudes were then plotted against time and fitted by a Boltzmann fit to assess the time constant τ and steady-state amplitude of synaptic depression. Whiskers represent the standard error. [**C**] τ was increased in both Stj^{RNAi} ($p = 0.001$) and $d\alpha_2\delta_1^{RNAi}$ ($p = 0.001$) compared to control (ANOVA, $p = 0.002$). [**D**] Steady-state of depression was reduced in Stj^{RNAi} ($p = 0.000$) but not in $d\alpha_2\delta_1^{RNAi}$ ($p = 0.705$) compared to control (ANOVA, $p = 0.000$). Boxes display median with 25 and 75% quartiles, whiskers represent 10 and 90% quartiles. The number of replicates is given inside the respective box. A one-way ANOVA and LSD posthoc tests were done for statistical analysis ($p < 0.05$*; $p < 0.01$**; $p < 0.001$***).

$\alpha_2\delta$ subunits are already known to play a role in synaptogenesis even before VGCC locate there (Kurshan *et al*., 2009). Therefore, changes in synaptic transmission could be a result of developmental defects in Stj and $d\alpha_2\delta_1$ knockdown animals. In previous studies, a reduced number of active zones was found in Stj mutant (hypomorphic mutations/deficiency) larvae. Furthermore, the Ca_V2 channel was absent from the larval NMJ of Stj mutants (hypomorphic mutations/deficiency, Ly *et al*., 2008).

To confirm these findings, antibody staining's against Brp as a marker for active zones and against HRP to label neuronal membranes were performed. Confocal image stacks of motoneuron boutons on M10 were done and analyzed with the Amira 5.4.5 software. The volume of synaptic *Is* type boutons was measured and the number of Brp puncta per bouton was counted and normalized to the bouton volume (Brp puncta/bouton volume). The data were non-normally distributed and thus, a Kruskal-Wallis ANOVA and pairwise comparison via Dunn-Bonferroni posthoc test were performed for statistical analysis. In larvae expressing Stj^{RNAi} (8.4 $\pm$ 2.4 μm^3) or $d\alpha_2\delta_1^{RNAi}$ (8.6 $\pm$ 2.6 μm^3) only in glutamatergic neurons, the bouton volume was unchanged (ANOVA, $p = 0{,}715$) compared to control (9.4 $\pm$ 2.7 μm^3) (Fig.31 A,B). Our data further confirm a reduced number (ANOVA, $p = 0.009$) of Brp puncta/bouton volume in Stj^{RNAi} larvae (1.8 $\pm$ 0.4; LSD, $p = 0.019$) compared to control (2.2 $\pm$ 0.3) (Fig.31 A,C). By contrast, the number of Brp puncta/bouton volume was unchanged in $d\alpha_2\delta_1^{RNAi}$ (2.3 $\pm$ 0.3; LSD, $p = 0.465$). Thus, the number of active zones per bouton seems reduced in Stj^{RNAi} but not in $d\alpha_2\delta_1^{RNAi}$. This should result in a reduced release probability of synaptic vesicles at the larval NMJ of Stj^{RNAi}. Together with the finding that PP facilitation is reduced in Stj^{RNAi}, this could hint at multiple defects in synaptic transmission.

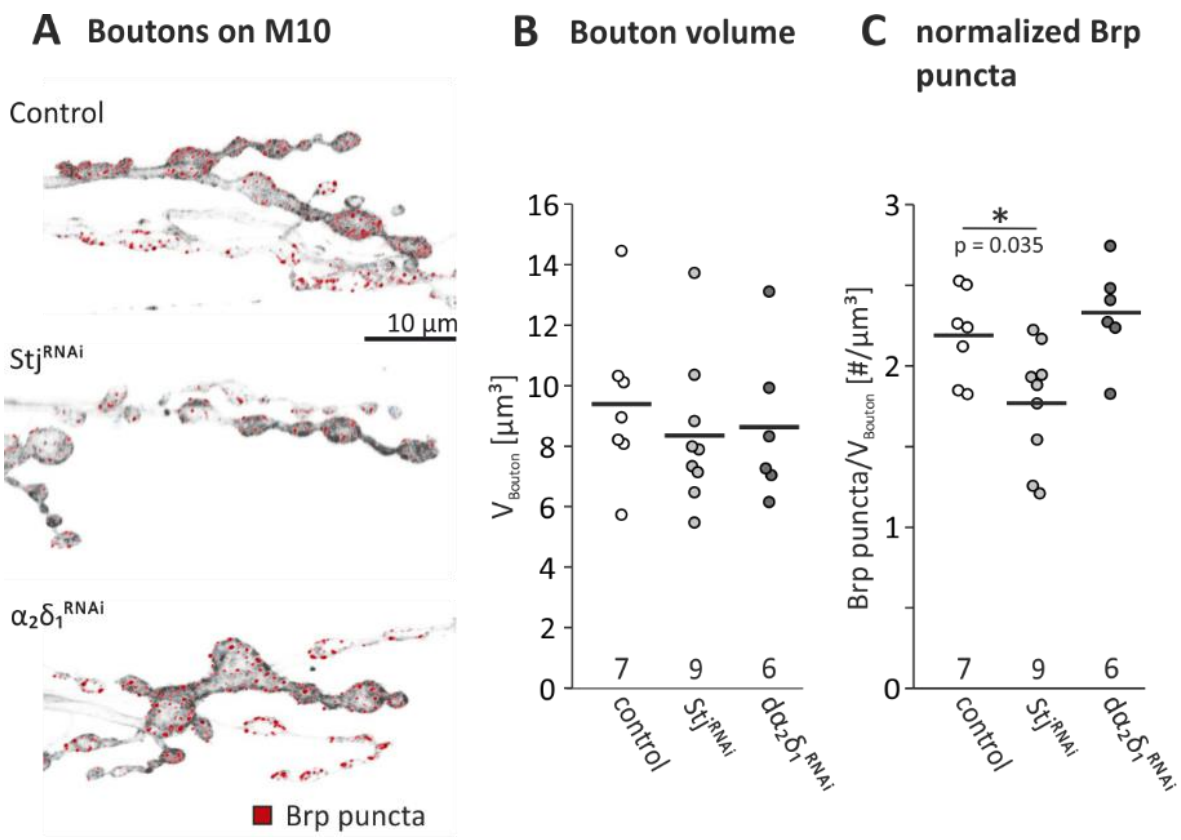

Fig.31: The number of active zones per bouton is decreased in Stj^{RNAi} but not in dα$_2$δ$_1^{RNAi}$ at the larval NMJ
[**A**] Double labeling of active zone marker Brp (red) and neuronal membranes (gray) by anti-HRP staining at the larval neuromuscular junction (NMJ) of muscle M10. Bouton volume (V_{Bouton}) of *Is* type boutons and the number of Brp puncta/V_{Bouton} were measured in controls (UAS-dcr2, white box) and larvae with targeted knockdown of Stj (UAS-Stj^{RNAi};UAS-dcr2, light gray box) or dα$_2$δ$_1$ (UAS- dα$_2$δ$_1^{RNAi}$;UAS-dcr2, dark gray box) in glutamatergic neurons (OK371-Gal4). [**B**] The bouton volume is unchanged in both Stj^{RNAi} and dα$_2$δ$_1^{RNAi}$ compared to control (ANOVA, p = 0.715). [**C**] The number of Brp puncta/V_{Bouton} was decreased in Stj^{RNAi} (p = 0.001) but not in dα$_2$δ$_1^{RNAi}$ (p = 0.001) compared to control (ANOVA, p = 0.002). The data is presented as single data points with the mean (bar). The number of replicates is given under the respective data points. A one-way ANOVA and LSD posthoc tests were done for statistical analysis (p < 0.05*; p < 0.01**; p < 0.001***).

We further analyzed changes in Ca_V2 density at the larval NMJ. Larvae with endogenously tagged Ca_V2 channels (Ca_V2^{GFP}) were used. Since the Ca_V2^{GFP} construct is localized on the X chromosome, only male larvae were utilized. Ca_V2^{GFP} was labeled with an anti-GFP nanobody. The nanobody has only one GFP binding site and is directly conjugated to a fluorophore. In contrast, Brp was stained with an indirect antibody staining which results in amplification of the signal since more than one secondary antibody will bind to the primary anti-Brp antibody. Consequently, the amount of Brp puncta counted in boutons cannot be directly compared to the number of counted Ca_V2^{GFP} puncta. Neuronal membranes were again labeled by anti-HRP staining. Confocal images from motoneuron terminals on M10 were taken and analyzed in Amira 5.4.5 software. The Ca_V2^{GFP} puncta per

bouton volume were counted in *Is* type boutons following expression of Stj^{RNAi} (b) and $d\alpha_2\delta_1{}^{RNAi}$ (c) in glutamatergic neurons (OK371-Gal4) and in the respective control (a).

a) $\frac{Ca_V2^{GFP}}{y}\,;\,\frac{+}{OK371\text{-}Gal4}\,;\,\frac{UAS\text{-}drc2}{+}$

b) $\frac{Ca_V2^{GFP}}{y}\,;\,\frac{UAS\text{-}Stj^{RNAi}}{OK371\text{-}Gal4}\,;\,\frac{UAS\text{-}dcr2}{+}$

c) $\frac{Ca_V2^{GFP}}{y}\,;\,\frac{UAS\text{-}d\alpha_2\delta_1{}^{RNAi}}{Ok371\text{-}Gal4}\,;\,\frac{UAS\text{-}dcr2}{+}$

The data were normally distributed and thus a one-way ANOVA and pairwise comparisons via LSD posthoc test were done. As expected from previous studies (Dickman *et al*., 2008; Ly *et al*., 2008) the amount of Ca_V2^{GFP} puncta per bouton was decreased (ANOVA, p = 0.000) in Stj^{RNAi} (0.33 $\pm$ 0.2; LSD, p = 0.000) compared to control. This should result in a reduced calcium influx during evoked synaptic transmission in Stj^{RNAi}, which will further result in a decreased amount of synaptic vesicle being release per EPSP (see above). In $d\alpha_2\delta_1{}^{RNAi}$ (0.93 $\pm$ 0.1; LSD, p = 0.156) the amount of Ca_V2^{GFP} puncta/bouton volume even tended to be increased, but was not significantly changed compared to control (0.86 $\pm$ 0.1) (Fig.32). Thus, Stj but not $d\alpha_2\delta_1$ is required for correct allocation of Ca_V2 to axon terminals of larval crawling motoneurons.

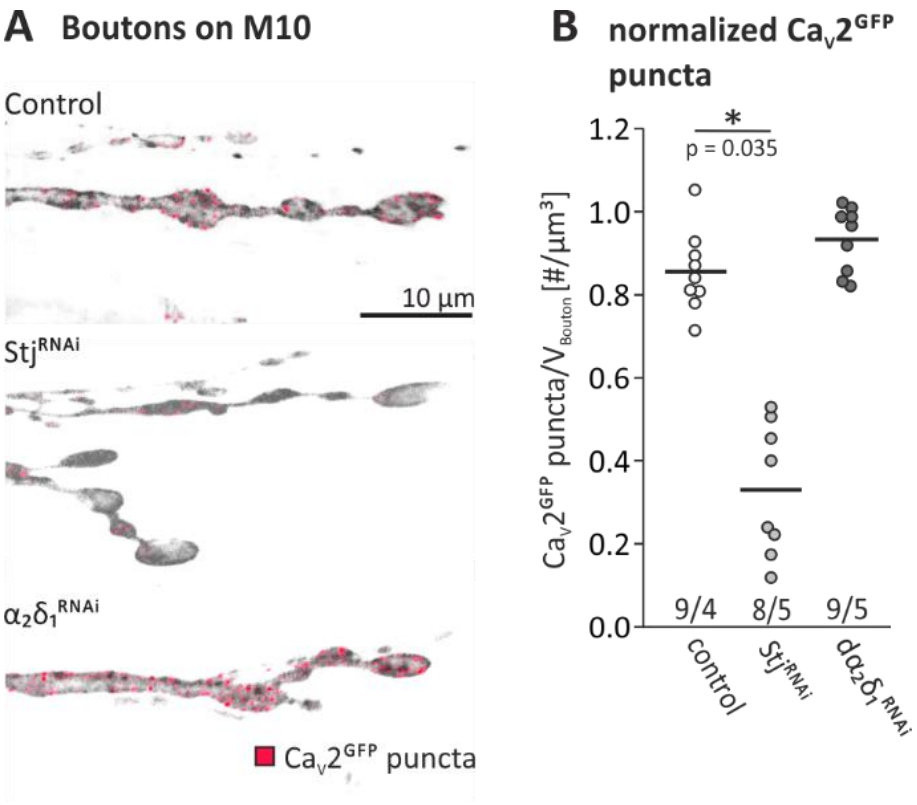

Fig.32: The number of Ca_V2^{GFP} channels per bouton is decreased in Stj^{RNAi} but not in $d\alpha_2\delta_1^{RNAi}$ at the larval NMJ
[**A**] Ca_V2^{GFP} channels (red) were labeled with a nanobody with only one binding site against GFP. In addition, neuronal membranes (gray) were labeled by anti-HRP staining. Bouton volume (V_{Bouton}) of *Is* type boutons and the number of Ca_V2^{GFP} puncta/V_{Bouton} were measured at the larval neuromuscular junction (NMJ) of muscle M10. Male larvae with a targeted knockdown of Stj (UAS-Stj^{RNAi}; UAS-dcr2, light gray) or $d\alpha_2\delta_1$ (UAS- $d\alpha_2\delta_1^{RNAi}$; UAS-dcr2, dark gray) in glutamatergic neurons (OK371-Gal4) plus controls (UAS-dcr2, white) were used. [**B**] The number of Ca_V2^{GFP} puncta/V_{Bouton} was decreased in Stj^{RNAi} ($p = 0.156$) but not in $d\alpha_2\delta_1^{RNAi}$ ($p = 0.001$) compared to control (ANOVA, $p = 0.002$). The data is presented as single data points with the mean (bar). The number of replicates is given under the respective data points (number of muscles/numbers of larvae). A one-way ANOVA and LSD posthoc tests were done for statistical analysis ($p < 0.05$*; $p < 0.01$**; $p < 0.001$***).

In previous studies (Klein, 2017) the Ca_V1 channel was also found in axon terminals of larval crawling motoneurons. In contrast to the Ca_V2 channel, which localizes to active zones of the NMJ, the Ca_V1 channel localizes to the peri active zone. We wanted to test whether either Stj or $d\alpha_2\delta_1$ may also be important for correct allocation of presynaptic Ca_V1 channels at the NMJ. An antibody is available against the *Drosophila* Ca_V1 channel, but double labeling of HRP and the Ca_V1 channel was not possible. Additional expression of mcd8GFP in larval crawling motoneurons also interfered with the Ca_V1 antibody staining. Therefore, a Ca_V1 protein trap was built in the curse of this study by using the MiMIC protein trap technique. Although the correct integration of the *mCherry* MiMIC construct was validated via PCR (see appendix 6.7), no signal could be detected. Thus, the Ca_V1 MiMIC protein trap seems to be not functional or the signal is below detection threshold.

In the end, we labeled Brp and Ca_V1 in larvae with Stj (b) and $d\alpha_2\delta_1$ (c) knockdown driven only in glutamatergic neurons (OK371-Gal4) and their respective control (a).

a) $; \frac{+}{\text{OK371-Gal4}} ; \frac{\text{UAS-drc2}}{+}$

b) $; \frac{\text{UAS-Stj}^{RNAi}}{\text{OK371-Gal4}} ; \frac{\text{UAS-dcr2}}{+}$

c) $; \frac{\text{UAS- } d\alpha_2\delta_1{}^{RNAi}}{\text{OK371-Gal4}} ; \frac{\text{UAS-dcr2}}{+}$

Counting Ca_V1 puncta was impossible due to the rather diffuse Ca_V1 signal in axon terminals. With only the Brp co-label measuring the bouton volume was also not possible. Since the Ca_V1 channel was found to be the most prominent channel to mediate calcium currents in larval body wall muscles (Hara *et al*., 2015; Ren *et al*., 1998) we detected high background signals at the postsynaptic side of the NMJ. Reducing the background by an additional postsynaptic knockdown of the Ca_V1 channel was not possible since these animals would die at very early larval stages (L1, data not shown). Unfortunately, the secondary antibody, used for the Ca_V1 antibody staining, additionally induced high dot-like background signals (Fig.33, white arrows). A quantitative analysis of the raw data was therefore not possible. Still, qualitative analysis of the raw data indicates that there might be a reduction of the Ca_V1 signal in *Is* boutons of Stj^{RNAi} compared to $d\alpha_2\delta_1{}^{RNAi}$ and control (Fig.33, white asterisk), which potentially hints at a reduction in Ca_V1 density at axon terminals of Stj^{RNAi} but not $d\alpha_2\delta_1{}^{RNAi}$. This needs to be further investigated and confirmed. Stainings could be redone with a different secondary antibody, but one would still have a high background signal in muscles (see above). To extract the presynaptic Ca_V1 signal from the postsynaptic Ca_V1 signal, one could try to produce a tagged UAS-Ca_V1 construct and express it only in glutamatergic neurons.

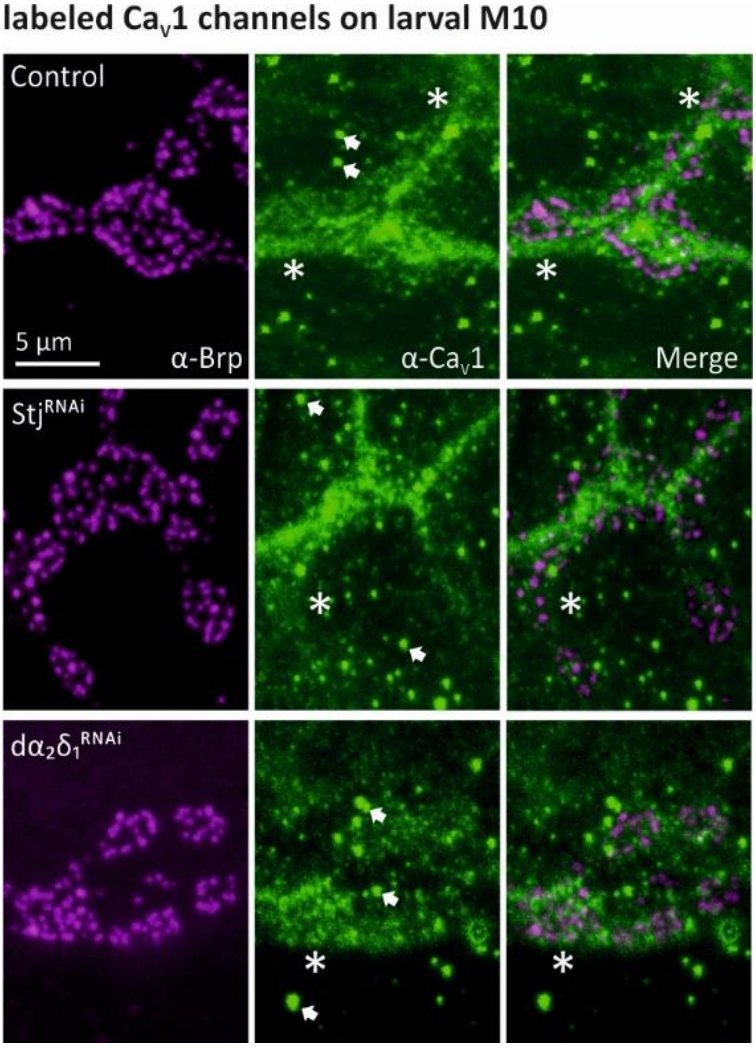

Fig.33: The Ca$_V$1 signal of *Is* type boutons seems reduced in Stj^{RNAi} but not in dα$_2$δ$_1$^{RNAi} at the larval NMJ
Double labeling of Ca$_V$1 channels (green) and the active zone marker Brp (magenta). Projection views of confocal image stacks (10 sections) of the larval neuromuscular junction (NMJ) of muscle M10. Larvae with a targeted knockdown of Stj (UAS-Stj^{RAi}; UAS-dcr2) or dα$_2$δ$_1$ (UAS- dα$_2$δ$_1$^{RNAi}; UAS-dcr2) to glutamatergic neurons (Ok371-Gal4) plus the respective controls (UAS-dcr2) were used. The Ca$_V$1 signal seems reduced in *Is* boutons of Stj^{RNAi} compared to dα$_2$δ$_1$^{RNAi} and control (white asterisk). Due to a high background signal (white arrow) differences in Ca$_V$1 signal between the different genotypes could not be quantified.

Reduction of Ca$_V$1 signal at the boutons of Stj^{RNAi} larvae could be due to reduced transport of the channel. To probe for changes in Ca$_V$1 transport we also measured the Ca$_V$1 signal in axons shortly before reaching the muscle. Again, the mean gray value was measured with Image J software. The data were normally distributed and thus a one-way ANOVA and LSD posthoc tests were done.

Compared to control (54 $\pm$ 33) Ca$_V$1 signal even tended to be increased, but was not significantly changed (ANOVA, p = 0.28) in Stj^{RNAi} (83 $\pm$ 41) and dα$_2$δ$_1$^{RNAi} (68 $\pm$ 31). However, variation in the data was very high. Still, axonal Ca$_V$1 signal was found in both Stj^{RNAi} and dα$_2$δ$_1$^{RNAi} (Fig.34), which indicates that Ca$_V$1 channel transport is not disrupted in either of the two knockdowns. This further indicates that Stj might be required for correct allocation or targeting of Ca$_V$1 to axon terminals of larval crawling motoneurons. Together with the finding that also the Ca$_V$2 channel is reduced in synaptic boutons of Stj^{RNAi} larvae (see

above), this would further suggest that Stj might interact with both Ca_V1 and Ca_V2 and that Stj function might be independent of the HVA α_1 subunit.

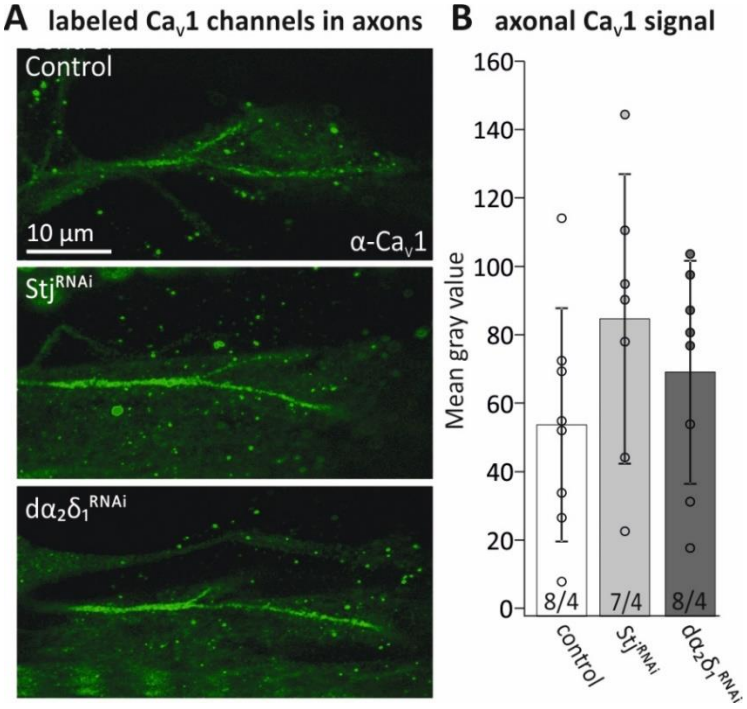

[**Fig.34: Axonal Ca_V1 signal is found in both Stj^{RNAi} and dα$_2$δ$_1$^{RNAi}**
A] Labeling of axonal Ca_V1 channels (green). Projection views of confocal image stacks (10 sections) of axons on muscle M10 of larvae with a targeted knockdown of Stj (UAS-Stj^{RNAi};UAS-dcr2, light gray) or dα$_2$δ$_1$ (UAS- dα$_2$δ$_1$^{RNAi};UAS-dcr2, dark gray) in glutamatergic neurons (OK371-Gal4) plus controls (UAS-dcr2, white) [**B**] The mean gray value of the Ca_V1 signal of *Is* type boutons was measured from single sections with Image J software and normalized to background. The Ca_V1 signal was not significantly changed in both Stj^{RNAi} and dα$_2$δ$_1$^{RNAi} compared to control (ANOVA, p = 0.28). The data is presented as single data points with the mean (bar). The number of replicates is given under the respective data points (number of muscles / numbers of larvae). A one-way ANOVA was done for statistical analysis.

3.3.2 Stj but not dα$_2$δ$_1$ is required for normal somatodendritic Ca_V1 current amplitudes in larval crawling motoneurons

In larval RP2 and aCC crawling motoneurons, the Ca_V1 channel is further known to mediate somatodendritic calcium currents (Worrell & Levine, 2008; Kadas *et al.*, 2017). To test whether Stj or dα$_2$δ$_1$ are important for normal somatodendritic Ca_V1 channel function we measured calcium currents from the soma of these neurons via the patch-clamp technique (see 2.8.2). Larvae with a mosaic expression (RN2-Gal4, UAS-GFP; Act<FRT.stop>-Gal4, UAS-FLP) of Stj^{RNAi} (b) and dα$_2$δ$_1$^{RNAi} (c) in larval crawling motoneurons and the respective control (a) were used. RP2 and aCC neurons expressing the RNAi could be identified by additional expression of mcd8GFP in those neurons.

a) $\quad ; \frac{+}{\text{RN2-Gal4,UAS-mcd8GFP}} ; \frac{\text{UAS-dcr2}}{\text{Act<FRT.stop>Gal4,UAS-FLP}}$

b) $\quad ; \frac{\text{UAS-Stj}^{RNAi}}{\text{RN2-Gal4,UAS-mcd8GFP}} ; \frac{\text{UAS-dcr2}}{\text{Act<FRT.stop>Gal4,UAS-FLP}}$

c) $; \frac{\text{UAS-d}\alpha_2\delta_1{}^{\text{RNAi}}}{\text{RN2-Gal4,UAS-mcd8GFP}} ; \frac{\text{UAS-dcr2}}{\text{Act<FRT.stop>Gal4,UAS-FLP}}$

To probe for possible changes in the voltage dependence of activation of Ca_V1 we analyzed I/V plots. I/V plots were fitted by a modified Boltzmann fit (Boltzmann, shifted). Additionally, the maximal calcium current amplitude was measured in Clampfit 10.7.

The voltage dependence of activation of Ca_V1 seemed unchanged in both Stj^{RNAi} and $d\alpha_2\delta_1{}^{RNAi}$ compared to control. Fitting the I/V plot for Ca_V1 was possible in $d\alpha_2\delta_1$ knockdown and control. By contrast, fitting Stj^{RNAi} with the same fit was not possible (Fig.35 C). This could hint at changes in the channel kinetics of Ca_V1 in Stj^{RNAi} larvae. However, since we recorded from the soma of very complex of neurons, especially changes in the inactivation kinetics of Ca_V1 channels are difficult to evaluate due to space clamping errors. Possible modulation of the channel kinetics of Ca_V1 by Stj should be further investigated but was not part of this work.

Still, the maximal calcium current amplitude was decreased by approx. 50 % in Stj^{RNAi} (-127 $\pm$ 61 pA; LSD, p = 0.000) compared to control (-235 $\pm$ 47 pA). By contrast, the maximal current amplitudes (-263 $\pm$ 104; LSD, p = 0.367) of somatodendritic Ca_V1 channels were unchanged in $d\alpha_2\delta_1{}^{RNAi}$ (Fig.35 A,B). Since the data was normally distributed a one-way ANOVA (p = 0.000) with LSD posthoc test was performed. Reduction of the maximal current amplitude in Stj^{RNAi} could either hint at changes in the channel conductance or at a reduced amount of somatodendritic calcium channels in membranes. This finding further indicates that Stj but not $d\alpha_2\delta_1$ is required for normal somatodendritic Ca_V1 currents in larval crawling motoneurons.

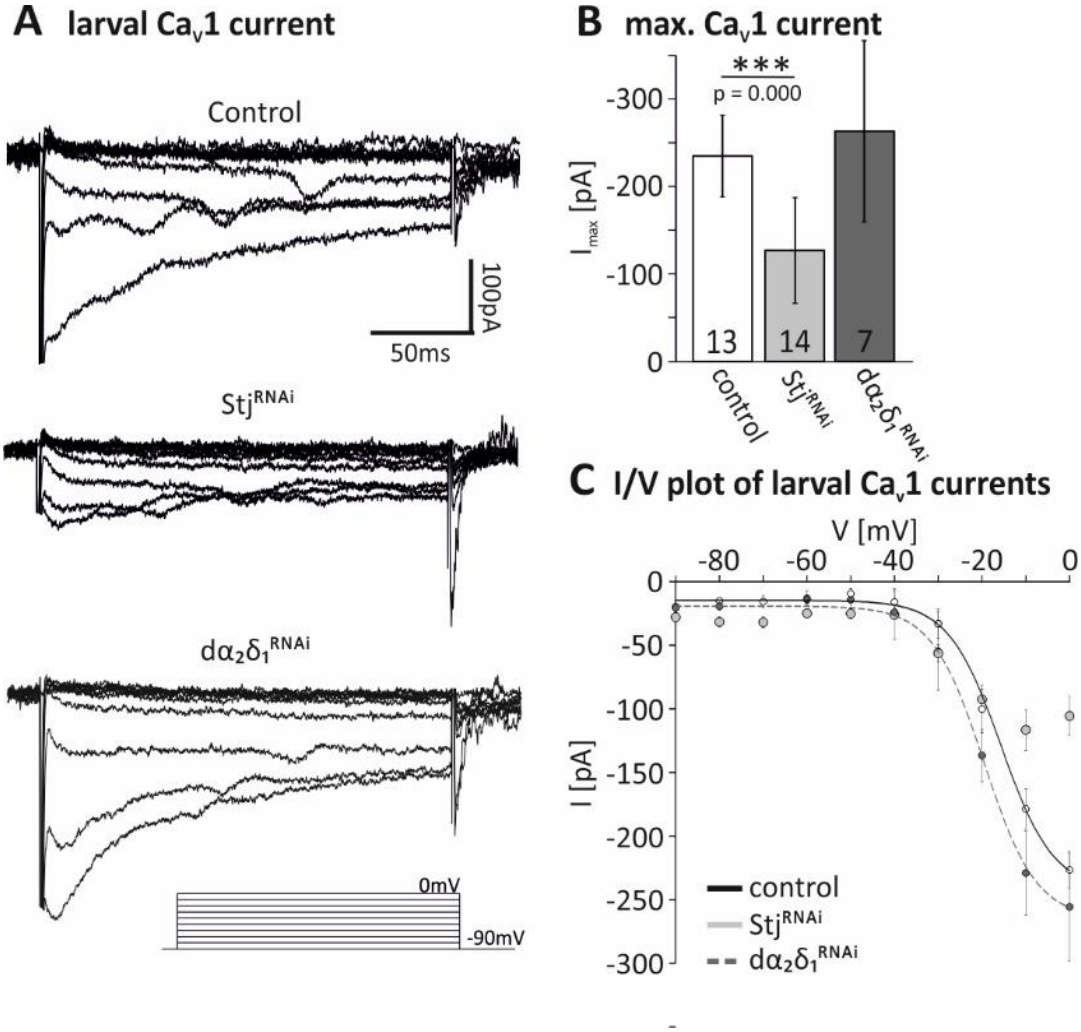

Fig.35: Stj but not $d\alpha_2\delta_1$ is required for normal somatodendritic Ca_V1 currents in larval crawling motoneurons (MN)
[**A**] Voltage clamp measurements of somatodendritic Ca_V1 currents recorded from the soma of larval crawling aCC and RP2 MNs. Voltage steps from -90 mV to 0 mV were done. Larvae with a mosaic knockdown (RN2-Gal4, UAS-GFP; Act<FRT.stop>-Gal4, UAS-FLP) of Stj (UAS-Stj^{RNAi}; UAS-dcr2, light gray) or $d\alpha_2\delta_1$ (UAS-$d\alpha_2\delta_1^{RNAi}$; UAS-dcr2, dark gray) plus control (UAS-dcr2, white) were used. Neurons expressing the RNAi or only dcr2, were identified by additional mcd8GFP expression. [**B**] The maximal Ca_V1 current amplitude was significantly reduced in Stj^{RNAi} ($p = 0.000$) but not in $d\alpha_2\delta_1^{RNAi}$ ($p = 0.367$) compared to control (ANOVA, $p = 0.000$). [**C**] I/V plots of $d\alpha_2\delta_1^{RNAi}$ seemed unchanged compared to control (fitted by modified Boltzmann, shifted). Voltage dependence of activation seemed unchanged in both Stj^{RNAi} and $d\alpha_2\delta_1^{RNAi}$ compared to control. Mean values are presented as bars with whiskers for the standard deviation or as single data points representing the mean plus whiskers as the standard error. The number of replicates is given inside the respective bar. A one-way ANOVA and LSD posthoc tests were done for statistical analysis ($p < 0.05$*; $p < 0.01$**; $p < 0.001$***). (Figure modified from Heinrich & Ryglewski in submission)

3.4 Stj and $d\alpha_2\delta_1$ are required for different functions in adult flight motoneurons

Both Stj and $d\alpha_2\delta_1$ are also expressed in adult flight motoneuron MN5 (see above). While targeted knockdown of Stj to the flight motoneurons results in flight inability, flies with a targeted knockdown of $d\alpha_2\delta_1$ even fly longer compared to control (see appendix 6.10). This indicates functional differences between Stj and $d\alpha_2\delta_1$ in those neurons. Interesting-

ly, in contrast to the larval crawling motoneurons RP2 and aCC, the Ca_V2 channel is the main somatodendritic calcium channel in MN5 (Ryglewski *et al*., 2012).

3.4.1 Stj but not $d\alpha_2\delta_1$ is needed for normal somatodendritic calcium current amplitudes in adult flight motoneurons

To test for functional differences of different Ca_V2-$d\alpha_2\delta$ combinations, we measured somatodendritic calcium currents from the soma of adult MN5 neurons in flies with targeted knockdowns of either Stj (b) or dα2δ1 (c) and the respective control (a) via the patch-clamp technique as described above (see 2.8.2).

a) $\; ; \frac{+}{\text{23H06-Gal4}} ; \frac{\text{UAS-dcr2}}{+}$

b) $; \frac{\text{UAS-Stj}^{RNAi}}{\text{23H06-Gal4}} ; \frac{\text{UAS-dcr2}}{+}$

c) $; \frac{\text{UAS-d}\alpha_2\delta_1{}^{RNAi}}{\text{23H06-Gal4}} ; \frac{\text{UAS-drc2}}{+}$

We again analyzed I/V plots and the current amplitude of Ca_V2 with Clampfit 10.7 software. The data were normally distributed. Neither in Stj^{RNAi} nor $d\alpha_2\delta_1{}^{RNAi}$ the voltage dependence of activation or the I/V plot of Ca_V2 seemed changed compared to control (Fig.36 A,C). Furthermore, Ca_V2 channels are still able to mediate HVA as well as LVA currents in both Stj^{RNAi} and $d\alpha_2\delta_1{}^{RNAi}$ (Fig.36 & Fig.37). This indicates that the ability of Ca_V2 channels to mediate HVA as well as LVA currents does not depend on interaction with either Stj or $d\alpha_2\delta_1$. Another $d\alpha_2\delta$ subunit ($d\alpha_2\delta_2$ or $d\alpha_2\delta_4$), or a completely different mechanism could be involved. One possible suggestion would be that the biophysical properties of Ca_V2 are altered through alternative splicing as already proposed in previous studies (Ryglewski et al., 2012).

Calcium current amplitudes of sustained somatodendritic HVA Ca_V2 channel currents were decreased (ANOVA, $p = 0.018$) in Stj^{RNAi} (-699 $\pm$ 148 pA; LSD, $p = 0.025$) but not in $d\alpha_2\delta_1{}^{RNAi}$ (-1213 $\pm$ 348 pA; LSD, $p = 0.456$) compared to control (-1089 $\pm$ 210 pA) (Fig.36 A,B). Reduction of the sustained HVA current amplitude in Stj^{RNAi} could again either hint at changes in the channel conductance or at a reduced amount of somatodendritic calci-

um channels. This finding further indicates that also in adult wing depressor neurons Stj but not $d\alpha_2\delta_1$ is required for normal somatodendritic Ca_V2 current amplitudes. Thus, Stj function in *Drosophila* motoneurons seems independent of the Ca_V channel and the developmental stage.

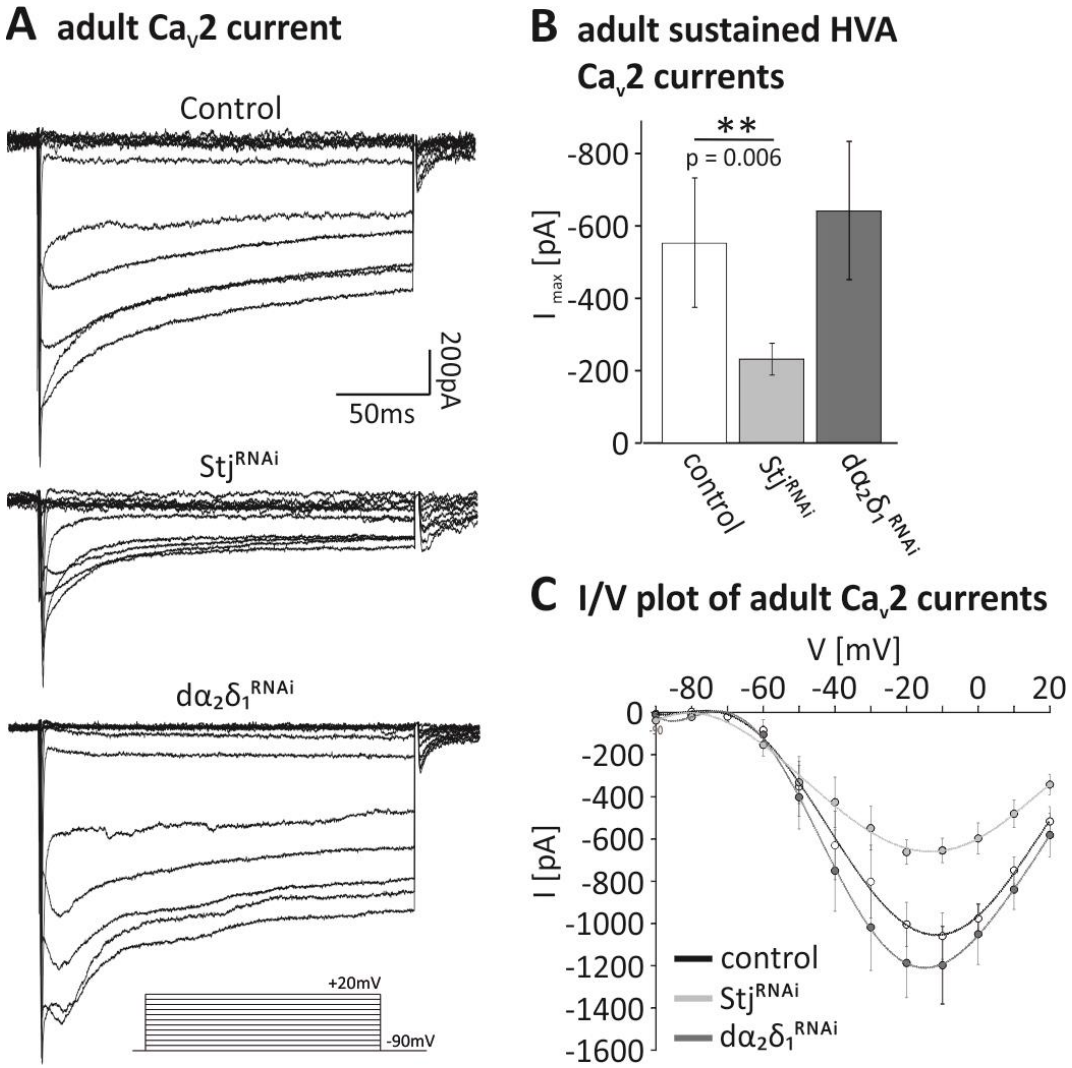

Fig.36: Stj but not $d\alpha_2\delta_1$ is required for normal somatodendritic HVA Ca_V2 currents in adult DLM motoneurons
[**A**] Voltage clamp measurements of somatodendritic Ca_V2 currents recorded from the soma of adult wing depressor neurons MN5. Voltage steps from -90 to +20 mV were done. Larvae with a targeted knockdown (23H06-Gal4) of Stj (UAS-Stj^{RNAi}; UAS-dcr2, light gray) or $d\alpha_2\delta_1$ (UAS- $d\alpha_2\delta_1^{RNAi}$; UAS-dcr2, dark gray) in MN1-5 and controls (UAS-dcr2, white) were used. [**B**] The maximal HVA Ca_V2 current amplitude was significantly reduced in Stj^{RNAi} ($p = 0.025$) but not in $d\alpha_2\delta_1^{RNAi}$ ($p = 0.456$) compared to control (ANOVA, $p = 0.018$). [**C**] Voltage dependence of activation seemed unchanged in both Stj^{RNAi} and $d\alpha_2\delta_1^{RNAi}$ compared to. Mean values are presented as bars with whiskers for the standard deviation or as single data points representing the mean plus whiskers as the standard error. The number of replicates is given inside the respective bar. A one-way ANOVA and LSD posthoc tests were done for statistical analysis ($p < 0.05$*; $p < 0.01$**; $p < 0.001$***). (Figure modified from Heinrich & Ryglewski in submission)

In addition, somatodendritic LVA Ca_V2 channel currents were decreased (ANOVA, $p = 0.004$) in Stj^{RNAi} (-230 $\pm$ 44 pA; LSD, $p = 0.006$) but not in $d\alpha_2\delta_1^{RNAi}$ (-642 + 192 pA; LSD,

p = 0.398) compared to control (-554 ± 180 pA) (Fig.37 A,B). If indeed different splice variants of Ca_V2 mediate HVA and LVA currents, this would indicate that Stj is also required for normal current amplitudes of different Ca_V2 splice variants.

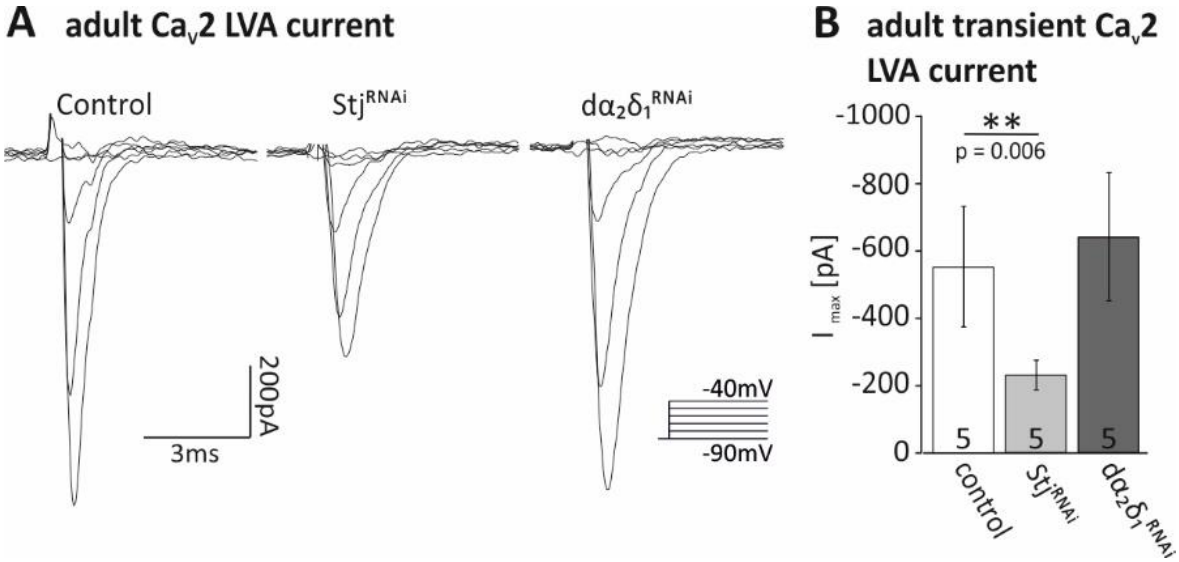

Fig.37: Stj but not dα$_2$δ$_1$ is required for normal somatodendritic LVA Ca$_V$2 currents in adult DLM motoneurons
[**A**] Voltage clamp measurements of somatodendritic Ca_V2 currents recorded from the soma of adult wing depressor neurons MN5. Voltage steps from -90 to -40 mV were done. Larvae with a targeted knockdown (23H06-Gal4) of Stj (UAS-Stj^{RNAi}; UAS-dcr2, light gray) or dα$_2$δ$_1$ (UAS- dα$_2$δ$_1^{RNAi}$; UAS-dcr2, dark gray) in MN1-5 and controls (UAS-dcr2, white) were used. [**B**] The maximal LVA Ca_V2 current amplitude was significantly reduced in Stj^{RNAi} (p = 0.006) but not in dα$_2$δ$_1^{RNAi}$ (p = 0.398) compared to control (ANOVA, p = 0.004). Mean values are presented as bars with whiskers for the standard deviation. The number of replicates is given inside the respective bar. A one-way ANOVA and LSD posthoc tests were done for statistical analysis (p < 0.05*; p < 0.01**; p < 0.001***). (Figure modified from Heinrich & Ryglewski in submission)

This was confirmed for pupal (P8) MN5 neurons. Again, maximal Ca_V2 current amplitude was significantly reduced (ANOVA, p = 0.000) by approx. 50 % in Stj^{RNAi} (-427 ± 188 pA, LSD, p = 0.000) but not in dα$_2$δ$_1^{RNAi}$ (-964 ± 284 pA; LSD, p = 0.531) compared to control (-895 ± 256 pA) (Fig.19). Interestingly a double knockdown (d) of dα$_2$δ$_1^{RNAi}$ and Stj^{RNAi}(BL) did not further reduce the maximal Ca_V2 current amplitude (-517 ± 152 pA; LSD, p = 0.426) compared to animals only expressing Stj^{RNAi} (Fig.38 A,B). This further suggests that dα$_2$δ$_1$ and Stj are unable to functionally compensate for each other in *Drosophila* NS.
The I/V plots for pupal Ca_V2 currents were fitted by a modified Boltzmann fit (Boltzmann, shifted) for controls. Fitting the I/V plot for Ca_V2 in Stj^{RNAi}, dα$_2$δ$_1^{RNAi}$ and double knockdowns with the same fit was not possible (Fig.38 C). This could again hint at changes in the kinetics of Ca_V2 in those knockdowns. As mentioned, we recorded from the soma of

very complex neurons, therefore changes in the inactivation kinetics of Ca_V2 channels are difficult to evaluate due to space clamping errors. Possible modulation of the channel kinetics of Ca_V1 by Stj should be further investigated but was not part of this work.

d) ; UAS-dα$_2$δ$_1$^{RNAi} / 23H06-Gal4 ; UAS-Stj^{RNAi}(BL) / UAS-dcr2

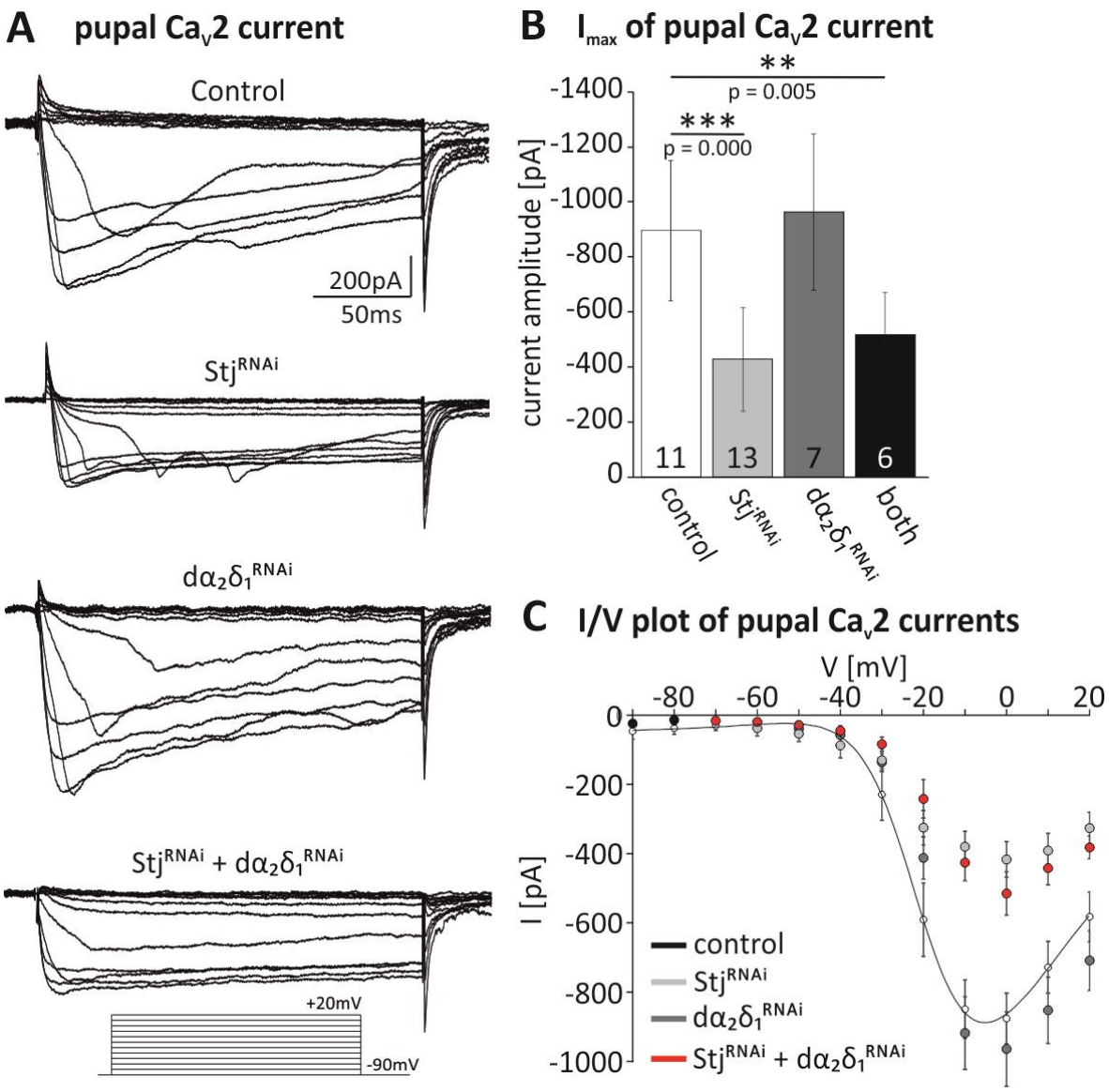

Fig.38: Stj but not $d\alpha_2\delta_1$ is required for normal somatodendritic Ca_V2 currents in pupal DLM motoneurons
[**A**] Voltage clamp measurements of somatodendritic Ca_V2 currents recorded from the soma of pupal (P8) wing depressor neurons MN5. Voltage steps from -90 to +20 mV were done. Pupae with a targeted knockdown (23H06-Gal4) of Stj (UAS-Stj^{RNAi}; UAS-dcr2, light gray) or $d\alpha_2\delta_1$ (UAS- $d\alpha_2\delta_1^{RNAi}$; UAS-dcr2, dark gray) in MN1-5 plus control (UAS-dcr2, white) were used. Additionally, pupae with a double knockdown of Stj + $d\alpha_2\delta_1$ (UAS-dcr2;23H06-Gal4 x UAS- $d\alpha_2\delta_1^{RNAi}$; UAS-Stj^{RNAi}(BL), black) were tested. [**B**] The maximal Ca_V2 current amplitude was significantly reduced in Stj^{RNAi} ($p = 0.000$) but not in $d\alpha_2\delta_1^{RNAi}$ ($p = 0.531$) compared to control (ANOVA, $p = 0.000$). Double knockdown of Stj^{RNAi} + $d\alpha_2\delta_1^{RNAi}$ did not further reduce the max. Ca_V2 current amplitude compared to Stj^{RNAi} ($p = 0.426$). [**C**] Voltage dependence of activation seemed unchanged in both Stj^{RNAi} and $d\alpha_2\delta_1^{RNAi}$ compared to. Mean values are presented as bars with whiskers for the standard deviation or as single data points representing the mean plus whiskers as the standard error. The number of replicates is given inside the respective bar. A one-way ANOVA and LSD posthoc tests were done for statistical analysis ($p < 0.05$*; $p < 0.01$**; $p < 0.001$***). (Figure modified from Heinrich & Ryglewski in submission)

3.4.2 Both Stj and $d\alpha_2\delta_1$ are needed for normal dendritic calcium channel function in adult flight motoneurons

Even though the somatodendritic current amplitudes were unchanged in $d\alpha_2\delta_1^{RNAi}$, the localization of the channels could still be altered. Patch-clamp measurements were done from the soma of MN5, which only enables us to record the entirety of somatic and dendritic calcium currents. Thus, if $d\alpha_2\delta_1$ would shift Ca_V2 channel localization we would not be able to detect them. To test for correct localization of Ca_V2 channels to the dendrites of MN5 in Stj^{RNAi} (b) and $d\alpha_2\delta^{RNAi}$ (c), we co-expressed the calcium indicator GCamp6s (UAS-GCamp6s; 23H06-Gal4) in addition to the RNAi knockdowns and in the respective control (a):

a) $; \frac{+}{\text{UAS-GCamp6s}} ; \frac{\text{UAS-dcr2}}{\text{23H06-Gal4}}$

b) $; \frac{\text{UAS-Stj}^{RNAi}}{\text{UAS-GCamp6s}} ; \frac{\text{UAS-dcr2}}{\text{23H06-Gal4}}$

c) $; \frac{\text{UAS-d}\alpha_2\delta_1^{RNAi}}{\text{UAS-GCamp6s}} ; \frac{\text{UAS-dcr2}}{\text{23H06-Gal4}}$

We then imaged MN5 while activating it via current injections (Fig.20 B). The changes in GCamp6s fluorescence were analyzed (Fig.39 A) with HOKAWO 3.10 software and ΔF/F was calculated by [F(firing)F(rest)]/F(rest). The data were non-normally distributed and thus a Kruskal-Wallis ANOVA and Dunn-Bonferroni posthoc tests were done. Interestingly, the increase in dendritic GCamp6s fluorescence upon activation of MN5 via current injections was significantly lower (ANOVA, $p = 0.000$) in Stj^{RNAi} (0.19 ± 0.12; Dunn, $p = 0.003$),

but also in $d\alpha_2\delta_1^{RNAi}$ (0.19 ± 0.14; Dunn, p = 0.000) compared to control (0.42 ± 0.31) (Fig.39 C,Ci). A reduced increase in GCamp6s fluorescence in $d\alpha_2\delta_1^{RNAi}$ in dendrites indicates a selective reduction in dendritic Ca_V2 density since somatodendritic Ca_V2 currents were unchanged. In Stj^{RNAi} a reduced increase in GCamp6s fluorescence in MN5 dendrites further confirms, that Stj is required for either normal functional Ca_V2 densities or normal Ca_V2 channel conductance.

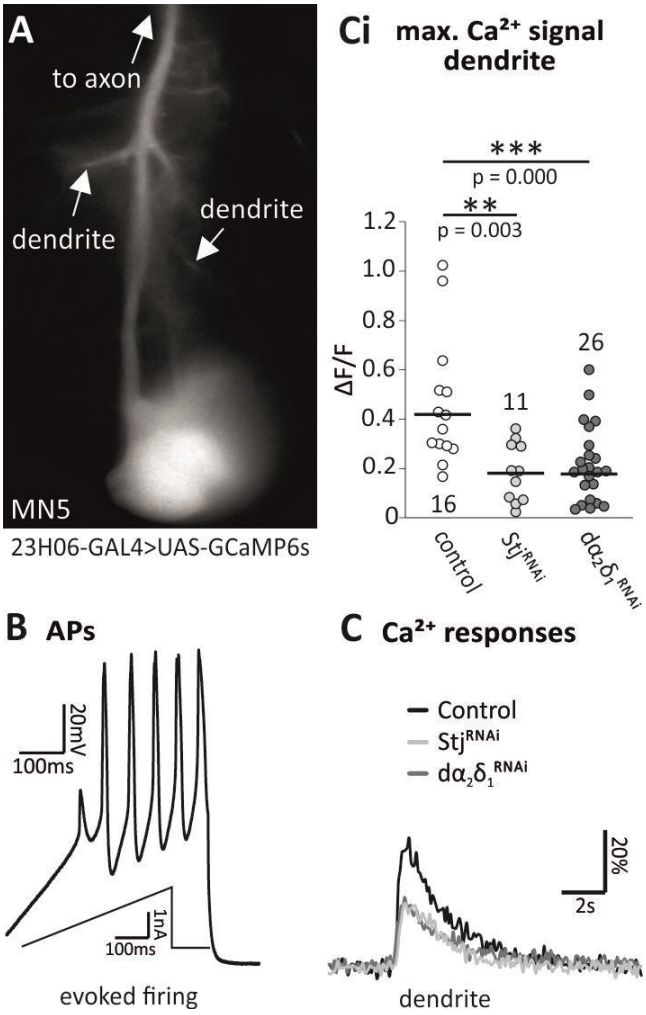

Fig.39: Both Stj and $d\alpha_2\delta_1$ are required for normal function of dendritic Ca_V channels in pupal MN5 motoneurons

[**A**] Calcium imaging was done from the dendrites of wing depressor neurons MN5 expressing the calcium sensor GCamp6s (UAS-GCamp6s;23H06-Gal4). Changes in calcium fluorescence were measured upon activation of MN5 via [**B**] current injections. [**C**] Ca^{2+} responses were recorded from flies additionally expressing Stj^{RNAi} (UAS-Stj^{RNAi};UAS-dcr2, light gray points) or $d\alpha_2\delta_1^{RNAi}$ (UAS- $d\alpha_2\delta_1^{RNAi}$;UAS-dcr2, dark gray points) and controls (UAS-dcr2, white points). [**Ci**] The increase in dendritic GCamp6s fluorescence upon activation of MN5 was significantly reduced (ANOVA, p = 0.000) in both Stj^{RNAi} (p = 0.003) and $d\alpha_2\delta_1^{RNAi}$ (p = 0.000) compared to control. The data is presented as single data points with the median (bar). The number of replicates is given under the respective data points. A Kruskal-Wallis ANOVA and Dunn-Bonferroni post-hoc tests were done for statistical analysis ($p < 0.05$*; $p < 0.01$**; $p < 0.001$***). (Figure modified from Heinrich & Ryglewski in submission)

To further confirm a reduction in dendritic Ca_V2 channels in $d\alpha_2\delta_1^{RNAi}$, we intracellularly dye-filled MN5 neurons and reconstructed the dendritic tree (see 2.12.2). A targeted RNAi knockdown (UAS-GFP; D42-Gal4, Cha-Gal80) of Ca_V2 is already known to lead to developmental defects and thereby to a reduction in the total dendritic length (TDL) of MN5 (Ryglewski *et al*., 2012). If loss of $d\alpha_2\delta_1$ indeed results in a decreased amount of dendritic Ca_V2 channels in DLM MNs, the TDL should also be reduced in $d\alpha_2\delta_1^{RNAi}$. The same would

be true for neurons expressing Stj^{RNAi}. Reconstruction and analysis of the dendritic trees of Stj^{RNAi} (b), $d\alpha_2\delta_1{}^{RNAi}$ (c) and the respective control (a) were done with the Amira software (see 2.12.3).

a) $; \frac{+}{\text{UAS-mcd8GFP}} ; \frac{\text{UAS-dcr2}}{\text{D42-Gal4, Cha-Gal80}}$

b) $; \frac{\text{UAS-Stj}^{RNAi}}{\text{UAS-mcd8GFP}} ; \frac{\text{UAS-dcr2}}{\text{D42-Gal4, Cha-Gal80}}$

c) $; \frac{\text{UAS-d}\alpha_2\delta_1{}^{RNAi}}{\text{UAS-mcd8GFP}} ; \frac{\text{UAS-dcr2}}{\text{D42-Gal4, Cha-Gal80}}$

The data was normally distributed. As expected the TDL of MN5 was significantly reduced (ANOVA, $p = 0.009$) in both $d\alpha_2\delta_1{}^{RNAi}$ (5043 $\pm$ 824 µm; LSD, $p = 0.007$) and Stj^{RNAi} (4796 $\pm$ 329 µm; LSD, $p = 0.004$) compared to control (6580 $\pm$ 408 µm) (Fig.40 A,B). Furthermore, the number of dendritic branches was significantly decreased (ANOVA, $p = 0.019$) in both $d\alpha_2\delta_1{}^{RNAi}$ (3112 $\pm$ 700; LSD, $p = 0.013$) and Stj^{RNAi} (2914 $\pm$ 586; LSD, $p = 0.009$) compared to control (4421 $\pm$ 382) (Fig.40 A,C). By contrast, the mean dendritic length (MDL; Fig. 40 A,D) as well as the mean dendritic radius (MDR; Fig.40 A,E) were not significantly increased (ANOVA: MDL, $p = 0.27$; MDR, $p = 0.79$) in both $d\alpha_2\delta_1{}^{RNAi}$ (MDL, 1.7 $\pm$ 0.1 µm; MDR, 0.25 $\pm$ 0.01) and Stj^{RNAi} (MDL, 1.7 $\pm$ 0.2 µm; MDR, 0.24 + 0.01) compared to control (MDL, 1.5 $\pm$ 0.1; MDR, 0.22 $\pm$ 0.003), which indicates that both Stj^{RNAi} and $d\alpha_2\delta_1{}^{RNAi}$ do not affect dendritic branch elongation. Instead both knockdowns seem to reduce new formation or maintenance of dendritic branches.

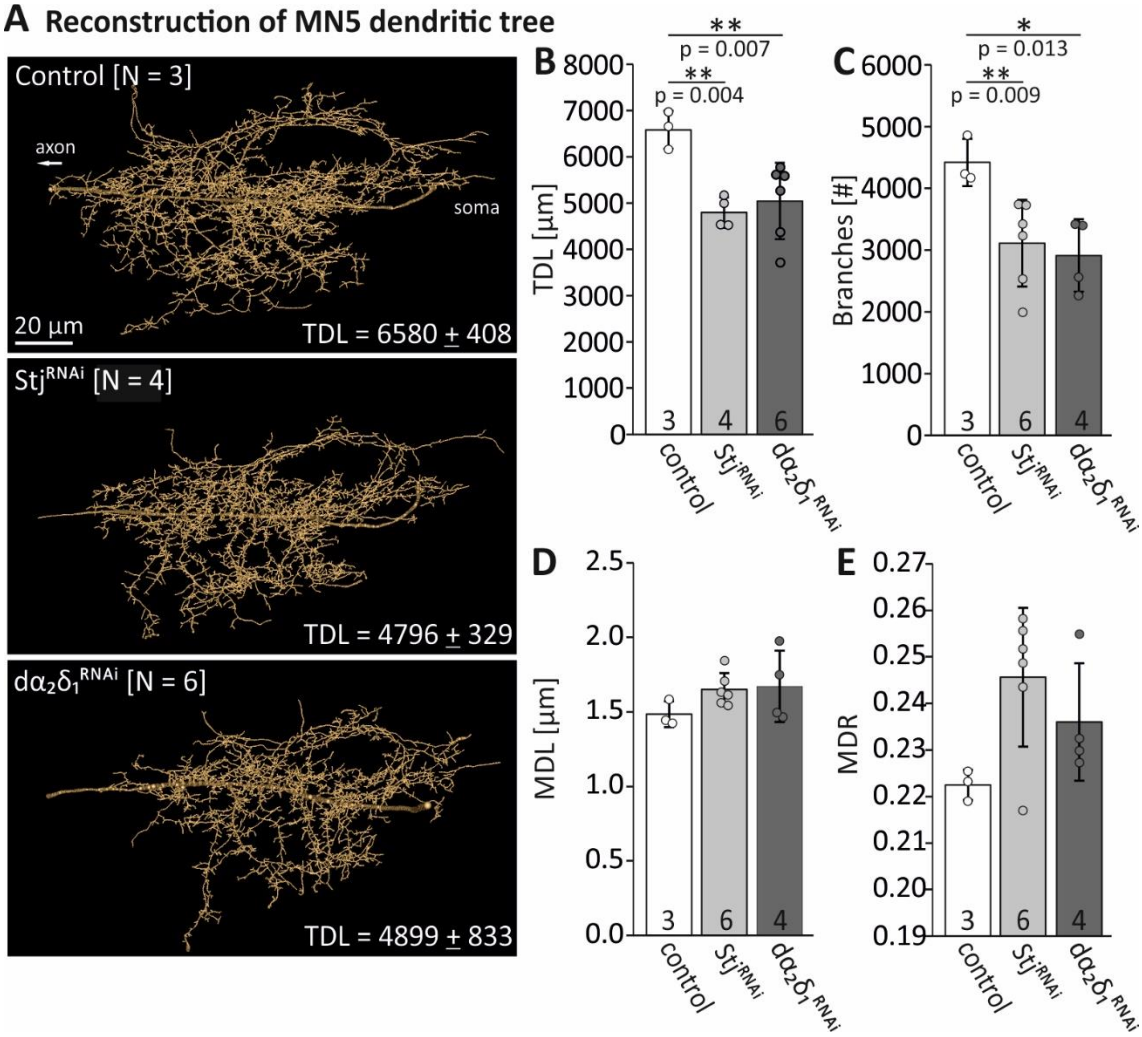

Fig.40: Both Stj and $d\alpha_2\delta_1$ are required for normal development of MN5 dendritic tree
[**A**] Reconstructions of MN5 dendritic tree from confocal image stacks of intracellularly dye-filled cells. Adult flies with a targeted knockdown (UAS-GFP; D42-Gal4, Cha-Gal80) of Stj (UAS-Stj^{RNAi}; UAS-dcr2, light gray) or $d\alpha_2\delta_1$ (UAS- $d\alpha_2\delta_1^{RNAi}$; UAS-dcr2, dark gray) in MN1-5 plus control were used. [**B**] The total dendritic length (TDL) was significantly (ANOVA, p = 0.009) reduced in both Stj^{RNAi} (p = 0.004) and $d\alpha_2\delta_1^{RNAi}$ (p = 0.007) compared to control. [**C**] The number of branches was significantly (ANOVA, p = 0.019) decreased in both Stj^{RNAi} (p = 0.009) and $d\alpha_2\delta_1^{RNAi}$ (p = 0.013) compared to control. [**D**] The mean dendritic length (MDL) and [**E**] mean dendritic radius (MDR) were unchanged in both Stj^{RNAi} and $d\alpha_2\delta_1^{RNAi}$ (ANOVA: MDL, p = 0.27; MDR, p = 0.79). Mean values are presented as bars with whiskers for the standard deviation. The number of replicates is given inside the respective bar and as single data points. A one-way ANOVA and LSD posthoc tests were done for statistical analysis ($p < 0.05$*; $p < 0.01$**; $p < 0.001$***). (Figure modified from Heinrich & Ryglewski in submission)

3.4.3 Both Stj and $d\alpha_2\delta_1$ are needed for normal axonal calcium channel function in adult flight motoneurons but have opposite effects

HVA calcium channels are also reported to have axonal functions (see introduction). For example, in *Drosophila* pupae sodium carried action potentials (AP) of MN5 neurons are additionally shaped by Ca_V2 calcium currents and consequently display a calcium component. Therefore, we wanted to assess changes in axonal Ca_V2 localization following targeted knockdown (23H06-Gal4) of either Stj (b) or $d\alpha_2\delta_1$ (c) in those MNs. Again, adult

flies with Ca_V2^{GFP} were used and confocal images of the live GFP signal (see 2.10) of MN1-5 axons were taken in RNAi knockdowns and the respective control (a).

a) $\frac{Ca_V2^{GFP}}{y}$; $\frac{+}{+}$; $\frac{UAS\text{-}dcr2}{23H06\text{-}Gal4}$

b) $\frac{Ca_V2^{GFP}}{y}$; $\frac{UAS\text{-}Stj^{RNAi}}{+}$; $\frac{UAS\text{-}dcr2}{23H06\text{-}Gal4}$

c) $\frac{Ca_V2^{GFP}}{y}$; $\frac{UAS\text{-}d\alpha_2\delta_1{}^{RNAi}}{+}$; $\frac{UAS\text{-}dcr2}{23H06\text{-}Gal4}$

Axons of the flight depressor neurons exit the VNC at the nerve root as an axon bundle. This enabled us to measure the mean gray value of the Ca_V2^{GFP} signal from the axon bundles from both sides. Mean gray values were measured from confocal image stacks with the Image J software. Per fly, the mean value of both axon bundles was calculated in Excel. The data were normally distributed. A one-way ANOVA and pairwise comparisons with LSD posthoc tests were performed.

Axonal Ca_V2^{GFP} was significantly reduced (ANOVA, $p = 0.000$) in Stj^{RNAi} (46 ± 13; LSD, $p = 0.006$) compared to control (66 ± 6). By contrast the axonal Ca_V2^{GFP} signal was significantly increased in $d\alpha_2\delta_1{}^{RNAi}$ flies (87 ± 17; LSD, $p = 0.001$) (Fig.41 A,B). Thus, knockdowns of $d\alpha_2\delta_1$ and Stj seem to have opposite effects on the axonal Ca_V2 channels density.

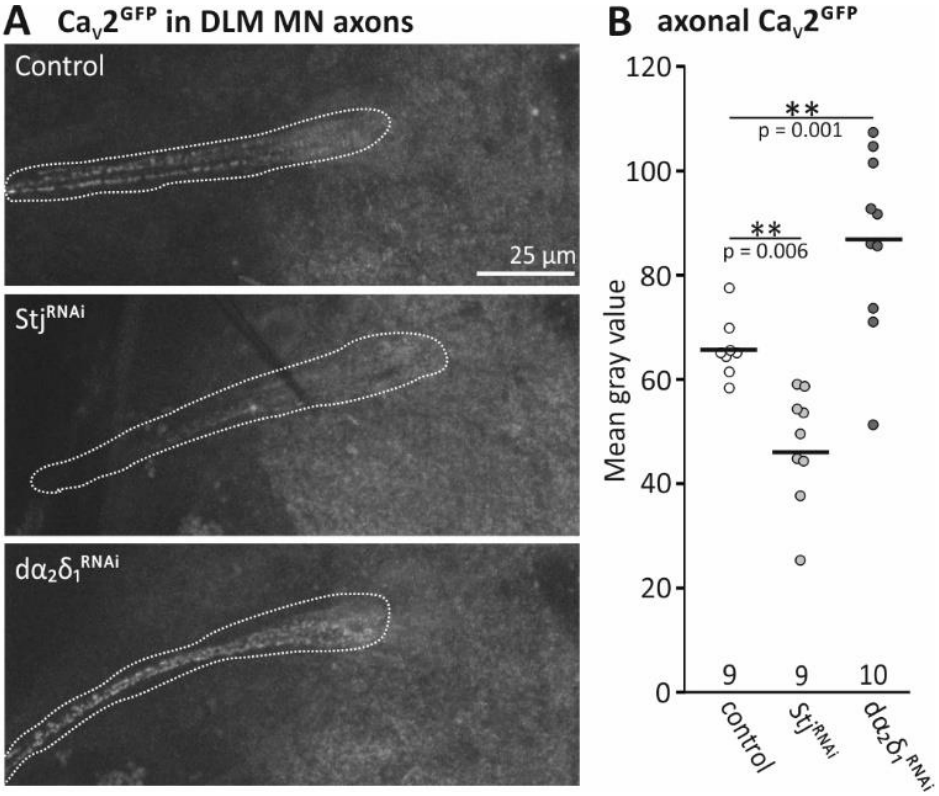

Fig.41: Stj^{RNAi} and dα$_2$δ$_1$^{RNAi} have opposite effects on axonal Ca$_V$2^{GFP} expression of adult flight motoneurons
[**A**] Confocal image stacks of live Ca$_V$2^{GFP} signal (gray) were taken from the axon bundles of wing depressor neurons MN1-5. Male flies with a targeted knockdown of Stj (UAS-Stj^{RNAi}; UAS-dcr2, light gray points) or dα$_2$δ$_1$ (UAS- dα$_2$δ$_1$^{RNAi}; UAS-dcr2, dark gray points) in MN1-5 (Ca$_V$2^{GFP};;23H06-Gal4) and the respective controls (UAS-dcr2, white points) were used. [**B**] The axonal Ca$_V$2^{GFP} signal was significantly (ANOVA, p = 0.000) decreased in Stj^{RNAi} (p = 0.006), but increased in dα$_2$δ$_1$^{RNAi} (p = 0.001) compared to control. The data is presented as single data points with the mean (bar). The number of replicates is given under the respective data points. A one-way ANOVA and LSD posthoc tests were done for statistical analysis (p < 0.05*; p < 0.01**; p < 0.001***). (Figure modified from Heinrich & Ryglewski in submission)

Changes in the axonal Ca$_V$2^{GFP} signal can hint either at changes in Ca$_V$2 channel transport or at an increased amount of functional Ca$_V$2 channels in axonal membranes. To test this, we did current clamp measurements in flies with a targeted knockdown (UAS-GFP; D42-Gal4, Cha-Gal80) of either Stj^{RNAi} (b) or dα$_2$δ$_1$^{RNAi} (c) and the respective control (a).

a) $; \frac{+}{\text{UAS-mcd8GFP}} ; \frac{\text{UAS-dcr2}}{\text{D42-Gal4, Cha-Gal80}}$

b) $; \frac{\text{UAS-Stj}^{RNAi}}{\text{UAS-mcd8GFP}} ; \frac{\text{UAS-dcr2}}{\text{D42-Gal4, Cha-Gal80}}$

c) $; \frac{\text{UAS-d}\alpha_2\delta_1{}^{RNAi}}{\text{UAS-mcd8GFP}} ; \frac{\text{UAS-dcr2}}{\text{D42-Gal4, Cha-Gal80}}$

During pupal development action potentials of the DLM neurons display a calcium component. This calcium component is most pronounced in pupal stage P8, which was therefore used to probe for changes in action potential shape in Stj^{RNAi} and $d\alpha_2\delta_1^{RNAi}$. The action potential (AP) half amplitude width was measured at membrane voltages of approx. -10 mV. The data were analyzed with Clampfit 10.7 software. Since the data were non-normally distributed a Kruskal-Wallis ANOVA and Dunn-Bonferroni posthoc tests were performed for statistical analysis.

In Stj^{RNAi} AP half amplitude width (3 $\pm$ 1 ms; Dunn, p = 0.03) was significantly decreased (ANOVA, p = 0.001) compared to control (6 $\pm$ 2 ms) (Fig.42 A,B). By contrast, the AP width seemed to be increased in $d\alpha_2\delta_1^{RNAi}$ (9 $\pm$ 9 ms) (Fig.42 B). Interestingly, approx. 50 % of the measurements in $d\alpha_2\delta_1^{RNAi}$ displayed APs with double or even triple peaks (Fig.42 A). This leads to very high variations in the data and explains why statistically no significant differences (Dunn, p = 1.000) were found compared to control.

To further confirm that changes in AP half amplitude width are due to changes in axonal Ca_V2 abundance we washed in Cadmium (500 µm) for 2 min. As VGCC blocker, Cadmium (Cd^{2+}) should erase the calcium component and thereby reduce AP width. The AP width was measured before and after washing in Cadmium and the percental decrease in AP width was calculated. Cd^{2+} abolished the calcium component of control APs and double-peak events of $d\alpha_2\delta_1^{RNAi}$ APs but seemed to have no effect on Stj^{RNAi} APs (Fig.42 A). Indeed, blocking VGCCs with Cd^{2+} decreased the AP width significantly more (ANOVA, p = 0.006) in both control (53 $\pm$ 15 %; Dunn, p = 0.014) and $d\alpha_2\delta_1^{RNAi}$ (35 $\pm$ 31 %; Dunn, p = 0.014) compared to Stj^{RNAi} (-20 $\pm$ 22 %) (Fig.42 C).

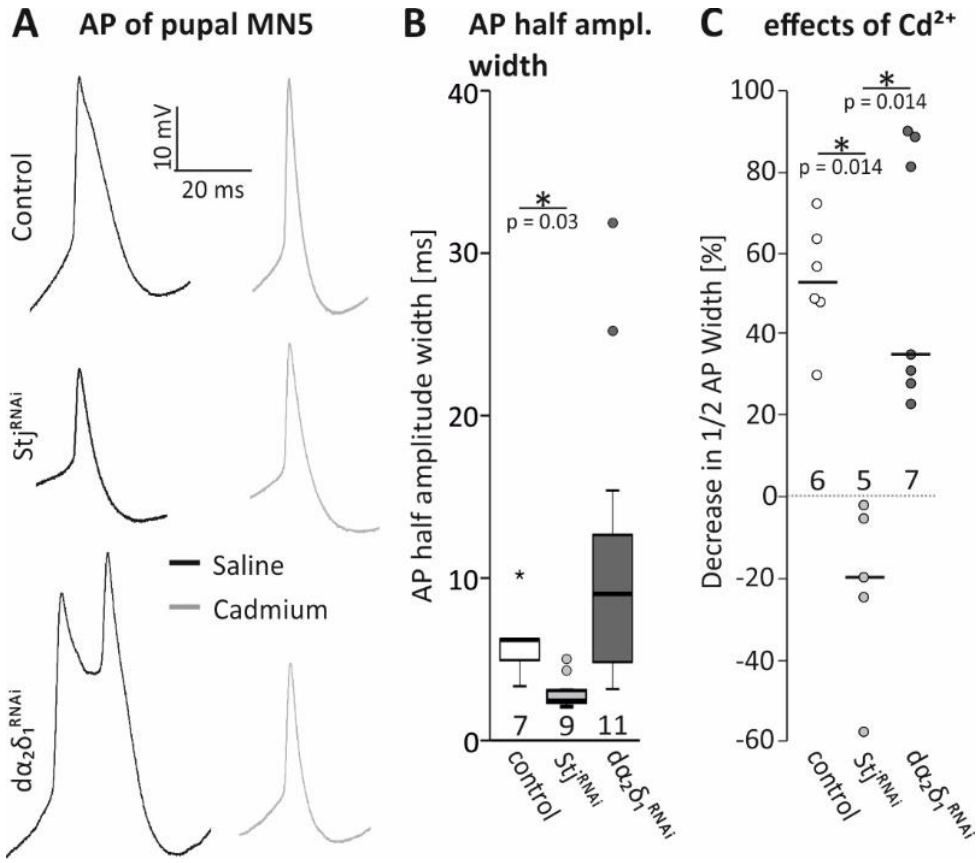

Fig.42: Stj^{RNAi} and dα$_2$δ$_1^{RNAi}$ have opposite effects on action potential (AP) shape of pupal MN5 motoneurons
[**A**] Current clamp measurements of APs recorded from the soma of pupal (P8) wing depressor neurons MN5. Square pulse current injections from 0 to 1.0 nA (Δ 0.1 nA) were done before and after a wash in of VGCC blocker Cadmium (500 µM, 2min). Pupae with a targeted knockdown (UAS-GFP; D42-Gal4, Cha-Gal80) of Stj (UAS-Stj^{RNAi}; UAS-dcr2, light gray) or dα$_2$δ$_1$ (UAS- dα$_2$δ$_1^{RNAi}$; UAS-dcr2, dark gray) in MN1-5 plus control were used. Cadmium erased calcium component of control APs and calcium-dependent double peak events in dα$_2$δ$_1^{RNAi}$ but had no effect on Stj^{RNAi}. [**B**] AP half amplitude width measured at membrane potentials of -10 mV was significantly reduced in Stj^{RNAi} (p = 0.03) but not in dα$_2$δ$_1^{RNAi}$ (p = 1.0) compared to control (ANOVA, p = 0.001). [**C**] Compared to Stj^{RNAi} AP width was significantly (ANOVA, p = 006) decreased by Cadmium (Cd^{2+}) in control (p = 0.014) and dα$_2$δ$_1^{RNAi}$ (p = 0.014).). Data are presented as boxes displaying the median with 25 and 75% quartiles and whiskers represent 10 and 90% quartiles or as single data points with the median (bar). The number of replicates is given inside the respective box or under the data points. A Kruskal-Wallis ANOVA and Dunn-Bonferroni posthoc tests were done for statistical analysis (p < 0.05*; p < 0.01**; p < 0.001***). (Figure modified from Heinrich & Ryglewski in submission)

These findings indicate, that knockdown of both Stj and dα$_2$δ$_1$ result in opposite changes in functional Ca_V2 density in axons. To further confirm this, we performed calcium imaging experiments from the axon of pupal (P8) MN5 neurons (see 2.11). To do so, we co-expressed the calcium indicator GCamp6s in DLM neurons (UAS-GCamp6s; 23H06-Gal4) in addition to Stj^{RNAi} or dα$_2$δ$_1^{RNAi}$ (c) and in the respective control (a):

a) $$; \frac{+}{\text{UAS-GCamp6s}} ; \frac{\text{UAS-dcr2}}{\text{23H06-Gal4}}$$

b) $; \frac{\text{UAS-Stj}^{RNAi}}{\text{UAS-GCamp6s}} ; \frac{\text{UAS-dcr2}}{\text{23H06-Gal4}}$

c) $; \frac{\text{UAS-d}\alpha_2\delta_1{}^{RNAi}}{\text{UAS-GCamp6s}} ; \frac{\text{UAS-dcr2}}{\text{23H06-Gal4}}$

We then imaged MN5 while activating it via current injections (Fig.43 B). Changes in axonal GCAMp6s fluorescence (Fig. 43 A) were analyzed with HOKAWO 3.10 software and ΔF/F was calculated by [F(firing)F(rest)]/F(rest). The data were non-normally distributed and thus a Kruskal-Wallis ANOVA and Dunn-Bonferroni posthoc tests were done.

Upon activation of MN5 via current injections the increase in axonal GCamp6s fluorescence is significantly lower (ANOVA, p = 0.000) in Stj^{RNAi} (0.04 + 0.03; Dunn, p = 0.000) as compared to control (0.80 + 0.17) (Fig.43 C,Ci). By contrast the increase in GCamp6s fluorescence upon activation of MN5 was significantly higher in $d\alpha_2\delta_1{}^{RNAi}$ (1.05 + 0.06; Dunn, p = 0.000).

In summary, $d\alpha_2\delta_1{}^{RNAi}$ seems to result in shifts of dendritic vs axonal Ca_V2 channel localization, while Stj seems to be required for normal function or cell-surfacing of all HVA CaV channels, in all subcellular compartments (dendrites, axon & axon terminals) and developmental stages of *Drosophila* motoneurons.

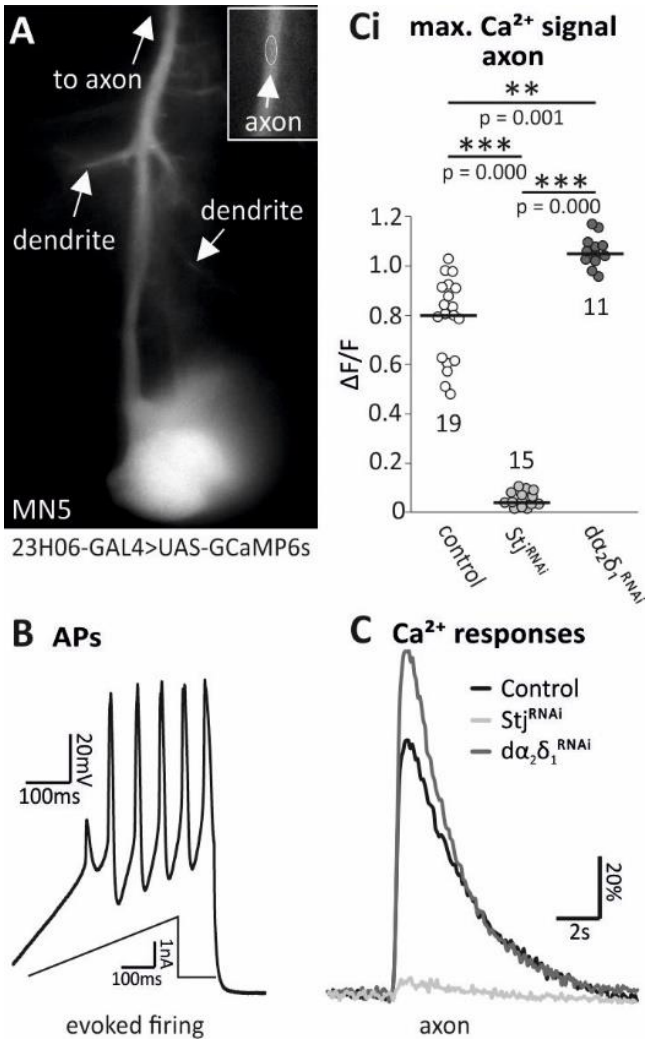

Fig.43: Both Stj and $d\alpha_2\delta_1$ have opposite effects on normal function of axonal Ca_V channels in pupal MN5 motoneurons
[**A**] Calcium imaging was done from the axons of wing depressor neurons MN5 expressing the calcium sensor GCamp6s (UAS-GCamp6s;23H06-Gal4). Changes in calcium fluorescence were measured upon activation of MN5 via [**B**] current injections. [**C**] Ca^{2+} responses were recorded from flies additionally expressing Stj^{RNAi} (UAS-Stj^{RNAi};UAS-dcr2, light gray points) or $d\alpha_2\delta_1{}^{RNAi}$ (UAS- $d\alpha_2\delta_1{}^{RNAi}$;UAS-dcr2, dark gray points) and controls (UAS-dcr2, white points). [**Ci**] The increase in axonal GCamp6s fluorescence upon activation of MN5 was significantly reduced (ANOVA, p = 0.000) in Stj^{RNAi} (p = 0.001), but increased in $d\alpha_2\delta_1{}^{RNAi}$ (p = 0.000) compared to control. The data is presented as single data points with the median (bar). The number of replicates is given under the respective data points. A Kruskal-Wallis ANOVA and Dunn-Bonferroni post-hoc tests were done for statistical analysis (p < 0.05*; p < 0.01**; p < 0.001***). (Figure modified from Heinrich & Ryglewski in submission)

3.5 Stj and $d\alpha_2\delta_1$ might be required for equal distribution of excitatory vs inhibitory dendritic input domains of adult flight motoneurons

$\alpha_2\delta$ proteins were already found to play important roles in synaptogenesis and seem to promote the formation of specific synapse types. Loss of function of specific $\alpha_2\delta$ subunits can, therefore, result in an imbalance of excitatory-inhibitory input in neurons (Eroglu *et al*., 2007; Geisler *et al*., 2019). For example, $\alpha_2\delta_1$ was found to be the postsynaptic receptor for thrombospondin in excitatory synapses in heterologous expression systems and mouse cortex. Thus, the interaction of $\alpha_2\delta_1$ with thrombospondin was found to promote the formation of excitatory synapses (Eroglu *et al*., 2009; Risher *et al*., 2018).

The dendritic tree morphology of DLM neuron MN5 is relatively stereotyped (Vonhoff & Duch, 2010). In geometric dendrite reconstructions the dendritic tree can be divided in a

proximal (meaning closer to the soma) and a distal (meaning closer to the axon) half as described above (see 2.12.4). Thereby, the proximal dendritic tree receives mainly excitatory/cholinergic input via Dα7nAChR, while the distal half receives mainly inhibitory/GABAergic input via Rdl $GABA_AR$ (Kuehn & Duch, 2013; Ryglewski *et al*., 2017). During development, synaptic input though the cholinergic and GABAergic input domains will locally guide the growth of dendrites. In control situation this results in an equal distribution of dendritic building material to the proximal (mainly cholinergic) and distal (mainly GABAergic) dendritic tree. Therefore the ratio of the dendritic length of the proximal vs the distal half is approx. 1.0 in control situation (Ryglewski *et al*., 2017). Promoting one side by genetic manipulations will result in an overgrowth of the promoted side and thereby reduce dendritic growth of the other side without affecting the total dendritic length. Vice versa, decreasing the input to one domain by genetic manipulation, will result in a dendritic shift towards the other domain. Thus, excitatory (cholinergic synapses) and inhibitory (GABAergic spaces) synapses seem to compete for dendritic building material during development (Ryglewski *et al*., 2017).

If for example $d\alpha_2\delta_1$ would also be needed for the correct formation of excitatory synapses in *Drosophila* MN5 motoneurons, expression of $d\alpha_2\delta_1^{RNAi}$ could potentially result in a reduction of dendritic cholinergic input domains. A potential decrease of cholinergic input domains during development should result in a dendritic shift towards the GABAergic input domains and thereby increase the dendritic length of the distal half of the dendritic tree. To test this, we analyzed the dendritic length of the distal (GABAergic input) vs the proximal (cholinergic input) dendritic tree in geometric reconstructions of MN5 from Stj^{R-NAi}, $\alpha_2\delta_1^{RNAi}$ and the respective control (see above).

As expected, the ratio between the proximal/distal dendritic length of MN5 was approx. 1.0 (0.93 $\pm$ 0.1 µm) in control flies (Fig.44 A,B). By contrast, the ratio seemed to be shifted towards the distal (inhibitory) side in $\alpha_2\delta_1^{RNAi}$ (0.75 $\pm$ 0.1 µm). Also, in Stj^{RNAi} the ratio tended to be shifted towards the distal dendritic input domains (0.85 $\pm$ 0.1 µm), but variation in the data was very high. Since the data was normally distributed, a one-way ANOVA was performed. Probably due to high variations in the data and the relatively low number of replicates, no significant changes in the ratio (prox/dist) could be found in Stj or $\alpha_2\delta_1$ knockdown compared to control (ANOVA, $p = 0.56$) (Fig.44 C). In addition, the results need to be viewed with caution, since also the total dendritic length of MN5 was reduced

in both Stj^{RNAi} and $d\alpha_2\delta_1^{RNAi}$. Furthermore, potential changes in cholinergic or GABAergic input domains through the expression of Stj^{RNAi} and $d\alpha_2\delta_1^{RNAi}$ are only assessed indirectly and need to be further investigated. Possible means to test this are discussed below.

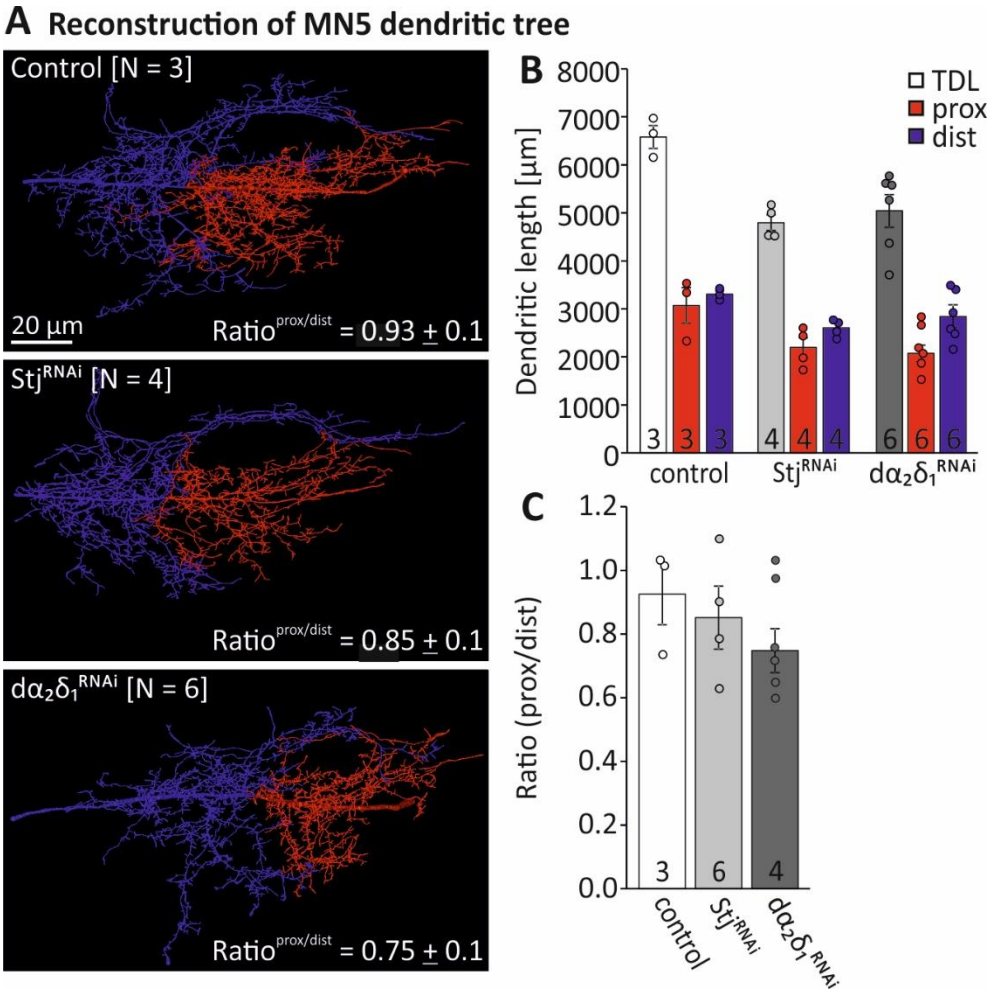

Fig.44: Both Stj and $d\alpha_2\delta_1$ seem required for equal distribution of dendritic input domains in MN5

[**A**] Reconstructions of MN5 dendritic tree from confocal image stacks of intracellularly dye-filled cells. Adult flies with a targeted knockdown (UAS-GFP; D42-Gal4, Cha-Gal80) of Stj (UAS-Stj^{RNAi}; UAS-dcr2, light gray) or $d\alpha_2\delta_1$ (UAS- $d\alpha_2\delta_1^{RNAi}$; UAS-dcr2, dark gray) in MN1-5 plus control (UAS-dcr2, white) were used. [**B**] The total dendritic length (white and gray bars) and dendritic length of the proximal (red bar) and distal (blue bar) dendritic input domains. [**C**] Ratio of proximal/distal dendritic length was tendentially but not significantly reduced (ANOVA, p = 0.56) in both Stj^{RNAi} and $d\alpha_2\delta_1^{RNAi}$ compared to control. Mean values are presented as bars with whiskers for the standard deviation. The number of replicates is given inside the respective bar and as single data points. A one-way ANOVA was done for statistical analysis ($p < 0.05$*; $p < 0.01$**; $p < 0.001$***).

3.6 Gabapentin might reduce the excitability of larval crawling MNs and muscles by acutely blocking Stj

Gabapentin was originally synthesized as an analog of the anticonvulsant γ aminobutyric acid (GABA) to be used as a new possible anti-epileptic drug. While gabapentin was indeed found to be effective in the treatment of epilepsy (Andrews & Fischer, 1994; Goa & Sorkin, 1993; Marson *et al*., 1996; McLean, 1995) and additionally in treating neuropathic pain (Backonja *et al*., 1998; Serpell, 2002) in clinical trials, it did not affect GABA metabolism (reviewed by Taylor *et al*., 1998). Instead, gabapentin was found to bind specifically to $\alpha_2\delta_1$ and $\alpha_2\delta_2$ in vertebrates (Gee *et al*., 1996; Gong *et al*., 2001). Still, its mechanisms of action are incompletely understood. By binding to $\alpha_2\delta$ proteins gabapentin was suggested to impair α_1- $\alpha_2\delta$ interaction and thereby to reduce HVA Ca_V channel activity, but data on acute effects of gabapentin on VGCC calcium current amplitudes are controversial. While gabapentin was found to reduce HVA Ca^{2+} currents in some neurons (Fink *et al*., 2000; Stefani *et al*., 1998), in other studies no acute gabapentin-induced changes in HVA calcium current amplitudes were detected (Rock *et al*., 1993; Schumacher *et al*., 1998). In heterologous expression systems and in mouse DRG neurons only chronic application of gabapentin reduced cell-surface expression of both $\alpha_2\delta_1$/$\alpha_2\delta_2$ and Ca_V2 and thereby reduced Ca_V2 activity (Hendrich *et al*., 2008). Chronic application of gabapentin was further found to prevent formation of new synapses by blocking interaction of $\alpha_2\delta_1$ with thrombospondin (Eroglu *et al*., 2009).

Since gabapentin was also found to reduce seizure-like activity in fly mutants exhibiting seizure-like behavior (*bangless* or *paralytic*; Streit *et al*., 2016), *Drosophila melanogaster* might be a useful model system to study the molecular mechanisms underlying the action of gabapentin. Therefore, we wanted to investigate, which $\alpha_2\delta$ protein is the target binding site for gabapentin in *Drosophila*. Furthermore, it would be advantageous to potentially have the means to pharmacological block one or more $\alpha_2\delta$s to investigate acute vs non-acute functions of $\alpha_2\delta$ proteins *in vivo*. Especially, since conditional knockdowns of $\alpha_2\delta$ subunits via genetic manipulations (UAS-$Gal80^{ts}$) did not work (data not shown).

In larval crawling motoneurons of *Drosophila* axonal Ca_V1 channels were found to modulate neuronal excitability (Worrell & Levine, 2008; Kadas *et al*., 2017). To test whether gabapentin acutely affects the excitability of larval crawling neurons by impairment of

Ca_V1- $\alpha_2\delta$ interaction, we recorded RP2 neurons in current-clamp mode and investigated for changes in firing frequencies, before and after application of gabapentin (25 µM, 5min). The F/I plots were analyzed with Clampfit software and fitted with a modified Boltzmann fit (Boltzmann, charge-voltage) (see 2.8.2.1). In control larvae (a), gabapentin significantly reduced (paired T-Test, p = 0.04) the firing frequency of RP2 neurons at high current injections by approx. 20 % (at 220 pA: before, 90 ± 18 Hz; after, 73 ± 15 Hz) (Fig.45 A,B Control). Thus, the application of gabapentin seems to reduce excitability of RP2 neurons. This further indicates that gabapentin might indeed have acute effects on larval crawling motoneurons *in vivo*.

To assess whether gabapentin might be a specific blocker for either Stj or $d\alpha_2\delta_1$, or both we tested if gabapentin still reduced the firing frequencies in larvae with a mosaic expression (RN2-Gal4, UAS-GFP; Act<FRT.stop>-Gal4, UAS-FLP) of Stj^{RNAi} (b) or $d\alpha_2\delta_1{}^{RNAi}$ (c) in larval crawling motoneurons. To further investigate whether potential changes in the RP2 firing frequencies are due to effects of gabapentin on HVA calcium channels, we additionally tested if gabapentin still reduced the firing frequency in RP2 neurons with a knockdown of the Ca_V1 channel (d). Neurons expressing RNAi knockdowns were identified by co-expression of mcd8GFP.

a) $\; ; \frac{+}{\text{RN2-Gal4,UAS-mcd8GFP}} ; \frac{\text{UAS-dcr2}}{\text{Act<FRT.stop>Gal4,UAS-FLP}}$

b) $\; ; \frac{\text{UAS-Stj}^{RNAi}}{\text{RN2-Gal4,UAS-mcd8GFP}} ; \frac{\text{UAS-dcr2}}{\text{Act<FRT.stop>Gal4,UAS-FLP}}$

c) $\; ; \frac{\text{UAS-d}\alpha_2\delta_1{}^{RNAi}}{\text{RN2-Gal4,UAS-mcd8GFP}} ; \frac{\text{UAS-dcr2}}{\text{Act<FRT.stop>Gal4,UAS-FLP}}$

d) $\; ; \frac{\text{UAS-Ca}_V1^{RNAi}}{\text{RN2-Gal4,UAS-mcd8GFP}} ; \frac{\text{UAS-dcr2}}{\text{Act<FRT.stop>Gal4,UAS-FLP}}$

Also in RP2 neurons with a targeted knockdown of $\alpha_2\delta_1$ the firing frequency seemed to be reduced by 20 % by application of gabapentin (at 220 pA: before, 81 Hz; after, 65 Hz). By contrast, the firing frequency was not significantly (paired T-Test, p = 0.07) reduced (approx. 6 %) in RP2 neurons expressing Stj^{RNAi} (at 220 pA: before, 72 ± 4 Hz; after, 68 ± 8 Hz) (Fig.45 B). Furthermore, the firing frequency was also not significantly reduced (approx. 11 %; paired T-Test, p = 0.16) by gabapentin in neurons expressing Ca_V1^{RNAi} (Fig.27 A,B

Ca_V1^{RNAi}) (at 220 pA; before, 92 ± 16 Hz; after, 82 ± 7 Hz). Thus, indicating that the effects of gabapentin might depend on the presence of Stj and the Ca_V1 channel.

We further analyzed if expression of Stj^{RNAi}, $d\alpha_2\delta_1^{RNAi}$ or Ca_V1^{RNAi} mimics the effects of gabapentin application in controls (Fig.45 C). Indeed the effects of gabapentin on RP2 firing frequency in controls seemed to be mimicked by Stj^{RNAi}, but not $d\alpha_2\delta_1^{RNAi}$, which suggests, that gabapentin might be a blocker for Stj in *Drosophila melanogaster*. Expression of Ca_V1^{RNAi} seemed to only partly mimic the effects of gabapentin; therefore potentially blocking Stj with gabapentin might not solely affect Ca_V1 channels.

Probably due to low input resistances during all current-clamp recordings of RP2 neurons, the data for Ca_V1^{RNAi} does not reflect data from previous studies (Worrell & Levine, 2008; Kadas *et al*., 2017). Still, input resistance was low in all recordings and therefore effects of gabapentin should be comparable between the tested genotypes.

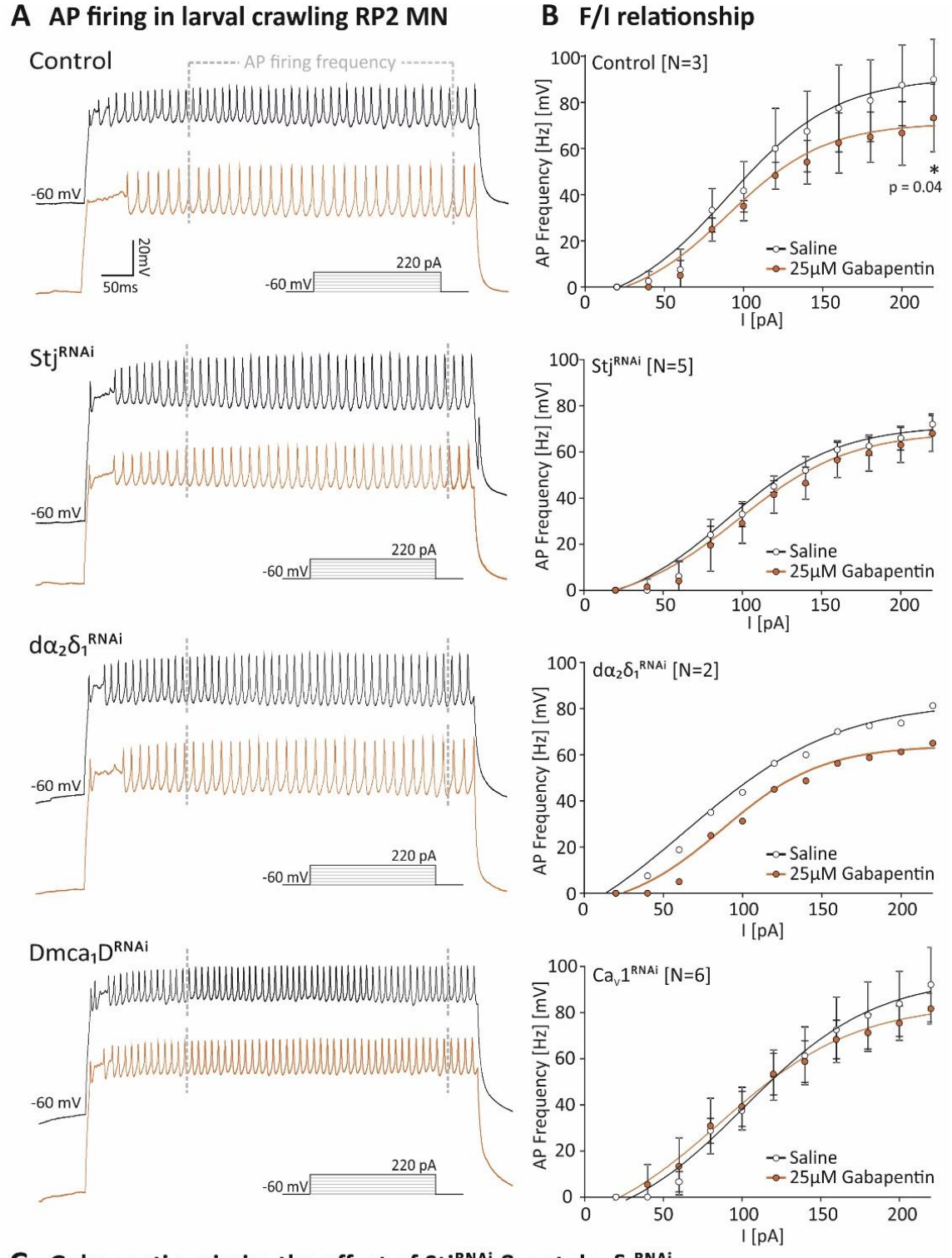
A AP firing in larval crawling RP2 MN
B F/I relationship
Control
AP firing frequency
-60 mV
20mV
50ms
220 pA
-60 mV
Stj^RNAi
dα2δ1^RNAi
Dmca1D^RNAi
Control [N=3]
Stj^RNAi [N=5]
dα2δ1^RNAi [N=2]
Cav1^RNAi [N=6]
AP Frequency [Hz] [mV]
I [pA]
Saline
25µM Gabapentin
*
p = 0.04
C Gabapentin mimics the effect of Stj^RNAi & not dα2δ1^RNAi
Stj^RNAi [N=5]
dα2δ1^RNAi [N=7]
Cav1^RNAi [N=7]
control + Gabap.

Fig.45: Gabapentin reduces firing frequency in controls and $d\alpha_2\delta_1^{RNAi}$ but not Stj^{RNAi} or Ca_V1^{RNAi} in larval RP2 crawling motoneurons

[**A**] Current clamp measurements of APs recorded from the soma of pupal (P8) wing depressor neurons MN5. Current injections from 0 to 220 pA (20 pA intervals) were done as square pulses before and after a wash in of gabapentin (25 µM, 5min). Larvae with mosaic knockdowns (RN2-Gal4, UAS-GFP; Act<FRT.stop>-Gal4, UAS-FLP) of Stj (UAS-Stj^{RNAi}; UAS-dcr2, light gray), $d\alpha_2\delta_1$ (UAS- $d\alpha_2\delta_1^{RNAi}$; UAS-dcr2, dark gray) or Ca_V1 (UAS-$Dmca1D^{RNAi}$) and the control (UAS-dcr2, white) were used. Neurons expressing the RNAi or only dcr2 were identified by additional mcd8GFP expression. [**B**] F/I curves were measured. Gabapentin significantly reduced AP firing frequency at high current injections (220 pA) in controls ($p = 0.04$) but not in Stj^{RNAi} ($p = 0.08$) and Ca_V1^{RNAi}. Gabapentin also seemed to reduce AP firing frequency in $d\alpha_2\delta_1^{RNAi}$. [**C**] The effects of gabapentin in controls seemed to mimic the effects of Stj^{RNAi} and partly of Ca_V1^{RNAi}, but not $d\alpha_2\delta_1^{RNAi}$. Data are presented as single data points and whiskers for standard deviation. The data were fitted in Clampfit 10.7 software with modified Boltzmann fit (charge-voltage). The number of replicates is given beside the respective genotype. Paired T-Tests were done for statistical analysis ($p < 0.05$*; $p < 0.01$**; $p < 0.001$***).

To further investigate if gabapentin might also have acute effects on neuromuscular synaptic transmission in *Drosophila* larvae, we washed in gabapentin (25 µM) for 5 min during intracellular muscle recordings of evoked postsynaptic potentials (EPSP) from muscle M10 (see above). We then analyzed the amplitude of single EPSPs (0.5 Hz stimulation frequency) before and after washing in gabapentin with the Clampfit 10.7 software. To prevent potential effects due to deterioration of the muscle, we performed control recordings, in which only saline was washed in for 5 min. Application of gabapentin reduced EPSP amplitude by approx. 18 % (18 $\pm$ 11 %). Washing in Saline for 5 min only reduced EPSP amplitude by approx. 3 % (3 $\pm$ 10 %). Compared to saline, gabapentin significantly reduced EPSP amplitudes (T-Test, $p = 0.007$) (Fig.46 A,B). Expression of Stj^{RNAi} in larval motoneurons also reduced the EPSP amplitude by approx. 50 % (see above). Although a reduction in the EPSP amplitude of Stj^{RNAi} mainly seems to be due to a reduced Ca_V2 density in synaptic boutons (as suggested by findings of this and previous studies; see above), gabapentin might still have acute effects on synaptic transmission by blocking Stj at axon terminals. If this assumption was correct, the effects of gabapentin on EPSP amplitude should be gone or reduced in animals expressing Stj^{RNAi} in larval motoneurons.

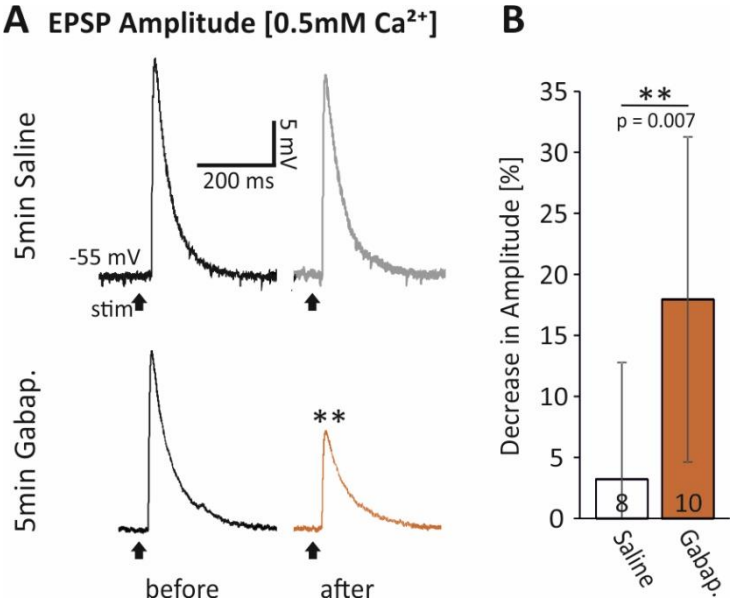

Fig.46: Gabapentin reduces EPSP amplitude at the larval NMJ
Evoked postsynaptic potentials (EPSP) were recorded intracellularly from muscle M10 in current-clamp mode while stimulating the respective nerve. A calcium concentration of 0.5 mM was used for the extracellular bath solution. [**A**] Single EPSP (0.5 Hz) were recorded in controls before and after washing in either saline (white bar) or gabapentin (25 µM, orange bar) for 5 min. [**B**] Gabapentin reduced the EPSP amplitude significantly more compared to saline (p = 0.007). Mean values are presented as bars with whiskers for the standard deviation. The number of replicates is given inside the respective bar. An unpaired T-tests were done for statistical analysis (p < 0.05*; p < 0.01**; p < 0.001***).

To test this, we again conducted current-clamp measurements of muscle M10 in larvae expressing a targeted knockdown of Stj (b) in larval crawling MNs (RN2-Gal4, UAS-GFP; Act<FRT.stop>-Gal4, UAS-FLP) and the respective control (a).

a) $; \frac{+}{\text{RN2-Gal4,UAS-mcd8GFP}} ; \frac{\text{UAS-dcr2}}{\text{Act<FRT.stop>Gal4,UAS-FLP}}$

b) $; \frac{\text{UAS-Stj}^{RNAi}}{\text{RN2-Gal4,UAS-mcd8GFP}} ; \frac{\text{UAS-dcr2}}{\text{Act<FRT.stop>Gal4,UAS-FLP}}$

Washing in gabapentin again reduced EPSP amplitude significantly (p = 0.02) in control (-27 ± 18 %), but gabapentin also seemed to reduce the EPSP amplitude in Stj^{RNAi} (-20 ± 49 %; p = 0.09). Furthermore, the percentage changes in EPSP amplitude were not significantly different in Stj^{RNAi} compared to control (Mann-Whitney-U, p = 0.53) (Fig.47 A,D), which indicates that effects of gabapentin are independent of the presence of Stj at axon terminals. This might either indicate that gabapentin is not a specific blocker for Stj in *Drosophila*, as suggested by previous findings of this study (see above), or that Stj has no acute function in synaptic transmission. This would mean that changes in EPSP amplitude

by gabapentin are not due to a presynaptic effect, but a postsynaptic (muscular) effect. Potential modulation of postsynaptic HVA Ca_V1 channels by gabapentin would indeed affect EPSP amplitudes. Furthermore, we already found that both Stj and $\alpha_2\delta_1$ are also functional in muscles (see above).

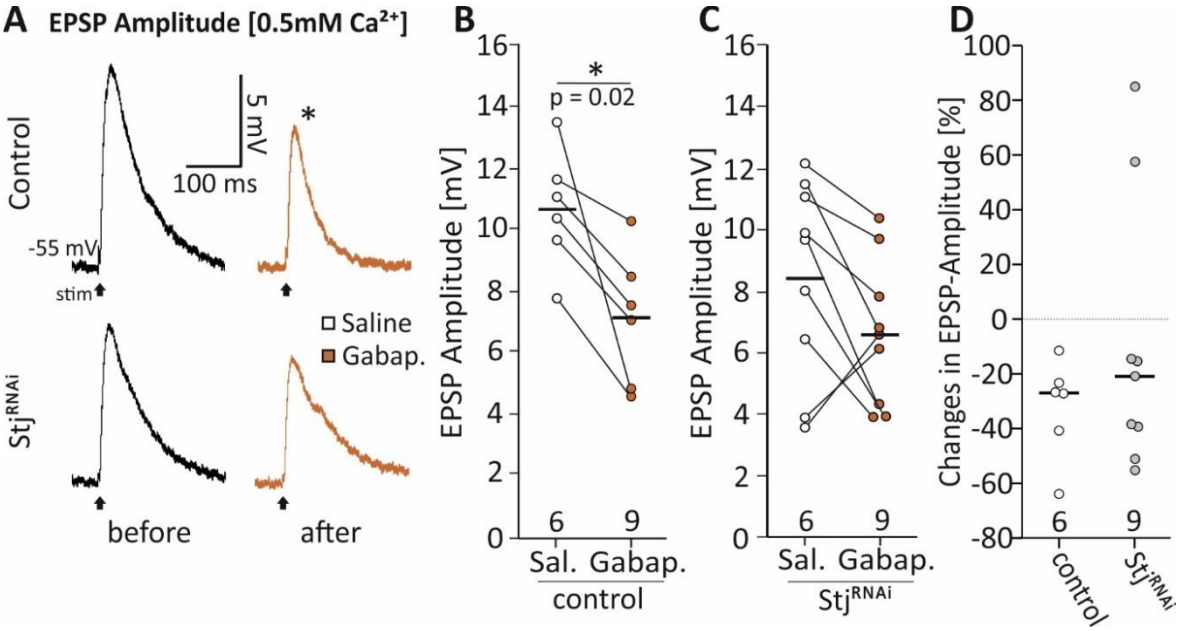

Fig.47: Gabapentin reduces EPSP amplitude in controls and neuronal Stj^{RNAi} at the larval NMJ
Evoked postsynaptic potentials (EPSP) were recorded intracellularly from muscle M10 in current-clamp mode while stimulating the respective nerve. A calcium concentration of 0.5 mM was used for the extracellular bath solution. [**A**] Single EPSP (0.5 Hz) were recorded in controls (UAS-dcr2) and targeted knockdowns (OK371-Gal4) of Stj (UAS-Stj^{RNAi}; UAS-dcr2) before (black traces) and after (orange traces) washing in Gabapentin (25 µM) for 5 min. [**B**] EPSP amplitude significantly reduces through Gabapentin in controls ($p = 0.02$) and [**C**] tendentially in Stj^{RNAi} ($p = 0.09$). The respective data points of EPSP amplitude before (white) and after an (orange) wash-in of Gabapentin are connected with a line. [**D**] Percental changes in EPSP amplitude through Gabapentin were not different ($p = 0.53$) in Stj^{RNAi} (gray points) compared to control (white points). The data is presented as single data points with the median (bar). The number of replicates is given under the respective data points. A one-way ANOVA and LSD posthoc tests were done for statistical analysis ($p < 0.05$*; $p < 0.01$**; $p < 0.001$***). (Figure modified from Heinrich & Ryglewski in submission. Paired T-tests (**B,C**) or a Mann-Whitney-U test (**D**) were done for statistical analysis ($p < 0.05$*; $p < 0.01$**; $p < 0.001$***).

To test whether changes in EPSP amplitude through gabapentin are indeed mediated by muscular effects, we did two-electrode voltage clamp (TEVC) measurements from M10. During TEVC measurements the membrane potential of the muscle will be clamped to -60 mV. Thus, Ca_V1 channels in the muscle which normally open at approx. -30 mV will not be able to open anymore. Consequently, we would expect that potential effects of gabapentin on EPSP amplitudes by modulating postsynaptic Ca_V1 channels should be gone in TEVC measurements.

We again measured EPSP amplitudes before and after washing in gabapentin (25 µM) for 5 min. Indeed, during TEVC measurements washing in gabapentin seemed to not reduce the EPSP amplitude more than washing in saline (both approx. 10 %) (Fig.48 A,B). This indicates that gabapentin reduces EPSP amplitudes by affecting the postsynaptic (muscle) and not the presynaptic side. This would further suggest that Stj might have no acute function in evoked synaptic transmission at axon terminals of larval crawling motoneurons.

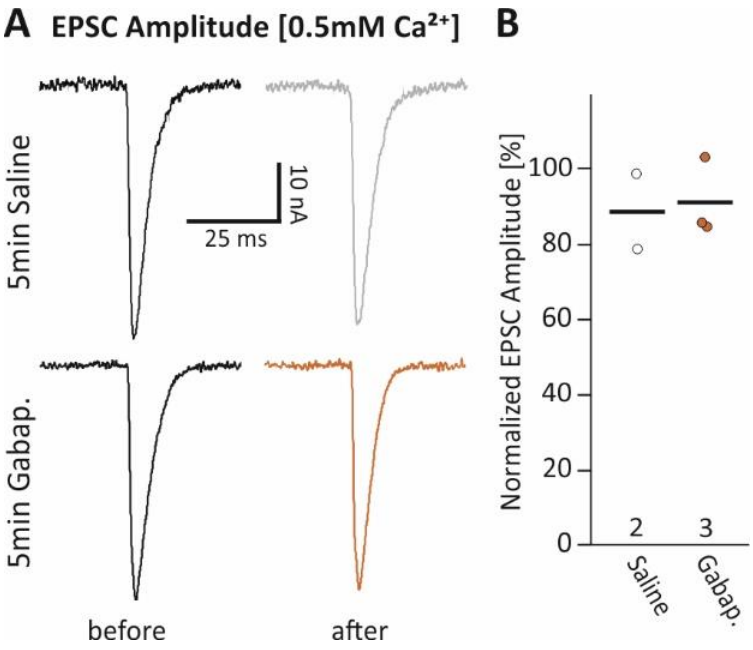

Fig.48: Effect of gabapentin on evoked synaptic transmission at larval NMJ must be postsynaptic, since it is gone in TEVC measurements
Evoked postsynaptic potentials (EPSP) were recorded intracellularly from muscle M10 in two-electrode voltage clamp (TEVC) while stimulating the respective nerve. A calcium concentration of 0.5 mM was used for the extracellular bath solution. [**A**] Single EPSP (0.5 Hz) were recorded in controls before (black traces) and after washing in either gabapentin (25 µM, orange traces) or saline (gray traces) for 5 min. [**B**] EPSP amplitude seemed unchanged by washing in gabapentin compared to saline. The data is presented as single data points with the mean (bar). The number of replicates is given under the respective data points.

4. Discussion

The aim of this study was to take advantage of the relatively simpler situation of *Drosophila melanogaster* as compared to mammals to probe for differential functions of different α_1-$\alpha_2\delta$ combinations for calcium channel function and localization. Although studies in heterologous expression systems indicate that all $\alpha_2\delta$ subunits are able to interact with all HVA α_1 proteins, different $\alpha_2\delta$ subunits seem to have different effects on different α_1 subunits, suggesting specific functional combinatorics. Furthermore, $\alpha_2\delta$ subunits seem to have partially overlapping but also differential cell- and tissue-specific expression patterns in vertebrates (Cole *et al*., 2005; Dolphin, 2012). Cell-specific functions for each $\alpha_2\delta$ protein were further confirmed in different $\alpha_2\delta$ mice mutants (Barclay *et al*., 2001; Fuller-Bicer *et al*., 2009; Neely *et al*., 2010). Therefore, in vertebrates, specific neuron types seem to express distinct α_1-$\alpha_2\delta$ combinations, and functional redundancy is not in accord with disease phenotypes manifesting in single $\alpha_2\delta$ mutations. In *Drosophila* the Ca_V2 channel is missing at the neuromuscular junction of larval crawling motoneurons of $d\alpha_2\delta_3$ (straightjacket, Stj) mutants (Dickman *et al*., 2008; Ly *et al*., 2008). This further indicates that $\alpha_2\delta$ subunits seem to have specific functions which cannot be compensated for by other $\alpha_2\delta$ proteins. Therefore we hypothesized that there is a division of labor between different $\alpha_2\delta$ subunits regarding the modification of HVA channel properties, localization, and density.

4.1 Stj and $d\alpha_2\delta_1$ are differentially expressed in the larval and adult VNC, but both localize to motoneurons

To test this hypothesis, we first investigated whether different $\alpha_2\delta$ subunits are also differentially expressed in the ventral nerve cord of *Drosophila melanogaster*. Labeling of endogenously tagged Stj ($d\alpha_2\delta_3$) and $d\alpha_2\delta_1$ revealed a broad expression of both subunits in many neurons. This is in accord with *in situ* hybridization studies in vertebrates, where $\alpha_2\delta_1$ and $\alpha_2\delta_3$ are also widely expressed throughout the CNS (Cole *et al*., 2005). By contrast, in *Drosophila* many neurons, including motoneurons seemed to express both Stj and $d\alpha_2\delta_1$. Although mammalian $\alpha_2\delta$ proteins seem to have largely tissue and cell-specific

expression patterns (Cole *et al*., 2005; Huang *et al*., 2013; Müller *et al*., 2015), transcripts of different $\alpha_2\delta$ proteins were detected in selectively harvested neurons (Fell *et al*., 2016). Therefore it is possible, that also in vertebrates neurons might express more than one $\alpha_2\delta$ protein, but due to lack of appropriate antibodies detection on protein level is rather difficult. As far as I know, we are the first to investigate the co-expression of different $\alpha_2\delta$ subunits on the protein level and *in vivo*. We thereby find co-expression of Stj and $d\alpha_2\delta_1$ in many neurons of *Drosophila*, including well-identified motoneurons.

Due to the lack of appropriate antibodies, the subcellular localization of different $\alpha_2\delta$ subunits is also not well examined in vertebrates. In rat CNS, $\alpha_2\delta_1$ mainly localized to neuropil regions and presynaptic terminals but was also found in the soma of neurons (Bauer *et al*., 2009; Taylor & Garrido, 2008). By contrast, in the retina of rodents both $\alpha_2\delta_1$ and $\alpha_2\delta_3$ were mainly found in the soma of multiple cell types (Huang *et al*., 2013; Müller *et al*., 2015). In our study, we were able to assess the subcellular localization of both $d\alpha_2\delta_1$ and Stj in the *Drosophila* VNC. Furthermore, co-labeling of $Stj^{mCherry}$ and $d\alpha_2\delta_1^{GFP}$ enabled us to probe for differential localization patterns of those two $\alpha_2\delta$ proteins. While $Stj^{mCherry}$ signal was found mainly in the somata and not the neuropil regions in the larval and adult VNC of *Drosophila*, endogenously tagged $d\alpha_2\delta_1^{GFP}$ seems to localize mainly to neuropil regions but also to somata. Furthermore, while Stj was already found to localize to presynaptic terminals at the neuromuscular junction of larval and embryonic motoneurons in *Drosophila* (Kurshan *et al*., 2009; Ly *et al*., 2008), we were not able to detect $d\alpha_2\delta_1^{GFP}$ at axon terminals of the larval NMJ (see appendix 6.9). Since both Stj and $d\alpha_2\delta_1$ seem to be co-expressed in subsets of neurons, including motoneurons, this further hints at a differential subcellular localization of those two $\alpha_2\delta$ proteins. It also indicates differential functions of Stj and $d\alpha_2\delta_1$ in the same neurons. Thus, controversial results on the subcellular localization of $\alpha_2\delta$ proteins in vertebrates could be explained by differential functions of the same $\alpha_2\delta$ subunit in different types of cells.

Even though Stj and $d\alpha_2\delta_1$ seem to predominantly localize to different subcellular compartments, the data has to be viewed with caution. Please note that the absence of presynaptic $d\alpha_2\delta_1^{GFP}$ signal either means that the protein is not targeted to the axon terminals, or that protein concentration is below detection level. Furthermore, our data indicate $d\alpha_2\delta_1$ expression in muscles (see below), which could result in low contrasts for detection of presynaptic $d\alpha_2\delta_1^{GFP}$ at the larval NMJ. Indeed, we also were not able to detect

either $Stj^{mCherry}$ or Stj^{HA} overexpressed by $elav^{C155}$-Gal4 or Stj-Gal4 at the larval NMJ. We even tried to overexpress Stj^{HA} (generously provided by Thomas L. Schwarz) pan-neural to rescue Stj mutants (as described in Kurshan *et al*., 2009), but expression of Stj^{HA} did not rescue the lethality of homozygous mutant flies (Stj^{k10814}; transposon insertion, hypomorphic mutant) and Stj^{HA} could not be detected at the larval NMJ of only heterozygous mutants. Additionally, the pan-neural expression of a different UAS-Stj^{HA} (FlyORF; F001252) construct was also not able to rescue the lethality of homozygous mutant flies (Stj^{DD106}; null mutation, www.flybase.org). There might be several explanations for this. First, since Stj is not only required in neurons, pan-neural expression of Stj^{HA} might not be sufficient to rescue lethality. Secondly, the mutant alleles might contain additional second-site mutations, which are responsible for lethality of flies and thirdly, the used Stj^{HA} constructs are only partly functional and thus, are not able to rescue lethality. Since pan-neural expression of Stj^{HA} was able to rescue lethality in transheterozygote mutant combinations (Dickman *et al*., 2008) or in genomic construct rescues of hypomorphic Stj mutant alleles (Stj mutant allele/Deficiency; Ly *et al*., 2008), a combination of the second and the third scenario are likely. Indeed, comparing the sequence (SD03196) of the UAS-Stj^{HA} construct (HA-tag at amino acid 246; from Kurshan *et al*., 2009) to the cDNA sequence of Stj revealed, that some exons might be missing. Therefore changes in function and protein localization of Stj^{HA} are possible.

Genomic construct rescues of the $Stj^{mCherry}$ allele ($Stj^{mCherry}$/deficiency) reach adulthood but are very lethargic. This further indicates that Stj function might be partly disrupted by the MiMIC construct, which might lead to changes in the localization or concentration of the tagged Stj protein. Still, mainly somatic localization of Stj was also found in antibody stainings against Stj in *Drosophila* brain (Neely *et al*., 2010), which confirms the localization of $Stj^{mCherry}$. To conclude, Stj and $d\alpha_2\delta_1$ might be differentially localized, but this will require further investigation. One could try to tag $\alpha_2\delta$ at well-selected positions in the $\alpha_2\delta$ protein to prevent changes in protein function. In vertebrates tagging $\alpha_2\delta$ with an HA-tag between amino acids, 652 and 653 did not change protein function (Davies *et al*., 2006). One could further try to produce specific antibodies against Stj and $d\alpha_2\delta_1$ as already described in previous studies (Neely *et al*., 2010).

4.2 Stj and dα$_2$δ$_1$ seem to be required for different and non-redundant functions in *Drosophila* nervous system

Even though Stj and dα$_2$δ$_1$ are co-expressed in many neurons, including well-identified larval crawling and adult wing depressor motoneurons, our data clearly indicate differential and non-redundant functions of the two α$_2$δ proteins in those neurons, since: (1) Pan-neural knockdown of Stj is lethal, while an even stronger knockdown of dα$_2$δ$_1$ is not. (2) Targeted knockdown of Stj in wing depressor neurons results in flight inability, while knockdown of dα$_2$δ$_1$ does not. (3) Neither Stj nor dα$_2$δ$_1$ is compensatory upregulated following knockdown of the other. By contrast, both Stj and dα$_2$δ$_1$ seem to mediate at least partially redundant functions in muscles. We are the first to show *in vivo*, that functional redundancy of α$_2$δ subunits might greatly differ depending on the cell type. This provides an explanation for controversial data from heterologous expression systems, in which all α$_2$δ subunits were able to interact with all HVA α$_1$ proteins (reviewed by Dolphin, 2013).

To test for differential functions of Stj and dα$_2$δ$_1$ in *Drosophila*, we probed for gross defects following validated knockdowns of Stj or dα$_2$δ$_1$ in different subsets of cells. As expected, flies with a relatively strong pan-neural knockdown (approx. 64 %) of Stj were not viable. This confirms a crucial function for Stj, especially in neurons and is in accord with previous studies, were pan-neural overexpression of UAS-Stj^{HA} in Stj mutants (transheterozygote mutant combinations and hypomorphic Stj mutants/deficiency) was sufficient to rescue lethality (Dickman et al., 2008; Ly *et al*., 2008). Our findings further indicate crucial functions for Stj in glutamatergic neurons, since flies expressing Stj^{RNAi} under the control of the vesicular glutamate transporter (OK371-Gal4) are lethargic. Also, Stj knockdown in all neurons except glutamatergic neurons results in lethargic flies, indicating that Stj is not solely required in those neurons. Furthermore, knockdown of Stj in cholinergic neurons results in the same lethargic phenotype. Thus, Stj seems to have crucial functions in many neurons, which is confirmed by Stj^{mCherry} expression patterns in the adult and larval VNC. It is also in agreement with previous studies, were GFP expression under control of the Stj-Gal4 promoter already revealed expression of Stj in neurons co-expressing the neuronal marker Elav and the motoneuron marker Even-skipped. In addition, Stj expression was also confirmed for GABAergic neurons (Dickman *et al*., 2008). In vertebrates, specific cell types seem to express specific α$_2$δ subunits. For example, excitatory neurons preferably express α$_2$δ$_1$, while inhibitory neurons seem to preferably express α$_2$δ$_2$ (Cole *et al*.,

2005). Hence, overexpression of $\alpha_2\delta_1$ and mutations in $\alpha_2\delta_2$ display different epileptic and seizure-like phenotypes (Brodbeck *et al*., 2002; Faria *et al*., 2017; Ivanov *et al*., 2004). By contrast, in *Drosophila* Stj seems required for the normal function of both cholinergic and GABAergic neurons. In addition, Stj mutants (genomic construct rescued hypomorphic Stj mutant allele/Df(2R)Exel7128 deficiency) also display hyperexcitability and seizure-like activity (Ly *et al*., 2008). Since vertebrate $\alpha_2\delta$ subunits do not correspond to *Drosophila* $d\alpha_2\delta$ subunits in a 1:1 manner, it is not unlikely to detect differences.

$d\alpha_2\delta_1^{GFP}$ was co-expressed with $Stj^{mCherry}$ in many neurons, but in contrast to $Stj^{RNAi,}$ an even stronger (approx. 98 %) pan-neural knockdown of $d\alpha_2\delta_1$ was viable and displayed no obvious defects. Still pan-neural knockdown of $d\alpha_2\delta_1$ results in reduced climbing speed and impaired flight performance of flies, indicating that $d\alpha_2\delta_1$ is also needed for normal motor behavior. Furthermore, while a targeted knockdown of Stj in adult wing depressor neurons results in flight inability, $d\alpha_2\delta_1^{RNAi}$ flies even fly longer compared to control (see appendix). Thus, at least Stj and $d\alpha_2\delta_1$ indeed seem to have different and non-redundant functions in neurons. That Stj and $d\alpha_2\delta_1$ cannot compensate for each other at least in *Drosophila* CNS is further confirmed by the finding that neither $Stj^{mCherry}$ nor $d\alpha_2\delta_1^{GFP}$ expression is changed following pan-neural knockdown of the other. Otherwise, we would expect compensatory upregulation of one $d\alpha_2\delta$ in order to compensate for the loss or reduction of the other. Upregulation of related genes due to loss of protein function was described in many organisms including *Drosophila*, zebrafish, and mice (for review see Elbrolosy & Stainier, 2017).

By contrast, knockdown of either Stj or $d\alpha_2\delta_1$ in the muscle (Mef2-Gal4) did not result in any obvious phenotype, while flies with a double knockdown of Stj and $d\alpha_2\delta_1$ in muscles died at a late pupal stage. This indicates that in *Drosophila* both Stj and $d\alpha_2\delta_1$ are expressed in muscle cells and mediate at least partially redundant functions, or operate in concert to mediate a vital function. Therefore Stj and $d\alpha_2\delta_1$ are not able to functionally compensate for each other in neurons, but they might be able to functionally compensate for each other in other cell types including muscles.

4.3 Stj and dα$_2$δ$_1$ have different functions in the same identified motoneurons

4.3.1 Stj^{RNAi} and dα2δ1^{RNAi} have different effects at the neuromuscular junction of larval crawling motoneurons

A crucial function of Stj in targeting Ca_V2 channels to synaptic boutons of larval crawling motoneurons was already described: In Stj mutants (transheterozygote mutant combinations and hypomorphic Stj mutants/deficiency) a reduced amount of Ca_V2 channels was found at the larval and embryonic NMJ (Ly *et al*., 2008; Dickman *et al*., 2008). Reduction in presynaptic Ca_V2 abundance is supposed to result in impairment of synaptic transmission and a reduction in EPSP amplitude. Spontaneous mPSPs were normal in terms of amplitude and frequency (Ly *et al*., 2008). Since our findings indicate also a muscular function for Stj, we wanted to confirm these results in larvae with a targeted knockdown of Stj only in motoneurons. An increase in synaptic bouton number per muscle and a reduction in muscle size in Stj transheterozygote mutants, but also in mutants with a neuronal rescue of Stj further indicates that Stj is also functional in muscles (Dickman *et al*., 2008).

Still, selective knockdown of Stj in neurons confirms a decreased number of Ca_V2^{GFP} puncta per bouton. Also, the EPSP amplitude was reduced, but mPSP amplitude remained normal. Thus, indicating a reduced number of vesicles being released per stimuli but normal postsynaptic glutamate receptor expression. Our study, therefore, confirms that Stj is required for targeting Ca_V2 channels to axon terminals of larval crawling motoneurons aCC and RP2 and thereby for evoked synaptic transmission. In addition, our data clearly indicate, that in contrast to Stj^{RNAi}, motoneuronal knockdown of dα$_2$δ$_1$ did not reduce the EPSP amplitude measured in muscle in response to motoneurons stimulation. Furthermore, the number of Ca_V2^{GFP} puncta per bouton was unaltered. Thus, indicating that dα$_2$δ$_1$ is not needed for targeting Ca_V2 channels to presynaptic terminals. This is contrary to data from heterologous expression systems, in which co-expression of any α$_2$δ protein enhanced cell-surface expression of any HVA α$_1$ protein (reviewed by Dolphin, 2013). Thereby, our study highlights the need for *in vivo* studies to test for differential functions of different α$_1$- α$_2$δ combinations.

Yet data on Stj^{RNAi} and dα$_2$δ$_1^{RNAi}$ effects on normal synaptic transmission at axon terminals are partly inconclusive (as discussed below). In addition, previous studies in transhetero-

zygote Stj mutants further provide conflicting data of Stj effects on synaptic short-term plasticity (Ly *et al* 2008; Dickman *et al*., 2008; Wang *et al*., 2016). Please note, that most changes in evoked synaptic transmission depend on changes in the release probability of synaptic vesicles and the size of the readily releasable pool (RRP) (Hennig, 2013), both of which can be changed due to developmental defects. At the NMJ of *Drosophila* embryos, Stj was already found to be required for synaptogenesis of presynaptic boutons even before calcium channels locate there (Kurshan *et al*., 2009). Thus, most effects of Stj^{RNAi} and $d\alpha_2\delta_1^{RNAi}$ on synaptic transmission at the larval NMJ could be explained by changes in synaptogenesis. In addition, the release probability crucially depends on spatial apposition of readily releasable vesicles to calcium nanodomains (reviewed by Kittel & Heckmann, 2016). Therefore alterations in calcium channel density, function (channel conductance and activation/inactivation kinetics) and/or in localization of Ca_V2 channels relative to vesicles would lead to changes in the release probability. Consequently, we might have a mixture of developmental and acute, but also non-acute effects of $d\alpha_2\delta$ proteins on synaptic transmission at the larval NMJ. It would be necessary to dissect acute, non-acute and developmental functions of $\alpha_2\delta$ subunits *in vivo* in future studies.

With Ca_V2 being reduced at the NMJ of Stj^{RNAi} the release probability should be reduced. Therefore, we expected an increase in paired-pulse facilitation, but instead, PP facilitation was reduced in Stj^{RNAi}. So far conflicting data is available on changes in PP facilitation in Stj mutants (transheterozygote mutant combinations and hypomorphic Stj mutants/deficiency). In some studies, PP facilitation was indeed increased (Ly *et al*., 2008), while in other studies PP facilitation is reduced in transheterozygote Stj mutant larvae (Wang *et al*., 2016). Reduction in PP facilitation was explained by an impaired coupling of vesicles to Ca^{2+} nanodomains (Wang *et al*., 2016). Indeed, at the NMJ of *Drosophila* synaptic vesicles are tethered to Brp and thereby in close spatial apposition to Ca^{2+} nanodomains (Hallermann *et al*., 2010) and BRP puncta/bouton volume was reduced in Stj^{RNAi}. In Brp mutants (Brp^{nude}) lacking only the C-terminal part of the protein and thus the ability to tether vesicles to active zones (AZ), PP facilitation was indeed reduced (Hallermann *et al*., 2010). In contrast, Brp mutants lacking only one of the two main Brp isoforms tethering of synaptic vesicles to AZ was reduced, but PP facilitation was unaltered (Matkovic *et al*., 2013). Therefore it seems unlikely that a 20 % reduction in BRP puncta/bouton volume in Stj^{RNAi} already explains the reduction in PP facilitation. Brp is

further needed to cluster calcium channels and thus increase functional presynaptic calcium nanodomains (Eggermann *et al*., 2012; reviewed Kittel & Heckmann, 2016), but a reduced clustering of Ca_V2 channels would result in a decrease of calcium nanodomains, which should reduce the release probability and thus increase PP facilitation. The most likely explanation would be an additional reduction in the RRP size in Stj^{RNAi}. If only a few vesicles were available for synaptic transmission, residual calcium could not increase the number of released vesicles. Reduction in RRP size in Stj^{RNAi} is confirmed by a faster synaptic depression. Synaptic short-term depression is mainly caused by depletion of the RRP (Zucker & Regehr, 2002). Thus, the time-course of depression depends on the release probability and the number of available vesicles (Henning, 2013). Depression is faster in Stj knockdowns. Since the number of released vesicles per action potential was decreased in Stj^{RNAi}, this indicates a reduction in RRP size.

Also, the steady-state of depression was reduced in Stj^{RNAi}, which further hints at changes in synaptic vesicle recycling. This is in accord with qualitative analysis of the Ca_V1 signal at axon terminals, which might indicate a reduction of Ca_V1 channel density in Stj^{RNAi}. In previous studies, the Ca_V1 channel was found to play a role in vesicle endocytosis at the *Drosophila* larval NMJ (Klein, 2016). Alternatively, reduced synaptic vesicle recycling could also result from developmental defects. Effects of Stj^{RNAi} on synaptic depression mimic the phenotype of a relatively weak motoneuronal Ca_V2 knockdown. The steady-state amplitude of synaptic depression was reduced and the time constant τ increased in Ca_V2^{RNAi} (see appendix 6.12). Thus, the reduction of Ca_V2 density in synaptic boutons of Stj^{RNAi} could already lead to developmental defects and thus result in changes in short-term plasticity. Additional future studies will be needed to tease these different possibilities apart.

Reduction in Ca_V2^{GFP} puncta and potential reduction in Ca_V1 signal in Stj^{RNAi} could be due to defects in channel transport or targeting of the channels to axon terminals. Labeling of Ca_V1 still revealed axonal Ca_V1 signal in Stj^{RNAi}, thus a defect in targeting Ca_V channels to axon terminal membranes of the NMJ is more likely. This is in accord with previous studies, which found overexpressed UAS-Ca_V2^{GFP} in axons, but not in axon terminals of larval crawling motoneurons of hypomorphic Stj mutants/deficiency (Ly *et al*., 2008). Also, in vertebrate's overexpression of $\alpha_2\delta$ subunits was found to increase VGCC abundance in axon terminals and thereby increase synaptic transmission (Hoppa *et al*., 2012). Further-

more, pharmacological blocking of $\alpha_2\delta_2$ with chronic application of Gabapentin reduced cell-surface expression of both the $\alpha_2\delta$ and α_1 subunit in heterologous expression systems (Hendrich *et al*., 2008).

While Ca_V2 channel density at axon terminals and EPSP amplitude were unaltered in $d\alpha_2\delta_1^{RNAi}$, synaptic transmission was still affected. For example, EPSPs area normalized to amplitude was reduced in $d\alpha_2\delta_1^{RNAi}$, but not in Stj^{RNAi}. One possible explanation for a reduction in EPSP area/amplitude would be a decrease in asynchronous release: Three different types of transmitter release are described for chemical synapses: synchronous, asynchronous and spontaneous release (for review see Kaeser & Regehr, 2014). Synchronous release is fast (< 1 ms after stimuli). Due to tethering of synaptic vesicles to active zones, the synaptic vesicle protein synaptotagmin, which is believed to be the calcium sensor for synchronous release is in spatial apposition to calcium nanodomains. Thus, slow calcium chelators like EGTA have only minor effects on synchronous release. Asynchronous release is also calcium-dependent but the calcium sensor is not in spatial apposition to calcium channels of the active zone (for review see Kaeser & Regehr, 2014). Therefore, asynchronous release often results in a prolonged vesicle release after stimulation, which can be inhibited by slow calcium chelators like EGTA (Hagler & Goda, 2001). At the *Drosophila* NMJ asynchronous release was found to prolong EPSP even after a single stimulus (Bronk *et al*., 2005). The decrease in EPSP area/amplitude in $d\alpha_2\delta_1^{RNAi}$ could, therefore, be a result of a reduction in asynchronous release. Indeed, synchronous release is believed to contribute approx. 90 % to the EPSP area (Kaeser & Regehr, 2014) and EPSP area/amplitude was reduced in $d\alpha_2\delta_1^{RNAi}$ by approx. 15 %. Since synchronous, asynchronous but also spontaneous release are further believed to compete for vesicles from the same vesicle pool (RRP) (Xu *et al*., 2009; reviewed by Kaeser & Regehr, 2014), an increased spontaneous release of vesicles would reduce releasable vesicles available for synchronous and asynchronous release. Indeed, spontaneous release was increased by approx. 30 % in $d\alpha_2\delta_1^{RNAi}$. Another explanation for changes in EPSP area might be alterations in Ca_V2 activation and inactivation kinetics. For example, a faster inactivation of Ca_V2 due to loss of $d\alpha_2\delta_1$ could result in a reduction of EPSP area. This would be contrary to findings in heterologous expression systems, were expression of $\alpha_2\delta$ subunits was found to increase inactivation of HVA calcium channels (reviewed by Davies *et al*., 2007). Still, the reduction in PP facilitation in $d\alpha_2\delta_1^{RNAi}$ could also hint at a reduction in asynchro-

nous release or an increased inactivation of Ca_V2 channels, since both would reduce the prolonged release of synaptic vesicles after the action potential and thereby result in faster repolarization of the muscle. Due to this, the subsequent EPSP would start at more negative muscle potentials, which could reduce EPSP amplitude.

A reduction in PP facilitation, as well as an increase in spontaneous release, could further indicate an increased release probability. Furthermore, synaptic depression is faster in $d\alpha_2\delta_1^{RNAi}$ but steady-state was unchanged, thus further confirming an increase in release probability or a reduction of the RRP size. As discussed RRP size might be reduced by an increased spontaneous release of synaptic vesicles (see above). An increase in the release probability could be explained by: Firstly, an increase in calcium nanodomains by an increase in Ca_V channel density or clustering at axon terminals. Secondly, an increased amount of synaptic vesicles tethered to active zones and/or thirdly, an increase in calcium nanodomains by an increase in the single-channel conductance of Ca_V2. Ca_V2 density and also Brp density tended to be increased in $d\alpha_2\delta_1^{RNAi}$ but were found unaltered by statistical comparison to control. An increase in the RRP or in Ca_V2 density or clustering should result in an increased release of vesicles and thereby in increased EPSP amplitude in $d\alpha_2\delta_1^{RNAi}$ larvae. EPSP amplitudes tended to be but were not significantly increased. Furthermore, co-expression of $\alpha_2\delta$ proteins was found to increase Ca_V2 cell surface expression in heterologous expression systems (Barclay *et al*., 2001; Brodbeck *et al*., 2002). Therefore it seems unlikely that loss or reduction of $d\alpha_2\delta_1$ through RNAi knockdown should increase Ca_V2 density *in vivo*. Still, spontaneous release is also calcium-dependent and VGCC antagonists were found to reduce mPSP frequency at some synapses (Goswami *et al*., 2012; Williams *et al*., 2012). Therefore an increase in the spontaneous release could be explained by an increased amount of Ca_V channels at the axon terminal. One could argue that the resolution of confocal microscopy is not high enough to assess changes in calcium channel density at active zones. Thus, super-resolution microscopy (Ehmann *et al*., 2015) would have to be conducted to test for possible changes in the amount of Ca_V2 channels, but based on the current data the benefit-cost ratio would be too low. An increase in Ca_V2 single-channel conductance seems also unlikely since $\alpha_2\delta$ proteins were found to have little effect on the single-channel conductance, but rather on the surface expression of Ca_V channels (Barclay *et al*., 2001; Brodbeck *et al*., 2002).

In GABAergic neurons, presynaptic $\alpha_2\delta$ subunits were further found to regulate receptor clustering at the postsynaptic side (Geisler *et al*., 2019). Even though changes in postsynaptic receptor localization or clustering are unlikely since mPSP amplitudes were unchanged in both Stj and $d\alpha_2\delta_1$ knockdowns, one might want to test for possible changes in postsynaptic receptor clustering by confocal microscopy. Furthermore, especially the area of the EPSP highly depends on the opening of postsynaptic receptors but is also affected by the opening of postsynaptic Ca_V1 channels. Opening of postsynaptic Ca_V1 can be prevented, by conducting two-electrode voltage-clamp measurements. During two-electrode voltage-clamp measurements (TEVC) the membrane potential of the muscle will be clamped to -60 mV. Thus, Ca_V1 channels in the muscle which normally open at approx. -30 mV will not be able to open anymore. To further confirm the effects of Stj and $d\alpha_2\delta_1$ knockdown on synaptic transmission at the NMJ, TEVC measurements from muscle M10 should be performed.

4.3.2 Stj is required for normal somatodendritic current amplitudes of both Ca_V1 and Ca_V2 channels

$\alpha_2\delta$ subunits were found to increase the calcium current amplitude of HVA VGCCs (Singer *et al*., 1991; Felix *et al*., 1997; Klugbauer *et al*., 1999; Herlitze *et al*., 2003). Instead of modulating the single-channel conductance $\alpha_2\delta$ was found to increase the cell-surface expression of Ca_V channels (Barclay *et al*., 2001; Brodbeck *et al*., 2002). This is in accord with findings from *Drosophila* larval motoneurons were Stj is required for normal Ca_V2 density and thus for normal synaptic transmission at axon terminals (Dickman *et al*., 2008; Ly *et al*., 2008 and this study).

To probe for changes in somatodendritic calcium currents, we conducted voltage-clamp measurements from identified larval crawling, but also adult and pupal wing depressor motoneurons in targeted knockdowns of Stj and $d\alpha_2\delta_1$. Interestingly somatodendritic calcium current amplitudes were reduced in both larval and adult/pupal motoneurons in Stj^{RNAi} but not $d\alpha_2\delta_1{}^{RNAi}$. Thus, Stj seems to be required for normal somatodendritic calcium current amplitudes of motoneurons during all developmental stages. Furthermore, somatodendritic calcium currents in larval crawling neurons are mediate by Ca_V1 channels (Worrell & Levine, 2008; Kadas *et al*., 2017), while Ca_V2 channels mediate somatodendrit-

ic calcium currents in adult and pupal wing depressor neurons (Ryglewski *et al*., 2012). Accordingly, Stj interacts with all HVA VGCCs in *Drosophila*. This is in agreement with studies from heterologous expression systems, which indicate that all $\alpha_2\delta$ subunits are able to interact with all HVA α_1 proteins (reviewed by Campiglio *et al*., 2015). In contrast, in heterologous expression systems, all $\alpha_2\delta$ subunits were able to increase Ca^{2+} current amplitude of all Ca_V channel types (reviewed by Campiglio *et al*., 2015), but our results suggest that $d\alpha_2\delta_1$ does not affect either Ca_V1 or Ca_V2 somatodendritic calcium current amplitudes as measured from the somata *in vivo*. Furthermore, neither Stj nor $d\alpha_2\delta_1$ were found to modulate the voltage dependence of HVA channel activation, as described for co-expression of $\alpha_2\delta$ and α_1 proteins in heterologous expression systems (Felix *et al*., 1997; Platano *et al*., 2000). This highlights the importance of *in vivo* studies to probe for differential functions of different $\alpha_2\delta$-α_1 combinations.

The reduction of dendritic calcium currents in Stj^{RNAi} was further confirmed by calcium imaging from pupal MN5 neurons. Still, somatic patch-clamp recordings and calcium imaging cannot distinguish whether Stj is required for correct cell-surface expression, targeting or normal single-channel conductance of Ca_V1 or Ca_V2. We propose a reduction in cell-surface expression of somatic and dendritic HVA Ca_V channels in Stj^{RNAi}, as already described for heterologous expression systems (Barclay *et al*., 2001; Brodbeck *et al*., 2002), DRG neurons in mice (Cassidy *et al*., 2014; Nieto-Rostro *et al*., 2018) and for the *Drosophila* larval NMJ (Ly *et al*., 2008; this study). To further test for potential effects on single-channel conductance one would need to conduct recordings from single calcium channels in controls and following Stj^{RNAi}.

4.3.3 Both Stj and $d\alpha_2\delta_1$ are needed for normal axonal calcium channel function in adult flight motoneurons but have opposite effects

Since calcium channels also have axonal functions, we tested for changes in axonal calcium channel abundance following Stj^{RNAi} or $d\alpha_2\delta_1^{RNAi}$. We find that axonal abundance of functional Ca_V2 channels is increased in $d\alpha_2\delta_1^{RNAi}$, but reduced in Stj^{RNAi}. Thereby we show that Stj^{RNAi} and $d\alpha_2\delta_1^{RNAi}$ have opposite effects on axonal Ca_V channel abundance, which again indicates functional differences between those two $d\alpha_2\delta$ proteins in the same neuron. This further reveals that Stj is needed for normal function of HVA calcium channels in

all subcellular compartments (soma, axons, dendrites, and axon terminals) of *Drosophila* motoneurons *in vivo*.

To test for changes in axonal Ca_V2 abundance we analyzed the axonal Ca_V2^{GFP} signal in adult MN1-5 neurons. We found GFP-clusters in the axons of controls, which were even more pronounced in $d\alpha_2\delta_1^{RNAi}$. By contrast, GFP-clusters were reduced and sometimes even absent following Stj^{RNAi}. Our findings further indicate that the increase in Ca_V2^{GFP} signal in $d\alpha_2\delta_1^{RNAi}$, as well as the decrease of Ca_V2^{GFP} signal in Stj^{RNAi}, was due to changes in the density of functional calcium channels in the axonal membrane. Calcium imaging experiments from axons revealed a reduction of activity-dependent calcium influx in Stj^{R-NAi} compared to control, while axonal calcium influx was increased in $d\alpha_2\delta_1^{RNAi}$. In addition, while the action potential (AP) half amplitude width was increased in P8 controls due to a calcium component, the AP width was significantly reduced in Stj^{RNAi}. An increased calcium component of pupal APs in $d\alpha_2\delta_1^{RNAi}$ even induced double peak events in 50 % of the measurements. Blocking VGCCs with cadmium reduced AP half amplitude width in control and $d\alpha_2\delta_1^{RNAi}$, but not in Stj^{RNAi}, which further confirmed that changes in AP width were indeed due to changes in axonal calcium channel density. This is in accord with studies in mouse sensory neurons, which show that changes in axonal VGCC calcium currents are caused by the loss of the respective $\alpha_2\delta$ subunit (Margas *et al*., 2016).

4.3.4 $d\alpha_2\delta_1$ is specifically required for correct dendritic Ca_V2 channel density in adult wing depressor neurons

While Stj is required for normal somatodendritic and axonal calcium current amplitudes, $d\alpha_2\delta_1$ is not. Instead, we find a clear shift in the dendritic versus the axonal calcium channel density in $d\alpha_2\delta_1^{RNAi}$. We, therefore, propose that $d\alpha_2\delta_1$ is required for correct allocation of Ca_V channels specifically to dendrites in *Drosophila* motoneurons, while Stj seems to be required for normal Ca_V function in all subcellular compartments. Thus, our data indicate a division of labor between different $d\alpha_2\delta$ proteins in the same neuron and thereby provide novel insights into functional VGCC diversity.

Somatodendritic calcium currents were unchanged in $d\alpha_2\delta_1^{RNAi}$ compared to control. We, therefore, expected no changes in dendritic calcium channel density. In contrast, calcium imaging from dendrites of MN5 neurons revealed a reduction in voltage-activated Ca^{2+}

influx in $d\alpha_2\delta_1^{RNAi}$. The reduction of dendritic calcium currents in $d\alpha_2\delta_1^{RNAi}$ was confirmed in two independent sets of calcium imaging experiments (see Fig.21 & appendix 6.13). It was further confirmed by the finding that the total dendritic length of MN5 was reduced in both $d\alpha_2\delta_1^{RNAi}$ and Stj^{RNAi}, as already described for a direct knockdown of the Ca_V2 channel (Ryglewski *et al.*, 2014).

Since patch-clamp measurements were done from the soma of MN5, we were only able to record the sum of somatic and dendritic calcium currents. Thus, if $d\alpha_2\delta_1^{RNAi}$ would result in shifts in the relative calcium channel localization to the soma but away from dendrites, we would not be able to detect them.

Our findings suggest a shift in functional Ca_V2 channel localization. While dendritic Ca_V2 abundance was reduced in $d\alpha_2\delta_1^{RNAi}$, we have an increased Ca_V2 channel density in axons. $\alpha_2\delta$ subunits were found to be involved in trafficking and sorting of α_1, but the exact underlying mechanism remains unknown. Previous studies from heterologous expression systems suggest $\alpha_2\delta$ subunits to bind to α_1 in the endoplasmatic reticulum via the metal ion-dependent adhesion site (MIDAS) of the Von-Willebrand factor A (VWA) domain (Canti *et al.*, 2005; Hendrich *et al.*, 2008). The α_1- $\alpha_2\delta$ complex is then transported via adaptor proteins (Macabuag & Dolphin, 2015). Therefore, we suggest $d\alpha_2\delta_1$ to specifically target Ca_V2 channels to dendrites in MN5 neurons. Assuming a predefined production of Ca_V2 channels in MN5, a decrease in Ca_V2 trafficking to dendrites could increase the availability of Ca_V2 channels for transport to other subcellular compartments. Thus, explaining a possible increase in somatic Ca_V2 channels and the increased abundance of Ca_V2 in axons.

Since Stj seems to have a defined function in motoneurons independent of the HVA Ca_V type or the developmental stage (see above), one could assume that $d\alpha_2\delta_1$ function is also preserved in motoneurons. Thus, a possible increase in Ca_V2 channel density at the NMJ of larval crawling motoneurons (see above) might also result from shifts in calcium channel localization following $d\alpha_2\delta_1^{RNAi}$.

4.4 Both Stj and dα$_2$δ$_1$ might be required for equal distribution of excitatory vs inhibitory dendritic input domains of adult flight motoneurons

α$_2$δ subunits are further known to play important roles in synaptogenesis. As the postsynaptic receptor for thrombospondin α$_2$δ$_1$ was found to promote the formation of excitatory synapses in heterologous expression systems and mouse cortex (Eroglu *et al*., 2009; Risher *et al*., 2018). Loss of function of specific α$_2$δ subunits can, therefore, result in an imbalance of excitatory-inhibitory input in neurons. At the NMJ of *Drosophila* embryos, Stj was already found to be required for synaptogenesis of presynaptic boutons even before calcium channels locate there (Kurshan *et al*., 2009).

In MN5 motoneuron excitatory and inhibitory postsynaptic input domains compete for dendritic building material during development. Thus, the ratio of the dendritic length of the excitatory (cholinergic/proximal) input domains vs the inhibitory (GABAergic/distal) input domains is approx. 1:1 in the control situation (Kuehn & Duch, 2013; Ryglewski *et al*., 2017). If the loss of either Stj or dα$_2$δ$_1$ would lead to a decrease in excitatory input, one would expect an increase in dendritic length for the inhibitory input domains. Indeed, dα$_2$δ$_1^{RNAi}$ seemed to shift the ratio towards the distal side, indicating an impaired development of excitatory synaptic input sites. Also, in Stj^{RNAi} the ratio might be shifted toward the distal side, but variation in the data was high. Since both Stj^{RNAi} and dα$_2$δ$_1^{RNAi}$ additionally reduced the total dendritic length as well as the branch number of MN5 analyzing the ratio between the proximal/distal dendritic length was rather difficult. Thus, the number of replicates should be increased especially for control and Stj^{RNAi}. Furthermore, one could label excitatory input domains with anti-Dα7 nAChR antibodies and inhibitory input domains by labeling the Rdl GABA$_A$ receptor. Changes in anti-Dα7 nAChR and anti-Rdl GABA$_A$ signal intensities could be assessed in GFP labeled MN1-5 neurons, in flies expressing either Stj^{RNAi} or dα$_2$δ$_1^{RNAi}$ and the respective control. Blocking α$_2$δ$_1$ by chronic application of gabapentin was further found to reduce synapse formation *in vitro* and *in vivo* (Eroglu *et al*., 2009). Since gabapentin might be functional in *Drosophila* (Streit *et al*., 2016; this study) feeding gabapentin to adult flies might also reduce excitatory synaptic input domains of neurons. Changes in excitatory input could be assessed by calcium imaging of MN5 dendrites upon activation by nicotine puffs in control and Stj^{RNAi} or dα$_2$δ$_1^{RNAi}$.

In mammals, α$_2$δ$_1$ expression seems to correlate with excitatory neurons, while expression of α$_2$δ$_2$ correlates with inhibitory neurons (Cole *et al*., 2005). In contrast, in *Drosophi-*

la both loss of Stj and $d\alpha_2\delta_1$ seems to affect excitatory input domains. Thus, it would be interesting to assess the function of $d\alpha_2\delta_2$ for the normal development of MN5 dendritic input domains. Previous studies found that while postsynaptic $\alpha_2\delta_1$ is needed to induce synaptogenesis in excitatory neurons (Eroglu *et al*., 2009), $\alpha_2\delta_2$ is required presynaptically for a correct density of postsynaptic GABA receptors (Geisler *et al*., 2019). Thus, to affect inhibitory input domains a knockdown in neurons presynaptic to MN1-5 may be required.

4.5 Gabapentin might reduce the excitability of larval crawling MNs and muscles by acutely blocking Stj

Elevated activity of neuronal networks is known to play a crucial role in epilepsy and neuropathic pain. Thus, potential anticonvulsants are believed to act by enhancing inhibitory processes by affecting GABA-metabolism, by reducing excitatory synaptic transmission of glutamatergic neurons, or by reducing neuronal excitability through modulation of ion channels in the membrane (reviewed by Upton, 1994). Gabapentin has been widely used in treating epilepsy and neuropathic pain for over 30 years. Yet its mechanisms of action are incompletely understood. Although gabapentin was synthesized as an analog of GABA, it does not affect GABA-metabolism but rather binds to $\alpha_2\delta$ subunits ($\alpha_2\delta_1$ and $\alpha_2\delta_2$) of VGCC (Marais *et al*., 2001). One proposed mode of action is a decreased formation of new excitatory synapses by gabapentin blocking the interaction of the vertebrate $\alpha_2\delta_1$ subunit with thrombospondin (Eroglu *et al*., 2009). Furthermore, chronic application of gabapentin (for 40 h) was found to reduce cell surface expression of HVA Ca_V channels and thereby calcium current amplitudes, through inhibition of $\alpha_2\delta$-Ca_V interactions. Nevertheless, due to its relatively rapid onset of action especially in neuropathic pain animal models (~30 min after injection; Alles *et al*., 2017) gabapentin solely acting on synaptogenesis or cell surface expression of Ca_V channels seems unlikely. Recently gabapentin was found to reduce synaptic transmission in glutamatergic neurons by blocking $\alpha_2\delta_1$-NMDAR interaction and thereby decreasing pre- and postsynaptic NMDAR activity 30 min after injection (Chen *et al*., 2018). Even though data on acute effects of gabapentin on VGCC calcium current amplitudes are controversial, gabapentin might also

acutely reduce single-channel conductance of VGCC by binding to $\alpha_2\delta$ (Stefani *et al*., 1998, 2001; Fink *et al*., 2000; Rock *et al*., 1993; Schumacher *et al*., 1998).

Due to its relative simplicity and its genetic power, *Drosophila melanogaster* might be a useful model system to study the molecular mechanism underlying the action of gabapentin, but the target binding site for gabapentin is unknown in *Drosophila*.

Our data show that application of gabapentin reduces the firing frequency of larval crawling motoneurons *in vivo* after only 5 min. In addition, we found that even though gabapentin has an acute effect on the firing frequency of larval crawling neurons, it has no acute effects on the axon terminal, but rather reduces synaptic transmission by affecting the muscle. We were further able to identify Stj as the potential target binding site for gabapentin in *Drosophila* since: (1) Gabapentin does not reduce the firing frequency in Stj^{RNAi} during currents clamp measurements of larval crawling motoneurons. (2) Expression of Stj^{RNAi} mimics the effects of gabapentin on the firing frequency in control. (3) Gabapentin seems to still reduce the firing frequency in $d\alpha_2\delta_1^{RNAi}$.

In contrast, gabapentin was found to block $\alpha_2\delta_1$ and $\alpha_2\delta_2$ in vertebrates. Still, the different *Drosophila* $d\alpha_2\delta$ subunits do not correspondent in a 1:1 fashion to the different vertebrate $\alpha_2\delta$ subunits. Both Stj and $d\alpha_2\delta_1$ also possess a VWA domain containing a MIDAS motif, as well as cache domains. Otherwise, sequence homology is not high enough to associate $d\alpha_2\delta$ subunits with one specific vertebrate $\alpha_2\delta$. For example, $d\alpha_2\delta_3$ sequence is only 33 % identical to human $\alpha_2\delta_3$ (Ly *et al*., 2008). From our findings and previous studies, Stj seems to functionally correspond to mammalian $\alpha_2\delta_1$ (see above). Thus, it is likely that gabapentin blocks Stj instead of $d\alpha_2\delta_1$ in *Drosophila*. To further test this, we washed in gabapentin at the *Drosophila* larval NMJ and tested for changes in EPSP amplitude, by recording the muscle and stimulating the respective nerve. Gabapentin indeed reduced EPSP amplitude, but this effect was found to be rather postsynaptic than presynaptic since the effect was gone in TEVC measurements. Thus, gabapentin seems to have no acute effect on synaptic transmission at presynaptic axon terminals. This finding further indicates that Stj might have no acute presynaptic function in synaptic transmission at the larval NMJ. Therefore, reduction of EPSP amplitude in Stj^{RNAi} is probably not due to changes in single-channel conductance or kinetics of Ca_V channels but rather in the cell surface expression of Ca_V2 or defects in synaptogenesis. This is in accord with previous studies which suggest that Stj is needed for correct targeting of Ca_V2 (Dickman *et al*.,

2008; Ly *et al*., 2008; this study) and normal synaptogenesis (Kurshan *et al*., 2009) at *Drosophila* NMJ. In heterologous expression systems, only chronic application of gabapentin (for 40 h) disrupted cell-surface expression of both $\alpha_2\delta_1/\alpha_2\delta_2$ and Ca_V2 (Hendrich *et al*., 2008). One might want to try feeding gabapentin to larvae from larval stage L1 on and test for changes in EPSP amplitude and Ca_V2 cell surface expression in L3, to dissect apart the different possibilities.

Still, Stj seems to have an acute axonal function in larval crawling motoneurons. Since, Ca_V1^{RNAi} only seemed to partly mimic the gabapentin effect in control, the effect of gabapentin might not solely or not at all depend on inhibition of Ca_V1-Stj interactions. This could be further assessed by imaging the activity-dependent calcium influx in RP2 axons before and after application of gabapentin through the expression of GCamp. Thereby, our findings might further hint at an additional interaction partner for Stj in the axon, maybe even independent from VGCC. This is in agreement with studies, in which $\alpha_2\delta$ subunits were found to be only loosely associated with α_1 at the cell membrane (Voigt *et al*., 2016). Furthermore, recently novel interaction partners of $\alpha_2\delta$ subunits independent from VGCC were found (Eroglu *et al*., 2009; Chen *et al*., 2018; Zhang *et al*., 2018; Zhou *et al*., 2018). Additional experiments will be needed to investigate the molecular mechanism underlying the action of gabapentin.

4.6 Conclusion

Even though $\alpha_2\delta$ proteins seem to have largely tissue and cell-specific expression patterns in vertebrates (Cole *et al*., 2005; Huang *et al*., 2013; Müller *et al*., 2013, 2015) expression was mostly investigated by *in situ* hybridization studies or with quantitative real-time PCR of selected cell-types (Fell *et al*., 2016). With the genetic power of *Drosophila*, we are the first to investigate for differential expression of two different $\alpha_2\delta$ subunits on the protein level and *in vivo* by using flies with endogenously tagged Stj and $d\alpha_2\delta_1$. Thereby we found that in *Drosophila* CNS both Stj and $d\alpha_2\delta_1$ are co-expressed in many neurons, including well-identified motoneurons, but might predominantly localize to different subcellular compartments. This finding indicates different functions of Stj and $d\alpha_2\delta_1$ in the *Drosophila* CNS. To test for differential and redundant functions of Stj and $d\alpha_2\delta_1$ we employed elec-

tro- and optophysiological methods in motoneurons with well-characterized Ca_V1 and Ca_V2 functions and subneuronal localizations. Targeted expression of validated Stj or $d\alpha_2\delta_1$ knockdowns or double-knockdowns of both indeed revealed that Stj and $d\alpha_2\delta_1$ exert fundamentally different effects on VGCC function and localization and are not able to functionally compensate for each other in those neurons. We find that Stj interacts with both Ca_V1 and Ca_V2 channels. At the larval NMJ Stj is required for normal synaptic transmission by targeting Ca_V2 channels to axon terminals. Stj is further crucial for normal somatodendritic Ca_V1 and Ca_V2 current amplitudes in motoneurons, independent of the developmental stage. In addition, Stj is required for normal Ca_V2 calcium current amplitudes in axons and thereby affects neuronal excitability and action potential shape. In contrast, $d\alpha_2\delta_1$ is neither required for normal somatodendritic Ca_V1 and Ca_V2 calcium current amplitudes nor for targeting Ca_V2 channels to axon terminals. Instead, $d\alpha_2\delta_1$ is crucial for correct targeting of Ca_V2 channels to dendrites in adult wing depressor motoneurons. Thus, our data demonstrate a division of labor between different $d\alpha_2\delta$ subunits in regulating distinctly different aspects of Ca_V1 and Ca_V2 channel function in the same motoneurons (Fig. 49) and thereby provide novel insights into functional VGCC diversity. This contrasts data from heterologous expression systems where redundant functions have been reported, but is in accord with specific $\alpha_2\delta$ mutations causing different human brain diseases.

While Stj and $d\alpha_2\delta_1$ are not able to functionally compensate for each other in *Drosophila* neurons, we find that both Stj and $d\alpha_2\delta_1$ mediate at least partially redundant functions, or operate in concert to mediate a vital function in muscles. Therefore, full functional diversity of $\alpha_2\delta$-α_1 interactions may unfold only in the CNS. This further provides an explanation for controversial data from heterologous expression systems, in which all $\alpha_2\delta$ subunits were able to modulate all HVA α_1 proteins. Thereby this study highlights the need for *in vivo* studies to understand the combinatorial code underlying $\alpha_2\delta$-α_1 interactions in regulating VGCC functional diversity. Our findings further start unraveling how different α_1-$\alpha_2\delta$ combinations regulate functional calcium channel diversity in different subneuronal compartments, and may provide an entry point toward understanding how mutations of different $\alpha_2\delta$ genes underlie brain diseases.

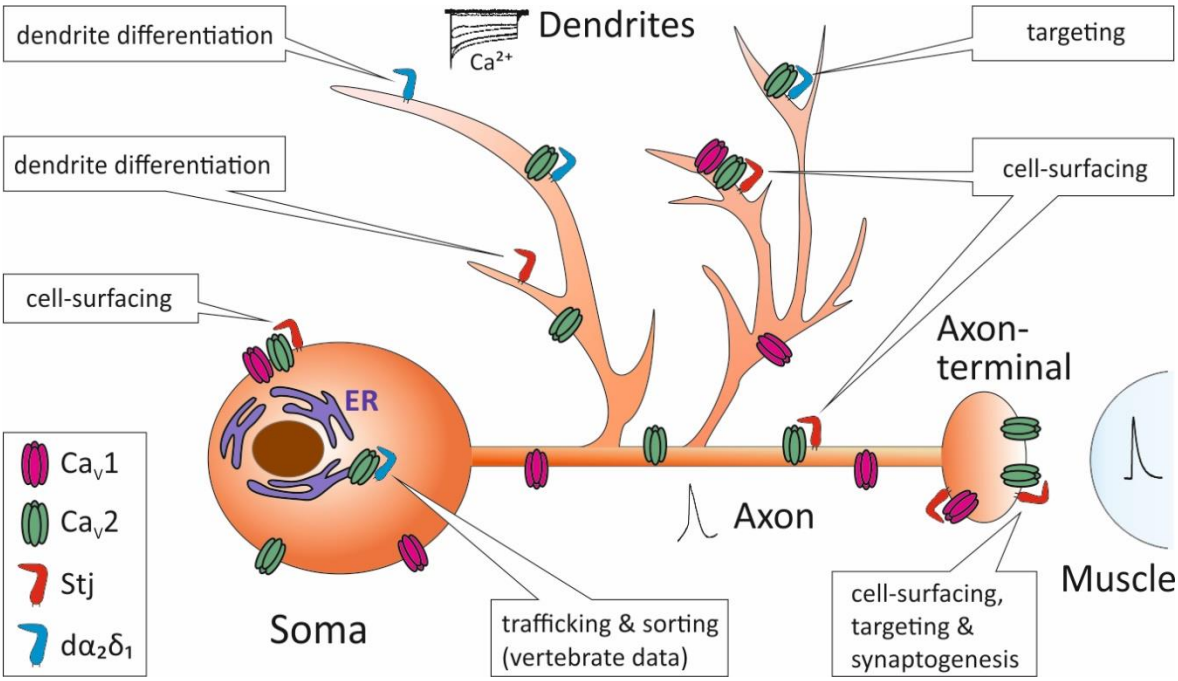

Fig.49: Division of labor between different dα$_2$δ subunits in motoneurons of *Drosophila melanogaster*

Schematic representation of how division of labor between dα$_2$δ$_1$ and dα$_2$δ$_3$ (Stj; straightjacket) potentially regulates distinctly different aspects of Ca$_V$1 and Ca$_V$2 channel function in *Drosophila* motoneurons. Stj (red) is required for normal function of Ca$_V$ channels in all subcellular compartments (soma, dendrites, axon & axon terminal). Thereby, Stj interacts with both Ca$_V$1 (pink) and Ca$_V$2 (green) channels. Stj potentially increases cell surface expression [as already described for heterologous expression systems (Barclay *et al*., 2001; Brodbeck *et al*., 2002), DRG neurons in mice (Cassidy *et al*., 2014; Nieto-Rostro *et al*., 2018) and for the *Drosophila* larval NMJ (Ly *et al*., 2008)] of somatodendritic and axonal Ca$_V$ channels and is consequently required for normal somatodendritic and axonal calcium current amplitudes. Thereby Stj affects neuronal excitability and normal action potential shape. Stj is further essential for targeting of Ca$_V$2 channels to axon terminals and thereby for normal synaptic transmission but was also found to play a role in synaptogenesis independent of its interaction with VGCC (Kurshan *et al*., 2009). In contrast, dα$_2$δ$_1$ (blue) is not required for normal somatodendritic calcium current amplitudes, surfacing of axonal Ca$_V$ channels or targeting of Ca$_V$2 channels to axon terminals, but for correct allocation of Ca$_V$2 channels to dendrites. dα$_2$δ$_1$ might bind to Ca$_V$2 in the endoplasmatic reticulum (ER, purple) and initiate trafficking and sorting of Ca$_V$2 channels as already described for α$_2$δ proteins in vertebrates (Canti *et al*., 2005; Hendrich *et al*., 2008). In addition, both Stj and dα$_2$δ$_1$ play a role in dendrite differentiation of *Drosophila* motoneurons.

5. Literature

Abbott, L. F., & Regehr, W. G. (2004). Synaptic computation. *Nature*, *431*, 796–803.

Adelman, J. P., Bond, C. T., & Mayliet, J. (1995). Episodic ataxia results from voltage-dependent potassium channels with altered functions. *Neuron*, *15*(6), 1449–1454. https://doi.org/10.1016/0896-6273(95)90022-5

Akerboom, J., Chen, T., Wardill, T. J., Tian, L., Marvin, J. S., Esposti, F., … Looger, L. L. (2012). Optimization of a GCaMP calcium indicator for neural activity imaging. *J Neurosci*, *32*(40), 13819–13840. https://doi.org/10.1523/JNEUROSCI.2601-12.2012

Akerboom, J., Ve, J. D., Guilbe, M. M. R., Malave, E. C. A., Hernandez, H. H., Tian, L., … Schreiter, E. R. (2009). Crystal structures of the GCaMP calcium sensor reveal the mechanism of fluorescence signal change and aid rational design. *J Biol Chem*, *284*(10), 6455–6464. https://doi.org/10.1074/jbc.M807657200

Alles, S. R. A., Bandet, M. V, Eppler, K., Noh, M., Winship, I. R., Baker, G., … Smith, P. A. (2017). Acute anti-allodynic action of gabapentin in dorsal horn and primary somatosensory cortex : Correlation of behavioural and physiological data. *Neuropharmacol*, *113*, 576–590. https://doi.org/10.1016/j.neuropharm.2016.11.011

Andrews, C. O., & Fischer, J. H. (1994). Gabapentin: A new agent for the management of epilepsy. *Ann Pharmacother*, *28*(10), 1188–1196. https://doi.org/https://doi.org/10.1177/106002809402801011

Backonja, M., Beydoun, A., & Edwards, K. R. (1998). Gabapentin for the symptomatic treatment of painful neuropathy in patients with diabetes mellitus a randomized controlled trial. *J Am Med Assoc*, *280*(21), 1831–1836.

Bainbridge, B. S. P., & Bownes, M. (1981). Staging the metamorphosis of Drosophila melanogaster. *Development*, *66*, 57–80.

Barclay, J., Balaguero, N., Mione, M., Ackerman, S. L., Letts, V. A., Brodbeck, J., … Rees, M. (2001). Ducky mouse phenotype of epilepsy and ataxia is associated with mutations in the Cacna2d2 gene and decreased calcium channel current in cerebellar purkinje cells. *J Neurosci*, *21*(16), 6095–6104.

Bauer, C. S., Nieto-Rostro, M., Rahman, W., Tran-van-minh, A., Ferron, L., Douglas, L., … Dolphin, A. C. (2009). The increased trafficking of the calcium channel subunit α2δ-1 to presynaptic terminals in neuropathic pain is inhibited by the α2δ ligand pregabalin. *J Neurosci*, *29*(13), 4076–4088. https://doi.org/10.1523/JNEUROSCI.0356-09.2009

Berridge, M. J., Bootman, M. D., & Lipp, P. (1998). Calcium – a life and death signal. *Nature*, *395*, 645–648.

Bódi, J., Nishio, H., Zhou, Y., Kimura, T., & Sakakibara, S. (1995). Synthesis of an O-palmitoylated 44-residue peptide amide (PLTX II) blocking presynaptic calcium channels in Drosophila. *Peptide Research*, *8*(4).

Borst, J. G. G., & Sakmann, B. (1996). Calcium influx and transmitter release at a fast CNS synapse. *Nature*, *383*, 431–434.

Bossing, T., & Technau, G. M. (1994). The fate of the CNS midline progenitors in Drosophila as revealed by a new method for single cell labelling. *Development*, *120*(7), 1895–1906.

Brandt, A., Khimich, D., & Moser, T. (2005). Few CaV 1.3 channels regulate the exocytosis of a synaptic vesicle at the hair cell ribbon synapse. *J Neurosci*, *25*(50), 11577–11585. https://doi.org/10.1523/JNEUROSCI.3411-05.2005

Brockhaus, X. J., Schreitmu, M., Repetto, D., Klatt, O., Reissner, X., Elmslie, X. K., … Missler, X. M. (2018). α-Neurexins together with α2δ1 auxiliary subunits regulate Ca2+ influx through CaV2.1 channels. *J Neurosci*, *38*(38), 8277–8294. https://doi.org/10.1523/JNEUROSCI.0511-18.2018

Brodbeck, J., Davies, A., Courtney, J. M., Meir, A., Balaguero, N., Canti, C., … Dolphin, A. C. (2002). The ducky mutation in Cacna2d2 results in altered Purkinje cell morphology and is associated with the expression of a truncated α2δ-2 protein with abnormal function. *J Biol Chem*, *277*(10), 7684–7693. https://doi.org/10.1074/jbc.M109404200

Bronk, P., Nie, Z., Klose, M. K., Dawson-scully, K., Zhang, J., Robertson, R. M., … Zinsmaier, K. E. (2005). The multiple functions of cysteine-string protein analyzed at Drosophila nerve terminals. *J Neurosci*, *25*(9), 2204–2214. https://doi.org/10.1523/JNEUROSCI.3610-04.2005

Cain, S. M., & Snutch, T. P. (2010). Contributions of T-type calcium channel isoforms to neuronal firing. *Channels*, *4*(6), 475–482. https://doi.org/10.4161/chan.4.6.14106

Campiglio, M., & Flucher, B. E. (2015). The Role of Auxiliary Subunits for the Functional Diversity of Voltage-Gated Calcium Channels. *J Cell Physiol*, *230*(9), 2019–2031. https://doi.org/10.1002/jcp.24998

Canti, C., Davies, A., Berrow, N. S., Butcher, A. J., Page, K. M., & Dolphin, A. C. (2001). Evidence for two concentration-dependent processes for β-Subunit effects on α1B calcium channels. *Biophys J*, *81*(3), 1439–1451. https://doi.org/10.1016/S0006-3495(01)75799-2

Cantí, C., Nieto-Rostro, M., Foucault, I., Heblich, F., Wratten, J., Richards, M. W., … Dolphin, a C. (2005). The metal-ion-dependent adhesion site in the Von Willebrand factor-A domain of alpha2delta subunits is key to trafficking voltage-gated Ca2+ channels. *PNAS USA*, *102*(32), 11230–11235. https://doi.org/10.1073/pnas.0504183102

Cassidy, J. S., Ferron, L., Kadurin, I., Pratt, W. S., & Dolphin, A. C. (2014). Functional exofacially tagged N-type calcium channels elucidate the interaction with auxiliary α2δ-1 subunits.pdf. *PNAS*, *111*(24), 8979–8984.

Catterall, W. a. (2000). S Tructure and R Egulation of. *Annu Rev Cell Dev Biol*, *16*(521), 555.

Catterall, W. A. (1991). Excitation-contraction coupling in vertebrate skeletal muscle: A tale of two calcium channels. *Cell*, *64*, 871–874.

Catterall, W. A. (2011). Voltage-gated calcium channels. *Cold Spring Harb Perspect Biol*, *3*(8), 1–23. https://doi.org/10.1101/cshperspect.a003947

Chen, J., Li, L., Chen, S., Zhou, M., Chen, J., Li, L., … Maclean, D. M. (2018). The α2δ-1-NMDA receptor complex is critically involved in neuropathic pain development and gabapentin therapeutic actions. *Cell Reports*, *22*(9), 2307–2321. https://doi.org/10.1016/j.celrep.2018.02.021

Chevalier, M., Lory, P., Mironneau, C., & Macrez, N. (2006). T-type Ca v 3 . 3 calcium channels produce spontaneous low-threshold action potentials and intracellular calcium oscillations. *Eur J Neurosci*, *23*(9), 2321–2329. https://doi.org/10.1111/j.1460-9568.2006.04761.x

Coggshall, J. C. (1978). Neurons associated with the dorsal longitudinal flight muscles of Drosophila melanogaster. *J Comp Neurol*, *177*(4), 707–720.

Cole, R. L., Lechner, S. M., Williams, M. E., Prodanovich, P. A. T., Bleicher, L. E. O., Varney, M. A., & Gu, G. (2005). Differential distribution of voltage- gated calcium channel alpha-2 delta (α2δ) subunit mRNA-containing cells in the rat central nervous system and the dorsal root ganglia. *J Comp Neurol*, *491*, 246–269. https://doi.org/10.1002/cne.20693

Consoulas, C., Restifo, L. L., & Levine, R. B. (2002). Dendritic remodeling and growth of motoneurons during metamorphosis of Drosophila melanogaster. *J Neurosci*, *22*(12), 4906–4917.

Contreras, D. (2006). The role of T-channels in the generation of thalamocortical rhythms. *CNS Neurol Disord Drug Targets*, *5*(6), 871–885. https://doi.org/https://doi.org/10.2174/187152706779025562

Davies, A., Douglas, L., Hendrich, J., Wratten, J., Minh, A. T. Van, Foucault, I., … Dolphin, A. C. (2006). The calcium channel α2δ-2 subunit partitions with CaV2.1 into lipid rafts in cerebellum: Implications for localization and function. *J Neurosci*, *26*(34), 8748–8757. https://doi.org/10.1523/JNEUROSCI.2764-06.2006

Davies, A., Kadurin, I., Alvarez-Laviada, A., Douglas, L., Nieto-Rostro, M., Bauer, C. S., … Dolphin, A. C. (2010). The α2δ subunits of voltage-gated calcium channels form GPI-anchored proteins, a posttranslational modification essential for function. *PNAS*, *107*(4), 1654–1659. https://doi.org/10.1073/pnas.0908735107

Destexhe, A., & Sejnowski, T. J. (2003). Interactions between membrane conductances underlying thalamocortical slow-wave oscillations. *Physiol Rev*, *83*(4), 1401–1453.

Dickman, D. K., Kurshan, P. T., & Schwarz, T. L. (2008). Mutations in a Drosophila α2δ voltage-gated calcium channel subunit reveal a crucial synaptic function. *J Neurosci*, *28*(1), 31–38. https://doi.org/10.1523/JNEUROSCI.4498-07.2008

Dolmetsch, R. E., Lewis, R. S., Goodnowt, C. C., & Healyt, J. I. (1997). Differential activation of transcription factors induced by Ca2+ response amplitude and duration. *Letters of Nature*, *386*, 855–858.

Dolphin, A. C. (2012). Calcium channel auxiliary α2δ and β subunits: trafficking and one step beyond. *Nat Rev Neurosci*, *13*(9), 664–664. https://doi.org/10.1038/nrn3317

Dolphin, A. C. (2013). The α2δ subunits of voltage-gated calcium channels. *Biochim Biophys Acta - Biomembranes*, *1828*(7), 1541–1549. https://doi.org/10.1016/j.bbamem.2012.11.019

Dolphin, A. C. (2018). Voltage-gated calcium channel α2δ subunits : an assessment of proposed novel roles. *F1000Research*, *7*, 1–14.

Duch, C., Vonhoff, F., & Ryglewski, S. (2008). Dendrite elongation and dendritic branching are affected separately by different forms of intrinsic motoneuron excitability. *J Neurophysiol*, *100*(5), 2525–2536. https://doi.org/10.1152/jn.90758.2008

Dunlap, K., Luebke, J. I., & Turner, T. J. (1995). Exocytotic Ca2+ channels in mammalian central neurons. *Trends Neurosci*, *18*(2), 89–98.

Dworakowska, B., & Dolowy, K. (2000). Ion channels-related diseases *. *Acta Biochim Pol*, *47*(3), 685–703.

Eggermann, E., Bucurenciu, I., Goswami, S. P., & Jonas, P. (2012). Nanodomain coupling between Ca2+ channels and sensors of exocytosis at fast mammalian synapses. *Nature Rev*, *13*, 7–21. https://doi.org/10.1038/nrn3125

Ehmann, N., Sauer, M., & Kittel, R. J. (2015). Quantitative super-resolution imaging of Bruchpilot distinguishes active zone states. *Front Cell Neurosci*, *9*(7), 1–8. https://doi.org/10.3389/fncel.2015.00007

El-brolosy, M. A., & Stainier, D. Y. R. (2017). Genetic compensation : A phenomenon in search of mechanisms. *PloS Genetics*, *13*, 1–17. https://doi.org/https://doi.org/10.1371/journal.pgen.1006780

Eroglu, Ç., Allen, N. J., Susman, M. W., O'Rourke, N. A., Park, C. Y., Özkan, E., … Barres, B. A. (2009). Gabapentin receptor α2δ-1 is a neuronal thrombospondin receptor responsible for excitatory CNS synaptogenesis. *Cell*, *139*(2), 380–392. https://doi.org/10.1016/j.cell.2009.09.025

Evers, J. F., Schmitt, S., Sibila, M., & Duch, C. (2005). Progress in functional neuroanatomy : precise automatic geometric reconstruction of neuronal morphology from confocal image stacks. *J Neurophysiol*, *93*(4), 2331–2342. https://doi.org/10.1152/jn.00761.2004.

Faria, L. C., Gu, F., Parada, I., Barres, B., Luo, Z. D., & Prince, D. A. (2017). Neurobiology of disease epileptiform activity and behavioral arrests in mice overexpressing the calcium channel subunit α2δ -1. *Neurobiol of Dis*, *102*, 70–80. https://doi.org/10.1016/j.nbd.2017.01.009

Felix, R., Gurnett, C. A., De Waard, M., & Campbell, K. P. (1997). Dissection of functional domains of the voltage-dependent Ca2+ channel alpha2delta subunit. *J Neurosci*, *17*(18), 6884–91. Retrieved from http://www.ncbi.nlm.nih.gov/pubmed/9278523

Fell, B., Eckrich, S., Blum, K., Eckrich, T., Hecker, D., Obermair, G. J., … Engel, J. (2016). α2δ2 controls the function and trans-synaptic coupling of Cav1.3 channels in mouse inner hair cells and is essential for normal hearing. *J Neurosci*, *36*(43), 11024–11036. https://doi.org/10.1523/JNEUROSCI.3468-14.2016

Fink, K., Meder, W., Dooley, D. J., & Go, M. (2000). Inhibition of neuronal Ca2+ influx by gabapentin and subsequent reduction of neurotransmitter release from rat neocortical slices. *Neuropharmacol*, *42*(2), 229–236.

Fletcher, E. V, Kullmann, D. M., & Schorge, S. (2011). Alternative splicing modulates inactivation of type 1 voltage-gated sodium channels by toggling an amino acid in the first S3-S4 linker *. *J Biol Chem*, *286*(42), 36700–36708. https://doi.org/10.1074/jbc.M111.250225

Fuller-Bicer, G. A., Varadi, G., Koch, S. E., Ishii, M., Bodi, I., Kadeer, N., … Schwartz, A. (2009). Targeted disruption of the voltage-dependent calcium channel ␣ 2 / ␦ -1-subunit. *Am J Physiol Heart Circ Physiol*, *297*(1), 117–124. https://doi.org/10.1152/ajpheart.00122.2009.

Gao, B., Sekido, Y., Maximov, A., Saad, M., Forgacs, E., Latif, F., … Minna, J. D. (2000). Functional properties of a new Voltage-dependent calcium channel α2δ auxiliary subunit gene (CACNA2D2). *J Biol Chem*, *275*(16), 12237–12242.

Gee, N. S., Brown, J. P., Dissanayake, V. U. K., Offord, J., Thurlow, R., & Woodruff, G. N. (1996). The novel anticonvulsant drug, gabapentin (Neurontin), binds to the α2δ subunit of a calcium channel. *J Biol Chem*, *271*(10), 5768–5776.

Geisler, S., Schöpf, C. L., Stanika, R., Kalb, M., Campiglio, M., Repetto, D., … Obermair, G. J. (2019). Presynaptic α2δ-2 calcium channel subunits regulate postsynaptic GABAA receptor abundance and axonal wiring. *J Neurosci*, *39*(14), 2581–2605.

Goa, K. L., & Sorkin, E. M. (1993). *Drugs*. *Gabapentin* (Vol. 46). Springer International Publishing. https://doi.org/ISSN 0012-6667

Gong, H. C., Hang, J., Kohler, W., Li, L., & Su, T. (2001). Tissue-specific expression and gabapentin-binding properties of calcium channel α2δ subunit subtypes. *J Membrane Biol*, *184*(1), 35–43. https://doi.org/10.1007/s00232-001-0072-7

Goswami, S. P., Bucurenciu, I., & Jonas, P. (2012). Miniature IPSCs in hippocampal granule cells are triggered by voltage-gated Ca2+ channels via microdomain coupling. *J Neurosci*, *32*(41), 14294–14304. https://doi.org/10.1523/JNEUROSCI.6104-11.2012

Green, E. W., Fedele, G., Giorgini, F., & Kyriacou, C. (2014). A Drosophila RNAi collection is subject to dominant phenotypic effects. *Nature Methods*, *11*(3), 222–223. https://doi.org/10.1038/nmeth.2856

Hagler, D. J., & Goda, Y. (2001). Properties of synchronous and asynchronous release during pulse train depression in cultured hippocampal neurons. *J Neurophysiol*, *85*(6), 2324–2334.

Hallermann, S., Kittel, R. J., Wichmann, C., Weyhersmu, A., Fouquet, W., Mertel, S., … Sigrist, S. J. (2010). Naked dense bodies provoke depression. *J Neurosci*, *30*(43), 14340–14345. https://doi.org/10.1523/JNEUROSCI.2495-10.2010

Hara, Y., Koganezawa, M., & Yamamoto, D. (2015). The Dmca1D channel mediates Ca2+ inward currents in Drosophila embryonic muscles. *J Neurogenet*, *29*(2–3), 117–123. https://doi.org/https://doi.org/10.3109/01677063.2015.1054991

Heady, T. N., Gomora, J. C., Macdonald, T. L., & Perez-reyes, E. (2001). Molecular Pharmacology of T-type Ca2+ channels. *Jpn J Pharmacol*, *85*(4), 339–350.

Heckman, C. J., Lee, R. H., & Brownstone, R. M. (2003). Hyperexcitable dendrites in motoneurons and their neuromodulatory control during motor behavior. *TINS*, *26*(12), 688–695. https://doi.org/10.1016/j.tins.2003.10.002

Hendrich, J., Minh, A. T. Van, Heblich, F., Nieto-rostro, M., Watschinger, K., Wratten, J., … Dolphin, A. C. (2008). Pharmacological disruption of calcium channel trafficking by the α2δ ligand gabapentin. *PNAS*, *105*(9), 3628–3633.

Hennig, M. H. (2013). Theoretical models of synaptic short term plasticity. *Front Comput Neurosci*, *7*(154). https://doi.org/https://doi.org/10.3389/fncom.2013.00045

Herlitze, S., Xie, M., Han, J., Alexander, H., Melnik-martinez, K. V, Moreno, R. L., & Mark, M. D. (2003). Targeting mechanisms of high voltage-activated Ca2+ channels. *J Bioenerg Biomembr*, *35*(6), 621–637.

Hille, B. (2001). Ion channels of excitable membrane. *Sinauer Associates Inc.*, *3rd editio*. Retrieved from ISBN 978-0-87893-321-1

Hoang, B., & Chiba, A. (2001). Single-cell analysis of drosophila larval neuromuscular synapses. *Dev Biol*, *229*, 55–70. https://doi.org/10.1006/dbio.2000.9983

Hoppa, M. B., Lana, B., Margas, W., Dolphin, A. C., & Ryan, T. A. (2012). alpha2delta expression sets presynaptic calcium channel abundance and release probability. *Nature*, *486*(7401), 122–125. https://doi.org/10.1038/nature11033.alpha2delta

Hou, J., Tamura, T., & Kidokoro, Y. (2008). Delayed synaptic transmission in Drosophila cacophony null embryos. *J Neurophysiol*, *100*(5), 2833–2842. https://doi.org/10.1152/jn.90342.2008.Ca

Huang, E. P. (1999). Synaptic plasticity : Regulated translation in dendrites. *Curr Biol*, *9*(5), 168–170.

Huang, J., Zhou, L., Wang, H., Luo, J., Zeng, L., Xiong, K., & Chen, D. (2013). Distribution of thrombospondins and their neuronal receptor α2δ1 in the rat retina. *Exp Eye Res*, *111*, 36–49.

Huguenard, J. R., & Prince, D. A. (1992). A novel T-type current underlies prolonged Ca2+ -dependent burst firing in GABAergic neurons of rat thalamic reticular nucleus. *J Neurosci*, *12*(10), 3804–3817.

Ikeda, K., & Koenig, J. . (1988). Morphological identification of the motor neurons innervating the dorsal longitudinal flight muscle of Drosophila melanogaster. *J Comp Neurol*, *273*(3), 436–444.

Ivanov, S. V, Ward, J. M., Tessarollo, L., Mcareavey, D., Sachdev, V., Fananapazir, L., … Lerman, M. I. (2004). Cerebellar ataxia, seizures, premature death, and cardiac abnormalities in mice with targeted disruption of the Cacna2d2 gene. *Am J Pathol*, *165*(3), 1007–1018. https://doi.org/10.1016/S0002-9440(10)63362-7

Jackman, S. L., & Regehr, W. G. (2017). The mechanisms and functions of synaptic facilitation. *Neuron*, *94*(3), 447–464. https://doi.org/10.1016/j.neuron.2017.02.047

Jun, K., Piedras-Renteria, E. S., Smith, S. M., Wheeler, D. B., Lee, S. B., Lee, T. G., … Shin, H. (1999). Ablation of P/Q-type Ca2+ channel currents , altered synaptic transmission , and progressive ataxia in mice lacking the α1A -subunit. *PNAS*, *96*(26), 15245–15250.

Kadas, D., Klein, A., Krick, X. N., Worrell, X. J. W., Ryglewski, S., Duch, C., & Bycontrast, D. (2017). Dendritic and axonal L-type calcium channels cooperate to enhance motoneuron firing output during Drosophila larval locomotion. *J Neurosci*, *37*(45), 10971–10982. https://doi.org/10.1523/JNEUROSCI.1064-17.2017

Kaeser, P. S., & Regehr, W. G. (2014). Molecular mechanisms for synchronous, asynchronous, and spontaneous neurotransmitter release. *Annu Rev Physiol*, *76*, 333–363. https://doi.org/10.1146/annurev-physiol-021113-170338.Molecular

Kaldurin, I., Alvarez-Laviada, A., Ng, S. F. J., Walker-Gray, R., D'Arco, M., Fadel, M. G., … Dolphin, A. C. (2012). Calcium currents are enhanced by α2δ-1 lacking its membrane anchor. *J Biol Chem*, *287*, 33554–33566.

Kawasaki, F., Collins, S. C., & Ordway, R. W. (2002). Synaptic calcium-channel function in Drosophila : analysis and transformation rescue of temperature-sensitive paralytic and lethal mutations of cacophony. *J Neurosci*, *22*(14), 5856–5864.

Kawasaki, F., Felling, R., & Ordway, R. W. (2000). A temperature-sensitive paralytic mutant defines a primary synaptic calcium channel in Drosophila. *J Neurosci*, *20*(13), 4885–4889.

Kawasaki, F., Zou, B., Xu, X., & Ordway, R. W. (2004). Active zone localization of presynaptic calcium channels encoded by the cacophony locus of Drosophila. *J Neurosci*, *24*(1), 282–285. https://doi.org/10.1523/JNEUROSCI.3553-03.2004

Kim, M. D., Wen, Y., & Jan, Y. (2009). Patterning and organization of motor neuron dendrites in the Drosophila larva. *Developmental Biology*, *336*(2), 213–221. https://doi.org/10.1016/j.ydbio.2009.09.041

Kittel, R. J., & Heckmann, M. (2016). Synaptic vesicle proteins and active zone plasticity. *Synaptiv Neurosci*, *8*(8), 1–8. https://doi.org/10.3389/fnsyn.2016.00008

Klein, A. (2016). *Presynaptic function of the voltage-gated calcium channel DmCa1D in Drosophila larval motoneurons*. Johannes Gutenberg-University.

Klugbauer, N., Lacinová, L., Marais, E., Hobom, M., & Hofmann, F. (1999). Molecular diversity of the calcium channel α2δ subunit. *J Neurosci*, *19*(2), 684–691.

Kuehn, C., & Duch, C. (2013). Putative excitatory and putative inhibitory inputs are localised in different dendritic domains in a Drosophila flight motoneuron. *Europ J Neurosci*, *37*(6), 860–875. https://doi.org/10.1111/ejn.12104

Kuromi, H., Ueno, K., & Kidokoro, Y. (2010). Two types of Ca 2 + channel linked to two endocytic pathways coordinately maintain synaptic transmission at the Drosophila synapse, *32*(April), 335–346. https://doi.org/10.1111/j.1460-9568.2010.07300.x

Kurshan, P. T., Oztan, A., & Schwarz, T. L. (2009). Presynaptic α2δ-3 is required for synaptic morphogenesis independent of its Ca2+-channel functions. *Nature Neurosci*, *12*(11), 1415–1423. https://doi.org/10.1038/nn.2417

Landgraf, M., Bossing, T., Technau, G. M., & Bate, M. (1997). The origin , location , and projections of the embryonic abdominal motorneurons of Drosophila. *J Neurosci*, *17*(24), 9642–9655.

Larkum, M. E., Zhu, J. J., & Sakmann, B. (1999). A new cellular mechanism for coupling inputs arriving at different cortical layers. *Nature*, *398*(6725), 338–341.

Lee, A., Wang, S., Williams, B., Hagen, J., Scheetz, T. E., & Haeseleer, F. (2015). Characterization of Cav1.4 complexes (α1 1.4, β2, and α2δ4) in HEK293T cells and in the retina. *J Biol Chem*, *290*(3), 1505–1521. https://doi.org/10.1074/jbc.M114.607465

Leroy, J., Richards, M. S., Butcher, A. J., Nieto-rostro, M., Pratt, W. S., Davies, A., & Dolphin, A. C. (2005). Interaction via a key tryptophan in the I – II linker of N-type calcium channels Is required for β1 but not for palmitoylated β2 , implicating an additional binding site in the regulation of channel voltage-dependent properties. *J Neurosci*, *25*(30), 6984–6996. https://doi.org/10.1523/JNEUROSCI.1137-05.2005

Levine, J. O. N. D., & Wyman, R. J. (1973). Neurophysiology of flight in wild-type and a mutant Drosophila. *Proc Nat Acad Sci*, *70*(4), 1050–1054.

Llinas, R., Sugimori, M., Lin, J.-W., & Cherksey, B. (1989). Blocking and isolation of a calcium channel from neurons in mammals and cephalopods utilizing a toxin fraction (FTX) from funnel-web spider poison. *PNAS*, *86*(1), 1689–1693.

Ly, C. V., Yao, C. K., Verstreken, P., Ohyama, T., & Bellen, H. J. (2008a). Straightjacket is required for the synaptic stabilization of cacophony, a voltage-gated calcium channel α1 Subunit. *J Cell Biol*, *181*(1), 157–170. https://doi.org/10.1083/jcb.200712152

Ly, C. V., Yao, C. K., Verstreken, P., Ohyama, T., & Bellen, H. J. (2008b). Straightjacket Is Required for the Synaptic Stabilization of Cacophony, a Voltage-Gated Calcium Channel A1 Subunit. *J Cell Biol*, *181*(1), 157–170. https://doi.org/10.1083/jcb.200712152

Macabuag, N., & Dolphin, A. C. (2015). Alternative splicing in CaV2.2 regulates neuronal trafficking via adaptor protein complex-1 adaptor protein motifs. *J Neurosci*, *35*(43), 14636–14652. https://doi.org/10.1523/JNEUROSCI.3034-15.2015

Marais, E., Klugbauer, N., & Hofmann, F. (2001). Calcium Channel α2δ subunits — structure and gabapentin binding. *Mol Pharmacol*, *69*(6), 1243–1248.

Margas, W., Ferron, L., Nieto-Rostro, M., Schwartz, A., & Dolphin, A. C. (2016). Effect of knockout of α2δ-1 on action potentials in mouse sensory neurons. *Philos Trans R Soc London [Biol]*, *371*(1700). https://doi.org/10.1098/rstb.2015.0430

Marson, A. G., Kadir, Z. A., & Chadwick, D. W. (1996). New antiepileptic drugs: a systematic review of their efficacy and tolerability. *BMJ*, *313*, 1169–1174. https://doi.org/https://doi.org/10.1136/bmj.313.7066.1169

Matkovic, T., Siebert, M., Knoche, E., Depner, H., Mertel, S., Owald, D., … Sigrist, S. J. (2013). The Bruchpilot cytomatrix determines the size of the readily releasable pool of synaptic vesicles, *202*(4), 667–683. https://doi.org/10.1083/jcb.201301072

McCormick, D. A., & Huguenard, J. R. (1992). A Model of the electrophysiological properties of thalamocortical relay neurons. *J Neurophysiol*, *68*(4), 1384–1400.

McLean, M. J. (1995). Gabapentin. *Epilepsia*, *36*(2), 73–86. https://doi.org/https://doi.org/10.1177/106002809402801011

Müller, L. P. de S., Sargoy, A., Liu, J., Brecha, N., Angeles, L., Angeles, L., … Angeles, L. (2015). Expression and cellular localization of the voltage-gated calcium channel α2 δ3 in the rodent retina. *J Cell Physiol*, *523*(10), 1443–1460. https://doi.org/10.1002/cne.23751.Expression

Neely, G. G., Hess, A., Costigan, M., Keene, A. C., Goulas, S., Langeslag, M., … Penninger, J. M. (2010). A genome-wide Drosophila screen for heat nociception identifies α2δ3 as an evolutionarily conserved pain gene. *Cell*, *143*(4), 628–638. https://doi.org/10.1016/j.cell.2010.09.047

Neher, E., & Sakaba, T. (2008). Review multiple roles of calcium ions in the regulation of neurotransmitter release. *Neuron*, *59*(6), 861–872. https://doi.org/10.1016/j.neuron.2008.08.019

Nieto-Rostro, M., Ramgoolam, K., Pratt, W. S., Kulik, A., & Dolphin, A. C. (2018). Ablation of α2δ-1 inhibits cell-surface trafficking of endogenous N-type calcium channels in the pain pathway in vivo. *PNAS*, *115*(51), E12043–E12052. https://doi.org/10.1073/pnas.1811212115

Nowycky, M. C., Fox, A. P., & Tsien, R. W. (1985). Three types of neuronal calcium channel with different calcium agonist sensitivity. *Nature*, *316*(1), 440–443.

Ophoff, R. A., Terwindt, G. M., Vergouwe, M. N., Eijk, R. Van, Oefner, P. J., Hoffman, S. M. G., … Frants, R. R. (1996). Familial hemiplegic migraine and episodic ataxia type-2 are caused by mutations in the Ca 2+ channel gene CACNL1A4. *Cell*, *87*, 543–552.

Pan, Z., Hu, H., Perring, P., & Andrade, R. (2001). T-type Ca 2+ channels mediate neurotransmitter release in retinal bipolar cells. *Neuron*, *32*, 89–98.

Pedersen, F. S., Owsianik, G., & Nilius, B. (2005). TRP channels : An overview. *Cell Calcium*, *38*, 233–252. https://doi.org/10.1016/j.ceca.2005.06.028

Perez-Reyes, E., Cribbs, L. L., & Daud, A. (1998). Molecular characterization of a neuronal low-voltage- activated T-type calcium channel. *Nature*, *391*, 896–900.

Pirone, A., Kurt, S., Zuccotti, A., Ruttiger, L., Pilz, P., Brown, D. H., … Engel, J. (2014). α2δ3 is essential for normal structure and function of auditory nerve synapses and is a novel candidate for auditory processing disorders. *J Neurosci*, *34*(2), 434–445. https://doi.org/10.1523/JNEUROSCI.3085-13.2014

Platano, D., Qin, N., Noceti, F., Birnbaumer, L., Stefani, E., & Olcese, R. (2000). Expression of the α2δ Subunit interferes with prepulse facilitation in cardiac L-type calcium channels. *Biophysic J*, *78*(6), 2959–2972. https://doi.org/10.1016/S0006-3495(00)76835-4

Qin, N., Olcese, R., Stefani, E., Birnbaumer, L., Olcese, R., & Stefani, E. (1998). Modulation of human neuronal α1E-type calcium channel by α2δ-subunit. *Cell Physiol*, *274*(5), 1324–1331.

Randall, A., & Tsien, R. W. (1995). Pharmacological dissection of multiple types of Ca2+ channel currents in rat cerebellar granule neurons. *J Neurosci*, *15*(4), 2995–3012.

Ren, D., Xu, H., Eberl, D. F., Chopra, M., & Hall, L. M. (1998). A mutation affecting dihydropyridine-sensitive current levels and activation kinetics in Drosophila muscle and mammalian heart calcium channels. *J Neurosci*, *18*(7), 2335–2341.

Risher, C. W., Kim, N., Koh, S., Choi, J.-E., Mitev, P., Spence, E. F., … Eroglu, C. (2018). Thrombospondin receptor α2δ-1 promotes synaptogenesis and spinogenesis via postsynaptic. *J Cell Biol*, *217*(10), 3747–3765.

Rock, D. M., Kelly, K. M., & Macdonald, R. L. (1993). Gabapentin actions on ligand- and voltage-gated in cultured rodent neurons responses. *Epilepsy Res*, *16*(2), 89–98.

Ryglewski, S., & Duch, C. (2009). Shaker and shal mediate transient calcium-independent potassium current in a Drosophila flight motoneuron. *J Neurophysiol*, *102*(6), 3673–3688. https://doi.org/10.1152/jn.00693.2009.

Ryglewski, S., Kilo, L., & Duch, C. (2014). Sequential acquisition of cacophony calcium currents, sodium channels and voltage-dependent potassium currents affects spike shape and dendrite growth during postembryonic maturation of an identified Drosophila motoneuron. *Eur J Neurosci*, *39*(10), 1572–1585. https://doi.org/10.1111/ejn.12517

Ryglewski, S., Lance, K., Levine, R. B., & Duch, C. (2012). Ca v 2 channels mediate low and high voltage-activated calcium currents in Drosophila motoneurons. *J Physiol*, *590*(4), 809–825. https://doi.org/10.1113/jphysiol.2011.222836

Ryglewski, S., Vonhoff, F., Scheckel, K., Duch, C., & Haven, N. (2017). Intra-neuronal competition for synaptic partners conserves the amount of dendritic building material. *Neuron*, *93*(3), 632–645. https://doi.org/10.1016/j.neuron.2016.12.043.Intra-neuronal

Schmid, A., Chiba, A., & Doe, C. Q. (1999). Clonal analysis of Drosophila embryonic neuroblasts : neural cell types , axon projections and muscle targets. *Development*, *126*(21), 4653–4689.

Schmitt, S., Evers, J. F., Duch, C., Scholz, M., & Obermayer, K. (2004). New methods for the computer-assisted 3-D reconstruction of neurons from confocal image stacks. *NeuroImage*, *23*(4), 1283–1298. https://doi.org/10.1016/j.neuroimage.2004.06.047

Schneggenburger, R., Han, Y., & Kochubey, O. (2012). Ca2+ channels and transmitter release at the active zone. *Cell Calcium*, *52*(3–4), 199–207. https://doi.org/10.1016/j.ceca.2012.04.011

Schumacher, B., Beck, H., Steinhauser, C., & Elger, C. E. (1998). Effects of phenytoin , carbamazepine , and gabapentin on calcium channels in hippocampal granule cells from patients with temporal lobe epilepsy. *Epilepsia*, *39*(4), 355–363.

Schützler, N., Girwert, C., Hügli, I., Mohana, G., Roignant, J., & Ryglewski, S. (2019). Tyramine action on motoneuron excitability and adaptable tyramine / octopamine ratios adjust Drosophila locomotion to nutritional state. *PNAS*, *116*(9), 3805–3810. https://doi.org/10.1073/pnas.1813554116

Serpell, M. G. (2002). Gabapentin in neuropathic pain syndromes : a randomised , double-blind , placebo-controlled trial. *Pain*, *99*(3), 557–566.

Shistik, E., Ivanina, T., Puri, T., Hosey, M., & Dascal, N. (1995). Ca2+ current enhancement by alpha2/delta and beta subunits in Xenopus oocytes : contribution of changes in channel gating and a 1 protein level. *J Physiol*, *489*(1), 55–62.

Singer-Lahat, D., Kotan, I., Itagaki, K., Schwartz, A., & Dascal, N. (1992). Evidence for the existence of RNA of Ca2+-channel α2/δ subunit in Xenopus oocytes. *Biochim Biophys Acta Mol Cell Res*, *1137*, 39–44.

Singer, D., Biel, M., Lotan, I., Flockerzi, V., Hofmann, F., & Dascal, N. (1991). The roles of the subunits in the function of the calcium channel. *Science*, *253*(5027), 1553–1557. https://doi.org/10.1126/science.1716787

Sink, H., & Whitington, P. M. (1991). Location and connectivity of abdominal motoneurons in the embryo and larva of Drosophila rnelanogaster. *J Neurobiol*, *22*(3), 298–311.

Spitzer, N. C. (2002). Activity-dependent neuronal differentiation prior to synapse formation : the functions of calcium transients. *J Physiol Paris*, *96*(1–2), 73–80.

Spitzer, N. C. (2006). Electrical activity in early neuronal development. *Nature*, *444*(7120), 707–712. https://doi.org/10.1038/nature05300

Sprunger, L. K., Escayg, A., Tallaksen-greene, S., Albin, R. L., & Meisler, M. H. (1999). Dystonia associated with mutation of the neuronal sodium channel Scn8a and identification of the modifier locus Scnm1 on mouse chromosome 3. *Hum Mol Genet*, *8*(3), 471–479.

Stefani, A., Spadoni, F., & Bernardi, G. (1998). Gabapentin inhibits calcium currents in isolated rat brain neurons. *Neuropharmacol*, *37*(1), 83–91.

Stefani, A., Spadoni, F., Giacomini, P., Lavaroni, F., & Bernardi, G. (2001). The effects of gabapentin on different ligand- and voltage-gated currents in isolated cortical neurons. *Epilepsy Res*, *43*(3), 239–248.

Steinlein, O. K., Mulley, J. C., Propping, P., Wallace, R. H., Phillips, H. A., Sutherland, G. R., … Berkovic, S. F. (1995). A missense mutation in the neuronal nicotinic acetylcholine receptor alpha4 subunit is associated with autosomal dominant nocturnal frontal lobe epilepsy. *Nat Gen*, *11*, 201–203.

Streit, A. K., Fan, Y. N., Masullo, L., & Baines, R. A. (2016). Calcium imaging of neuronal activity in Drosophila can identify anticonvulsive compounds. *Plos One*, *11*(2), 1–15. https://doi.org/10.1371/journal.pone.0148461

Takahashi, T., & Momiyama, A. (1993). Different types of calcium channels mediate central synaptic transmission. *Letters of Nature*, *366*, 156–158.

Tanabe, T., Takeshima, H., Mikami, A., Flockerzi, V., Takahashi, H., Kangawat, K., … Hirose, T. (1987). Primary structure of the receptor for calcium channel blockers from skeletal muscle. *Nature*, *328*(6128), 313–318.

Tatsch, L. (2018). *α2δ-1 auxiliary subunit function in Drosophila motoneurons*. *Bachelor Thesis*. Johannes Gutenberg-University.

Taylor, C. P., Angelotti, T., & Fauman, E. (2007). Pharmacology and mechanism of action of pregabalin : The calcium channel α2-δ (alpha 2 — delta) subunit as a target for antiepileptic drug discovery. *Epilepsy Res*, *73*(2), 137–150. https://doi.org/10.1016/j.eplepsyres.2006.09.008

Taylor, C. P., & Garrido, R. (2008). Immunostaining of rat brain, spinal cord, sensory neurons and skeletal muscle for calcium channel alpha2-delta type 1 protein. *Neuroscience*, *155*(2), 510–521. https://doi.org/10.1016/j.neuroscience.2008.05.053

Taylor, C. P., Gee, N. S., Su, T., Kocsis, J. D., Welty, D. F., Brown, J. P., … Boden, P. (1998). A summary of mechanistic hypotheses of gabapentin pharmacology. *Epilepsy Res*, *29*(3), 233–249.

Tong, X. J., López-Soto, E. J., Li, L., Liu, H., Nedelcu, D., Lipscombe, D., … Kaplan, J. M. (2017). Retrograde synaptic inhibition is mediated by α-Neurexin binding to the α2δ subunits of N-type calcium channels. *Neuron*, *95*, 1–15. https://doi.org/10.1016/j.neuron.2017.06.018

Upton, N. (1994). Mechanisms of action of new antiepileptic drugs: rational design and serendipitous findings. *Trends Pharmacol Sci*, *12*(12), 456–463.

Venken, K. J. T., Schulze, K. L., Haelterman, N. A., Pan, H., He, Y., Evans-Holm, M., … Bellen, H. J. (2011). MiMIC: a highly versatile transposon insertion resource for engineering Drosophila melanogaster genes. *Nature Methods*, *8*(9), 737–743. https://doi.org/10.1038/nmeth.1662

Voigt, A., Freund, R., Heck, J., Missler, M., Obermair, G. J., Thomas, U., & Heine, M. (2016). Dynamic association of calcium channel subunits at the cellular membrane. *Neurophotonics*, *3*(4), 041809:1-13. https://doi.org/10.1117/1.NPh.3.4.041809

Vonhoff, F., & Duch, C. (2010). Tiling among stereotyped dendritic branches in an identified Drosophila motoneuron. *J Comp Neurol*, *518*(12), 2169–2185. https://doi.org/10.1002/cne.22380

Wakamori, M., Mikala, G., & Mori, Y. (1999). Auxiliary subunits operate as a molecular switch in determining gating behaviour of the unitary N-type Ca2+ channel current in Xenopus oocytes. *J Physiol*, *517*(3), 659–672.

Wang, T., Jones, R. T., Whippen, J. M., & Davis, G. W. (2016). α2δ-3 Is required for rapid transsynaptic homeostatic signaling. *Cell Reports*, *16*(11), 2875–2888. https://doi.org/10.1016/j.celrep.2016.08.030

West, A. E., Chen, W. G., Dalva, M. B., Dolmetsch, R. E., Kornhauser, J. M., Shaywitz, A. J., … Greenberg, M. E. (2001). Calcium regulation of neuronal gene expression. *PNAS*, *98*(20), 11024–11031.

West, A. E., & Greenberg, M. E. (2011). Neuronal Activity – Regulated Gene Transcription in Synapse Development and Cognitive Function. *Cold Spring Harb Perspect Biol*, *3*(6), 1–22.

Wheeler, D. G., Groth, R. D., Ma, H., Barrett, C. F., Owen, S. F., Safa, P., & Tsien, R. W. (2012). CaV1 and CaV2 channels engage distinct modes of Ca2+ signaling to control CREB-dependent gene expression. *Cell*, *149*(5), 1112–1124. https://doi.org/10.1016/j.cell.2012.03.041

Williams, C., Chen, W., Lee, C., Yaeger, D., Vyleta, N. P., & Smith, S. M. (2012). Coactivation of multiple tightly coupled calcium channels triggers spontaneous release of GABA. *Nature Neurosci*, *15*(9), 1195–1197. https://doi.org/10.1038/nn.3162

Worrell, J. W., & Levine, R. B. (2008). Characterization of voltage-dependent Ca2+ currents in identified Drosophila motoneurons in situ. *J Neurophysiol*, *100*(2), 868–878. https://doi.org/10.1152/jn.90464.2008.

Xu, J., Pang, Z. P., Shin, O., & Su, T. C. (2009). Synaptotagmin-1 functions as a Ca2+ sensor for spontaneous release. *Nature Neurosci*, *12*(6), 759–766. https://doi.org/10.1038/nn.2320

Zhang, F.-X., Gadotti, V. M., Souza, I. A., Chen, L., & Zamponi, G. W. (2018). BK potassium channels suppress Cavα2δ subunit function to reduce inflammatory and neuropathic pain. *Cell Reports*, *22*(8), 1956–1964.

Zhou, J.-J., Li, S.-R., Luo, Y., & Pan, H.-L. (2018). The α2δ-1–NMDA receptor coupling is essential for corticostriatal long-term potentiation and is involved in learning and memory. *J Biol Chem*, *293*(50), 19354–19364.

Zucker, R. S., & Regehr, W. G. (2002). Short-term synaptic plasticity. *Annu Rev Physiol*, *64*, 355–405. https://doi.org/10.1146/annurev.physiol.64.092501.114547

6. Appendix

6.1 Fly Lines

Genotype	Obtained from	Descriptive name	Experiment
P{w[+mW.hs]=GawB}elav[C155]	BDSC_458	elav-Gal4: pan-neural driver	Tab.3; Fig. 25
w[1118];P{w[+mW.hs]=GawB} VGlut[OK371]	BDSC_26160	OK371-Gal4: expression of Gal4 in glutamatergic neurons	Tab.3; Fig. 27-31,33,34
;;P{y[+t7.7]w[+mC]=GMR23H06-GAL4}attP2	discontinued at BDSC	23H06-Gal4: driver (expression pattern: http://flweb.janelia.org/cgibin/flew.cgi)	Fig.36-38
y[1] w[*]; P{w[+mC]=GAL4-Mef2.R}3	BDSC_27390	Mef2-Gal4: Gal4 expression in muscle cells; on 3rd chromosome	Tab.3
y[1] w[*];P{w[+mC]=UAS-Dcr-2.D}2;P{w[+mC]=GAL4-Mef2.R}3	Crossed from: BDSC_24650 BDSC_27390	UAS-Dcr2;Mef2-Gal4: UAS construct of dcr2 on 2nd and Gal4 expression in muscle cells; on 3rd chromosome	Tab.3
P{w[+mC]=UAS-Dcr-2.D}10	BDSC_24651	dcr2; UAS-dcr2 on 3rd chromosome	Tab.3; Fig. 24-48
y[1] w[67c23]; Mi{PT-GFSTF.2}CG4587[MI01722-GFSTF.2]	BDSC_59289	$d\alpha_2\delta_1^{GFP}$: $d\alpha_2\delta_1$ protein trap with endogenously tagged with GFP	Fig.21 & 23
P{w[+mW.hs]=GawB} elav[C155]; Mi{PTGFSTF.2}CG4587 [MI01722-GFSTF.2]	Crossed from BDSC_458; BDSC_59289	elav-Gal4; $d\alpha_2\delta_1^{GFP}$: elav-Gal4 driver on 1st with $d\alpha_2\delta_1^{GFP}$ on 2nd chromosome	Fig.25 & 26
y[1]w[*];Mi{y[+mDint2]=MIC} stj[MI00783]/SM6a	BDSC_34109	MiMIC cassette in an coding intron of Stj	Material & Methods: 2.2
y[1]w[*];Mi{PTGFSTF.0} stj[MI00783mCherry.0]/CyO Tb	Made with BDSC_34109	$Stj^{mCherry}$/Cyo,Tb: Stj protein trap with endogenously tagged with mCherry balanced by Cyo,Tb	Fig.21 & 23
P{w[+mW.hs]=GawB} elav[C155];Mi{PTGFSTF.0} stj[MI00783mCherry.0]/CyO Tb	Crossed from BDSC_458; $Stj^{mcherry}$/Cyo,Tb	elav-Gal4;$Stj^{mCherry}$/Cyo,Tb: elav-Gal4 driver on 1st and StjmCherry/Cyo,Tb on 2nd chromosome	Fig.25 & 26

w[1118];P{KK106795}VIE-260B; P{y[+t7.7]v[+t1.8]=TRiP.JF01825} attP2	Crossed from VDRC_108150 (rep); BDSC_25807	$d\alpha_2\delta_1^{RNAi}$ KK; Stj^{RNAi} (BL): UAS- $d\alpha_2\delta_1$RNAi on 2nd and UAS-StjRNAi on 3rd chromosome	Tab.3; Fig.38
y* w*; P{GawB}stjNP1574 / CyO, P{UASlacZ.UW14}UW14	Ly *et al*. 2008	Stj-Gal4: expression of Gal4 under control of Stj	Fig.22
w[1118];P{KK101267}VIE-260B; P{w[+mC]=UAS-Dcr-2.D}10	Crossed with VDRC_108156; BDSC_24651	Stj^{RNAi} KK; dcr2: UAS-StjRNAi on 2nd and UAS-dcr2 on 3rd chro-mosome	Tab.3; Fig. 24,26-48
w[1118];P{KK106795}VIE-260B; P{w[+mC]=UAS-Dcr-2.D}10	Crossed from VDRC_108150; BDSC_24651	$d\alpha_2\delta_1^{RNAi}$ KK; dcr2: UAS- $\alpha_2\delta_1$RNAi on 2nd and UAS-dcr2 on 3rd chromosome	Tab.3; Fig. 24-45
w[1118]; P{y[+t7.7] w[+mC]=20XUAS-IVSGCaMP6s}attP40; P{y[+t7.7] w[+mC]=GMR23H06-GAL4}attP2	Crossed from BDSC_42746; 23H06-GAL4	GCamp6s;23H06-Gal4: Ca^{2+} indicator UAS-GCamp6s under the control of 23H06-Gal4	Fig.39 & 43
cacsfGFP-N;; P{y[+t7.7] w[+mC]=GMR23H06-GAL4}attP2	Crossed from Gratz *et al*. 2019; 23H06-Gal4	cac^{GFP};;23H06-Gal4: endogenously GFP tagged Ca_V2 channel (cac) on 1st with 23H06-Gal4 on 3rd chromosome	Fig.41
cacsfGFP-N; P{w[+mW.hs]=GawB} VGlut[OK371]	Crossed from Gratz *et al*. 2019; BDSC_26160	cac^{GFP};OK371-Gal4: en-dogenously GFP tagged Ca_V2 channel (cac) on 1st with OK371-Gal4 on 2nd chromosome	Fig.32
w[*]; P{w[+mC]=eve-GAL4.RN2}P, P{w[+mC]=UAS-mCD8::GFP.L}LL5/ CyO;P{w[+mC]=Act(FRT.stop)GAL4}, P{w[+mC]=UAS-FLP.D}JD2	From Dr. S. Sanyal, Calico labs, San Francisco	RN2-Gal4,GFP;Act,FLP: Mosaic expression in MN1s and MN1b crawl-ing MNs through eve-Gal4, UAS-FLP and Act(FRT.stop)-Gal4. Neurons are marked by UAS-GFP	Fig.35 & 45-48
w[*];P{w[+mC]=UAS-mCD8::GFP.L} LL5; P{w[+mW.hs]=GawB}D42, Cha-Gal80	BDSC_8816;	GFP;D42-Gal4: expres-sion of Gal-4 under the control of the troll6 receptor narrowed by expression of Gal80 in all cholinergic neurons	Fig.40, 44 & 42

;;UAS-Stj-HA	from Schwarz lab (Dickman *et al.*, 2009)	UAS construct of Stj with an HA-tag (SD03196) on the 3rd chromosome	Fig.22
y[1] M{vas-int.B}ZH-2A w[*]; sna[Sco]/CyO, P{ry[+t7.2]=sevRas1.V12}FK1	BDSC_36312	vasa;Sna^{Sco}/Cyo: expression of ϕC31 integrase in the germ line under the control of vasa	Material & Methods: 2.2
y[1] w[*];CyO/sna[Sco]	lab stock	Balancer/marker line for 2nd chromosome in *yellow* background	Material & Methods: 2.2
;Chal-Gal4	lab stock	expression of Gal4 under the control of the choline acetyltransferase (all cholinergic neurons); on 2nd chromosome	Tab.3
yw;DDα2δ3-106/Cyo	from Schwarz lab (Dickman *et al.*, 2008)	Stj null mutant with an early stop codon (R92Stop)	Discussion: 4.2
y1 w67c23; P{lacW}stjk10814/CyO	BDSC_11004	Hypomorphic mutant of Stj: Transposon insertion in k10814 (2nd chromosoma)	Discussion: 4.2
y,w[1118];P{empty} VIE-260B, P{empty} VIE-40D3	VDRC_60100	Annotated insertion: landing site VIE-260B (position chr2L: 22019296, cytological band 40D3) and non-annotated insertion: (position chr2L: 9437482, cytological band 30B3)	Material & Methods: 2.5
y[1] v[1];; P{y[+t7.7] v[+t1.8]=TRiP.JF01825}attP2	BDSC_25807	Stj^{RNAi}(BL): UAS construct for RNAi of Stj on 3rd chromosome	Tab.3; Fig. 38
y;;M{UAS-stj.ORF.3xHA}ZH-86Fb	FlyORF_F001252	UAS construct of Stj tagged with HA on 3rd chromosome	Discussion: 4.2

6.2 List of Chemicals

chemicals	Manufacturer	Cat#
30% Acrylamide/Bis Solution 29:1	Bio-Rad Laboratories	1610156
4-AP	Sigma-Aldrich	MKBN8495V
Acetic Acid (99 %)	Carl Roth GmbH	7332.1
Agarose Standard	Carl Roth GmbH	38102
Agar-Agar	Carl Roth GmbH	5210.5
Albumin from bovine serum	Sigma-Aldrich	SLBS3968V
Ammonium Persulfate	Bio-Rad Laboratories	1610700
Ascorbic acid	Carl Roth GmbH	3525.3
1-Butanol	Carl Roth GmbH	7724.1
$BaCl_2$	Carl Roth GmbH	5051.2
Benzoic acid	Apex	9976.3
Bleaching solution	DanKlorix	-
Block ACE	Bio-Rad	BUF029
Boric acid	Carl Roth GmbH	6943.1
Bromophenol blue	Bio-Rad Laboratories	161-0404
CaCl	Sigma-Aldrich	SLBJ2662V
Cadmium	Sigma-Aldrich	MKBB2360V
Color Protein Standard Broad Range	BioLabs	P7712S
Cornmeal	Detemer	420505
CsCl	Sigma-Aldrich	MKBH2919V
dNTP mix	BioLabs	N0447S
Donkey serum	Sigma-Aldrich	D9663
Dry yeast	Saf-instant	
DTT	Bio-Rad Laboratories	1610611
D(+)-Saccharose	Carl Roth GmbH	4621.1
D(+)-Trehalose Dihydrat	Carl Roth GmbH	5151.4
EGTA	Carl Roth GmbH	3054.1
Ethanol 99% HPLC Gradient Grade	Carl Roth GmbH	P076.1
Gabapentin	Sigma-Aldrich	128K1528
Glycin	Carl Roth GmbH	0079.4
Glycerol	Sigma-Aldrich	STBC1888V
Glucose	Carl Roth GmbH	X997.5
H_2O_{dd} Nuklease free	Gibco	1722234
HEPES	Carl Roth GmbH	9105.2
HCL	Carl Roth GmbH	0281.1
Immunilon Western Chemiluminescent HRP substrate	Millipore	WBKLS0500
KGluc	Sigma-Aldrich	SLBB9013V
Methanol	Carl Roth GmbH	4627.4
MgATP	Sigma-Aldrich	091M5153V
Milk powder (Milchpulver)	Carl Roth GmbH	T145.2

Na_2GTP	Carl Roth GmbH	K056.1
NaCl	Carl Roth GmbH	3957.1
$NaHCO_3$	Sigma-Aldrich	MKBP8798V
SDS	Carl Roth GmbH	0183.1
Sodium dodecyl sulfate (SDS)	Carl Roth GmbH	0183-1
Sodium hydrogencarbonate	Sigma-Aldrich	MKBP8798V
Sodium hydroxide solution (1N)	Carl Roth GmbH	K021.1
10x Thermopol buffer	BioLabs	B9004S
Taq Polymerase	BioLabs	M02675
TEA-Br	Sigma-Aldrich	MKBN7373V
TEA-Cl	Sigma-Aldrich	BCBL6884V
Tris-Cl	Carl Roth GmbH	9090.2
Triton®-X100	Sigma-Aldrich	MKBH7028V
Trizma® base	Sigma-Aldrich	SLBH5524V
TTX	Carl Roth GmbH	6973.1
Tween® 20	Merck KGaA	V9000548
Patent blue V sodium salt	Sigma-Aldrich	BCBS1418V
Paraformaldehyde	Sigma-Aldrich	SLBC3029V
PBS	Sigma-Aldrich	SLBX3017
Phospocreatin di tris	Sigma-Aldrich	SLBK4243V
Ponceau S	Sigma-Aldrich	BCBG6694V
Protease	Sigma Aldrich	P5147
Potassium chloride	Sigma-Aldrich	SLBM5524V
Potassium hydroxide solution (1N)	Carl Roth GmbH	K017.1
Roti®-GelStain Red	Carl Roth GmbH	0984.1
Vectashield	Vector Laboratories Inc.	H-1000

6.3 List of Devices

Device	**Product name**	**Manufacturer**
Chemiluminescence Imaging	Fusion SL	Vilber Lourmat
Power supply	Power Pac HC	Bio-Rad
Gel chamber	Hoefer® SE 400 Series Sturdier	Thermo Fischer Scientific Inc.
High intensity illuminator	Fiber Lite MI-150	Dolan-Jenner Industries
Table centrifuge	Rotilabo mini centrifuge	Carl Roth GmbH
Flaming/Brown Micropipette puller	Model P-97	Sutter Instruments Co.
Waterbath	Wise Bath® Fuzzy Control System	Wisd. Laboratory Instr.

Transfer chamber Western	Hoefer® TE42 Tank transfer unit	Thermo Fischer Scientific Inc.
Comb for Gel electrophoresis	Hoefer® Sturdier, 15W 1.5MM CMB Sp	Thermo Fischer Scientific Inc.
Nitrocellulose membrane	Nitrocellulose blotting membrane	GE Healthcare Life science
Blotting paper	Rotilabo Blottingpapier	Carl Roth GmbH
Precision balance	XB220A	Precisa Gravimetrics AG
Vertical electrode puller	Model PC-10	Narshige
Headstage	HS-1A	Axon Instruments Molecular Devices
Fluorescence microscope	Axioskop 2 FS plus	Carl Zeiss
Amplifier patch clamp	Axopatch 200B	Axon Instruments Molecular Devices
Amplifier muscle recordings	Axoclamp 2B	Axon Instruments Molecular Devices
Digidata patch clamp	Axon Digidata 1322A	Axon Instruments Molecular Devices
Digidate muscle recordings	Axon Digidata 1550	Axon Instruments Molecular Devices
Micromanipulator patch clamp	MP-225 micromanipulator	Sutter Instruments Co.
Micromanipulator muscle rec.	ROE-200	Sutter Instruments Co.
Differential AC Amplifier	Model 1700	A-M Systems
Isolated pulse stimulator	Model 2100	A-M Systems
Pipette holder	1-HL-U	Axon Instruments Molecular Devices
40 x water immersion lens	LUMPlanFl 40x / 0.80 w	Olympus
20 x water immersion lens	LUMPlanFl 20x / 0.50 w	Olympus
Gel chamber PCR	Mini-Sub® Cell GT	Bio-Rad
Gel detection PCR	E-Box VX5	Viber Lourmat
PCR machine	T Gradient	Biometra®
Perfusion system	BPS-8 perfusion system	ALA Scientific Instr.
Confocal microscope	TCS SP8 confocal microscope	Leica
40x oil immersion objective	HC PL APO 40x/1.30 Oil CS2	Leica

20x oil immersion objective	HC PL APO 20x/0.75 Imm Corr CS2	Leica
Injection system	FemtoJet 4x	Eppendorf
Inverted microscope (Injections)	Axiovert 135	Zeiss
Electrode glass:		
Intracell. muscle recording	with filament; cat#1503347	WPI
Stimulation electrode (NMJ rec.)/Intracellular fillings (MN5)	With filament; BF100-50-10	Sutter Instruments
Injection electrode glass	with filament; cat#GB100TF-8P	Science Products
Patch clamp electrode glass	No filament; cat#PG52151-4	WPI

6.4 List of Antibodies

Primary antibodies			
name	**usage**	**Conc.**	**Manufacturer, cat#**
rabbit α-GFP	Western blot	1:1000	Life Technologies, A11122
mouse α-actin	Western blot	1:10000	DSHB, JLA20
rabbit α-mCherry	Western blot	1:1000	Abcam, EPR20579
chicken α-GFP	Immuno	1:400	Invitrogen, A10262, AB_2534023
mouse α-Brp	Immuno	1:200	DSHB, AB_2314867
rat α-HA	Immuno	1:100	Roche life science, 11867423001
rat α-mCherry	Immuno	1:5000	Invitrogen, 16D7, M11217
goat α-DmCa1D	Immuno	1:100	Santa Cruz Biotechnology, Sc-32083
goat α-HRP	Immuno	1:400	Jackson ImmunoResearch, 23-005-021
α-GFP FluoTag® Cy5	Immuno	1:100	NanoTag Biotechn., N0301-At647N-S
Streptavidin Cy5	Immuno	1:750	Jackson ImmunoResearch,116-600-084

Secondary antibody			
name	**usage**	**Conc.**	**Manufacturer, cat#**
goat α-rabbit IgG	Western blot	1:10000	Jackson ImmunoResearch, 11-035-144
goat α-mouse HRP	Western blot	1:4000	Millipore, 12-349
goat α-chicken Cy2	Immuno	1:400	ThermoFisher, A-11039
donkey α-goat Cy2	Immuno	1:400	Jackson ImmunoResearch, 705-175-147

donkey α-chicken Cy2	Immuno	1:400	Dianova, 703-505-155
donkey α-rat Cy3	Immuno	1:400	Invitrogen, A-21209
goat α-mouse Cy5	Immuno	1:400	Jackson ImmunoResearch, 115-175-166
donkey α-mouse Cy5	Immuno	1:400	Invitrogen, A-31357

6.4.1 Performed Antibody Stainings

Staining	**Blocker**	**1. Antibodies**	**2. Antibodies**
Triple label: $Stj^{mCherry}$, $d\alpha_2\delta_1^{GFP}$, Brp (Fig.21)	10 % NDS	chicken α-GFP, rat α-mCherry, mouse α-Brp	donkey α-chicken Cy2, donkey α-rat Cy3, donkey α-mouse Cy5
Stj^{HA} (Fig.22)	5 % BSA	rat α-HA	donkey α-rat Cy5
Double label: $Stj^{mCherry}$, Brp (Fig.23)	10 % NDS	rat α-mCherry, mouse α-Brp	donkey α-rat Cy3, donkey α-mouse Cy5
Double label: $d\alpha_2\delta_1^{GFP}$, Brp (Fig.23)	none	chicken α-GFP, mouse α-Brp	goat α-chicken Cy2, goat α-mouse Cy5
Double label: HRP, Brp (Fig.31)	none	goat α-HRP, mouse α-Brp	donkey α-goat Cy2, donkey α-mouse Cy5
Double label: GFP, HRP (Fig.32)	5 % BSA	α-GFP NanoTag Cy5, goat α-HRP	donkey α-goat Cy2
Double label: Dmca1D, Brp (Fig.33, 34)	5 % BSA	goat α-DmCa1D, mouse α-Brp	donkey α-goat Cy2, donkey α-mouse Cy5
Streptavidin (Fig.40, 44)	none	Streptavidin Cy5	none

6.5 List of Primers

Primer name	**Primer Sequence**	**Usage**
Orientation-MiL-F	GCGTAAGCTACCTTAATCTCAAGAAGAG	MiMIC validation
Orientation-MiL-R	CGCGGCGTAATGTGATTTACTATCATAC	MiMIC validation
mCherry-Seq-F	ACGGCGAGTTCATCTACAAG	MiMIC validation

mCherry-Seq-R	TTCAGCCTCTGCTTGATCTC	MiMIC validation
C_Genomic_F	GCCCACTGTCAGCTCTCAAC	KK-RNAi validation
NC_Genomic_F	GCTGGCGAACTGTCAATCAC	KK-RNAi validation
pKC26_R	TGTAAAACGACGGCCAGT	KK-RNAi validation
pKC43_R	TCGCTCGTTGCAGAATAGTCC	KK-RNAi validation

6.6 Recipes

6.6.1 Fly Food

chemicals	**mass**
H_2O_{dd}	1000 ml
Glucose	116,9 g
Cornmeal	55,3 g
Yeast	29,2 g
Agarose	10,7 g
Tegosept (10%)	12,3 ml
Ascorbic acid	0,6 g

- H_2O_{dd} is heated to 90 °C
- add Glucose, Yeast, Cornmeal and Agarose
- cook at 90 °C for 1 h
- cook at 85 °C for 1h add tegosept and ascorbic acid after cooled to 67 °C and pour into plastic vials

6.6.2 Generation of MiMIC protein trap

Grape juice agar

chemicals	**mass**
Grape juice	200 ml
Agarose	3 g
Sucrose	6 g
Boil up in a microwave, when cooled down (approx. 67 °C) add:	
Acetic acid (99 %)	1.5 ml
Ethanol (96 %)	3 ml

- pour in plastic vials

Agarose gel for embryo alignment

chemicals	**mass**
Agar	6,4 g
Patent blue	spatula tip
H_2O_{dd}	200 ml

- boil up in microwave
- pour in petri dishes
- store at 4 °C

50 % Bleaching solution

chemicals	**mass**
Bleaching solution	50 %
H_2O_{dd}	50 %

Squishing buffer

chemicals	**mass**
Tris-Cl (pH = 8.2)	10 mM
EDTA	1 mM
NaCl	25 mM

- add Proteinase K (200µg/ml final concentration) shortly before usage

6.6.3 Western Blot

8 % Running Gel

chemicals	**mass**
30% bis-acrylamide	10.7 ml
4x Tris-HCl / SDS (pH 8.8)	10 ml
H_2O_{dd}	18.8 ml
Added shortly before pouring:	
10% Ammonium persulfate (dissolved in H_2O_{dd})	400 µl
TEMED	16 µl

5 % Stacking Gel

chemicals	**mass**
3% bis-acrylamide	1.7 ml
4x Tris-HCl / SDS (pH 6.8)	1.25 ml
H_2O_{dd}	6.8 ml
Added shortly before pouring:	

10% Ammonium persulfate (dissolved in H_2O_{dd})	100 ml
TEMED	10 ml

4x Tris-HCl / SDS (pH 8,8)

chemicals	**mass**
H_2O_{dd}	300 ml
Trizma® base	91 g
Sodium dodecyl sulfate (SDS)	2 g

- adjust to pH 8,8 with HCl
- add H_2O_{dd} to 500 ml
- filter through 0,45 µm sterile filter

4x Tris-HCl / SDS (pH 6,8)

chemicals	**mass**
H_2O_{dd}	40 ml
Trizma® base	6,05 g
Sodium dodecyl sulfate (SDS)	0.4 g

- adjust to pH 6,8 with HCl
- add H_2O_{dd} to 100 ml
- filter through 0,45 µm sterile filter

Transfer buffer

chemicals	**mass**
Trizma® base	21.23 g
Glycine	100.92 g
Methanol (99 %)	1050 ml

- add H2Odd to 7000 ml

Sample buffer

chemicals	**mass**
4x Tris-HCl / SDS (pH 6,8)	25 ml
Gycerol	20 ml
Sodium dodecyl sulfate (SDS)	4 g
DTT	0.31 g
Bromophenol blue	1 mg

- add H_2O_{dd} to 100 ml
- filter through 0,45 µm sterile filter

5x SDS-glycine-Tris electrophoresis buffer (Running buffer)

chemicals	mass
Trizma® base	15.1 g
Glycine	72 g
Sodium dodecyl sulfate (SDS)	5 g
- Add H_2O_{dd} to 1000 ml	

Tris-buffered saline + Tween-20 (TBST)

chemicals	mass
1 M Trizma® base (pH 7,5)	10 ml
5 M NaCl	30 ml
Tween® 20	1 ml
- add H_2O_{dd} to 1000 ml	

10 % Milk solution

chemicals	mass
Milk powder	1 g
- add TBST to 30 ml	

BlockAce solution

chemicals	mass
BlockAce	1 pkg
- add TBST to 100 ml	

Ponceau S

chemicals	mass
Ponceau S	0.5 g
Glacial acetic acid	1 ml
- add H_2O_{dd} to 100 ml	

6.6.4 Solutions for Electrophysiology

Standard Saline (pH 7,24 – 7,25 / mOsM 300 – 310)

chemicals	concentration
NaCl	128 mM
$MgCl_2$	4 mM
KCl	2 mM

$CaCl_2$	1.8 mM
HEPES	5 mM
Sucrose	35 mM

- dissolved in H_2O_{dd}
- adjust pH with NaOH

HL3.1 Saline (pH 7,24 – 7,25 / mOsM 300 – 310)

chemicals	**concentration**
NaCl	62.5 mM
$MgCl_2$	10 mM
KCl	5 mM
$CaCl_2$	0.5 mM
$NaHCO_3$	10 mM
Trebulose	5 mM
HEPES	5 mM
Sucrose	35 mM

- dissolve in H_2O_{dd}
- adjust pH with NaOH
- adjust osmolality with sucrose

Intracellular patch solution (pH 7,24 / mOsM 300 - 305)

chemicals	**concentration**
KGluc	140 mM
$MgCl_2$	2 mM
EGTA	11 mM
HEPES	10 mM
MgATP	2 mM

- dissolve in H_2O_{dd}
- adjust pH with KOH
- adjust osmolality with glucose

Extracellular Ca^{2+} recording solution (pH 7,24 – 7,25 / mOsM 320)

chemicals	**concentration**
NaCl	93 mM
$MgCl_2$	4 mM
KCl	5 mM
$CaCl_2$	1.8 mM
$BaCl_2$	1.8 mM
TEA-Cl	30 mM
4-AP	2 mM
Sucrose	35 mM

HEPES	5 mM

- dissolve in H_2O_{dd}
- adjust pH with NaOH
- adjust osmolarity with sucrose
- TTX was added at 10^{-7} M (adult, pupae) or 10-4 M (larvae) to block Na^+ currents (5 min)
- TEA and 4-AP blocked K^+ currents

Intracellular Ca^{2+} recording solution (pH 7,24 / mOsM 327)

chemicals	**concentration**
CsCl	140 mM
CaCl	0.5 mM
EGTA	11 mM
HEPES	10 mM
MgATP	2 mM
TEA-Br	20 mM
4-AP	0.5 mM

- dissolve in H_2O_{dd}
- adjust pH with 1N CsOH
- adjust osmolality with glucose

Intracellular Ca^{2+} imaging solution (pH 7,24 / mOsM 313

chemicals	**concentration**
KGluc	140 mM
Mg-ATP	2 mM
MgCl	2 mM
Phosphocreatine di tris	10 mM
Na_2GTP	0.3 mM
HEPES	10 mM
Sucrose	35 mM

- dissolve in H_2O_{dd}
- adjust pH with KOH
- adjust osmolality with sucrose

6.6.5 Solutions for PCR

Squishing buffer

chemicals	concentration
Tris-Cl pH 8.2	10 mM
EDTA	1 mM
NaCl	25 mM
- stored at 25 °C	

Proteinase K stock solution

chemicals	concentration
Proteinase K	20 mg/ml
- dissolve in H_2O_{dd}	
- stored at - 28 °C	

PCR Mastermix – Taq polymerase

components	volume
10x Thermopol buffer	2 µl
10 mM dNTP mix	0.5 µl
Forward Primer 10 µM	0.5 µl
Reverse Primer 10 µl	0.5 µl
Taq Polymerase	0.1 µl
H_2O_{dd} Nuklease free	add to 20 µl
CDNA	x µl
- add DNA at the end	

TBE buffer (5x)

chemicals	mass
Trizma® base	54 g
Boric acid	27.5 g
0.5 M EDTA (pH 8.0)	20 ml
- add Trizma base and boric acid to 700 ml H_2O_{dd}	
- stir until dissolved	400 µl
- add EDTA	16 µl
- adjust volume to 1000 ml with H_2O_{dd}	

6.7 PCR validation of RMCE events during protein trap generation of Stj-Mi[mCherry]MIC & Ca_V1-Mi[mCherry]MIC

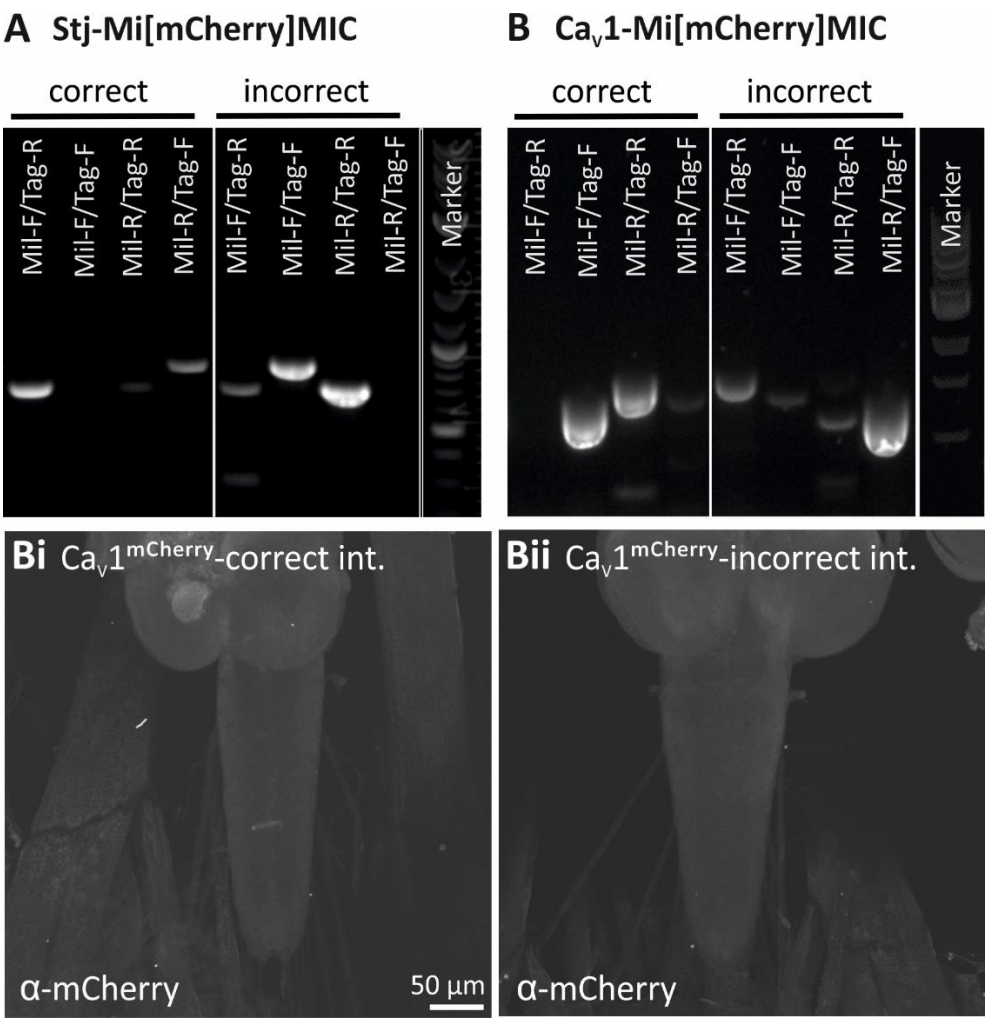

Fig.S1: PCR validation of RMCE events during protein trap generation of Stj_Mi[mCherry]MIC & Ca_V1_Mi[mCherry]MIC

The MiMIC cassette can be replaced with a plasmid construct via recombinase-mediated cassette exchange (RMCE, black crosses). Thereby, the construct will be integrated with either of two different orientations. Only one of those two orientations will result in the expression of the desired construct. To validate for correct integration of the construct, four PCR reactions are done (1. MiL-F/Tag-R; 2. Mil-F/Tab-F; 3. Mil-R/Tag-R; 4. Mil-R/Tag-F). Correct integration depends on the orientation of the MiMIC cassette relative to the respective gene (Venken *et al*., 2011). [**A**] MiMIC cassette is orientated in the same direction as Stj gene, therefore correct integration resulted in PCR products for primer combinations 1 and 4 Primer combinations. [**B**] By contrast, MiMIC cassette is orientated in the opposite direction as Ca_V1 gene, thus correct integration resulted in PCR products for primer combinations 2 and 3. [**Bi, Bii**] Confocal image stacks of anti-mCherry staining in Ca_V1_Mi[mCherry]MIC flies. Even though the construct integrated correctly in CaV1_Mi[]MIC, no signal could be detected in the larval CNS of animals with [Bi] correct and [Bii] incorrect integration of mCherry.

6.8 PCR analysis of VDRC - KK RNAi Fly lines

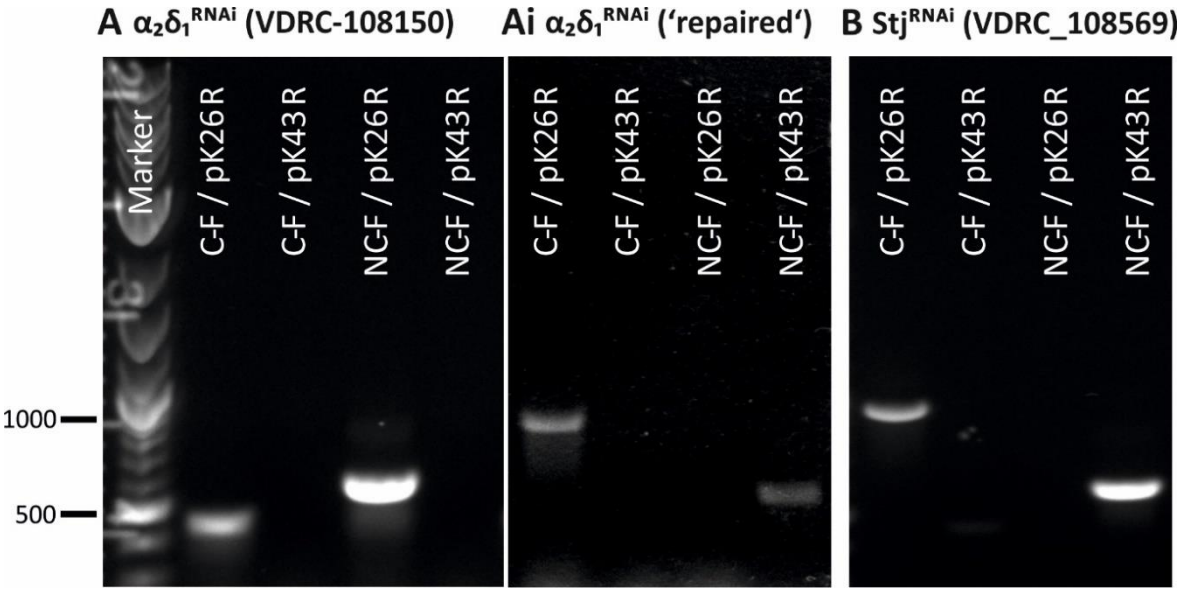

Fig.S2: PCR analysis of VDRC - KK RNAi Fly lines

Integration of pKC26 into the annotated site (40D landing site) will result in a PCR product of approx. 450 bp (C_Genomic_F / pKC26_R), while an empty site will result in a product of approx. 1050 bp (C_Genomic_F / pKC43_R). Integration of the construct into the non-annotated site (30D landing site) will result in a PCR product of approx. 600 bp (NC_Genomic_F / pKC26_R). By contrast, an empty 30D landing site results in a product of approx. 1200 bp (C_Genomic_F / pKC43_R). [**A**] Therefore, integration of construct in both landing sites was found in $d\alpha_2\delta_1^{RNAi}$ (VDRC-108150). [**Ai**] $d\alpha_2\delta_1^{RNAi}$ (VDRC-108150) was 'repaired' by genomic recombination with VDRC_60100 (in which both landing sites are empty). 'Repaired' flies will have the construct in the 30D landing site; the 40D landing site will be empty. [**B**] In Stj^{RNAi} (VDRC_108156) construct had integrated correctly into the 30D landing site and the 40D landing site was empty.

6.9 Stj & dα$_2$δ$_1$ cannot be detected at the larval NMJ

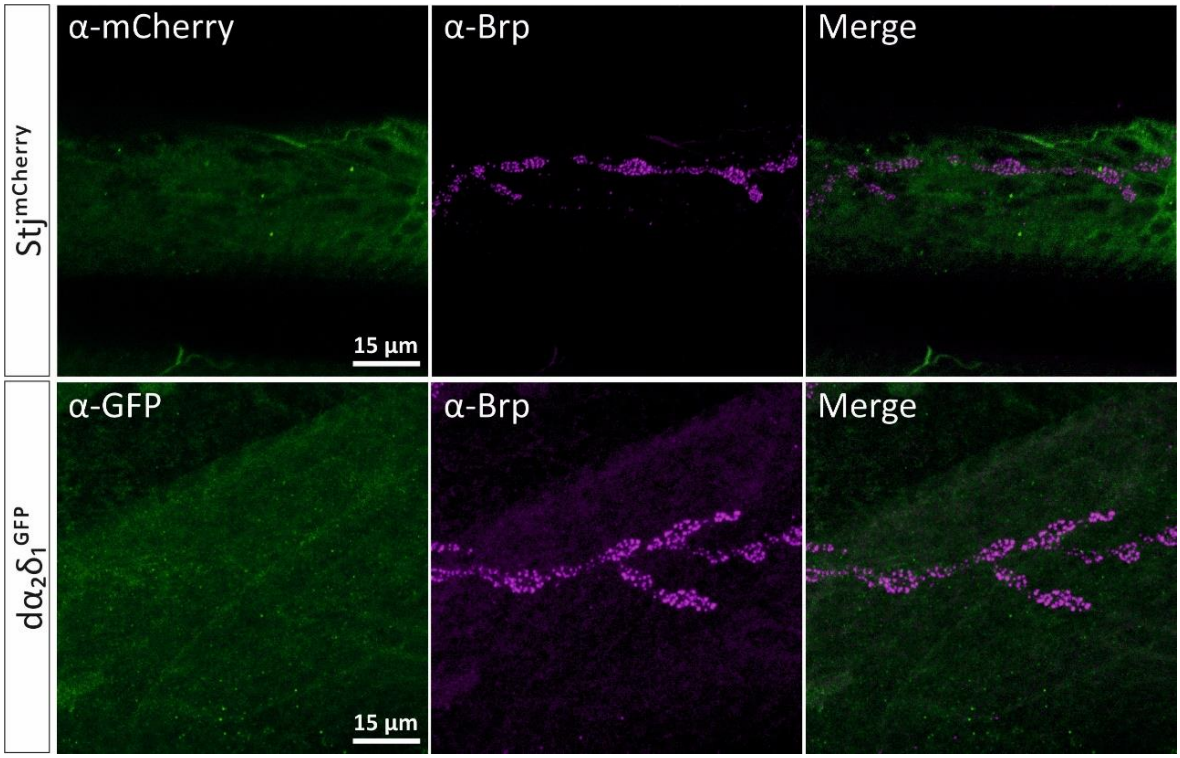

Fig.S3: Stj & dα$_2$δ$_1$ cannot be detected at the larval NMJ
[**Stj^{mCherry}**] Double labeling of Stj^{mCherry} (green) plus the synaptic marker Brp (magenta) and [**dα$_2$δ$_1$^{GFP}**] double labeling of dα$_2$δ$_1$^{GFP} (green) plus Brp (magenta) at the larval NMJ on muscle M10. Projection views reveal that neither Stj^{mCherry} nor dα$_2$δ$_1$^{GFP} signal can be detected at axon terminals of larval crawling motoneurons.

6.10 Following expression of dα$_2$δ$_1$^{RNAi} in wing depressor neurons flies fly longer

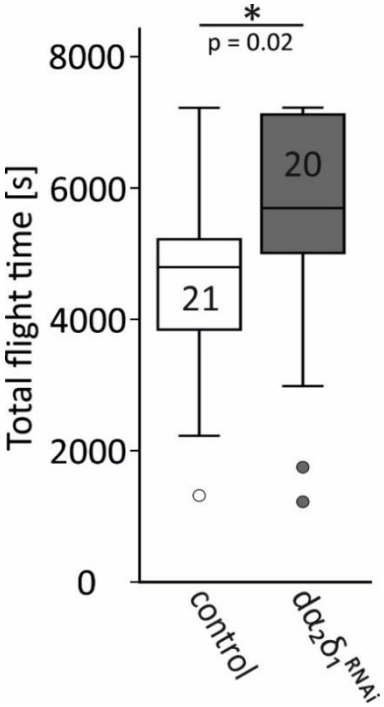

Fig.S4: Flies expressing dα$_2$δ$_1$^{RNAi} fly longer
Flies with a targeted (D42-Gal4,Cha-Gal80) knockdown of dα$_2$δ$_1$ (UAS-dα$_2$δ$_1$^{RNAi};UAS-dcr2) fly longer (p = 0.02) compared to control (UAS-dcr2). Boxes display median with 25 and 75% quartiles, whiskers represent 10 and 90% quartiles. The number of replicates is given inside the respective box. A Mann-Whitney-U test was done for statistical comparison (p < 0.05*; p < 0.01**; p < 0.001***). Modified from Tatsch, 2018

6.11 Inter pulse interval for recordings of PP facilitation at the larval NMJ

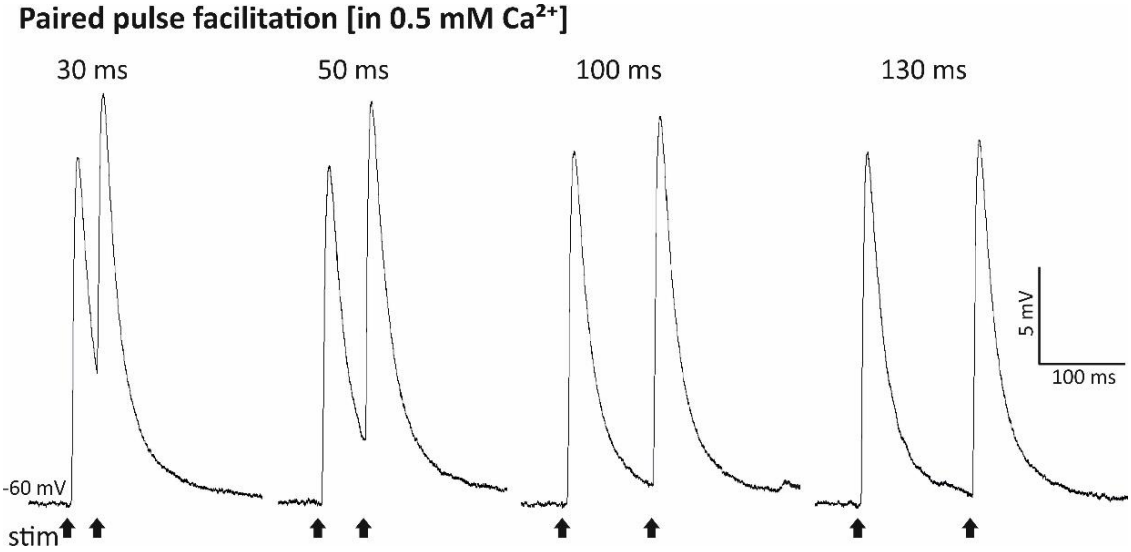

Fig.S5: Paired pulse (PP) interval to record PP facilitation at the larval NMJ

Evoked postsynaptic potentials (EPSP) were recorded intracellularly from muscle M10 in current-clamp mode while stimulating the respective nerve. A calcium concentration of 0.5 mM was used for the extracellular bath solution. Paired pulses with an inter pulse interval of 30, 50, 100 & 130 ms were applied. At 30 and 50 ms, the rising phase of second EPSP was riding on the falling phase of the first EPSP, and thus, the amplitude of the second EPSP was difficult to determine. At 100 ms inter-pulse interval, the first EPSP was not fully, but mostly repolarized before the second occurred and the amplitude of the second EPSP was facilitated. At 130 ms the muscle was still not fully repolarized from the first EPSP, but PP facilitation was already relatively low.

6.12 Synaptic depression phenotype of Stj^{RNAi} mimics the effects of a relatively weak Ca$_V$2 knockdown

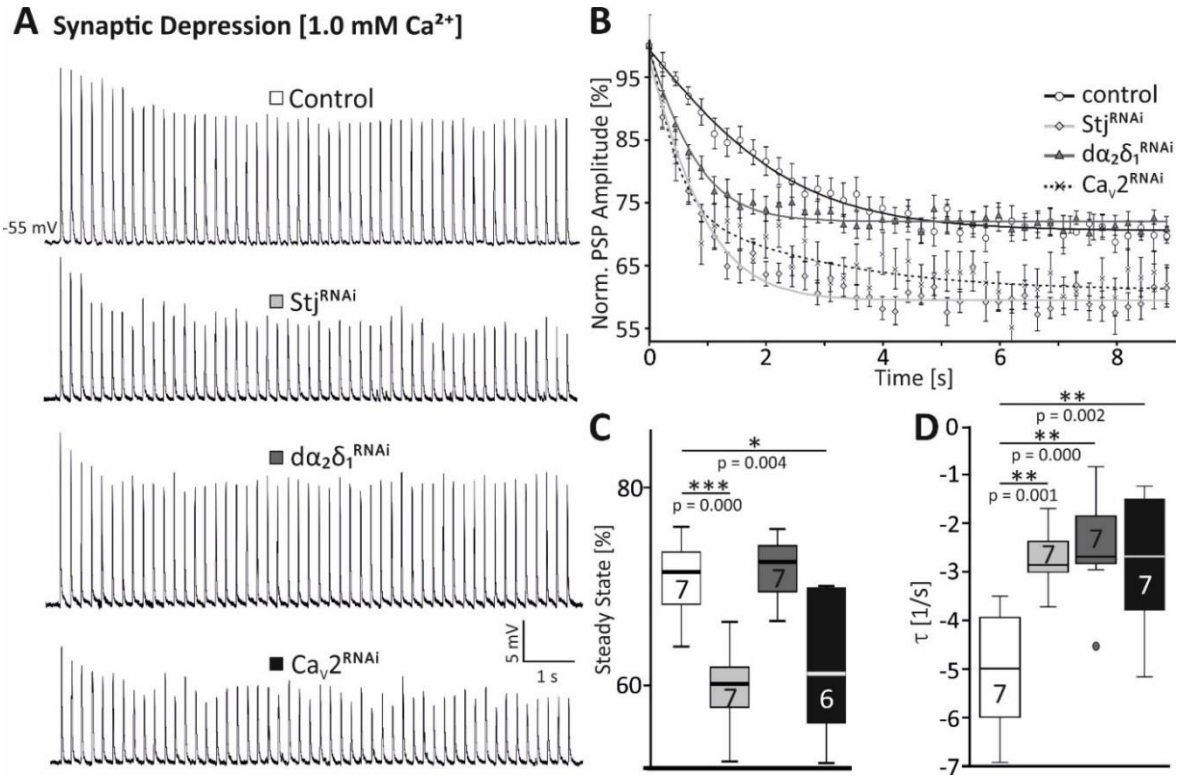

Fig.S6: Synaptic depression phenotype of Stj^{RNAi} mimics the effects of a relatively weak Ca$_V$2 knockdown
Evoked postsynaptic potentials (EPSP) were recorded intracellularly from muscle M10 in current-clamp mode while stimulating the respective nerve. A calcium concentration of 1.0 mM was used for the extracellular bath solution. [**A**] EPSP trains (5 Hz for 10 s) were recorded in controls (UAS-dcr2, white box) and larvae with targeted knockdown of Stj (UAS-Stj^{RNAi}; UAS-dcr2, light gray box), dα$_2$δ$_1$ (UAS- dα$_2$δ$_1{}^{RNAi}$; UAS-dcr2, dark gray box) and Ca$_V$2 (UAS-Ca$_V$2^{RNAi}, black box) in glutamatergic neurons (OK371-Gal4). [**B**] EPSP amplitudes were measured and normalized to the first EPSP. The normalized EPSP amplitudes were then plotted against time and fitted by a Boltzmann fit to assess the time constant τ and steady-state amplitude of synaptic depression. Whiskers represent the standard error. [**C**] τ was increased in Stj^{RNAi} (p = 0.001), dα$_2$δ$_1{}^{RNAi}$ (p = 0.000) and Ca$_V$2^{RNAi} (p = 0.002) compared to control (ANOVA, p = 0.002). [**D**] Steady-state of depression was reduced in both Stj^{RNAi} (p = 0.000) and Ca$_V$2^{RNAi}, but not in dα$_2$δ$_1{}^{RNAi}$ (p = 0.705) compared to control (ANOVA, p = 0.000). Boxes display median with 25 and 75% quartiles, whiskers represent 10 and 90% quartiles. The number of replicates is given inside the respective box. A one-way ANOVA and LSD posthoc tests were done for statistical analysis (p < 0.05*; p < 0.01**; p < 0.001***).

6.13 dα₂δ₁ is required for normal dendritic Ca^{2+} currents in pupal MN5 motoneurons

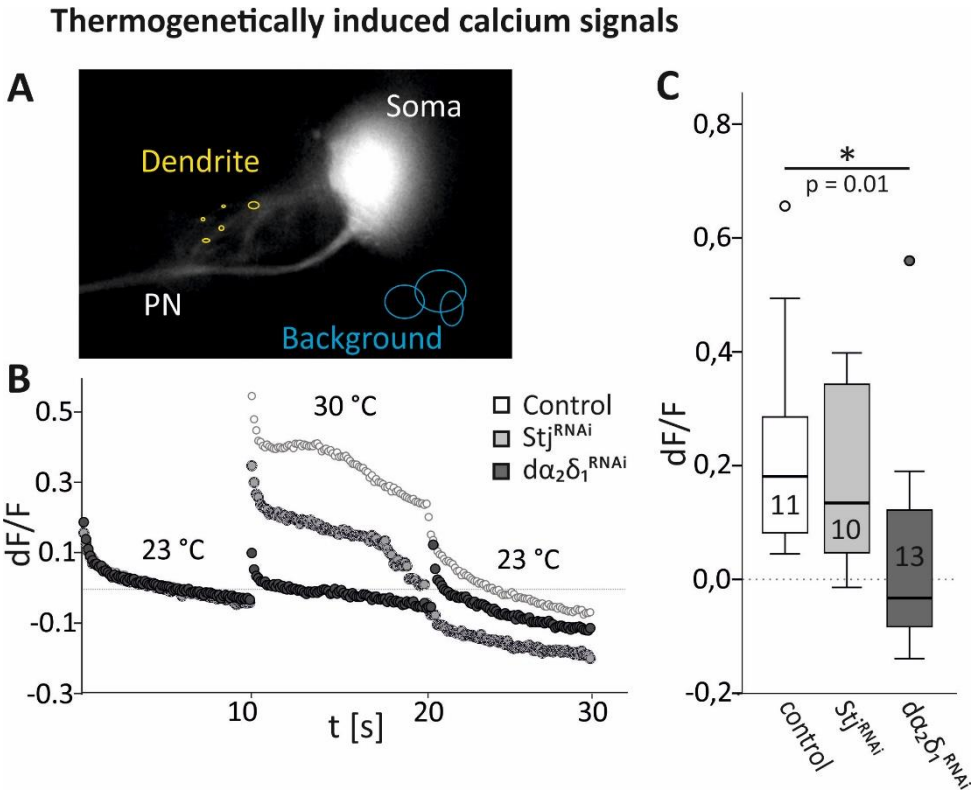

Fig.S7: dα₂δ₁ is required for normal dendritic Ca^{2+} currents in pupal MN5 motoneurons

[**A**] Calcium imaging was done from dendrites (yellow circles) of wing depressor neuron MN5 expressing the calcium sensor GCamp6s and a temperature-sensitive TrpA channel (UAS-GCamp6s,UAS-$TrpA^{ts}$;D42-Gal4,Cha-Gal80). Changes in calcium fluorescence were measured upon activation of MN5 via thermogenetic manipulations; at 23 °C, 30 °C and again at 23 °C for 10s each. Ca^{2+} responses were recorded from flies additionally expressing Stj^{RNAi} (UAS-Stj^{RNAi};UAS-dcr2, light gray boxes) or dα₂$δ_1^{RNAi}$ (UAS- dα₂$δ_1^{RNAi}$;UAS-dcr2, dark gray boxes) and controls (UAS-dcr2, white boxes). [**B**] Representative sample measurements of each genotype with dF/F ($\Delta F/F = (F_{active}/F_{Rest})/F_{Rest}$) plotted over time. [**C**] The increase in GCamp6s fluorescence upon thermogenetic activation of MN5 was evaluated. Per neuron the mean value of all data points measured at 30 °C was calculated. The increase in GCamp6s fluorescence was reduced in dendrites of dα₂$δ_1^{RNAi}$ ($p = 0.01$) compared to control (ANOVA, $p = 0.009$), but not in Stj ($p = 1.00$). Boxes display median with 25 and 75% quartiles, whiskers represent 10 and 90% quartiles. The number of replicates is given inside the respective box. A Kruskal-Wallis ANOVA and Dunn-Bonferroni post-hoc tests were done for statistical analysis ($p < 0.05$*; $p < 0.01$**; $p < 0.001$***).